



UiT The Arctic University of Norway

Faculty of Science and Technology

Department of Geosciences

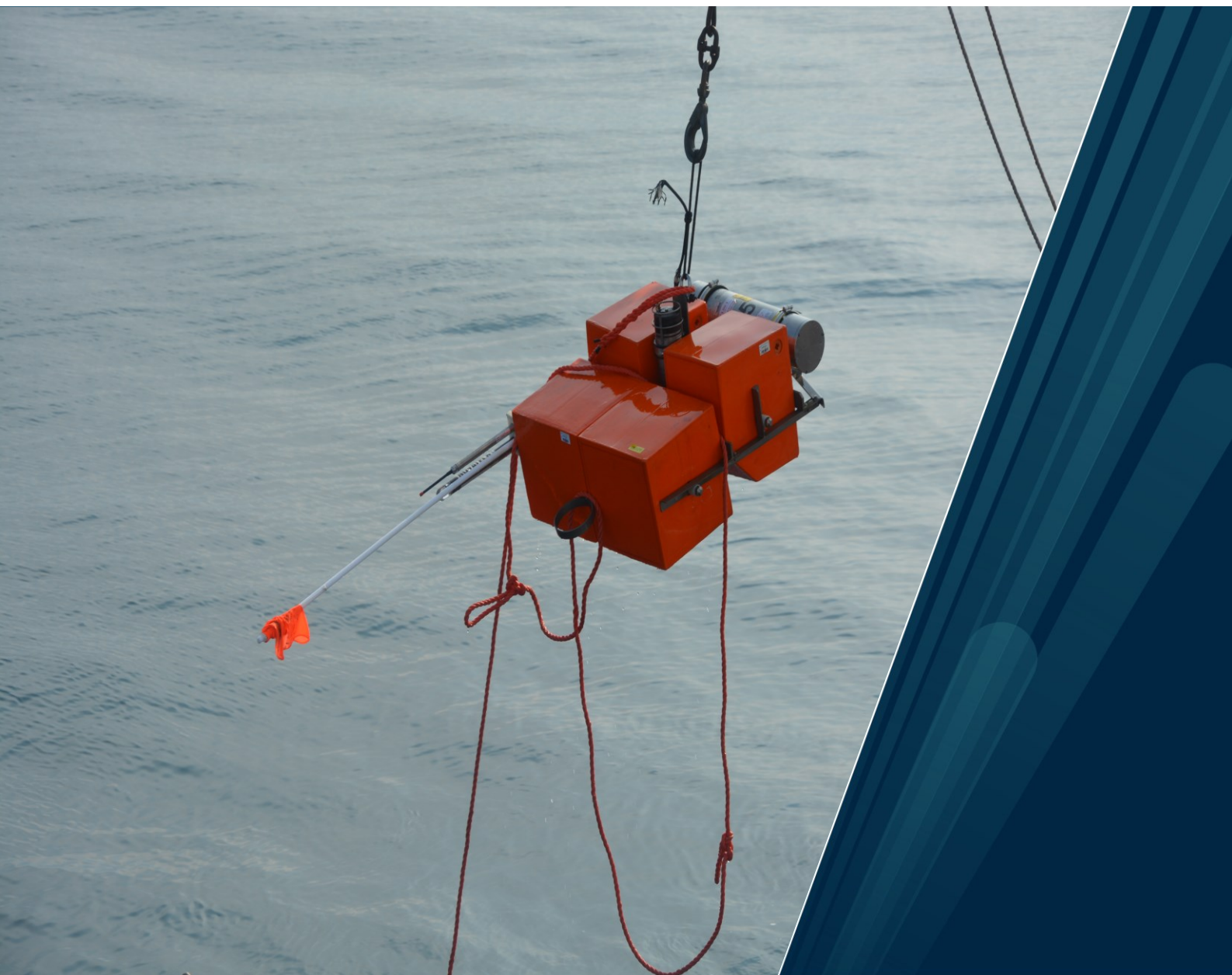
Seismicity of the western-Svalbard margin and its relationship with near surface fluid flow and seepage systems

A study using ocean bottom seismometers

Przemysław Domel

A dissertation for the degree of Philosophiae Doctor (PhD)

August 2023



Seismicity of the western-Svalbard margin and its relationship with near surface fluid flow and seepage systems

A study using ocean bottom seismometers

Przemysław Domel

A dissertation for the degree of Philosophiae Doctor

UiT The Arctic University of Norway

Faculty of Science and Technology

Department of Geosciences

August 2023



UiT The Arctic
University of Norway

Supervisors:

Associate Professor Andreia Plaza-Faverola

Department of Geosciences
Faculty of Science and Technology
UiT The Arctic University of Norway, Tromsø, Norway

Professor Vera Schlindwein

Alfred Wegener Institute, Helmholtz Centre for Polar and Marine Research
Bremerhaven, Germany

Faculty of Geosciences
University of Bremen, Bremen, Germany

Professor Stefan Bünz

Department of Geosciences
Faculty of Science and Technology
UiT The Arctic University of Norway, Tromsø, Norway

ISBN: 978-82-8236-537-6

© Przemysław Domel, 2023

The material in this publication is covered by the provisions of the Copyright Act.

Front page image: Ocean bottom seismometer straight after the recovery

Taken by: Manuel Moser

Pamięci babci Petroneli

Acknowledgements

This PhD work occupied me almost completely in the last four years. There were many moments of doubts, frustration and wondering whether I will manage to see the end of it. And I am pretty sure I would not, if not dedication, help and friendship of many people who I encountered while working here. The credit for this thesis goes in the equal manner to them as it is to me, therefore I believe some more detailed recognition is in order.

Firstly, I would like to thank my main supervisor Andreia Plaza-Faverola. She always had the time to look at my work, give me suggestions, reply quickly even in the middle of the night, and give me the support when I needed it the most. She was also from time to time a source of some degree of frustration on my part. More often than not, she was right to curb my enthusiasm just a little bit. The comments and critique she raised was often valid and through her insistence I only became better at doing what I did, so thank you, Andreia. I would like to thank my co-supervisors equally warmly: Vera Schindwein at AWI in Germany and Stefan Bünz here in Tromsø. Vera provided a wealth of knowledge in seismology and taught me about many aspects of working with ocean bottom data. She was equally patient with me in providing comments, feedback, and suggestions. She was also kind enough to host me at AWI for 4 months in 2022 which greatly benefitted my PhD work. I need to thank Stefan Bünz for level head during each cruise I participated in with him, his knowledge and calm manner ensured that I was lucky to work with so much exciting data in the end. His help was also clearly felt at the office, and he was always happy to chat and give me suggestions whenever he had the time. I would also like to thank here Clément Hibert from University of Strasbourg, France, for a very fruitful collaboration and teaching me many things related to machine learning.

Since I mentioned my stay in Germany, I would like here to thank Mechita Schmidt-Aursch and Henning Kirk from AWI for help with the deployment of seismometers and its recovery and expertly taking care by the obtained data by Mechita. Similarly, for separate cruises, I want to thank Anke Dannowski and Bettina Schramm from GEOMAR in Germany for help in obtaining another dataset. Big thanks for all the help to our engineers (current and past): Steinar, Truls and Stormer.

When I arrived in Tromsø, I was brought up to speed by Peter Franek who shared the data, some of his work and useful suggestions with me, so big thank you for this. After I got a bit in the rhythm there was however someone else who gave me great advice both in work and in personal matters. Thank you SO much Sunny Singhroha. We had so many great discussions and I was always overwhelmed by your wit and kindness in helping me out. Good luck at the new workplace and all the best to you and your family.

I want to thank other co-workers (in no particular order) and apologize in advance for omitting someone. Sunil for help during cruises, in the office and moving my stuff around Tromsø. Manuel for a great friendship, many enjoyable evenings with great and terrible movies. Jenny for honest conversations and good advice. Mariana, Zeynep, Lone and Fabio for all the help with administrative matters and patience to listen to my complaints. Naima for being a great friend, great supporter, and a warm and wonderful human being. Kasia for the solid dose of skepticism and a steady supply of memes. Stephan, Marie, and Magnus for our misadventures in the world of board games. Harih for all the help and many complaining sessions together.

Julian, Max, Marina, and Stine for being such a cool people. Claudio for being a good friend and good advisor. Fatih, Knut Ola, Frank, Cornelia, Lina, and Frank for being excellent office mates in buildings old and new. Special shoutout to Griselda, who started with me and will finish in similar time, thank you for the help in the last stretch. It really helped to have someone to share the same struggles at the very end. Thank you to her great office mates: Adele, Freya, and Christine. I promise I will not interrupt your work anymore.

Marie, thank you for being my companion, my partner in crime and a fellow space enthusiast. I am extremely lucky to be with you and you have no idea how much you helped me to get through all of this. Merci beaucoup.

I wreszcie, moim rodzicom: Krystynie i Henrykowi. To wam zawdzięczam wszystko, sposób w jaki zostałem wychowany, moją edukację i wszystko co osiągnąłem do tej pory. Nawet gdy nie zawsze zgadzaliście się z moim decyzjami, zawsze je wspieraliście. Dziękuję za wszystko.

Przemek

Preface

This thesis is a result of four years (2019-2023) of doctoral education under the supervision of Assoc. Prof. Andrea Plaza-Faverola and Prof. Stefan Bünz from the Department of Geosciences at the UiT The Arctic University of Norway, Tromsø, with the external supervision of Prof. Vera Schlindwein at the Alfred Wegener Institute, Helmholtz Centre for Polar and Marine Research, Bremerhaven, Germany and Faculty of Geosciences, University of Bremen, Bremen, Germany. This work was a part of the SEAMSTRESS project, funded by the Research Council of Norway and Tromsø Research Foundation (grant number 287865). Until February 2023, it was also a part of Centre for Arctic Gas Hydrate, Environment and Climate (CAGE), funded by the Research Council of Norway and supported by the Research Council of Norway Centers of Excellence funding scheme (grant number 223259).

The main objective of this PhD was to use seismological data from ocean bottom seismometer deployments to improve understanding of the fluid flow systems in the Fram Strait, offshore Svalbard. For this purpose, three separate datasets have been used. The initial processing of the third dataset took place at Alfred Wegener Institute in Bremerhaven, Germany, where I stayed for a total of four months. This research stay was financially supported by the UiT travel grant for PhD candidates.

The mandatory educational component was fulfilled by the participation in four courses (three at UiT and one at the University Centre in Svalbard – UNIS) and one educational cruise at UiT. I took part in Marine Geophysics course (GEO-8123), Philosophy of Science and Ethics course (SVF-8600), Arctic Seismic Exploration course (AG-835 at UNIS), and Arctic marine geology and geophysics workshop (GEO-8145). I also participated in Marine geology and geophysics cruise (GEO-8144) in 2021. During the course of my PhD education, I was affiliated with following research schools: Geoscience Research Academy of Tromsø (GReAT), Research School on Changing Climates in the Coupled Earth System (CHESS), Norwegian Geophysical Society (Norsk Geofysisk Forening – NGF), and Norwegian Research School for Dynamics and Evolution of Earth and Planets (DEEP). Between 2019 and 2021, I participated in following research cruises: CAGE19-1 (June – July 2019), CAGE19-2 (July 2019), CAGE19-3 (October – November 2019), CAGE20-5 (August 2020), CAGE20-6 (October 2020), CAGE21-1 (May - June 2021), CAGE21-3 (July 2021), and CAGE21-5 (October 2021).

I have participated and presented the scientific results of my work at several national and international conferences and workshops, including AGU Fall Meeting 2020 (American Geophysical Union; online participation), CAGE Invites Conference (May 2022, Tromsø), CAGE International Conference (September 2022, Tromsø), EGU23 General Assembly

(European Geosciences Union; April 2023, Vienna) and Nordic Seismology Seminar 2023 (June 2023, Bergen, Norway).

The first part of my thesis introduces motivation and objectives, including the background of the project and overall framework. In the second part, I discuss the scientific approach used to produce the research finding documented in this work. The third part provides the necessary geological framework of the study area from the tectonic and sedimentological perspective. The fourth part contains a summary of all research articles presented in this thesis. Finally, the overall outcome of the thesis is discussed in the fifth chapter and potential avenues of future research directions are suggested. Subsequently, the three research articles of this thesis are presented.

This thesis consists of an introduction to the following research papers:

- **Article 1:**

Domel, P., Singhroha, S., Plaza-Faverola, A., Schlindwein, V., Ramachandran, H., & Bünz, S. (2022). **Origin and Periodic Behavior of Short Duration Signals Recorded by Seismometers at Vestnesa Ridge, an Active Seepage Site on the West-Svalbard Continental Margin.** *Frontiers in Earth Science*, 10. <https://doi.org/10.3389/feart.2022.831526>

Data related to this paper: <https://doi.org/10.18710/TCWUQN>

- **Article 2:**

Domel, P., Hibert, C., Schlindwein, V., & Plaza-Faverola, A. (2023). **Event recognition in marine seismological data using Random Forest machine learning classifier.** *Geophysical Journal International*, 235(1), 589-609. <https://doi.org/10.1093/gji/ggad244>

Data related to this paper to be published in UiT Open Research Data repository.

- **Manuscript 3:**

Domel, P., Plaza-Faverola, A., Schlindwein, V., & Bünz, S. (2023). **Local seismicity and sediment deformation in the west Svalbard margin: Implications of neotectonics for seafloor seepage.** Manuscript submitted to *Geophysics, Geochemistry, Geosystems*.

Data related to this paper: <https://doi.pangaea.de/10.1594/PANGAEA.952424>

Table of Contents

Acknowledgements	I
Preface	III
SECTION I Synthesis	1
1 Introduction	3
1.1 Scope of the thesis.....	3
1.2 Motivation and objectives	3
1.3 Fluid flow processes in near surface sediments	5
1.4 Fluid flow, fractures, and seismicity generation	8
1.4.1 Earthquakes.....	9
1.4.2 Signals related to fluid flow.....	11
1.5 External triggers and modulators of fluid flow	14
2 Scientific approach	17
2.1 OBS instruments	17
2.2 Datasets.....	18
2.3 OBS data processing	18
2.3.1 Seismometer deployment.....	19
2.3.2 Event detection/recognition (Article 2).....	21
2.3.3 Phase picking – absolute time.....	24
3 Study area	25
3.1 Tectonic setting	25
3.2 Sedimentary setting.....	26
3.3 Seepage systems in the study area.....	26
4 Summary of research papers	29
4.1 Main findings.....	29
5 Concluding remarks and outlook	33
6 References	37
SECTION II Research papers	51

SECTION I Synthesis

1 Introduction

1.1 Scope of the thesis

The PhD work was conducted as a part of the SEAMSTRESS project – Tectonic stress effects on Arctic methane seepage. The SEAMSTRESS project goal is to quantify the amount of tectonic influence on the release of greenhouse gases from the ocean floor in the Arctic. This means taking a multidisciplinary approach that includes stress modelling, seismic data interpretation, in-situ measurements and modelling, and seismological observations. This thesis aims to improve the understanding of the relationship between seismic activity and focused fluid flow systems driving the seepage using the recordings from ocean bottom seismometers (OBS). This work includes both an analysis of microseismicity potentially linked to the seepage and a study of regional earthquake patterns to improve the knowledge about tectonic stress regime. A methodological prerequisite for this study was the development of a new automated signal classification method for ocean bottom seismological data sets.

1.2 Motivation and objectives

Submarine flow of liquids and gases from the seafloor is a ubiquitous process documented in continental margins worldwide (e.g., Judd & Hovland, 2007; Etiope, 2015). It drives the natural gas release (“*seepage*”) into the water column in a form of “*cold*” seeps. Natural gas, mostly methane, which reaches the water column provides an ample source of energy for bacterial communities, but also contributes to ocean acidification (increase of CO₂), and reduction of the oxygen in the water (Reeburgh, 2007). Transient increase of the fluid pore pressure is the most efficient way of reducing shear strength of sediments, therefore fluid flow plays an important role in submarine landslide generation and potential tsunami hazard (Huhn et al., 2020). Landslides also pose a risk for the ever-expanding network of submarine telecommunication cables (Carter et al., 2014), and can lead to earthquakes that cause damage to people and infrastructure in the coastal areas (e.g., Gardner et al., 2001). Conversely, monitoring of the seepage can also provide a forecasting before occurrence of large magnitude earthquakes (Hovland et al., 2002). Direct observations in the water column are usually short-term and therefore we lack the understanding of mechanisms causing seepage, the way its intensity changes and how it varies on shorter and longer timescales (Riedel et al., 2018).

The objective of this thesis is to investigate naturally occurring (referred hereafter as “*passive*”) seismological signals that were recorded on the ocean seafloor and their connection to fluid flow processes occurring in shallow sediments on a continental margin. OBS observations can

provide long-term (up to a year), continuous information about seismological processes and their potential relation to fluid flow. This investigation is done both on a local and a more regional scale. We studied local seismic signals (dubbed *short duration events* in the literature) in the vicinity of seepage sites (micro seismicity studies, **Article 1**). We also analyzed the earthquake occurrence in the region to better understand the tectonic setting and large-scale forces (regional stress field) acting on sediments filled with gas (**Manuscript 3**). The processing of OBS recordings is challenging due to the unknown orientation and tilt of the seismometer (unless placed by a remotely operated vehicle), the large variety of noise sources that have to be differentiated from the useful signal, the large data volume, and in general the lower signal-to-noise ratio compared to records from land. This necessitates the development of a new, semi-automatic processing approach for marine seismological data which is also presented in this thesis (**Article 2**).

This study incorporates three separate OBS datasets from fluid flow systems on the west Svalbard continental margin (Figure 1). This area is interesting due to the proposed tectonic control of the nearby ultraslow spreading system as well as of glacio-tectonics on the seepage distribution at present and in the past (Plaza-Faverola et al., 2015; Plaza-Faverola & Keiding, 2022). Passive seismological observations can provide unique insight in the present-day tectonic activity influence on the seepage and complement seismic interpretation, seepage and tectonic stress modelling, in-situ geotechnical measurements and sediment core analyses to obtain a comprehensive understanding of the fluid flow system.

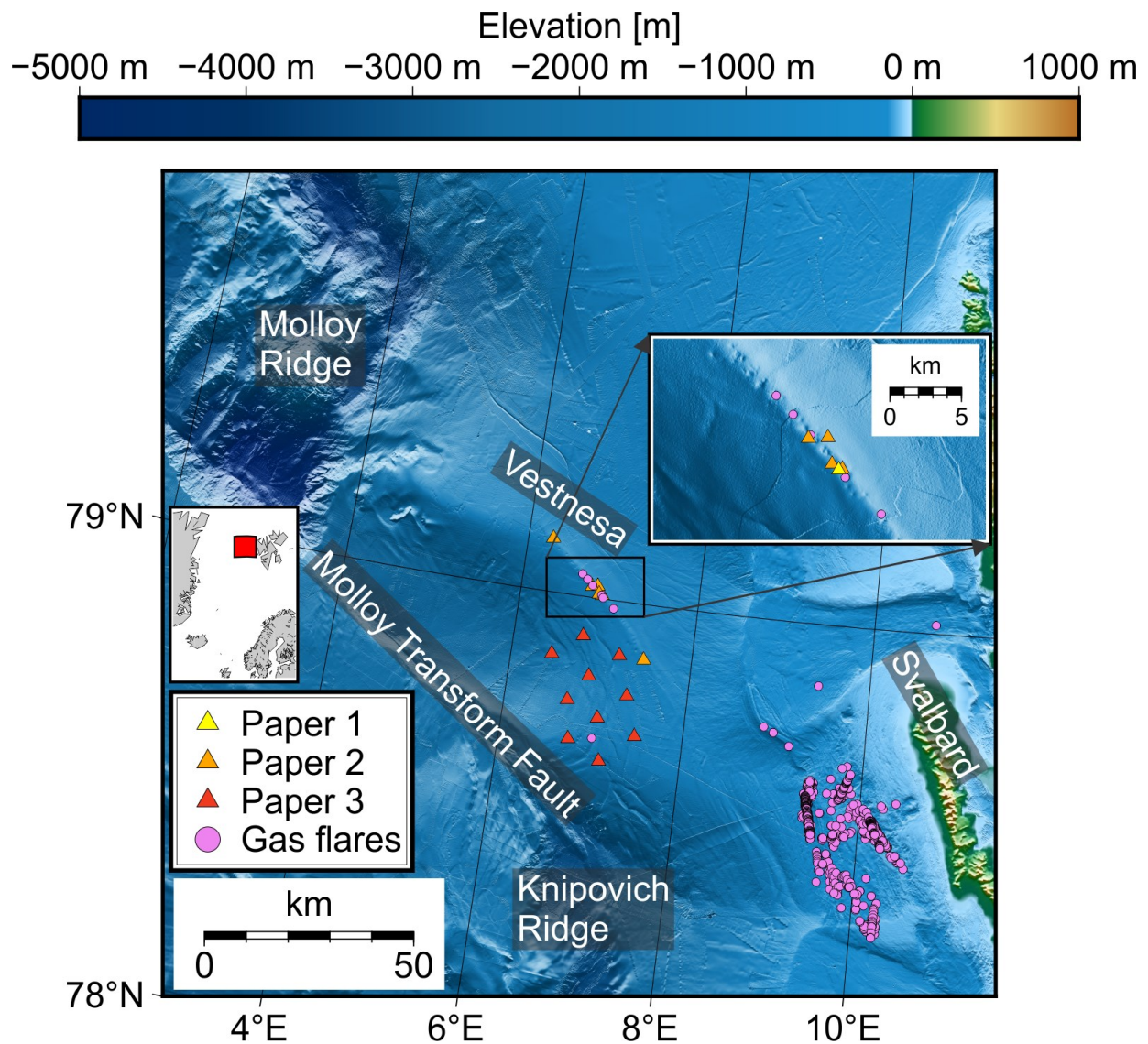


Figure 1. The geographic position of OBS datasets presented in this thesis with the corresponding manuscript number, along with the documented gas seepage sites for west Svalbard continental margin. Gas seepage locations from e.g., Smith et al., (2014); Panieri et al., (2017).

1.3 Fluid flow processes in near surface sediments

Sedimentary basins in continental margin settings are dynamic environments. Water, hydrocarbons, and magmatic gases migrate toward the surface. The excess fluid in a rock comes from a variety of sources. During the sediment deposition, compaction processes lead to a large volume of brine to be expelled due to the sediment weight (Judd & Hovland, 2007). In the coastal areas, submarine groundwater discharge is an important source of water. Hot water and gases can be provided by the magmatic source at depth (Judd & Hovland, 2007). Hydrocarbons are being produced at depth from the decomposition of biological matter in rocks (Tissot & Welte, 1984), but natural gas (mostly methane) can also be a result of the lifecycle of methanogenetic archaea close to the seafloor (e.g., Claypool & Kaplan, 1974). In the shallow subsurface, within a specific temperature and pressure interval, accumulated gas can

form hydrates (Sloan, 1998). The process of hydrate formation and dissociation can be very dynamic close to the seafloor and hydrate dissociation is another source of fluid in the rocks (Valentine, 2010).

Two main processes control the migration of the fluids: diffusion and advection (Etioppe, 2015). Uniform spreading of the pore fluid molecules to equalize its concentrations occurs through diffusion. When the movement is dictated by the pressure gradient (from high to low) and the entire pore medium mobilizes, the process is driven by advection (Figure 2).

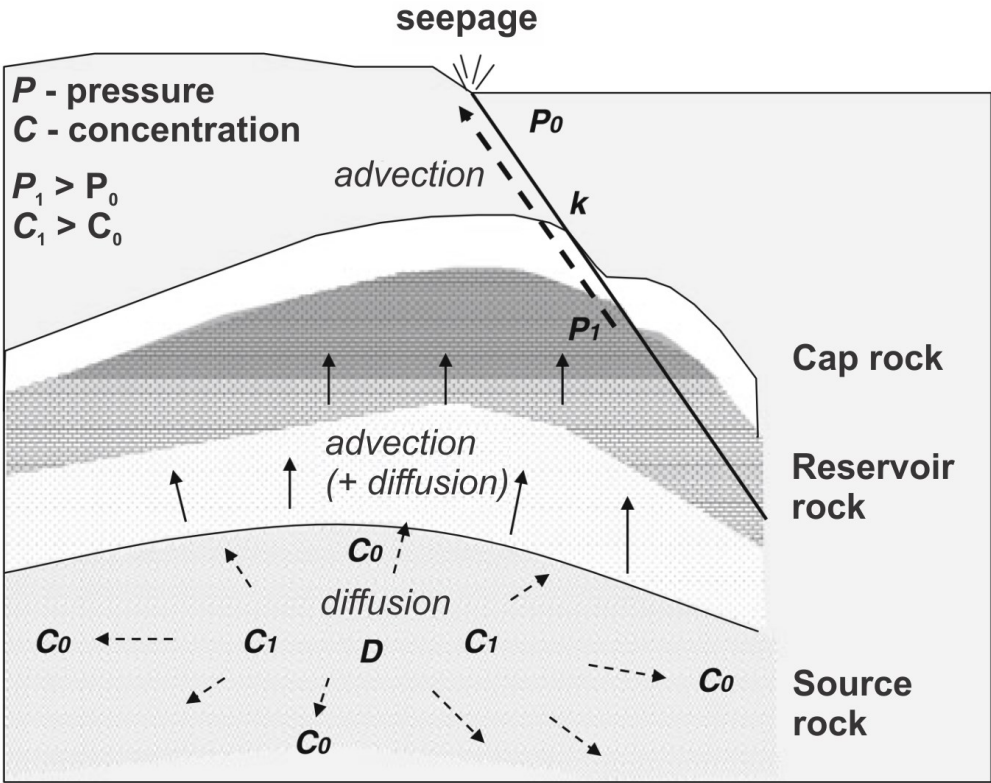


Figure 2. The processes controlling gas migration to the surface (modified from Etioppe, 2015).

When the advective process is a dominant driver, the flow becomes focused and leads to creation of pipes and chimneys that can be observed using geophysical methods (Berndt, 2005). Focused fluid flow manifests itself on the seafloor in a variety of form (Judd & Hovland, 2007), including:

- Pockmarks
 - Pingos
 - Mud volcanoes
 - Mud diapirs
 - Hydrothermal vents
- } Cold seeps

The fundamental driver behind the advective flow of fluid is an excess pressure (*overpressure*) of pore fluid compared to hydrostatic equilibrium (Figure 3; e.g., Dugan & Sheahan, 2012). Overpressure is common in subsurface rocks, especially at depth, and can be generated locally by a variety of processes. In sedimentary basins, the speed of deposition controls the rock compaction and expulsion of fluids. Under normal conditions, compaction of rocks occurs slowly enough for fluid to migrate towards the surface (Osborne & Swarbrick, 1997). With the increase of depth, the decrease of the available pore space leads pressure of the pore fluid to rise. When the sedimentation is rapid, there is not enough time for fluids to migrate towards the surface and overpressure is generated at shallower depths. In the presence of gas hydrates, progressive subsidence of the rock leads to hydrate instability and dissolved gas can also generate overpressure (Hunt, 1979). Fluids, usually hydrocarbons, migrating from the source rock at greater depths will increase the pore pressure under lower than original hydrostatic load (Dugan & Sheahan, 2012). At greater (>1 km) depths, thermal and chemical processes can lead to the increase of fluid pressure. Vertical load of the water column due to the sea level rise also leads to increase in the pore pressure fluid in shallow sediments (Smith et al., 2013). Overpressure is also created by the forces acting laterally. Tectonic processes, acting in present day and/or in the past can cause compression of the rock intervals and buildup of the pressure (Osborne & Swarbrick, 1997). For the areas experiencing glacial episodes in the past, such as the one presented in this thesis, glacial isostatic rebalancing can induce overpressure as the structures bend due to the presence and subsequent lack of the glacial load (e.g., Thorson, 2000; Grollmund & Zoback, 2000). It is important to emphasize that overpressure can occur at very shallow depths (e.g., Dugan & Sheahan, 2012; Plaza-Faverola et al., 2023a).

The difference between the externally applied stress on the sediment and the pore pressure is termed *effective* stress (Zoback, 2010). The relation between effective stresses acting on a sediment and the internal rock strength controls when and in what way the rock will fracture. Faulting of the sediments plays a major role in the distribution of the fluid flow (e.g., Knipe, 1992, 1993; Faulkner et al., 2010). Fault zones usually provide higher permeability medium for fluids to travel, but can also restrict fluid movement (Caine et al., 1996). In the presence of overpressure, fluids will much more likely re-open existing faults and undergo movement instead of creating new fractures, since the tensile strength of existing faults is equal to zero (Talukder, 2012). Similarly, faults play a fundamental role in the fluid expulsion at the seafloor. Gas seepage has been associated with all types of faults in both compressive and extensional regimes (e.g., Bernard et al., 1976; Hovland & Curzi, 1989; Macgregor, 1993; Schroot et al., 2005; Chen et al., 2010; Gasperini et al., 2012; Plaza-Faverola et al., 2013; Grall et al., 2018). The content of the fluid circulating through sediments influence the medium characteristics as

well. For example, presence of gas alters the elastic and mechanical properties of the soft sediments and can enhance fracturing (e.g., Daigle & Dugan, 2010; Barry et al., 2012; Boudreau, 2012). Processes related to the sediment fracturing and the flow of fluid can manifest itself in a form of recordable seismic signals.

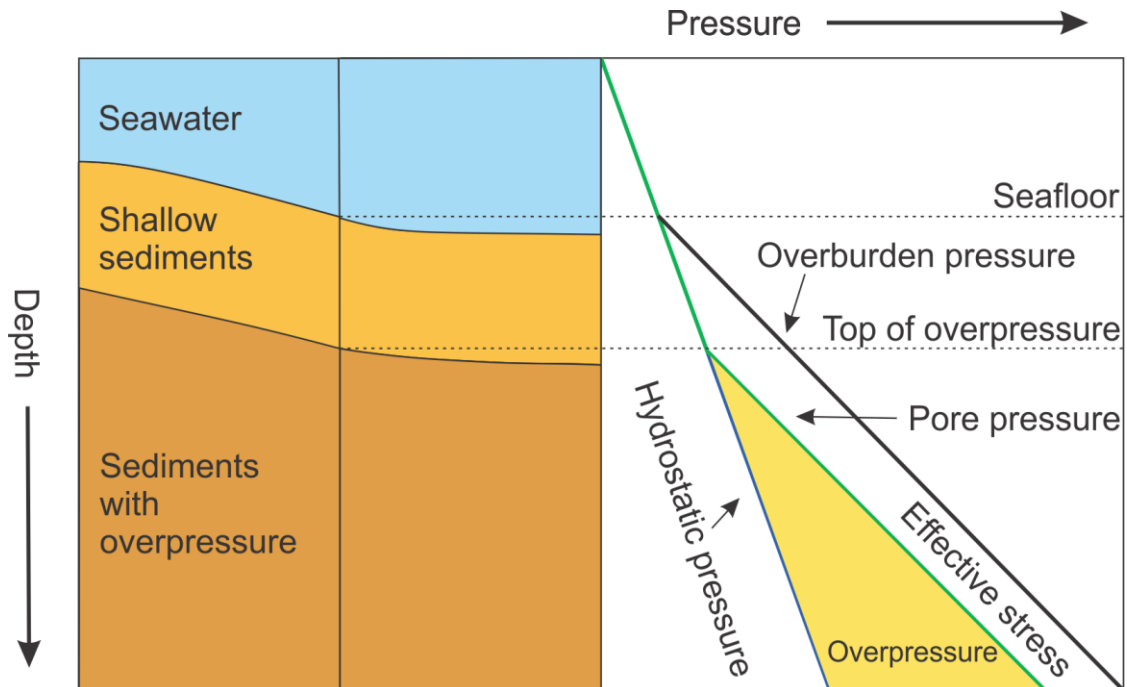


Figure 3. Pressure-depth relation for over pressured sediments (modified from Li et al., 2022).

1.4 Fluid flow, fractures, and seismicity generation

In the presence of gas, shallow sediments can fracture in two different ways. The first is hydraulic fracturing driven by pore fluid pressure or high capillary entry pressures of free gas, and the second is caused by the shear failure of the sediments (Daigle & Dugan, 2010; Scholz, 2019). The majority of investigations related to hydraulic fracturing comes from the studies related to fracturing the rocks for geothermal and hydrocarbon extraction purposes and it is generally perceived that hydraulic fracturing is a result of a tensile process due to increased pore pressure (Maxwell & Cipolla, 2011; Stoeckhert et al., 2011). However, modelling and field experiments related to seismic signal suggest that significant component of fracturing also involves shear and tensile-shear modes (e.g., Urbancic & Maxwell, 2010; Duan, 2016; Naoi et al., 2020). Tensile mode fracturing is well observed through laboratory experiments and the measurement of acoustic emission events in the rock samples. These energetic signals are recorded in the kHz-MHz range, follow Gutenberg-Richter law, and resemble earthquakes on time-series and spectrograms in shape, but their frequencies are much higher, and their duration is measured in microseconds (e.g., Graham et al., 2010; Stanchits et al., 2011; Grosse et al., 2021). However, they can only be recorded by high-sampling sensors placed

directly on the rock. It is not yet determined though, if the rock cohesion in most reservoirs (at depths greater $> 1\text{km}$) is strong enough to produce micro seismicity in the pure tensile mode detectable by seismometers (Duan, 2016). Following the same logic, this seems even less likely in weakly cohesive shallow sediments. Most micro seismic studies are therefore dedicated to the analysis of weak earthquakes of magnitude 0 and less (e.g., Rubinstein & Mahani, 2015; Atkinson et al., 2020; Schultz et al., 2020).

1.4.1 Earthquakes

An earthquake is a result of the stress exerted on the rock exceeding its internal strength. Following the classification of Anderson (1905, 1951), we can describe the state of stress in the subsurface using three principal components: one vertical, perpendicular to the earth surface; and two horizontals, perpendicular to each other and the vertical one. Their relative magnitude reflects the mode of faulting occurring when the strength of the rock is exceeded (Figure 4). It is generally assumed that all the principal stresses in the Earth are compressive, due to the weakness of rock under tension (Kanamori & Brodsky, 2004). When least principal stress is greater than the strength of the rock, tensile fracturing occurs. The shear fracturing of the rock is controlled by the relation between maximum and minimum effective stresses (Mohr-Coulomb criterion; Scholtz, 2019). The earthquake process itself is driven by the shear failure of a brittle rock under the compression. As an approximation, an earthquake can be considered as a dynamically running shear crack (Kanamori & Brodsky, 2004; Scholz, 2019).

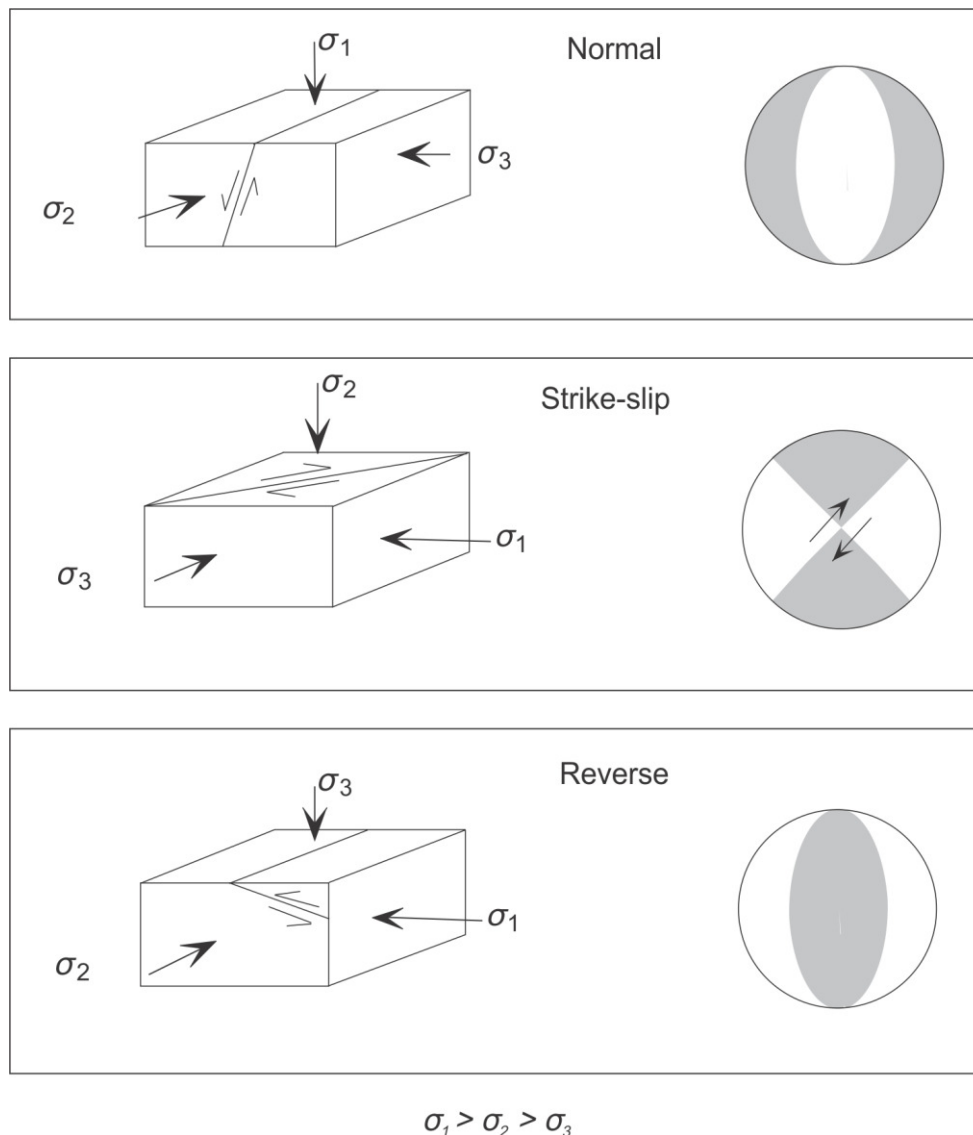


Figure 4. Modes of faulting under different stress conditions (modified from Zoback, 2010)

Pore fluid modifies the overall stress affecting the rock and makes it easier to fail when rock is over pressured (Figure 5A; Kanamori & Brodsky, 2004). In a similar manner to the excess pore fluid influence, the amount of stress required for the slip on an existing fault is reduced through the lowered coefficient of friction (Figure 5B). Fluid overpressure is one of the primary mechanisms for tectonic fault slip, because fluids lubricate the fault and fluid pressure reduces the effective normal stress that holds the fault in place (e.g., Hubbert & Rubey, 1959; Scuderi & Colletini, 2016).

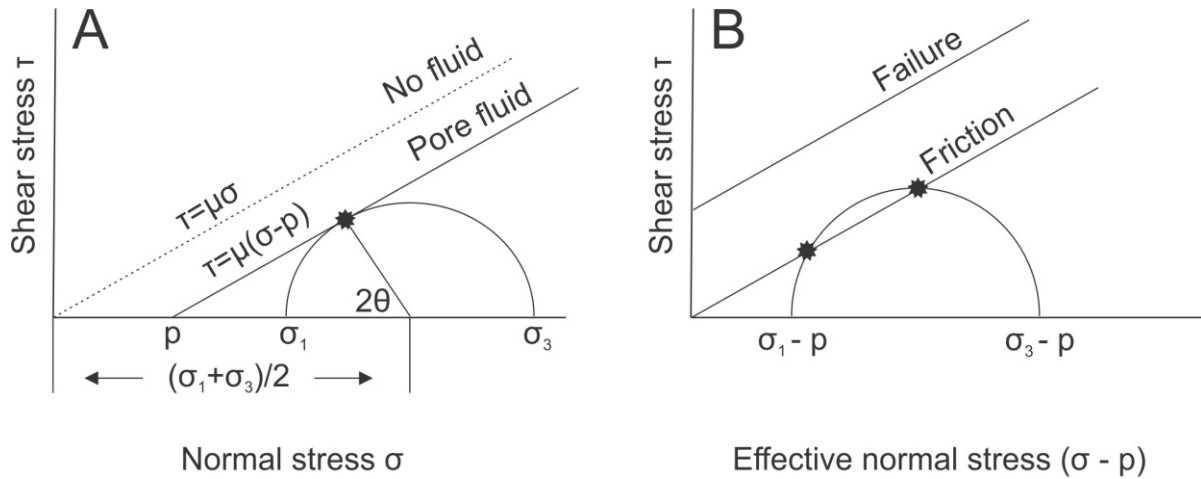


Figure 5. Mohr diagrams showing possible combinations of the maximum and minimum principal stresses with the failure criteria with/without presence of pore fluid (A) and failure and friction depiction in the case of existing fault plane (B). Modified from Kanamori & Brodsky (2004).

Ultimately, the shear failure of the rock (from microscopic scale to hundreds of kilometers) leads to a stress drop and radiation of energy that generates elastic wavefield recorded as an earthquake on seismograms. Only a portion of energy is radiated, some is dissipated mechanically and some thermally (Kanamori & Brodsky, 2004). The mechanical process itself can be modelled in different ways, such as dynamically propagating crack, sliding on a frictional surface, a mixture of both and other (Kanamori & Brodsky, 2004). The influence of thermal radiation can be important, especially in large earthquakes. It can cause pore fluid pressurization and overpressure in the rock; the fault surface can undergo melting and fault zone can exhibit reduced friction due to lubrication.

1.4.2 Signals related to fluid flow

In addition to mechanical failure, processes related to the fluid movement itself have been shown to generate distinct seismic signature, especially in the near field. The presence of fluids in rupture process is often linked to tremor-like signals and long-period events, observed in different geological contexts, such as volcanism, hydraulic fracturing, subduction zones, crustal faults, glacial dynamics and even landslides (Obara, 2002; Chouet, 2003; Ide et al., 2007; Peng & Gombert, 2010; Das & Zoback, 2011; Gräff et al., 2019). Inducing of these signals was directly observed through fluid injection into the fault (Derode et al., 2015), and in laboratory experiments (Nakagawa et al., 2016, Cao et al., 2021). The fluid in question can be cold (brine with or without hydrocarbons) or hot (magma), the source mechanism appears similar (Tary et al., 2014a; Fazio et al., 2017). The generation process is commonly related to the presence of a slow wave trapped between the surfaces of a crack, called “*Krauklis wave*,” also referred in literature as “*crack wave*” (Krauklis, 1962; Aki et al., 1977; Chouet, 1986; Ferrazini & Aki, 1987). The wave recorded by the sensors is the result of the crack wave

diffraction at the tip of the crack (Korneev, 2011). The frequency response of each mode of the wave depends on the crack geometry, excitation pulse and the properties of fluid and rock (Korneev, 2008; Tary et al., 2014a; Tary et al., 2014b).

The proposed mechanism of inducing this seismicity is connected to fracture opening/extension and the corresponding sudden drop in the fluid pressure or sudden depressurization and fracture collapse (Aki et al., 1977; Chouet, 1988; Tary, 2014a; Figure 6A). Other explanations propose instabilities in the flow of fluid through cracks (Ferrick et al., 1982; Rust et al., 2008; Tary et al., 2014a; Figure 6B). The fracturing can occur due to fluid flow itself, temperature change (magma intrusion), steam injection, CO₂ injection or hydraulic fracturing treatment (Ferrick et al., 1982; Konstantinou & Schlindwein, 2003; Chouet et al., 2005; Maxwell et al., 2007; Bohnoff & Zoback, 2010; Das & Zoback, 2011). Tremor-like signals and long-period events have been observed using ocean bottom seismometers near active volcanoes and hydrothermal systems (Sohn et al., 1995; D'Alessandro et al., 2009; Sgroi et al., 2009). Other, more impulsive signals potentially connected to the fluid-flow processes have also been observed in this context (D'Alessandro et al., 2009; Bowman & Wilcock, 2014; Sgroi et al., 2014).

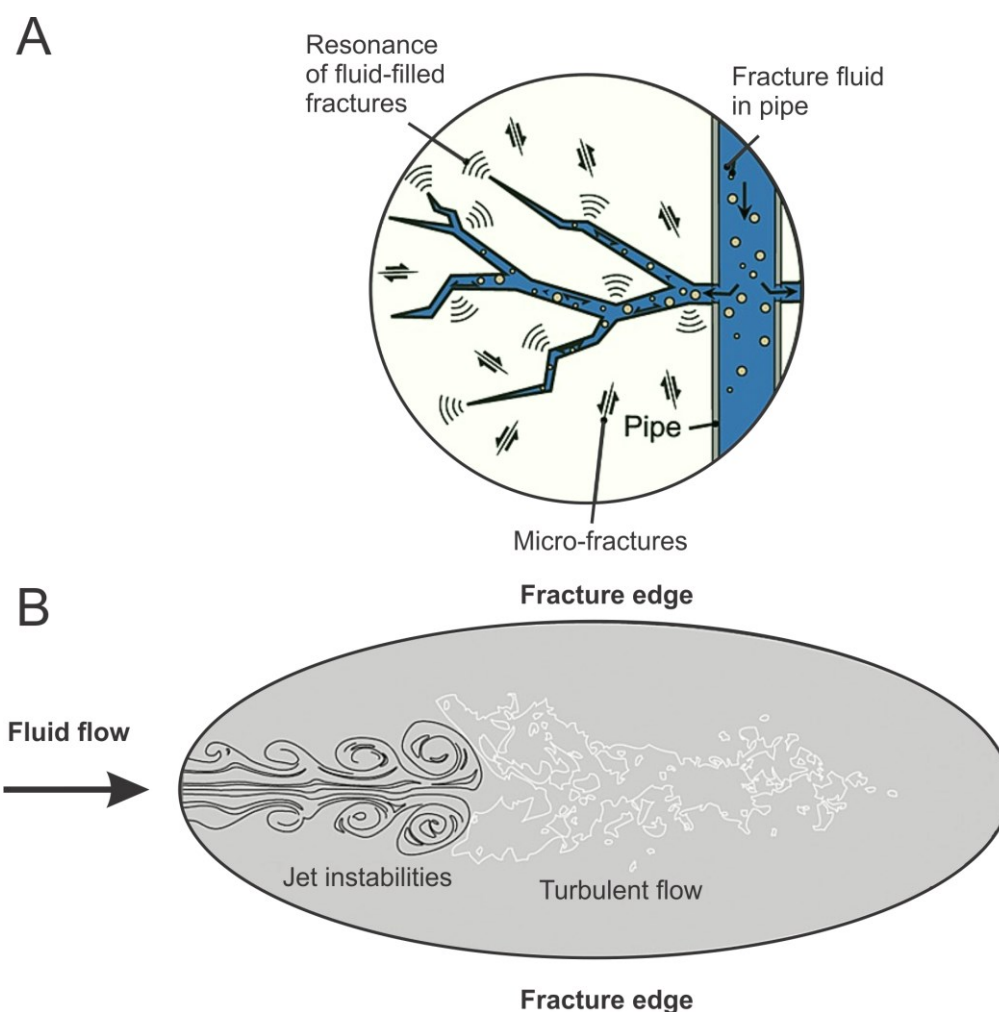


Figure 6. Conceptual explanation of the fluid resonance propagating from the crack edge in hydraulic fracturing case (A) and instabilities in the flow of fluid within the fracture causing propagating seismic wave (B). Modified from Tary et al., 2014a.

These short, energetic signals dubbed “*short duration events*” (SDE) have been observed in a wide range of marine settings (e.g., Buskirk et al., 1981; Bowman & Wilcock, 2014; Embriaco et al., 2014, Franek et al., 2014, 2017; Sohn et al., 1995). SDEs, similarly to tremors and long-period events, are hypothesized to be an indication of fluid flow processes, but in shallow sediments. Some observations notice increased presence of SDEs immediately after OBS deployment, which may be linked to sediment disturbance by instrument weight (Ostrovsky et al., 1989; Tary et al., 2012). SDEs have been directly correlated to the intensity of the gas emissions from the seafloor (Bayrakci et al., 2014; Embriaco et al., 2014).

The proposed physical mechanisms for observed signals include resonance of fluid-filled cracks in sediments and corresponding crack wave propagation (Díaz et al., 2007; Figure 6A), and vertical gas migration through opening of pre-existing fractures, with mainly horizontal movements of the conduit walls generating high amplitude Scholte waves (Tary et al., 2012; Hsu et al., 2013; Figure 7). The generation of signals resembling SDEs through gas expulsion

from shallow sediments have been demonstrated in a lab experiment (Batsi et al., 2019), and signals resembling SDEs have been directly observed in monitoring of the fluid injection into natural fault (Derode et al., 2015). In the past, biological activity of the fauna has been proposed as one of the explanations for SDE generation (Buskirk et al., 1981), but scarce amount of monitoring data currently available challenges this interpretation (Batsi et al., 2019). In some studies, SDEs are classified as microseismic events of very small magnitudes (Sohn et al., 1995; Sgroi et al., 2014). In some cases, SDEs are attributed to the underwater currents (Chang et al., 2016; Ugalde et al., 2019), however current-induced noise is usually described as a persistent tremor-like signal (Ramakrushana Reddy et al., 2020; Essing et al., 2021).

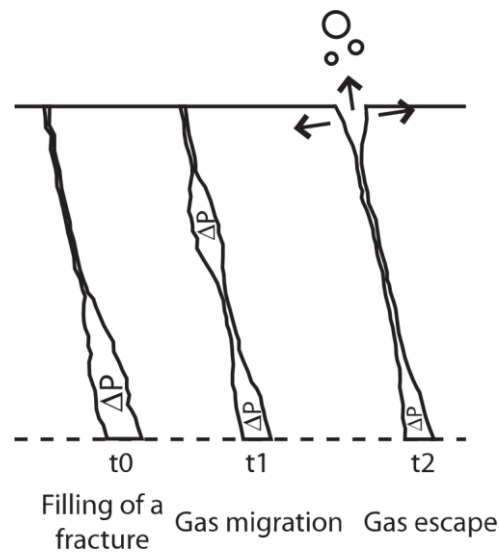


Figure 7. Schematic showing the vertical gas expulsion from the seafloor as a potential mechanism responsible for SDEs. Taken from Tary et al., (2012).

While the processes involved in the movement of the fluid in sediments can be a source of the seismic signal, both near- and far-field seismicity not directly linked to the system can influence existing fluid flow and local seismic signal generation. Similarly, the physical phenomena controlling the temporal variation of seismicity can influence and modulate the seepage processes at the seafloor and fluid migration in sediments.

1.5 External triggers and modulators of fluid flow

As previously stated, fluid flow is driven by the pressure of the pore fluid, but the change in the local stress field influencing it does not have to be local nor continuous. Fracturing connected to an earthquake produces a near-instant response in the system and the potential influence of earthquakes on the fluid flow system is well documented. Earthquakes can cause water level, flow rate, temperature, and chemical composition changes in ground water on land (Manga et al., 2012; Skelton et al., 2014; Manga & Yang, 2015). These changes can vary temporally and the energy responsible can be very local or propagating from thousands of

kilometers away (e.g., Sato et al., 2000; Yan et al., 2014; Manga & Yang, 2015). Hydrothermal systems are equally affected, both on land and in marine settings (e.g., Fornari et al., 1998; Sohn et al., 1998; Dziak et al., 2003; Yan et al., 2020). Similarly, methane release in cold seeps can increase following an earthquake activity (e.g., Mau et al., 2007; Tsunogai et al., 2012; Menapace et al., 2017).

Distant energy release does not have to influence fluid flow directly, it can also trigger local seismological activity and fault opening/slip (Gomberg et al., 1997; Hill & Prejean, 2007; Brodsky & van der Elst, 2014). In general, it can be assumed that the Earth's crust is in near-critical stress state and the force required for triggering of a rock failure may be small (Zoback & Zoback, 2002). The dynamic stress change required to cause a seismic response can be in the order of only several kilopascals (Peng & Gromberg, 2010; Wang et al., 2022). Distant earthquake triggering can induce other seismological signals that may indicate active fluid flow processes, such as non-volcanic tremors (Rubinstein et al., 2007; Guilhem et al., 2010; Chao et al., 2013).

Stress changes required to modulate fluid flow can also come from periodic, local, and global processes. On land, hydrological systems can induce temporal stress load changes (Gupta, 2002; Chanard et al., 2014; Craig et al., 2017). Thermoelastic processes driven by the surface temperature variations also produce stress variation (Tsai, 2011). Large atmospheric phenomena also induce short-term changes (Liu et al., 2009). In colder climates, snow loading can be important enough in varying the seismological intensity (Heki, 2001, 2003). Permafrost changes due to a variation in ground temperature and ground thermal stress can be monitored passively using cryo-seismic signals (Romeyn et al., 2021, 2022). On a longer timescale, glacial isostasy contributes to the present-day stress field both on land and at sea (Fjeldskaar et al., 2000; Brooks & Adams, 2020; Vachon et al., 2022).

Finally, Earth's movement and rotation with respect to other celestial bodies produces predictably varying changes in the stress due to solid Earth tides and ocean tides. Tides are caused by the difference between the gravitational accelerations (produced by other bodies) and centrifugal accelerations (produced by the orbital motion of the body) (Wenzel, 1997). The difference between the two accelerations is called tidal acceleration. All celestial bodies in the Solar System produce tidal accelerations on Earth, but the two dominant components of tidal acceleration come from the Sun (rotation around the star) and the Moon (motion of the Earth and the Moon around the barycenter of the two-body system, which is located inside the Earth's body). To represent the influence of tides for a given position on the Earth's surface, instead of the tidal acceleration, a scalar tidal potential V is used (Wenzel, 1997). The tidal acceleration is the gradient of the tidal potential. The scalar potential V for a given location on

the Earth's surface is computed using an expansion of Legendre's polynomials into a series of spherical harmonics. This series expansion converges rapidly, and to accurately represent almost all of the forces acting on Earth's surface, it is enough to expand the series up to a 6th term for the Moon and up to the 3rd term for the Sun. Zero order spherical expansion is related to long period waves (14 days – 18.6 years), 1st order expansion is referred to as diurnal waves (~ 24 h period), 2nd order is called semi-diurnal (~ 12 h period) and so on. The largest contribution comes from the 2nd term which provides about 98% of the total scalar potential (Wenzel, 1997). From the spherical harmonics' formulation, it can be inferred that the long-period tidal waves have their maximum at the poles, diurnal waves at +/- 45 ° latitude and semi-diurnal waves at the equator (Wenzel, 1997). The most obvious consequence of tidal accelerations is a presence of ocean tides, but Earth's interior also reacts to tidal forces and tidal patterns can be observed in i.e., gravity measurements.

Forces generated by tides change the earthquake activity on land and in oceans (e.g., Tolstoy et al., 2002; Cochran et al., 2004; Stroup et al., 2007; Métivier et al., 2009). The intensity and composition of venting hydrothermal fluids often shows tide-induced variation (Tivey et al., 2002; Chen et al., 2005). The same relation is observed at cold seep sites (Krabbenhoft et al., 2013; Hsu et al., 2013; Riedel et al., 2018). Correspondingly, tremor-like signals, long-period events and short duration events all have been postulated to undergo tidal modulation (e.g., Rubinstein et al., 2008; Lambert et al., 2009; Hsu et al., 2013; Han et al., 2018).

2 Scientific approach

In this section, I list the information about the ocean bottom seismology (OBS) instrumentation and datasets used in this thesis. All data was obtained through research cruises on R/V *Helmer Hanssen* operated by UiT The Arctic University of Norway. Subsequently, I briefly describe the processing steps necessary to obtain catalogs of events to analyze from OBS data (be it earthquakes or other signals of interest), which form a foundation of articles and manuscript in this thesis. A separate subsection is dedicated to the development of signal classification method which is the main outcome of the **Article 2**.

2.1 OBS instruments

The main component of each OBS is a seismometer used to measure ground displacement due to elastic wave propagation in the subsurface (Figure 7). In this thesis, we used short-period seismometers (**Article 1 & Article 2**), and a combination of short-period units together with broadband seismometers (**Manuscript 3**). The *K/MT 210* seismometer from *KUM* contains three short-period geophones that have a corner frequency of 4.5 Hz, and a flat frequency response to about 100 Hz. The *Trillium Compact* broadband seismometers have a flat frequency response from 120 s to 100 Hz. Each OBS was equipped with a hydrophone recording in the same frequency range as a seismometer. Two recording systems were used: *Geolon MLS* (**Article 1**) & *KUM 6D6* (**Article 2 & Manuscript 3**).



K/MT 210



Trillium Compact

Figure 7. Seismometers used in this thesis.

2.2 Datasets

This thesis is based on three separate OBS datasets acquired at and in the vicinity of Vestnesa Ridge contourite drift. Below is the list of the acquired data, corresponding cruises, cruise leaders, cruise reports and data repositories (where applicable). Datasets for the **Article 2** and the **Manuscript 3** were acquired in collaboration with GEOMAR, Helmholtz Centre for Ocean Research, Kiel, Germany, and Alfred Wegener Institute, Helmholtz Centre for Polar and Marine Research, Bremerhaven, Germany, respectively.

Article 1

Cruises: CAGE15-4 & CAGE16-6

Cruise reports:

<https://doi.org/10.7557/cage.6935> (CAGE15-4; Bünz, S., 2023a)

<https://doi.org/10.7557/cage.6929> (CAGE16-6; Bünz, S., 2023b)

OBS dataset: <https://doi.org/doi:10.18710/TCWUQN> (Domel et al., 2021)

Article 2

Cruises: CAGE19-1 & CAGE20-5

Cruise reports:

<https://doi.org/10.7557/cage.6909> (CAGE19-1; Bünz, S., 2023c)

<https://doi.org/10.7557/cage.6914> (CAGE20-5; Bünz, S., 2023d)

OBS dataset: *To be published in Dataverse.no*

Manuscript 3

Cruises: CAGE20-5 & CAGE21-3

Cruise reports:

<https://doi.org/10.7557/cage.6914> (CAGE20-5; Bünz, S., 2023d)

<https://doi.org/10.7557/cage.6722> (CAGE21-3; Plaza-Faverola et al., 2022a)

OBS dataset: <https://doi.org/10.1594/PANGAEA.952424> (embargo until 31.12.2024; Plaza-Faverola et al., 2022b)

2.3 OBS data processing

Remote, independent observations of passive seismological signals on the seafloor are a well-established method dating almost a century (Ewing & Vine, 1938). Obtained datasets expand the coverage of global networks (temporarily, and sometimes permanently) for global studies of wave propagation. They are particularly useful, however, in the local seismological monitoring of tectonic processes related to e.g., mid-ocean ridge spreading, subduction zones,

hydrothermal and volcanic systems, and cold seeps (e.g., Sato et al., 1995; Schlindwein et al., 2005; Bowman et al., 2013; Grevemeyer et al., 2021; Chen et al., 2022). Past challenges related to power consumption and data storage are now addressed well enough to allow a continuous record lasting a year and more (e.g., Suetsugu & Shiobara, 2014). In a very general sense, the processing of OBS data for creating an interpretable catalog of events does not differ much from land data processing. However, some specific steps in the workflow require an additional effort and bring challenges that are unique to OBS. These steps and methodology are described in greater detail below. A simplified processing routine for data analysis (with an asterisk denoting additional *processing* consideration for OBS), is presented in Figure 8.

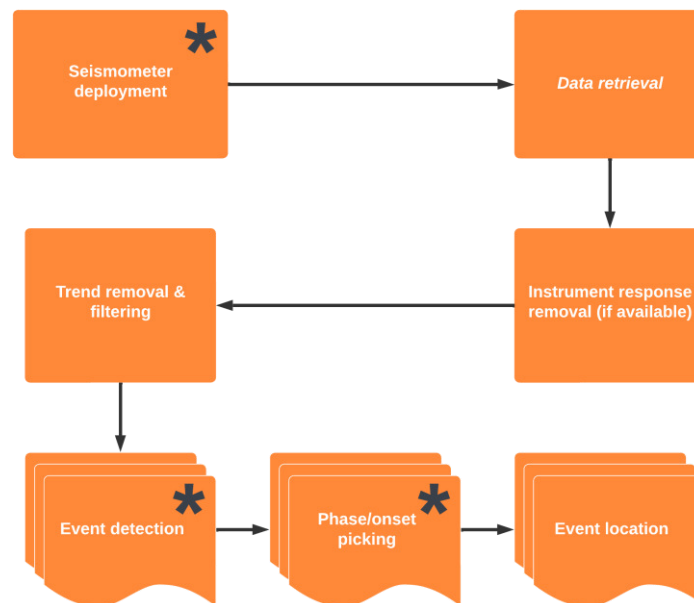


Figure 8. Basic processing routine to create an event catalog from OBS data. Asterisks represent steps which require additional consideration compared to land data processing and are discussed in detail below.

2.3.1 Seismometer deployment

OBSs are usually deployed by free fall from a vessel and during sinking their horizontal position drifts due to the water currents. Deployment on the Vestnesa Ridge showed a horizontal drift observed between the deployment location and the seafloor position can usually reach 200-300 m (**Article 2**). For locating nearby seismicity, it is important to establish an accurate position of the seismometer at the seafloor. We utilized active seismic shots in the vicinity of the deployed devices for seafloor location.

We want to find a position of OBS at the seafloor based on the direct wave travel time and wave velocity in the water. The initial solution to the problem can be depicted as a vector of OBS position, true water velocity and P-wave travel time for a given seismic source position:

$$m^0 = (x_0, y_0, z_0, v_0, t_0)$$

For each seismic shot i from the ship, we obtain:

- Source position ($x_{src,i}$, $y_{src,i}$, $z_{src,i}$ coordinates of a local grid)
- Source origin time (t_{source})

From the OBS we obtain the direct wave arrival time ($t_{observed,i}$) for each shot. We can compute the expected direct wave travel time for each seismic i shot from the equation:

$$t_{calc,i} = \frac{\sqrt{(x_{obs} - x_{src})^2 + (y_{obs} - y_{src})^2 + (z_{obs} - z_{src})^2}}{v_{water}}$$

We can make the non-linear problem of calculating arrival time from five independent variables linear by Taylor series expansion. For each shot point i and expected travel time formula, we create a matrix of partial derivatives G_{ij} :

$$G_{i1} = \frac{\partial t_{calc,i}}{\partial x} = (x_{obs} - x_{src,i}) * \frac{1}{\sqrt{(x_{obs} - x_{src,i})^2 + (y_{obs} - y_{src,i})^2 + (z_{obs} - z_{src,i})^2}}$$

$$G_{i2} = \frac{\partial t_{calc,i}}{\partial y} = (y_{obs} - y_{src,i}) * \frac{1}{\sqrt{(x_{obs} - x_{src,i})^2 + (y_{obs} - y_{src,i})^2 + (z_{obs} - z_{src,i})^2}}$$

$$G_{i3} = \frac{\partial t_{calc,i}}{\partial z} = (z_{obs} - z_{src,i}) * \frac{1}{\sqrt{(x_{obs} - x_{src,i})^2 + (y_{obs} - y_{src,i})^2 + (z_{obs} - z_{src,i})^2}}$$

$$G_{i4} = \frac{\partial t_{calc,i}}{\partial v} = \frac{-\sqrt{(x_{obs} - x_{src,i})^2 + (y_{obs} - y_{src,i})^2 + (z_{obs} - z_{src,i})^2}}{v_{water}^2}$$

$$G_{i5} = \frac{\partial t_{calc,i}}{\partial t} = 1$$

As initial position, we use the deployed location of the OBS. We assume the P wave velocity of water (v_{water}) of around 1500 m/s or use the information from conductivity-temperature-density (CTD) sensor onboard for the initial solution. We seek to minimize the difference between the observed and calculated travel time from each shot Δt_i for the best solution Δm_j which can be written as:

$$t_{observed,i} - t_{calc,i}^0 = \sum_j [G_{ij} m_j] - \sum_j [G_{ij} [m_j]^0] \Delta t_i = \sum_j [G_{ij} \Delta m_j]$$

We do this by computing the least-square function from all shots:

$$\chi^2 = \sum_i \left(\Delta t_i - \sum_j [G_{ij} \Delta m_j] \right)^2$$

We can solve this function by setting the partial derivatives (gradient) to zero to obtain the generalized inverse solution (Gauss-Newton method; Menke, 2018):

$$\Delta m = (G^T G)^{-1} G^T \Delta t$$

We add small amount of damping to the matrix multiplication to make the solution more robust in finding general minimum (damped least squares method). We successfully established OBS positions for two experiments (**Article 2 & Manuscript 3**). Technical issues related to the time synchronization of seismic shots prohibited the similar treatment of data presented in the **Article 1**.

2.3.2 Event detection/recognition (Article 2)

Large datasets make manual event detection impractical and, in many situations, almost impossible due to the amount of time required. In the case of micro seismic signals that we investigated in relation to fluid flow (SDEs), the number of signals on one station can reach hundreds of thousands (e.g., Franek et al., 2017). Local and regional seismicity in the region investigated in this thesis is usually in the range of few hundreds of earthquakes per year (e.g., Jeddi et al., 2021). The de facto standard for detecting earthquakes in the last 4 decades is a trigger algorithm based on the ratio between short-term average of the signal amplitude over the longer window (long-term), commonly known as STA/LTA (Allen, 1982). It is a measurement of the ratio between two average amplitude values in two arbitrarily selected windows. When the ratio exceeds a specific value (determined on case-by-case basis), the detection is triggered. Similarly, when the said ratio drops below another, also manually selected number, the detection termination is marked. The main disadvantage of this method is related to the fact, that the window lengths and the trigger and de-trigger values have to be individually adjusted to be sensitive to different signals. Different amplitudes and lengths of earthquakes (local, regional or tele seismic), SDEs or other signals of interest means that a search has to be performed individually for each event type. Additional limitation is related to the fact that other types of signal present in the data may cause a detection, if their average amplitude ratios are similar enough to the signals sought.

In OBS data a number of different phenomena produces a seismic signal that triggers the STA/LTA detection method. Active seismic surveys produce either a direct or refracted wave arrival that will trigger a detector set to pick up local seismicity. Underwater currents can lead

to tremor signal generation that is caused by the vibrations of the OBS components due to the movement of the water around it (e.g., Essing et al., 2021). Marine mammals produce vocalizations that can exceed the amplitude ratio required for triggering detection (e.g., Soule & Wilcock, 2013). All these signals can obscure the events of interest, especially in the high noise conditions usually encountered in marine data.

Noise levels in OBS data are usually larger than what is encountered on land due to several reasons. Naturally occurring noise sources in deep water (> 1 km) include tilt noise (related to the underwater currents mentioned before affecting vertical channel due to tilt of the OBS), compliance noise and microseisms (Bell et al., 2015). Compliance noise only affects very low frequencies in deep water (< 0.04 Hz) and is caused by the vertical motion of the seabed induced by pressure variations in the water (Crawford et al., 1998). Microseisms are Rayleigh waves generated by the surface water motion. It produces two specific peaks at the noise spectrum, called primary and secondary microseism peak (Friedrich et al., 1998). Primary microseisms have the same frequency as the surface water waves, usually around 0.07 Hz. The secondary microseism peak, usually much stronger has about twice as high frequency maximum (around 0.14 Hz) and it is caused by two surface waves travelling in opposite directions creating a standing wave (Figure 9; Friedrich et al., 1998; Bell et al., 2015).

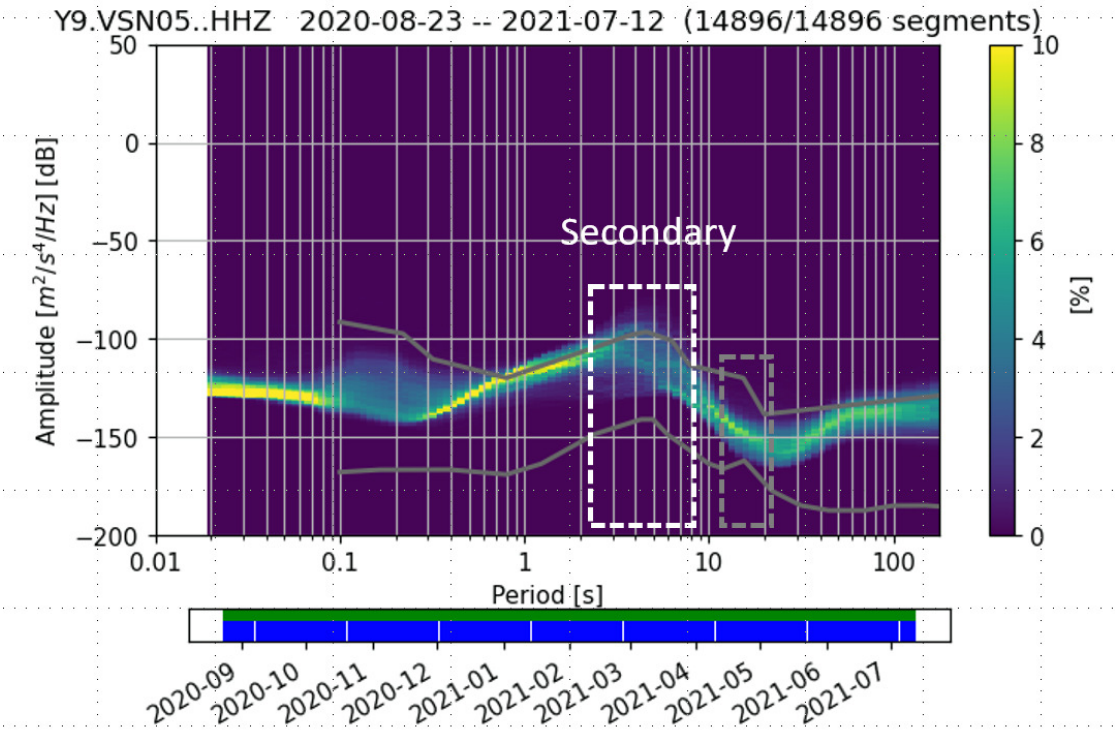


Figure 9. Power-density spectrum plot, representing noise levels for station VSN05 (Manuscript 3). Secondary microseism peak is clearly visible as higher noise level. The location of expected primary microseism peak (not seen) in a gray rectangle.

Recent years have brought a large development in deep-learning approaches for the purposes of the signal detection and phase picking (e.g., Mousavi et al., 2020; Zhu & Beroza, 2018). These algorithms work very well applied to stations on land, but we found that either the amount of false detections is too high to take the data reliably or, when we lower the sensitivity, large earthquakes with clear phase arrivals are regularly omitted (**Article 2**). They also specifically target earthquake detections; micro seismicity, such as SDEs, has not been an object of intensive research in the field.

In collaboration with the University of Strasbourg, France, I tried to improve the automatic detection and recognition of signals using STA/LTA detection dataset as an input to machine learning classification (**Article 2**). The aim was to automatically recognize earthquakes, short duration events, and separate them from marine noise. I automatically created a set of detections to analyze by running the STA/LTA algorithm twice, with the different parameters meant to trigger on short, impulsive SDEs and longer duration local and regional earthquakes. To extract the waveforms for classification, I incorporated kurtosis-based onset adjustment provided by the University of Strasbourg (Baillard et al., 2014). Kurtosis is a statistical measure that represents the shape of a given distribution and is defined as the standardized fourth moment of the mean. It has a value of 3 for Gaussian distribution (DeCarlo, 1997) and the onset of a seismic wave temporarily creates a different statistical distribution of the data that raises the kurtosis value. By computing the kurtosis in small windows over the given signal, the onset of the detection can be found as a time when kurtosis start to increase. STA/LTA detector can mark the end of the detection too quickly if the noise level is high compared to the seismic wave amplitude. To alleviate that, I used the average amplitude of the signal further in the future than the expected signal duration and terminated the detection when the signal amplitude reached 1.5 of this value.

To distinguish between earthquakes, SDEs and noise, I trained a Random Forest classifier following the approach presented in Provost et al., (2017), also provided by the University of Strasbourg. For each extracted waveform, a large number of waveform, spectral and polarity attributes is computed, and the obtained values are used as a basis for recognition of different type of signals. The Random Forest method is based on large number of individual decision trees (within each tree a decision is made into what category signal belongs; Breiman, 2001). The decision is made on the basis of the random selection of one or more computed attributes. From all decision trees computed, the class that won most of the votes is then used to assign the signal into the specific category. This classification approach was used in datasets for the **Article 2** & the **Manuscript 3**.

2.3.3 Phase picking – absolute time

Seismological data heavily relies on accurate arrival times of the events. At the ocean bottom, the time is kept by the internal clock of the recorder that drifts over the duration of experiment due to the changes of crystal oscillations that measure the passing of time (e.g., Gardner & Collins, 2012). The choice of clock is dictated by the power usage required and the crystal clocks are designated in the way that they deviate from the accurate time in the linear manner over the course of the experiment. This linear drift can be adjusted after the experiment by the synchronization of the clock with GPS signal before the deployment and after the recovery of the OBS. However, this linear relationship is often found not to be true (e.g., Gouédard et al., 2014). The difference between the absolute and measured time can reach several seconds at the end of a year-long experiment and render phase picks for earthquakes useless in the earthquake location procedure. Obtaining accurate phase picks is crucial in correct earthquake hypocenter determination. Therefore, an alternative approach to establish the clock drift is needed to make a proper correction.

I utilized the approach based on the daily ambient noise correlation between the stations (Hanneman et al., 2014). The correlation function between the station pair should not change during the duration of the survey for any other reason than the drift of the clocks. By averaging the cross-correlation value and monitoring its change over time, it is possible to track the drift change over the duration of the experiment. Analysis of the correlation plots helps to establish for which station the clock drifts in linear station. On this assumption, this station clock can be corrected linearly using GPS synchronizations and the other stations can be adjusted in relation to this “reference” OBS. This approach requires a large number cross-correlations between stations computed and is therefore time-consuming. The method was successfully implemented in the dataset for the **Manuscript 3**.

3 Study area

The fluid flow system investigated in this thesis developed within the sedimentary deposits offshore Svalbard, in the Fram strait (Figure 1). The main present-day tectonic processes are driven by the nearby mid-ocean ridge system (Molloy Ridge, Molloy Transform Fault and Knipovich Ridge). The repeated cycle of glaciations since 3.6 Ma (Knies et al., 2009), caused stress variations influencing present day stress state. Sediment thickness, reaching upwards to 5 km (Eiken & Hinz, 1993), contributes to the forces acting in the subsurface due to the gravitational load. Sediment deposition is predominantly controlled by the current-driven processes and repeated past glaciations affecting Svalbard and its shelf. Active indicators of fluid flow, in the form of documented gas seepage from the seafloor are mostly constrained within the crest of Vestnesa Ridge contourite drift. On its western flank, bathymetric features indicate recent, but currently dormant gas release sites (Hustoft et al., 2009; Bünz et al., 2012; Plaza-Faverola et al., 2015).

3.1 Tectonic setting

The North Atlantic Ocean started to open northward around 56 Ma (Talwani & Eldholm, 1977). The opening in the Fram Strait was caused by the change in the plate movement between Svalbard and Greenland from strike slip to oblique divergence (Myhre & Eldholm, 1988). The shearing between the plates led to western Spitsbergen orogeny which increased sedimentation in the basin (Harland et al., 1974). Another change of the plate movement in Oligocene led to the creation of Spitsbergen Shear Zone that acted as a precursor to the ridge spreading (Harland et al., 1974; Steel et al., 1985). The northernmost part of the Knipovich Ridge is believed to have opened about 20 Ma ago, and aeromagnetic data suggests an eastward ridge jump at about 18 Ma ago (Dumais et al., 2021). The spreading process at Molloy Ridge originated between 20-10 Ma ago, possibly around the same time as Knipovich Ridge (Engen et al., 2008; Dumais et al., 2021). Both ridges are classified as ultraslow (Dick et al., 2003). The northern portion of Knipovich Ridge spreads asymmetrically (7.1 mm/y to the west, 5.9 mm to the east; Dumais et al., 2021). Molloy Ridge spreading is more uniform, with around 6.5 mm/y for the western portion and 6.3 mm/y for the eastern part (Ehlers & Jokat, 2009). The Molloy Transform Fault connects Knipovich Ridge and Molloy Ridge in an oblique fashion. Available focal mechanism solutions for the area (presented in the **Manuscript 3**), indicate mostly extensional forces at the ridges and predominantly strike-slip movement at the Molloy Transform Fault. Modelling of the stress field distribution indicates an asymmetric distribution of the tectonic forces from the ridge processes, due to the different orientation of Molloy and Knipovich Ridge, and non-orthogonal placement of the Molloy Transform Fault between them (Plaza-Faverola & Keiding, 2019). The influence of glacial load alternated

between compressive and tensile for the past 123 ka, and remains currently tensile (modelling by Vachon et al., 2022). Shallow sediments on the flanks and the crest of Vestnesa Ridge are densely faulted, with different fault orientations partially associated with glaciotectonics in the last 1.2 million years (Plaza-Faverola et al., 2015; Cooke et al., 2023).

3.2 Sedimentary setting

Beyond the shelf break of west Svalbard, sediments are predominantly composed of turbiditic, pelagic and hemipelagic facies (Howe et al., 2007). The interpretation of seismic facies suggests sediment deposition under the influence of underwater contourite bottom currents, represented at present by the West Spitsbergen Current (Eiken & Hinz, 1993). Northward deposition of sediments was influenced by the movement of the tectonic plates at Molloy Ridge, leading to a NW shift of contourite deposits at Vestnesa Ridge (Johnson et al., 2015). The onset of glacial deposits in the area of Vestnesa Ridge is estimated at 2.7 ma, at a boundary between regional seismic units YP-1 and YP-2 (Eiken & Hinz, 1993; Knies et al., 2009). Younger seismic units consist of glaciomarine contourites interlaced with a component of turbidites close to the shelf edge (Mattingsdal et al., 2014). At Vestnesa, young sediments consist mostly of silty and muddy-silty turbidites with abundant ice-rafted debris (Howe et al., 2007; Knies et al., 2014; Schneider et al., 2018). Since the Late Pliocene, large amounts of hemipelagic sediments were deposited on the shelf break (e.g., Faleide et al., 1996). The thickness of sediments reaches upwards of 5 km for the south-east portion of Vestnesa Ridge (Ritzmann et al., 2004). The northern part of the Knipovich Rift valley exhibits a large difference between eastern and western flank height (water depth), due to the limited westward extent of the deposition range for glacial sediments and potentially gravity-driven compaction of the sedimentary load (Amundsen et al., 2011; Kvarven et al., 2014).

3.3 Seepage systems in the study area

The most documented fluid flow system in the region is located at the Vestnesa Ridge contourite drift, investigated in the **Article 1** and the **Article 2**. Seepage there is driven mainly by thermogenic hydrocarbons originating from deep reservoirs by a complex network of faults and fractures, with some component of microbial methane production close to the surface (Plaza-Faverola et al., 2017; Smith et al., 2014; Pape et al., 2020). Large amounts of natural gas present in the pore fluids allowed for a widespread presence of gas hydrates below the seafloor, mapped by the presence of so-called bottom-simulating reflector in the seismic data (Hustoft et al., 2009; Petersen et al., 2010; Smith et al., 2014). The boundary of the gas hydrate stability zone has been established to about 160-195 m below the seafloor (Petersen et al., 2010; Bünz et al., 2012; Smith et al., 2014; Plaza-Faverola et al., 2015, 2017).

The transport of fluids is facilitated by a complex network of near-vertical fractures and faults that create acoustic chimney structures visible in seismic data (Hustoft et al., 2009; Bünz et al., 2012; Smith et al., 2014; Plaza-Faverola et al., 2015). Fault orientations in the shallow sediments show a varying preferential orientation correlated temporally to glacial and interglacial periods in the last 1.2 ma (Cooke et al., 2023). Directly at the seafloor, complicated networks of microfractures direct the gas exhumation and impact the microbial activity (Yao et al., 2019). Faults at smaller (closer to the seafloor) depths than the gas hydrate stability zone can also potentially be plugged by the localized presence of gas hydrates and restrict the fluid flow (Madrussani et al., 2010; Goswami et al., 2017). Gas hydrates have been directly sampled from shallow sedimentary cores (e.g., Hong et al., 2021). Conversely, close proximity to the spreading Knipovich Ridge results in a high (> 80-120 C) geothermal gradient, which can drive the warmer fluid migration upwards (Goswami et al., 2015; Waghorn et al., 2018).

The outlet of the fluid flow system is represented by numerous semicircular depressions (pockmarks) in the seafloor at the crest of Vestnesa (Vogt et al., 1994; Bünz et al., 2012; Panieri et al., 2017). Natural gas, visible in the hydroacoustic data, is being released presently from the pockmarks at the eastern section of the ridge crest (Hustoft et al., 2009; Bünz et al., 2012; Smith et al., 2014). Pockmarks in the western section of the crest are currently dormant, but were active in the past (Consolaro et al., 2015; Szybor & Rasmussen, 2017; Cooke et al., 2023). The presence and intensity of gas release occurred in an episodic manner at Vestnesa Ridge for at least 23 500 years (Ambrose et al., 2015; Schneider et al., 2018). The variable nature of seepage has been attributed to tectonic forces from the ridge system (Plaza-Faverola et al., 2015; Plaza-Faverola & Keiding, 2019) and/or glacially induced stress (Schneider et al., 2018; Himmler et al., 2019; Vachon et al., 2022).

We discussed the intensity and variation of micro-seismic signals in relation to well-researched fluid flow system at Vestnesa in the **Article 1**, however a large portion of west-Svalbard continental margin may be capable of a near-surface fluid migration and seafloor seepage. The presence of gas hydrates and free gas accumulations have been documented for almost the entire area between the Vestnesa Ridge and the northern termination of the Knipovich Ridge (Vanneste et al., 2005; Madrussani et al., 2010). Evidence of seepage in hydroacoustic data has recently been found in a group of pockmarks adjacent to one of the sedimentary faults in this location (Plaza-Faverola, 2022), and seafloor gas emissions that vary with tidal cycles have also been inferred from in-situ pressure data in the depression 20 km eastwards from sedimentary faults termination (Sultan et al., 2020). We targeted this area in the **Manuscript 3** to better understand the tectonic processes in the region, the corresponding local stress variation, and how this affects the present-day seepage locations. The processing

of earthquakes and SDEs in this dataset was expedited using methodology developed in the **Article 2**.

4 Summary of research papers

In this chapter, I provide a summary of the main research outcomes from the papers included in this thesis. **Article 1** investigated the intensity and temporal variation of short duration signals (SDE) that are suggested to represent shallow fluid flow processes. The results suggest some degree of correlation between the signal occurrence intensity and ocean tides. Difficulties related to processing the data, where the number of automatic signal detections reached several hundreds of thousands, was the main motivation to pursue a different, more reliable method of automatic data classification presented in the **Article 2**. A separate dataset used for this purpose allowed a second look at the SDE temporal patterns for the same, although expanded study area, and we again observed that the periodicity of SDE occurrence shows a connection to ocean tides. In the **Manuscript 3**, we utilized the signal detection and recognition method from the **Article 2** to take a more regional look at the earthquake distribution and discuss the present-day tectonic processes in the context of investigated fluid flow systems. This summary is followed by a research outlook which outlines potential topics for future research.

4.1 Main findings

The main findings of all papers included in this thesis can be summarized as follows:

Article 1: Origin and Periodic Behavior of Short Duration Signals Recorded by Seismometers at Vestnesa Ridge, an Active Seepage Site on the West-Svalbard Continental Margin

Short duration events are a type of impulsive signal reported in marine settings that is hypothesized to be linked to fluid flow. The current explanations include fluid movement causing resonance in fractures, or fracturing/reopening of existing fractures (Diaz et al., 2007; Tary et al., 2012). In this study, we investigated the data from a roughly one-year-long deployment of three ocean bottom seismometers placed in the vicinity of a gas seepage site at Vestnesa Ridge in the Fram Strait. We discovered a large number (> 300 000) of short duration events (SDE) on all three instruments and produced a dataset of SDE occurrence using an automatic STALTA detector. Analysis of the periodograms of the SDE datasets showed a clear connection to semi-diurnal tides at two stations, and potentially a weaker link on the third one. We found a similar connection between a tremor-like signal and tides, which is interpreted to be the result of the tidally controlled underwater currents (e.g., Ramakrushana Reddy et al., 2020). To investigate the relationship of SDEs with ocean tides, we modelled the sea height variation caused by tidal forces for the entire duration of the experiment. By juxtaposing the results, we found that SDE usually occur in large bursts near the positive peaks of the sea level change, but these peaks are only observed every few full tidal cycles. To

measure the strength of the connection, we cross-correlated the normalized functions of SDE intensity and the mean sea level height. We found a generally weak (~ 0.1) correlation between the functions for the entire dataset that indicated an increase of the SDE function close to the maximum tidal height. Monthly cross-correlations indicated that this link can be much stronger (up to a value of ~ 0.5) during specific months and the overall correlation is lowered by the seasonal periods with no distinctive connection between the variables. Following the proposed links between tides and gas seepage (e.g., Boles et al., 2001, Hsu et al., 2013), and between SDEs and seepage (Embriaco et al., 2014; Hsu et al., 2013), we suggested two mechanisms of micro seismicity modulation that would match the pattern we observed. Firstly, the small change in the hydrostatic pressure during a tidal cycle would lead to a larger vertical stress difference between the gas-filled sediments and the water column, which in turn would increase the gas migration in the sediments and drive the SDE generation. Secondly, we modelled the behavior of shallow gas hydrates (recovered in the area by e.g., Hong et al., 2021) and found that in a specific set of conditions the solubility of methane would decrease with the increase of the pore fluid pressure, favoring gas exsolution during high tides. This could lead to either gas hydrate formation or generation of methane bubbles that could fracture very shallow sediments and generate micro-seismic signal. A large number of detections that could not be verified manually in full and the pursuit of better recognition of SDEs and earthquakes led to the work that was the focus of the **Article 2**.

Article 1 was published in *Frontiers in Earth Science* in March 2022.

Article 2: Event recognition in marine seismological data using Random Forest machine learning classifier

We implemented a Random Forest classification algorithm in the processing workflow of the OBS data to automatically separate signals of interest from marine noise. We used a dataset containing five three-month long and two year-long recordings from ocean bottom seismometers deployed along the Vestnesa Ridge in the Fram Strait in 2019-2020. The workflow consisted of two separate steps: detection and classification. For the detection step, we used the STALTA approach from the **Article 1** twice, with separate sets of parameters adjusted for the sensitivity in picking up SDEs and local earthquakes. The onsets of individual detections were adjusted using a kurtosis-based method (Baillard et al., 2013). In the second step, we extracted parts of continuous record to compute a large (178) number of metrics related to the signal energy, frequency content, spectral characteristics and polarity using three-component seismic data (Provost et al., 2017; Hibert et al., 2017). The differences in the calculated values for different signal types (SDEs, earthquakes and noise) were used to first train a machine learning model and then subsequently classify signals. We created an initial

model using a small number of each event types (100) and tested its accuracy on a single OBS dataset. We subsequently incorporated more event examples into the training procedure and progressively tested the model on subsequent stations, with manual verification where feasible. We found that using already 100 examples per class our model achieves the accuracy of 86 % in event classification and the final model reached the value of 96 %. Analysis of the model performance indicated that SDE recognition is the part least dependent on the amount of training examples, and that marine noise is most likely not properly captured in the model even with a large amount of over-fitting. Out of all calculated signal characteristics, the most important ones in the correct classification were related to the kurtosis of the signal in different frequency ranges, the maximum frequency of the signal, the nature of the signal decay and the signal duration. We repeated the analysis of SDE occurrence and intensity shown in the **Article 1** in this new dataset, having additionally the precise OBS positions on the seafloor for this experiment. We observed a large difference between average daily SDE intensity between the stations, variable SDE intensity in relation to the distance from documented gas seepage sites and a sustained number of SDE detections on stations located far away from any known seepage locations. We subsequently successfully used the trained model to create a dataset of earthquake detections investigated in the **Manuscript 3**.

Article 2 was published in Geophysical Journal International in June 2023.

Manuscript 3:

This manuscript provides a comprehensive analysis of the regional seismicity and investigation of the amount of influence that present day ocean spreading might have on the fluid flow systems documented in the area. It uses data from a network of ocean bottom seismometers deployed between August 2020 – July 2021 around the set of bathymetric faults located south of the Vestnesa Ridge and north of the Knipovich Ridge termination. In this area the presence of gas hydrates and free gas accumulations have been documented using seismic reflection data (Vanneste et al., 2005; Madrussani et al., 2010). In addition, a direct observation of gas seepage in the water column has been made recently in a location within the deployed network (Plaza-Faverola, 2022). We used the detection and classification approach presented in the **Article 2** to create a catalog of regional earthquakes. We documented seismicity related to ocean floor spreading, but also made several new observations. We found that the earthquakes recorded at Molloy Transform Fault (southwest to the network) generally occur to the S-SW from the fault outline observable on the bathymetry. We used a high-resolution seismic profile crossing the fault to illustrate that the shallow sediments on the S-SW side from the fault are highly segmented in comparison to undisturbed sediments on the opposite side. We observed, previously seen, but not analyzed intense seismic activity on the extension of

the intersection between the Molloy Transform Fault and the Knipovich Ridge, to the east from the ridge valley. We indicated a recent syn-sedimentary faulting in the shallow sediments in this area and proposed that the northernmost part of the Knipovich Ridge spreading center is currently buried under the sedimentary deposits of marine and glaci-pelagic nature. We have not observed any seismological activity within the deployed network which means that the faults did not accommodate any large tectonic movement during the experiment duration. Two weak (magnitude 1.2 & 2.0) earthquakes were recorded in the vicinity of the Vestnesa Ridge crest. No continuous seismic activity directly connected to the spreading ridges and the orientation of the faults in seismic data suggest gravitational or glaci-tectonic processes, with the potential reactivation of deeper crustal faults established during seafloor spreading in the past. The observations from this study provide a new insight on the potential relationship between the tectonic stress regime in the area and documented fluid flow systems.

Manuscript 3 was submitted to Geochemistry, Geophysics, Geosystems in August 2023.

5 Concluding remarks and outlook

This thesis showed the use of local seismicity data for addressing questions related to fluid flow and seepage along continental margins. Seismological data can provide new insights into the processes controlling fluid flow through the observation of different seismic signals. In this thesis, I focused on two signal types: earthquakes and short duration events (SDE). These two groups are not necessarily easy to separate, therefore a significant portion of the research has gone into the development of improved tools for this purpose (**Article 2**). However, much more can be done in this area, and this should be a focus of future studies.

SDEs are often documented in marine data, but rarely investigated, and they can be very helpful in understanding fluid flow systems once more effort is put into explaining their exact nature. The observed connection between SDEs and ocean tides is not a direct relationship, but a more complex behavior that still has to be understood better. Similarly, SDE intensity at a specific location is not a simple function of the distance from a seepage site, therefore there must be other controlling factors. The combination of work presented in the **Article 1** and **Article 2** showed that a systematic inventory of SDE occurrence from a variety of sites, with dedicated networks of sensors, might help to shed a light on SDE source mechanisms and understand its potential in monitoring seepage systems. This thesis paved the way for a routine extraction of SDEs from ocean bottom records and a separation of them from other signals, thus enabling data mining of large datasets to recognize their monitoring potential.

Another way to get a better understanding of seepage systems is by characterizing local tectonic stress that may control fluid release. This thesis showed that investigated fluid flow systems are not related to present-day tectonic spreading despite the proximity to two ridge systems in a tectonically complicated setting. Scattered seismicity documented in tele seismic, and regional studies fueled the assumption that tectonic stresses caused by the plate motion are not confined to plate boundaries but extend further beyond. However, the analysis of different datasets with strict quality criteria, using a dedicated, dense network with high sensitivity, showed clearly that seismicity is mostly confined to plate boundaries (with exceptions discussed in **Manuscript 3**) and tectonic stress is released efficiently there, therefore not affecting seepage systems more than 50 km away. The observations that deviate from this pattern are supported by the use of high-resolution seismic profiles, that in agreement with observed present-day seismicity, show the evidence of syn-rift deposition in shallow, faulted sediments. The combined use of this data allows us to generalize our short-term (max. 1 year) snapshots of seismicity to a longer geological timeframe.

This thesis investigated gravitational loading and glacial isostasy as the potential reason for fluid flow system distribution. Seismic observations showed that if these processes play a role, they do so mainly aseismically. Either the magnitudes of potential events are too low to observe or the amount of shear stress that can accumulate in sediments is too low for a failure. Two very weak seismic events observed at Vestnesa indicate that the occasional faulting of the crust at greater depths can produce a measurable seismic energy. Source mechanisms of such events would help in understanding the controlling mechanisms, but they may be very difficult to obtain experimentally. One would need a dense network of stations deployed in just the right area at just the right time to record a sporadic earthquake that occurs in mostly aseismic region. The design and maintenance of such a network therefore presents a challenge.

Below, I describe several possible research directions in a greater detail.

The signal detection approach used in the **Article 2** and **Manuscript 3** is still de-facto standard, but it is fairly basic and relies only on the amplitude difference computed for two overlapping time windows (STA/LTA; Allen, 1982). The difference between the length of the signal of interest and the noise levels encountered in different datasets requires manual adjustment of the detector parameters, but ultimately some signals do not get properly captured regardless of the settings. The correct determination of the onset signal, while not critical for the documented results, likely leaves a lot of to be desired. We improved onset determination with a kurtosis-based approach (Baillard et al., 2013), which works relatively well only if the signal to noise ratio is high. I tried to use machine learning based detectors (e.g., Mousavi et al., 2020; Zhu & Beroza, 2018), which are the current state-of-the art approaches and a topic of intense research. Unfortunately, the presence of impulsive noise signals in our data produced too many false detections to use them reliably. I tested the detectors with trained machine learning models that were provided. The training datasets contained only land earthquake detections, therefore there were not intended for OBS data. It could be interesting to train new models using only signals from ocean bottom seismometers and see if they produce more accurate results. We tried one recently published model that was trained with OBS data for earthquake detection (Bornstein et al., 2023), but the results were worse than what we obtained with our method. Perhaps more examples of earthquakes from different settings are needed to achieve a better generalization. No models exist for the detection of short duration signals, so any models, trained even with a small amount of examples, would be a novelty that could be investigated deeper. To tackle the detection problem from a different direction, it would be interesting to investigate noise removal approaches (e.g., Dolenc et al., 2007; Bell et al., 2015; Zali et al., 2023), beyond the signal

filtering, and see whether they work well in marine seismological data and potentially improve already tried detection methods.

We analyzed the way SDEs vary in time referring to their occurrence and intensity in the **Article 1**, and (to a lesser extent) in the **Article 2**. This work was done following the assumption of the inherent link between this type of signal with the fluid flow processes. This link, however, is still not fully established (Diaz et al., 2007; Tary et al., 2012). The reasons for this are numerous. To have a direct connection with the gas seepage, we would have to observe SDE while simultaneously monitoring gas emissions into the water column, perhaps using hydroacoustic monitoring or video footage. This requires more equipment deployed precisely on the seafloor and likely greater power consumption. Moreover, we would need observations to be synchronized in time, which sometimes can be an issue present in all manner of instrumentations, as demonstrated in the **Manuscript 3** for the OBS data.

SDEs do not exhibit phase separation, indicating local source, but also rendering P-S wave time difference location methods impossible. Source location would rely in this case on simultaneous detections on more than one station, which has not yet been observed, perhaps due to still too large OBS separation distance in our studies. Once this would be achieved, we could use a directionality of the signal to establish a source position. This can be done using e.g., polarity-based methods (e.g., Vidale, 1986; Jurkevics, 1988; Zenhäusern et al., 2022). Proper polarization analysis requires a good knowledge of the seismometer orientation, which is another challenge for OBS units deployed by freefall. Different methods used for seismometer orientation do not always work and in the best case leave an uncertainty of more than 10-20 degrees. SDEs have a duration of 1-2 s on average, much lower than local earthquakes. Because of this, proper polarity analysis would require higher signal sampling than is generally used in long term OBS deployments. Higher sampling corresponds to shorter recording time for a given amount of storage, which is a compromise that has to be made in remote, independent observations.

To establish a connection between the SDEs and fluid flow beyond a doubt, we would need to place a group of seismometers with a high precision for position and orientation, within several meters around the gas seep. This could potentially be done with remotely operated vehicle, but it likely would be prohibitively expensive. So far, only one experiment combined observations of SDEs with the simultaneous video monitoring, but this was done in a shallow water, away from seepage sites (Batsi et al., 2019). Perhaps another way of investigating these signals is by the use of analogue fluid flow systems documented on land. An experiment involving seismometers around a permafrost hill (“pingo”), with the spring on top that discharges fluid rich in gas on Svalbard (e.g., Hodson et al., 2020), is currently underway. If

SDEs are observed in this setting, further evidence towards the proposed explanations can be established.

The connection between weak seismicity observed at Vestnesa Ridge and the documented fluid flow system could not be established due to the inability to properly constrain the hypocentral depth of the events. To unambiguously make a connection to a specific fault system, we would need to have deeper penetrating seismic reflection profiles and earthquake detections located within the network for the depth calculation. Since we recorded two events, the activity can be considered sporadic and there is a high likelihood that future targeted OBS experiments would not record any seismicity.

Seismic activity documented in the zone between Knipovich Ridge – Molloy Transform Fault intersection is an interesting new target for a designated investigation using OBSs. Additional seismic surveys could help verify the hypothesis about the presence of the spreading center under the sedimentary layers. Recent nearby discoveries indicate that there may be undocumented seepage sites in the area (Plaza-Faverola, 2022). With the local network of instruments, we would be able to better locate the earthquakes and calculate their hypocentral depths. With enough azimuthal coverage, we could also compute focal mechanisms and establish the faulting regime for the area. The amount of activity reported in the **Manuscript 3** indicates that even shorter survey would provide a sufficient dataset of earthquakes to investigate. The results from **Manuscript 3** showed a very nice agreement between the locations of seismicity and corresponding seismic reflection profiles. This provided us with a better framework for the interpretation of earthquake origins. It would be beneficial to complement OBS deployments with at least some seismic lines in the same study area more often.

It may be interesting to investigate the potential that the recent introduction of optic fiber cables (distributed acoustic systems, e.g., Landrø et al., 2022) into Arctic seismology have when it is used in localized observations of fluid flow systems. This technology can enable very dense monitoring (virtual spacing of receivers ~ every few meters) with a single cable and can help i.e., in pin-pointing the exact location of signals such as SDEs.

6 References

- Aki, K., Fehler, M., & Das, S. (1977). Source mechanism of volcanic tremor: fluid-driven crack models and their application to the 1963 kilauea eruption. *Journal of Volcanology and Geothermal Research*, 2(3), 259-287.
- Allen, R. (1982). Automatic phase pickers: Their present use and future prospects. *Bulletin of the Seismological Society of America*, 72(6B), S225-S242.
- Ambrose, W. G., Panieri, G., Schneider, A., Plaza-Faverola, A., Carroll, M. L., Åström, E. K. L., et al. (2015). Bivalve shell horizons in seafloor pockmarks of the last glacial-interglacial transition: a thousand years of methane emissions in the Arctic Ocean. *Geochemistry Geophysics Geosystems*, 16(12), 4108-4129.
- Amundsen, I. M. H., Blinova, M., Hjelstuen, B. O., Mjelde, R., & Hafliðason, H. (2011). The Cenozoic western Svalbard margin: sediment geometry and sedimentary processes in an area of ultraslow oceanic spreading. *Marine Geophysical Research*, 32(4), 441-453.
- Anderson, E. M. (1905). The dynamics of faulting. *Transactions of the Edinburgh Geological Society*, 8(3), 387-402.
- Anderson, E. M. (1951). *The Dynamics of Faulting and Dyke Formation with applications to Britain* (Second Edit.): Oliver and Boyd.
- Atkinson, G. M., Eaton, D. W., & Igonin, N. (2020). Developments in understanding seismicity triggered by hydraulic fracturing. *Nature Reviews Earth & Environment*, 1(5), 264-277.
- Baillard, C., Crawford, W. C., Ballu, V., Hibert, C., & Mangeney, A. (2013). An Automatic Kurtosis-Based P- and S-Phase Picker Designed for Local Seismic Networks. *Bulletin of the Seismological Society of America*, 104(1), 394-409.
- Barry, M. A., Boudreau, B. P., & Johnson, B. D. (2012). Gas domes in soft cohesive sediments. *Geology*, 40(4), 379-382.
- Batsi, E., Tsang-Hin-Sun, E., Klingelhoefer, F., Bayrakci, G., Chang, E. T. Y., Lin, J. Y., et al. (2019). Nonseismic Signals in the Ocean: Indicators of Deep Sea and Seafloor Processes on Ocean-Bottom Seismometer Data. *Geochemistry, Geophysics, Geosystems*, 20(8), 3882-3900.
- Bayrakci, G., Scalabrin, C., Dupré, S., Leblond, I., Tary, J.-B., Lanteri, N., et al. (2014). Acoustic monitoring of gas emissions from the seafloor. Part II: a case study from the Sea of Marmara. *Marine Geophysical Research*, 35(3), 211-229.
- Bell, S. W., Forsyth, D. W., & Ruan, Y. (2015). Removing Noise from the Vertical Component Records of Ocean-Bottom Seismometers: Results from Year One of the Cascadia Initiative. *Bulletin of the Seismological Society of America*, 105(1), 300-313.
- Bernard, B. B., Brooks, J. M., & Sackett, W. M. (1976). Natural gas seepage in the Gulf of Mexico. *Earth and Planetary Science Letters*, 31(1), 48-54.
- Berndt, C. (2005). Focused fluid flow in passive continental margins. *Philosophical Transactions of the Royal Society A: Mathematical, Physical and Engineering Sciences*, 363(1837), 2855-2871.
- Bohnhoff, M., & Zoback, M. D. (2010). Oscillation of fluid-filled cracks triggered by degassing of CO₂ due to leakage along wellbores. *Journal of Geophysical Research: Solid Earth*, 115(B11).
- Boles, J. R., Clark, J. F., Leifer, I., & Washburn, L. (2001). Temporal variation in natural methane seep rate due to tides, Coal Oil Point area, California. *Journal of Geophysical Research: Oceans*, 106(C11), 27077-27086.

- Boudreau, B. P. (2012). The physics of bubbles in surficial, soft, cohesive sediments. *Marine and Petroleum Geology*, 38(1), 1-18.
- Bornstein, T., Lange, D., Münchmeyer, J., Woollam, J., Rietbrock, A., Barcheck, G., ... & Tilmann, F. (2023). PickBlue: Seismic phase picking for ocean bottom seismometers with deep learning. *arXiv preprint arXiv:2304.06635*.
- Bowman, D. C., & Wilcock, W. S. D. (2013). Unusual signals recorded by ocean bottom seismometers in the flooded caldera of Deception Island volcano: volcanic gases or biological activity? *Antarctic Science*, 26(3), 267-275.
- Breiman, L., 2001. Random forests. *Mach. Learn.*, 45 (1), 5–32.
- Brodsky, E. E., & Elst, N. J. v. d. (2014). The Uses of Dynamic Earthquake Triggering. *Annual Review of Earth and Planetary Sciences*, 42(1), 317-339.
- Brooks, G. R., & Adams, J. (2020). A review of evidence of glacially-induced faulting and seismic shaking in eastern Canada. *Quaternary Science Reviews*, 228, 106070.
- Buskirk, R. E., Frohlich, C., Latham, G. V., Chen, A. T., & Lawton, J. (1981). Evidence that biological activity affects ocean bottom seismograph recordings. *Marine Geophysical Researches*, 5(2), 189-205.
- Bünz, S., Polyanov, S., Vadakkepuliambatta, S., Consolaro, C., & Mienert, J. (2012). Active gas venting through hydrate-bearing sediments on the Vestnesa Ridge, offshore W-Svalbard. *Marine Geology*, 332, 189-197.
- Bünz, S. (2023a). Cruise CAGE15-4. *CAGE – Centre for Arctic Gas Hydrate, Environment and Climate Report Series*, 3.
- Bünz, S. (2023b). CAGE16-6 Cruise Report: Cruise CAGE16-6. *CAGE – Centre for Arctic Gas Hydrate, Environment and Climate Report Series*, 4.
- Bünz, S. (2023c). CAGE19-1 Cruise Report: Passive and active ocean-bottom seismic surveys at Vestnesa Ridge, west-Svalbard margin within the framework of the SEAMSTRESS project. *CAGE – Centre for Arctic Gas Hydrate, Environment and Climate Report Series*, 7.
- Bünz, S. (2023d). CAGE20-5 Cruise Report: Tectonic stress studies and seismic surveys on the West-Svalbard margin. *CAGE – Centre for Arctic Gas Hydrate, Environment and Climate Report Series*, 8.
- Caine, J. S., Evans, J. P., & Forster, C. B. (1996). Fault zone architecture and permeability structure. *Geology*, 24(11), 1025-1028.
- Cao, H., Medici, E., & Askari, R. (2021). Physical modeling of fluid-filled fractures using the dynamic photoelasticity technique. *Geophysics*, 86(1), T33-T43.
- Carter, L., Gavey, R., Talling, P. J., & Liu, J. T. (2014). Insights into Submarine Geohazards from Breaks in Subsea Telecommunication Cables. *Oceanography*, 27(2), 58-67.
- Chanard, K., Avouac, J. P., Ramillien, G., & Genrich, J. (2014). Modeling deformation induced by seasonal variations of continental water in the Himalaya region: Sensitivity to Earth elastic structure. *Journal of Geophysical Research: Solid Earth*, 119(6), 5097-5113.
- Chang, E. T. Y., Chao, B. F., Chen, G. Y., & Liaw, J. M. (2016). Internal tides recorded at ocean bottom off the coast of Southeast Taiwan. *Journal of Geophysical Research: Oceans*, 121(5), 3381-3394.
- Chao, K., Peng, Z., Gonzalez-Huizar, H., Aiken, C., Enescu, B., Kao, H., et al. (2013). A Global Search for Triggered Tremor Following the 2011 Mw 9.0 Tohoku Earthquake. *Bulletin of the Seismological Society of America*, 103(2B), 1551-1571.

- Chen, C.-T. A., Zeng, Z., Kuo, F.-W., Yang, T. F., Wang, B.-J., & Tu, Y.-Y. (2005). Tide-influenced acidic hydrothermal system offshore NE Taiwan. *Chemical geology*, 224(1), 69-81.
- Chen, S.-C., Hsu, S.-K., Tsai, C.-H., Ku, C.-Y., Yeh, Y.-C., & Wang, Y. (2010). Gas seepage, pockmarks and mud volcanoes in the near shore of SW Taiwan. *Marine Geophysical Researches*, 31(1), 133-147.
- Chouet, B. (1988). Resonance of a fluid-driven crack: Radiation properties and implications for the source of long-period events and harmonic tremor. *Journal of Geophysical Research: Solid Earth*, 93(B5), 4375-4400.
- Chouet, B. (1986). Dynamics of a fluid-driven crack in three dimensions by the finite difference method. *Journal of Geophysical Research: Solid Earth*, 91(B14), 13967-13992.
- Chouet, B. (2003). Volcano Seismology. *pure and applied geophysics*, 160(3), 739-788.
- Chouet, B., Dawson, P., & Arciniega-Ceballos, A. (2005). Source mechanism of Vulcanian degassing at Popocatepetl Volcano, Mexico, determined from waveform inversions of very long period signals. *Journal of Geophysical Research: Solid Earth*, 110(B7).
- Claypool, G. E., & Kaplan, I. R. (1974). The origin and distribution of methane in marine sediments. In *Natural gases in marine sediments* (pp. 99-139): Springer.
- Cochran, E. S., Vidale, J. E., & Tanaka, S. (2004). Earth Tides Can Trigger Shallow Thrust Fault Earthquakes. *Science*, 306(5699), 1164-1166.
- Consolaro, C., Rasmussen, T. L., Panieri, G., Mienert, J., Bunz, S., & Szybor, K. (2015). Carbon isotope ($\delta C-13$) excursions suggest times of major methane release during the last 14 kyr in Fram Strait, the deep-water gateway to the Arctic. *Climate of the Past*, 11(4), 669-685.
- Cooke, F., Plaza-Faverola, A., Bünz, S., Sultan, N., Ramachandran, H., Bedle, H., et al. (2023). Sedimentary deformation relating to episodic seepage in the last 1.2 million years: a multi-scale seismic study from the Vestnesa Ridge, eastern Fram Strait. *Frontiers in Earth Science*, 11.
- Craig, T. J., Chanard, K., & Calais, E. (2017). Hydrologically-driven crustal stresses and seismicity in the New Madrid Seismic Zone. *Nature Communications*, 8(1), 2143.
- Crawford, W. C., Webb, S. C., & Hildebrand, J. A. (1998). Estimating shear velocities in the oceanic crust from compliance measurements by two-dimensional finite difference modeling. *Journal of Geophysical Research: Solid Earth*, 103(B5), 9895-9916.
- D'Alessandro, A., D'Anna, G., Luzio, D., & Mangano, G. (2009). The INGV's new OBS/H: Analysis of the signals recorded at the Marsili submarine volcano. *Journal of Volcanology and Geothermal Research*, 183(1-2), 17-29.
- Daigle, H., & Dugan, B. (2010). Origin and evolution of fracture-hosted methane hydrate deposits. *Journal of Geophysical Research: Solid Earth*, 115(B11).
- Das, I., & Zoback, M. D. (2011). Long-period, long-duration seismic events during hydraulic fracture stimulation of a shale gas reservoir. *The Leading Edge*, 30(7), 778-786.
- DeCarlo, L. T. (1997). On the meaning and use of kurtosis. *Psychological Methods*, 2(3), 292-307.
- Derode, B., Guglielmi, Y., De Barros, L., & Cappa, F. (2015). Seismic responses to fluid pressure perturbations in a slipping fault. *Geophysical Research Letters*, 42(9), 3197-3203.
- Díaz, J., Gallart, J., & Gaspà, O. (2007). Atypical seismic signals at the Galicia Margin, North Atlantic Ocean, related to the resonance of subsurface fluid-filled cracks. *Tectonophysics*, 433(1-4), 1-13.
- Dick, H. J. B., Lin, J., & Schouten, H. (2003). An ultraslow-spreading class of ocean ridge. *Nature*, 426(6965), 405-412.

- Dolenc, D., Romanowicz, B., Uhrhammer, R., McGill, P., Neuhauser, D., & Stakes, D. (2007). Identifying and removing noise from the Monterey ocean bottom broadband seismic station (MOBB) data. *Geochemistry, Geophysics, Geosystems*, 8(2).
- Domel, P., Singhroha, S., Plaza-Faverola, A., Schlindwein, V., Ramachandran, H., & Bünz, S. (2021). Replication data for: Origin and periodic behavior of short duration signals recorded by seismometers at Vestnesa Ridge, an active seepage site on the west-Svalbard continental margin. *DataVerseNO*.
- Duan, B. (2016). Spontaneous rupture on natural fractures and seismic radiation during hydraulic fracturing treatments. *Geophysical Research Letters*, 43(14), 7451-7458.
- Dugan, B., & Sheahan, T. C. (2012). Offshore sediment overpressures of passive margins: Mechanisms, measurement, and models. *Reviews of Geophysics*, 50(3).
- Dumais, M. A., Gernigon, L., Olesen, O., Johansen, S. E., & Brønner, M. (2021). New interpretation of the spreading evolution of the Knipovich Ridge derived from aeromagnetic data. *Geophysical Journal International*, 224(2), 1422-1428.
- Dziak, R. P., Chadwick, W. W., Jr., Fox, C. G., & Embley, R. W. (2003). Hydrothermal temperature changes at the southern Juan de Fuca Ridge associated with MW 6.2 Blanco Transform earthquake. *Geology*, 31(2), 119-122.
- Ehlers, B.-M., & Jokat, W. (2009). Subsidence and crustal roughness of ultra-slow spreading ridges in the northern North Atlantic and the Arctic Ocean. *Geophysical Journal International*, 177(2), 451-462.
- Eiken, O., & Hinz, K. (1993). Contourites in the Fram Strait. *Sedimentary Geology*, 82(1-4), 15-32.
- Embriaco, D., Marinaro, G., Frugoni, F., Monna, S., Etiope, G., Gasperini, L., et al. (2014). Monitoring of gas and seismic energy release by multiparametric benthic observatory along the North Anatolian Fault in the Sea of Marmara (NW Turkey). *Geophysical Journal International*, 196(2), 850-866.
- Engen, Ø., Faleide, J. I., & Dyreng, T. K. (2008). Opening of the Fram Strait gateway: A review of plate tectonic constraints. *Tectonophysics*, 450(1-4), 51-69.
- Essing, D., Schlindwein, V., Schmidt-Aursch, M. C., Hadziioannou, C., & Stähler, S. C. (2021). Characteristics of Current-Induced Harmonic Tremor Signals in Ocean-Bottom Seismometer Records. *Seismological Research Letters*.
- Etiope, G. (2015). *Natural Gas Seepage: The Earth's Hydrocarbon Degassing*: Springer.
- Faleide, J. I., Solheim, A., Fiedler, A., Hjelstuen, B. O., Andersen, E. S., & Vanneste, K. (1996). Late Cenozoic evolution of the western Barents Sea-Svalbard continental margin. *Global and Planetary Change*, 12(1-4), 53-74.
- Faulkner, D. R., Jackson, C. A. L., Lunn, R. J., Schlische, R. W., Shipton, Z. K., Wibberley, C. A. J., & Withjack, M. O. (2010). A review of recent developments concerning the structure, mechanics and fluid flow properties of fault zones. *Journal of Structural Geology*, 32(11), 1557-1575.
- Fazio, M., Benson, P. M., & Vinciguerra, S. (2017). On the generation mechanisms of fluid-driven seismic signals related to volcano-tectonics. *Geophysical Research Letters*, 44(2), 734-742.
- Ferrazzini, V., & Aki, K. (1987). Slow waves trapped in a fluid-filled infinite crack: Implication for volcanic tremor. *Journal of Geophysical Research: Solid Earth*, 92(B9), 9215-9223.
- Ferrick, M. G., Qamar, A., & St. Lawrence, W. F. (1982). Source mechanism of volcanic tremor. *Journal of Geophysical Research: Solid Earth*, 87(B10), 8675-8683.
- Fjeldskaar, W., Lindholm, C., Dehls, J. F., & Fjeldskaar, I. (2000). Postglacial uplift, neotectonics and seismicity in Fennoscandia. *Quaternary Science Reviews*, 19(14), 1413-1422.

- Fornari, D. J., Shank, T., Von Damm, K. L., Gregg, T. K. P., Lilley, M., Levai, G., et al. (1998). Time-series temperature measurements at high-temperature hydrothermal vents, East Pacific Rise 9°49'–51°N: evidence for monitoring a crustal cracking event. *Earth and Planetary Science Letters*, 160(3), 419-431.
- Franek, P., Mienert, J., Buenz, S., & Géli, L. (2014). Character of seismic motion at a location of a gas hydrate-bearing mud volcano on the SW Barents Sea margin. *Journal of Geophysical Research: Solid Earth*, 119(8), 6159-6177.
- Franek, P., Plaza-Faverola, A., Mienert, J., Buenz, S., Ferré, B., & Hubbard, A. (2017). Microseismicity Linked to Gas Migration and Leakage on the Western Svalbard Shelf. *Geochemistry, Geophysics, Geosystems*, 18(12), 4623-4645.
- Friedrich, A., Krüger, F., & Klinge, K. (1998). Ocean-generated microseismic noise located with the Gräfenberg array. *Journal of Seismology*, 2(1), 47-64.
- Gardner, A. T., & Collins, J. A. (2012, 14-19 Oct. 2012). *Advancements in high-performance timing for long term underwater experiments: A comparison of chip scale atomic clocks to traditional microprocessor-compensated crystal oscillators*. Paper presented at the 2012 Oceans.
- Gardner, J. V., van den Aamele, E. J., Gelfenbaum, G., Barnhardt, W., Lee, H., & Palmer, S. (2001). Mapping southern Puget Sound delta fronts after 2001 earthquake. *Eos, Transactions American Geophysical Union*, 82(42), 485-489.
- Gasperini, L., Polonia, A., Del Bianco, F., Etiope, G., Marinaro, G., Favali, P., et al. (2012). Gas seepage and seismogenic structures along the North Anatolian Fault in the eastern Sea of Marmara. *Geochemistry, Geophysics, Geosystems*, 13(10).
- Gomberg, J., Blanpied, M. L., & Beeler, N. M. (1997). Transient triggering of near and distant earthquakes. *Bulletin of the Seismological Society of America*, 87(2), 294-309.
- Goswami, B. K., Weitemeyer, K. A., Minshull, T. A., Sinha, M. C., Westbrook, G. K., Chabert, A., et al. (2015). A joint electromagnetic and seismic study of an active pockmark within the hydrate stability field at the Vestnesa Ridge, West Svalbard margin. *Journal of Geophysical Research: Solid Earth*, 120(10), 6797-6822.
- Goswami, B. K., Weitemeyer, K. A., Bunz, S., Minshull, T. A., Westbrook, G. K., Ker, S., & Sinha, M. C. (2017). Variations in pockmark composition at the Vestnesa Ridge: Insights from marine controlled source electromagnetic and seismic data. *Geochemistry Geophysics Geosystems*, 18(3), 1111-1125.
- Gouédard, P., Seher, T., McGuire, J. J., Collins, J. A., & van der Hilst, R. D. (2014). Correction of Ocean-Bottom Seismometer Instrumental Clock Errors Using Ambient Seismic Noise. *Bulletin of the Seismological Society of America*, 104(3), 1276-1288.
- Graham, C. C., Stanchits, S., Main, I. G., & Dresen, G. (2010). Comparison of polarity and moment tensor inversion methods for source analysis of acoustic emission data. *International Journal of Rock Mechanics and Mining Sciences*, 47(1), 161-169.
- Grall, C., Henry, P., Dupré, S., Géli, L., Scalabrin, C., Zitter, T. A. C., et al. (2018). Upward migration of gas in an active tectonic basin: An example from the sea of Marmara. *Deep Sea Research Part II: Topical Studies in Oceanography*, 153, 17-35.
- Gräff, D., Walter, F., & Lipovsky, B. P. (2019). Crack wave resonances within the basal water layer. *Annals of Glaciology*, 60(79), 158-166.
- Grollmund, B., & Zoback, M. D. (2000). Post glacial lithospheric flexure and induced stresses and pore pressure changes in the northern North Sea. *Tectonophysics*, 327(1), 61-81.
- Grosse, C. U., Ohtsu, M., Aggelis, D. G., & Shiotani, T. (2021). *Acoustic emission testing: Basics for research–applications in engineering*: Springer Nature.

- Guilhem, A., Peng, Z., & Nadeau, R. M. (2010). High-frequency identification of non-volcanic tremor triggered by regional earthquakes. *Geophysical Research Letters*, 37(16).
- Gupta, H. K. (2002). A review of recent studies of triggered earthquakes by artificial water reservoirs with special emphasis on earthquakes in Koyana, India. *Earth-Science Reviews*, 58(3), 279-310.
- Han, J., Vidale, J. E., Houston, H., Schmidt, D. A., & Creager, K. C. (2018). Deep Long-Period Earthquakes Beneath Mount St. Helens: Their Relationship to Tidal Stress, Episodic Tremor and Slip, and Regular Earthquakes. *Geophysical Research Letters*, 45(5), 2241-2247.
- Hannemann, K., Krüger, F., & Dahm, T. (2014). Measuring of clock drift rates and static time offsets of ocean bottom stations by means of ambient noise. *Geophysical Journal International*, 196(2), 1034-1042.
- Harland, W. B., Cutbill, J. L., Friend, P. F., Gobbett, D. J., Holliday, D. W., Maton, P. I., ... & Wallis, R. H. (1974). The Billefjorden Fault Zone, Spitsbergen: the long history of a major tectonic lineament.
- Heki, K. (2001). Seasonal Modulation of Interseismic Strain Buildup in Northeastern Japan Driven by Snow Loads. *Science*, 293(5527), 89-92.
- Heki, K. (2003). Snow load and seasonal variation of earthquake occurrence in Japan. *Earth and Planetary Science Letters*, 207(1), 159-164.
- Hibert, C., Provost, F., Malet, J.-P., Maggi, A., Stumpf, A., & Ferrazzini, V. (2017). Automatic identification of rockfalls and volcano-tectonic earthquakes at the Piton de la Fournaise volcano using a Random Forest algorithm. *Journal of Volcanology and Geothermal Research*, 340, 130-142.
- Hill, D. P., & Prejean, S. G. (2007). 4.09 - Dynamic Triggering. In G. Schubert (Ed.), *Treatise on Geophysics* (pp. 257-291). Amsterdam: Elsevier.
- Himmler, T., Sahy, D., Martma, T., Bohrmann, G., Plaza-Faverola, A., Bünz, S., et al. (2019). A 160,000-year-old history of tectonically controlled methane seepage in the Arctic. *Science Advances*, 5(8), eaaw1450.
- Hodson, A. J., Nowak, A., Hornum, M. T., Senger, K., Redeker, K., Christiansen, H. H., ... & Marca, A. (2020). Sub-permafrost methane seepage from open-system pingos in Svalbard. *The Cryosphere*, 14(11), 3829-3842.
- Hong, W. L., Pape, T., Schmidt, C., Yao, H., Wallmann, K., Plaza-Faverola, A., et al. (2021). Interactions between deep formation fluid and gas hydrate dynamics inferred from pore fluid geochemistry at active pockmarks of the Vestnesa Ridge, west Svalbard margin. *Marine and Petroleum Geology*, 127.
- Hovland, M., & Curzi, P. V. (1989). Gas seepage and assumed mud diapirism in the Italian central Adriatic Sea. *Marine and Petroleum Geology*, 6(2), 161-169.
- Hovland, M., Gardner, J. V., & Judd, A. G. (2002). The significance of pockmarks to understanding fluid flow processes and geohazards. *Geofluids*, 2(2), 127-136.
- Howe, J. A., Shimmield, T. M., Harland, R. E. X., & Eyles, N. (2007). Late Quaternary contourites and glaciomarine sedimentation in the Fram Strait. *Sedimentology*, 55(1), 179-200.
- Hsu, S.-K., Wang, S.-Y., Liao, Y.-C., Yang, T. F., Jan, S., Lin, J.-Y., & Chen, S.-C. (2013). Tide-modulated gas emissions and tremors off SW Taiwan. *Earth and Planetary Science Letters*, 369-370, 98-107.
- Huhn, K., Arroyo, M., Cattaneo, A., Clare, M. A., Gràcia, E., Harbitz, C. B., et al. (2019). Modern Submarine Landslide Complexes. In *Submarine Landslides* (pp. 181-200).
- Hunt, J. (1995). Petroleum geochemistry and geology (textbook). *Petroleum Geochemistry and Geology (Textbook)*. (2nd Ed.), WH Freeman Company.

- Hustoft, S., Bunz, S., Mienert, J., & Chand, S. (2009). Gas hydrate reservoir and active methane-venting province in sediments on < 20 Ma young oceanic crust in the Fram Strait, offshore NW-Svalbard. *Earth and Planetary Science Letters*, 284(1-2), 12-24.
- Ide, S., Shelly, D. R., & Beroza, G. C. (2007). Mechanism of deep low frequency earthquakes: Further evidence that deep non-volcanic tremor is generated by shear slip on the plate interface. *Geophysical Research Letters*, 34(3).
- Jeddi, Z., Ottemöller, L., Sørensen, M. B., Rezaei, S., Gibbons, S. J., Strømme, M. L., et al. (2021). Improved Seismic Monitoring with OBS Deployment in the Arctic: A Pilot Study from Offshore Western Svalbard. *Seismological Research Letters*, 92(5), 2705-2717.
- Johnson, J. E., Mienert, J., Plaza-Faverola, A., Vadakkepuliambatta, S., Knies, J., Buenz, S., et al. (2015). Abiotic methane from ultraslow-spreading ridges can charge Arctic gas hydrates. *Geology*, 43(5), 371-374.
- Judd, A., & Hovland, M. (2007). *Seabed fluid flow : the impact on geology, biology, and the marine environment*. Cambridge: Cambridge University Press.
- Jurkevics, A. (1988). Polarization analysis of three-component array data. *Bulletin of the Seismological Society of America*, 78(5), 1725-1743.
- Konstantinou, K. I., & Schlindwein, V. (2003). Nature, wavefield properties and source mechanism of volcanic tremor: a review. *Journal of Volcanology and Geothermal Research*, 119(1-4), 161-187.
- Korneev, V. (2007). Slow waves in fractures filled with viscous fluid. *Geophysics*, 73(1), N1-N7.
- Krauklis, P. (1962). About some low frequency oscillations of a liquid layer in elastic medium. *PMM*, 26(6): 1111–1115. In: Russian.
- King Hubbert, M., & Rubey, W. W. (1959). Role of fluid pressure in mechanics of overthrust faulting: I. Mechanics of fluid-filled porous solids and its application to overthrust faulting. *GSA Bulletin*, 70(2), 115-166.
- Kanamori, H., & Brodsky, E. E. (2004). The physics of earthquakes. *Reports on Progress in Physics*, 67(8), 1429.
- Knies, J., Matthiessen, J., Vogt, C., Laberg, J. S., Hjelstuen, B. O., Smelror, M., et al. (2009). The Plio-Pleistocene glaciation of the Barents Sea–Svalbard region: a new model based on revised chronostratigraphy. *Quaternary Science Reviews*, 28(9-10), 812-829.
- Knies, J., Mattingsdal, R., Fabian, K., Grøsfjeld, K., Baranwal, S., Husum, K., et al. (2014). Effect of early Pliocene uplift on late Pliocene cooling in the Arctic–Atlantic gateway. *Earth and Planetary Science Letters*, 387, 132-144.
- Knipe, R. (1992). Faulting processes and fault seal. In *Structural and tectonic modelling and its application to petroleum geology* (pp. 325-342): Elsevier.
- Knipe, R. J. (1993). The Influence of Fault Zone Processes and Diagenesis on Fluid Flow. In A. D. Horbury & A. G. Robinson (Eds.), *Diagenesis and Basin Development* (Vol. 36, pp. 0): American Association of Petroleum Geologists.
- Krabbenhoef, A., Bialas, J., Klauke, I., Crutchley, G., Papenberg, C., & Netzeband, G. L. (2013). Patterns of subsurface fluid-flow at cold seeps: The Hikurangi Margin, offshore New Zealand. *Marine and Petroleum Geology*, 39(1), 59-73.
- Kvarven, T., Hjelstuen, B. O., & Mjelde, R. (2014). Tectonic and sedimentary processes along the ultraslow Knipovich spreading ridge. *Marine Geophysical Research*, 35(2), 89-103.

- Lambert, A., Kao, H., Rogers, G., & Courtier, N. (2009). Correlation of tremor activity with tidal stress in the northern Cascadia subduction zone. *Journal of Geophysical Research: Solid Earth*, 114(B8).
- Landrø, M., Bouffaut, L., Kriesell, H. J., Potter, J. R., Rørstadbotnen, R. A., Taweasantanon, K., et al. (2022). Sensing whales, storms, ships and earthquakes using an Arctic fibre optic cable. *Scientific Reports*, 12(1), 19226.
- Li, C., Zhan, L., & Lu, H. (2022). Mechanisms for Overpressure Development in Marine Sediments. *Journal of Marine Science and Engineering*, 10(4), 490.
- Liu, C., Linde, A. T., & Sacks, I. S. (2009). Slow earthquakes triggered by typhoons. *Nature*, 459(7248), 833-836.
- Macgregor, D. S. (1993). Relationships between seepage, tectonics and subsurface petroleum reserves. *Marine and Petroleum Geology*, 10(6), 606-619.
- Madrussani, G., Rossi, G., & Camerlenghi, A. (2010). Gas hydrates, free gas distribution and fault pattern on the west Svalbard continental margin. *Geophysical Journal International*, 180(2), 666-684.
- Manga, M., Beresnev, I., Brodsky, E. E., Elkhoury, J. E., Elsworth, D., Ingebritsen, S. E., et al. (2012). Changes in permeability caused by transient stresses: Field observations, experiments, and mechanisms. *Reviews of Geophysics*, 50(2).
- Manga, M., & Wang, C. Y. (2015). 4.12 - Earthquake Hydrology. In G. Schubert (Ed.), *Treatise on Geophysics (Second Edition)* (pp. 305-328). Oxford: Elsevier.
- Mattingsdal, R., Knies, J., Andreassen, K., Fabian, K., Husum, K., Grøsfjeld, K., & De Schepper, S. (2014). A new 6 Myr stratigraphic framework for the Atlantic–Arctic Gateway. *Quaternary Science Reviews*, 92, 170-178.
- Mau, S., Rehder, G., Arroyo, I. G., Gossler, J., & Suess, E. (2007). Indications of a link between seismotectonics and CH₄ release from seeps off Costa Rica. *Geochemistry, Geophysics, Geosystems*, 8(4).
- Maxwell, S., Du, J., Shemeta, J., Zimmer, U., Boroumand, N., & Griffin, L. (2007). Monitoring SAGD Steam Injection Using Microseismicity and Tiltmeters. Paper SPE 110634 presented at the SPE Annual Technical Conference and Exhibition, Anaheim, California, USA, 11–14 November.
- Maxwell, S. C., & Cipolla, C. (2011). *What does microseismicity tell us about hydraulic fracturing?* Paper presented at the SPE Annual Technical Conference and Exhibition.
- Meier, M., Schlindwein, V., Scholz, J. R., Geils, J., Schmidt-Aursch, M. C., Kruger, F., et al. (2021). Segment-Scale Seismicity of the Ultraslow Spreading Knipovich Ridge. *Geochemistry Geophysics Geosystems*, 22(2), e2020GC009375.
- Menapace, W., Völker, D., Sahling, H., Zoellner, C., dos Santos Ferreira, C., Bohrmann, G., & Kopf, A. (2017). Long-term in situ observations at the Athina mud volcano, Eastern Mediterranean: Taking the pulse of mud volcanism. *Tectonophysics*, 721, 12-27.
- Menke, W. (2018). *Geophysical data analysis: Discrete inverse theory*. Academic press.
- Métivier, L., de Viron, O., Conrad, C. P., Renault, S., Diament, M., & Patau, G. (2009). Evidence of earthquake triggering by the solid earth tides. *Earth and Planetary Science Letters*, 278(3), 370-375.
- Mousavi, S. M., Ellsworth, W. L., Zhu, W., Chuang, L. Y., & Beroza, G. C. (2020). Earthquake transformer-an attentive deep-learning model for simultaneous earthquake detection and phase picking. *Nat Commun*, 11(1), 3952.
- Myhre, A. M., & Eldholm, O. (1988). The western Svalbard margin (74–80 N). *Marine and Petroleum Geology*, 5(2), 134-156.

- Nakagawa, S., & Korneev, V. A. (2014). Effect of fracture compliance on wave propagation within a fluid-filled fracture. *The Journal of the Acoustical Society of America*, 135(6), 3186-3197.
- Naoi, M., Chen, Y., Yamamoto, K., Morishige, Y., Imakita, K., Tsutumi, N., et al. (2020). Tensile-dominant fractures observed in hydraulic fracturing laboratory experiment using eagle ford shale. *Geophysical Journal International*, 222(2), 769-780.
- Obara, K. (2002). Nonvolcanic Deep Tremor Associated with Subduction in Southwest Japan. *Science*, 296(5573), 1679-1681.
- Osborne, M. J., & Swarbrick, R. E. (1997). Mechanisms for Generating Overpressure in Sedimentary Basins: A Reevaluation. *AAPG Bulletin*, 81(6), 1023-1041.
- Ostrovsky, A. (1989). On the nature of microshocks recorded by ocean bottom seismographs. *Marine Geophysical Researches*, 11(2), 113-118.
- Panieri, G., Bunz, S., Fornari, D. J., Escartin, J., Serov, P., Jansson, P., et al. (2017). An integrated view of the methane system in the pockmarks at Vestnesa Ridge, 79 degrees N. *Marine Geology*, 390, 282-300.
- Pape, T., Bünz, S., Hong, W. L., Torres, M. E., Riedel, M., Panieri, G., et al. (2020). Origin and Transformation of Light Hydrocarbons Ascending at an Active Pockmark on Vestnesa Ridge, Arctic Ocean. *Journal of Geophysical Research: Solid Earth*, 125(1).
- Peng, Z., & Gombert, J. (2010). An integrated perspective of the continuum between earthquakes and slow-slip phenomena. *Nature Geoscience*, 3(9), 599-607.
- Petersen, C. J., Bünz, S., Hustoft, S., Mienert, J., & Klaeschen, D. (2010). High-resolution P-Cable 3D seismic imaging of gas chimney structures in gas hydrated sediments of an Arctic sediment drift. *Marine and Petroleum Geology*, 27(9), 1981-1994.
- Plaza-Faverola, A., Pecher, I., Crutchley, G., Barnes, P. M., Bünz, S., Golding, T., et al. (2014). Submarine gas seepage in a mixed contractional and shear deformation regime: Cases from the Hikurangi oblique-subduction margin. *Geochemistry, Geophysics, Geosystems*, 15(2), 416-433.
- Plaza-Faverola, A., Bünz, S., Johnson, J. E., Chand, S., Knies, J., Mienert, J., & Franek, P. (2015). Role of tectonic stress in seepage evolution along the gas hydrate-charged Vestnesa Ridge, Fram Strait. *Geophysical Research Letters*, 42(3), 733-742.
- Plaza-Faverola, A., Vadakkepuliambatta, S., Hong, W. L., Mienert, J., Bunz, S., Chand, S., & Greinert, J. (2017). Bottom-simulating reflector dynamics at Arctic thermogenic gas provinces: An example from Vestnesa Ridge, offshore west Svalbard. *Journal of Geophysical Research-Solid Earth*, 122(6), 4089-4105.
- Plaza-Faverola, A., & Keiding, M. (2019). Correlation between tectonic stress regimes and methane seepage on the western Svalbard margin. *Solid Earth*, 10(1), 79-94.
- Plaza-Faverola, A. (2022). CAGE21-5 Cruise Report: Test of offshore instrumentation for in-situ sediment pressure measurements, west-Svalbard continental margin. *CAGE – Centre for Arctic Gas Hydrate, Environment and Climate Report Series*, 9.
- Plaza-Faverola, A., Schlindwein, V., Domel, P., Schmidt-Aursch, M., Cooke, F. A., Holm, T., & Jensen, S. A. (2022a). CAGE21-3 Cruise Report: Ocean bottom seismics and acoustic surveys on the West-Svalbard margin – a study of local seismicity and its effect on methane seepage. *CAGE – Centre for Arctic Gas Hydrate, Environment and Climate Report Series*, 9.
- Plaza-Faverola, A., Domel, P., Bünz, S., Schmidt-Aursch, M., Schlindwein, V. (2022b): Project SEAMSTRESS: DEPAS ocean-bottom seismometer operations on Vestnesa Ridge in 2020-2021. *PANGAEA*.

- Plaza-Faverola, A., Sultan, N., Lucchi, R. G., El bani Altuna, N., Ramachandran, H., Singhroha, S., et al. (2023). Spatial Changes in Gas Transport and Sediment Stiffness Influenced by Regional Stress: Observations from Piezometer Data Along Vestnesa Ridge, Eastern Fram Strait. *Journal of Geophysical Research: Solid Earth*, 128(5).
- Provost, F., Hibert, C., & Malet, J. P. (2017). Automatic classification of endogenous landslide seismicity using the Random Forest supervised classifier. *Geophysical Research Letters*, 44(1), 113-120.
- Ramakrushana Reddy, T., Dewangan, P., Arya, L., Singha, P., & Kamesh Raju, K. A. (2020). Tidal Triggering of the Harmonic Noise in Ocean-Bottom Seismometers. *Seismological Research Letters*, 91(2A), 803-813.
- Reeburgh, W. S. (2007). Oceanic Methane Biogeochemistry. *Chemical Reviews*, 107(2), 486-513.
- Riedel, M., Scherwath, M., Romer, M., Veloso, M., Heesemann, M., & Spence, G. D. (2018). Distributed natural gas venting offshore along the Cascadia margin. *Nat Commun*, 9(1), 3264.
- Ritzmann, O., Jokat, W., Czuba, W., Guterch, A., Mjelde, R., & Nishimura, Y. (2004). A deep seismic transect from Hovgård Ridge to northwestern Svalbard across the continental-ocean transition: A sheared margin study. *Geophysical Journal International*, 157(2), 683-702.
- Romeyn, R., Hanssen, A., Ruud, B. O., Stemland, H. M., & Johansen, T. A. (2021). Passive seismic recording of cryoseisms in Adventdalen, Svalbard. *The Cryosphere*, 15(1), 283-302.
- Romeyn, R., Hanssen, A., & Köhler, A. (2022). Long-term analysis of cryoseismic events and associated ground thermal stress in Adventdalen, Svalbard. *The Cryosphere*, 16(5), 2025-2050.
- Rubinstein, J. L., Vidale, J. E., Gomberg, J., Bodin, P., Creager, K. C., & Malone, S. D. (2007). Non-volcanic tremor driven by large transient shear stresses. *Nature*, 448(7153), 579-582.
- Rubinstein, J. L., La Rocca, M., Vidale, J. E., Creager, K. C., & Wech, A. G. (2008). Tidal Modulation of Nonvolcanic Tremor. *Science*, 319(5860), 186-189.
- Rubinstein, J. L., & Mahani, A. B. (2015). Myths and Facts on Wastewater Injection, Hydraulic Fracturing, Enhanced Oil Recovery, and Induced Seismicity. *Seismological Research Letters*, 86(4), 1060-1067.
- Rust, A. C., Balmforth, N. J., Mandre, S., Lane, S. J., & Gilbert, J. S. (2008). The feasibility of generating low-frequency volcano seismicity by flow through a deformable channel. In *Fluid Motions in Volcanic Conduits: A Source of Seismic and Acoustic Signals* (Vol. 307, pp. 0): Geological Society of London.
- Sato, T., Sakai, R., Furuya, K., & Kodama, T. (2000). Coseismic spring flow changes associated with the 1995 Kobe Earthquake. *Geophysical Research Letters*, 27(8), 1219-1222.
- Schneider, A., Panieri, G., Lepland, A., Consolaro, C., Crémière, A., Forwick, M., et al. (2018). Methane seepage at Vestnesa Ridge (NW Svalbard) since the Last Glacial Maximum. *Quaternary Science Reviews*, 193, 98-117.
- Scholz, C. H. (2019). *The Mechanics of Earthquakes and Faulting* (3 ed.). Cambridge: Cambridge University Press.
- Schroot, B. M., Klaver, G. T., & Schüttenhelm, R. T. E. (2005). Surface and subsurface expressions of gas seepage to the seabed—examples from the Southern North Sea. *Marine and Petroleum Geology*, 22(4), 499-515.
- Schultz, R., Skoumal, R. J., Brudzinski, M. R., Eaton, D., Baptie, B., & Ellsworth, W. (2020). Hydraulic Fracturing-Induced Seismicity. *Reviews of Geophysics*, 58(3), e2019RG000695.
- Scuderi, M. M., & Collettini, C. (2016). The role of fluid pressure in induced vs. triggered seismicity: insights from rock deformation experiments on carbonates. *Scientific Reports*, 6(1), 24852.

- Sgroi, T., Montuori, C., Agrusta, R., & Favali, P. (2009). Low-frequency seismic signals recorded by OBS at Stromboli volcano (Southern Tyrrhenian Sea). *Geophysical Research Letters*, *36*(4).
- Sgroi, T., Monna, S., Embriaco, D., Giovanetti, G., Marinaro, G., & Favali, P. (2014). Geohazards in the Western Ionian Sea: Insights from Non-Earthquake Signals Recorded by the NEMO-SN1 Seafloor Observatory. *Oceanography*, *27*(2), 154-166.
- Skelton, A., Andrén, M., Kristmannsdóttir, H., Stockmann, G., Mörth, C.-M., Sveinbjörnsdóttir, Á., et al. (2014). Changes in groundwater chemistry before two consecutive earthquakes in Iceland. *Nature Geoscience*, *7*(10), 752-756.
- Sloan, E. D. (1998). Gas Hydrates: Review of Physical/Chemical Properties. *Energy & Fuels*, *12*(2), 191-196.
- Smith, A. J., Mienert, J., Bünz, S., & Greinert, J. (2014). Thermogenic methane injection via bubble transport into the upper Arctic Ocean from the hydrate-charged Vestnesa Ridge, Svalbard. *Geochemistry, Geophysics, Geosystems*, *15*(5), 1945-1959.
- Smith, D. E., Harrison, S., & Jordan, J. T. (2013). Sea level rise and submarine mass failures on open continental margins. *Quaternary Science Reviews*, *82*, 93-103.
- Sohn, R. A., Hildebrand, J. A., Webb, S. C., & Fox, C. G. (1995). Hydrothermal microseismicity at the megaplume site on the southern Juan de Fuca Ridge. *Bulletin of the Seismological Society of America*, *85*(3), 775-786.
- Sohn, R. A., Fornari, D. J., Von Damm, K. L., Hildebrand, J. A., & Webb, S. C. (1998). Seismic and hydrothermal evidence for a cracking event on the East Pacific Rise crest at 9° 50' N. *Nature*, *396*(6707), 159-161.
- Soule, D. C., & Wilcock, W. S. (2013). Fin whale tracks recorded by a seismic network on the Juan de Fuca Ridge, Northeast Pacific Ocean. *J Acoust Soc Am*, *133*(3), 1751-1761.
- Stanchits, S., Mayr, S., Shapiro, S., & Dresen, G. (2011). Fracturing of porous rock induced by fluid injection. *Tectonophysics*, *503*(1), 129-145.
- Steel, R., Gjelberg, J., Helland-Hansen, W., Kleinspehn, K., Nøttvedt, A., & Rye-Larsen, M. (1985). The Tertiary strike-slip basins and orogenic belt of Spitsbergen.
- Stoekert, F., Molenda, M., Brenne, S., & Alber, M. (2015). Fracture propagation in sandstone and slate – Laboratory experiments, acoustic emissions and fracture mechanics. *Journal of Rock Mechanics and Geotechnical Engineering*, *7*(3), 237-249.
- Stroup, D. F., Bohnenstiehl, D. R., Tolstoy, M., Waldhauser, F., & Weekly, R. T. (2007). Pulse of the seafloor: Tidal triggering of microearthquakes at 9°50'N East Pacific Rise. *Geophysical Research Letters*, *34*(15).
- Sultan, N., Plaza-Faverola, A., Vadakkepuliambatta, S., Buenz, S., & Knies, J. (2020). Impact of tides and sea-level on deep-sea Arctic methane emissions. *Nat Commun*, *11*(1), 5087.
- Sztybor, K., & Rasmussen, T. L. (2017). Diagenetic disturbances of marine sedimentary records from methane-influenced environments in the Fram Strait as indications of variation in seep intensity during the last 35 000 years. *Boreas*, *46*(2), 212-228.
- Talukder, A. R. (2012). Review of submarine cold seep plumbing systems: leakage to seepage and venting. *Terra Nova*, *24*(4), 255-272.
- Talwani, M., & Eldholm, O. (1977). Evolution of the Norwegian-Greenland Sea. *GSA Bulletin*, *88*(7), 969-999.

- Tary, J. B., Géli, L., Guennou, C., Henry, P., Sultan, N., Çağatay, N., & Vidal, V. (2012). Microevents produced by gas migration and expulsion at the seabed: a study based on sea bottom recordings from the Sea of Marmara. *Geophysical Journal International*, 190(2), 993-1007.
- Tary, J. B., van der Baan, M., & Eaton, D. W. (2014a). Interpretation of resonance frequencies recorded during hydraulic fracturing treatments. *Journal of Geophysical Research: Solid Earth*, 119(2), 1295-1315.
- Tary, J. B., van der Baan, M., Sutherland, B., & Eaton, D. W. (2014b). Characteristics of fluid-induced resonances observed during microseismic monitoring. *Journal of Geophysical Research: Solid Earth*, 119(11), 8207-8222.
- Thorson, R. M. (2000). Glacial tectonics: a deeper perspective. *Quaternary Science Reviews*, 19(14), 1391-1398.
- Tissot, B. P., & Welte, D. H. (1984). *Petroleum Formation and Occurrence A New Approach to Oil and Gas Exploration*: Springer.
- Tivey, M. K., Bradley, A. M., Joyce, T. M., & Kadko, D. (2002). Insights into tide-related variability at seafloor hydrothermal vents from time-series temperature measurements. *Earth and Planetary Science Letters*, 202(3), 693-707.
- Tolstoy, M., Vernon, F. L., Orcutt, J. A., & Wyatt, F. K. (2002). Breathing of the seafloor: Tidal correlations of seismicity at Axial volcano. *Geology*, 30(6), 503-506.
- Tsai, V. C. (2011). A model for seasonal changes in GPS positions and seismic wave speeds due to thermoelastic and hydrologic variations. *Journal of Geophysical Research: Solid Earth*, 116(B4).
- Tsunogai, U., Maegawa, K., Sato, S., Komatsu, D. D., Nakagawa, F., Toki, T., & Ashi, J. (2012). Coseismic massive methane release from a submarine mud volcano. *Earth and Planetary Science Letters*, 341-344, 79-85.
- Ugalde, A., Gaite, B., Ruiz, M., Villaseñor, A., & Ranero, C. R. (2019). Seismicity and Noise Recorded by Passive Seismic Monitoring of Drilling Operations Offshore the Eastern Canary Islands. *Seismological Research Letters*.
- Urbancic, T., & Maxwell, S. (2002). *Source parameters of hydraulic fracture induced microseismicity*. Paper presented at the SPE Annual Technical Conference and Exhibition.
- Vachon, R., Schmidt, P., Lund, B., Plaza-Faverola, A., Patton, H., & Hubbard, A. (2022). Glacially Induced Stress Across the Arctic From the Eemian Interglacial to the Present—Implications for Faulting and Methane Seepage. *Journal of Geophysical Research: Solid Earth*, 127(7).
- Valentine, D. L. (2010). Emerging Topics in Marine Methane Biogeochemistry. *Annual Review of Marine Science*, 3(1), 147-171.
- Vanneste, M., Guidard, S., & Mienert, J. (2005). Bottom-simulating reflections and geothermal gradients across the western Svalbard margin. *Terra Nova*, 17(6), 510-516.
- Vidale, J. E. (1986). Complex polarization analysis of particle motion. *Bulletin of the Seismological society of America*, 76(5), 1393-1405.
- Vogt, P. R., & Crane, K. (1994). Methane-generated () pockmarks on young, thickly sedimented oceanic crust in the Arctic. Vestnesa ridge, Fram strait. *Geology*, 22(3).
- Waghorn, K. A., Vadakkepuliymbatta, S., Plaza-Faverola, A., Johnson, J. E., Bunz, S., & Waage, M. (2020). Crustal processes sustain Arctic abiogenic gas hydrate and fluid flow systems. *Sci Rep*, 10(1), 10679.

- Wang, W., Shearer, P. M., Vidale, J. E., Xu, X., Trugman, D. T., & Fialko, Y. (2022). Tidal modulation of seismicity at the Coso geothermal field. *Earth and Planetary Science Letters*, 579, 117335.
- Wenzel, H. G. (2005). Tide-generating potential for the Earth. *Tidal phenomena*, 9-26.
- Yan, R., Woith, H., & Wang, R. (2014). Groundwater level changes induced by the 2011 Tohoku earthquake in China mainland. *Geophysical Journal International*, 199(1), 533-548.
- Yan, X., Shi, Z., Zhou, P., Zhang, H., & Wang, G. (2020). Modeling Earthquake-Induced Spring Discharge and Temperature Changes in a Fault Zone Hydrothermal System. *Journal of Geophysical Research: Solid Earth*, 125(7), e2020JB019344.
- Yao, H., Hong, W. L., Panieri, G., Sauer, S., Torres, M. E., Lehmann, M. F., et al. (2019). Fracture-controlled fluid transport supports microbial methane-oxidizing communities at Vestnesa Ridge. *Biogeosciences*, 16(10), 2221-2232.
- Zali, Z., Rein, T., Krüger, F., Ohrnberger, M., & Scherbaum, F. (2023). Ocean bottom seismometer (OBS) noise reduction from horizontal and vertical components using harmonic–percussive separation algorithms. *Solid Earth*, 14(2), 181-195.
- Zhu, W., & Beroza, G. C. (2018). PhaseNet: A Deep-Neural-Network-Based Seismic Arrival Time Picking Method. *Geophysical Journal International*.
- Zoback, M. D., & Zoback, M. L. (2002). Stress in the Earth's lithosphere. *Encyclopedia of physical science and technology*, 16, 143-154.
- Zoback, M. D. (2010). *Reservoir geomechanics*: Cambridge University Press.

SECTION II Research papers

Article 1



Origin and Periodic Behavior of Short Duration Signals Recorded by Seismometers at Vestnesa Ridge, an Active Seepage Site on the West-Svalbard Continental Margin

P. Domel^{1*}, S. Singhroha¹, A. Plaza-Faverola¹, V. Schlindwein^{2,3}, H. Ramachandran¹ and S. Bünz¹

OPEN ACCESS

Edited by:

Mourad Bezzeghoud,
Universidade de Évora, Portugal

Reviewed by:

Kimihiro Mochizuki,
The University of Tokyo, Japan
Christopher Schmidt,
Helmholtz Association of German
Research Centres (HZ), Germany

*Correspondence:

P. Domel
przemyslaw.domel@uit.no

Specialty section:

This article was submitted to
Solid Earth Geophysics,
a section of the journal
Frontiers in Earth Science

Received: 08 December 2021

Accepted: 02 February 2022

Published: 02 March 2022

Citation:

Domel P, Singhroha S,
Plaza-Faverola A, Schlindwein V,
Ramachandran H and Bünz S (2022)
Origin and Periodic Behavior of Short
Duration Signals Recorded by
Seismometers at Vestnesa Ridge, an
Active Seepage Site on the West-
Svalbard Continental Margin.
Front. Earth Sci. 10:831526.
doi: 10.3389/feart.2022.831526

¹CAGE—Centre for Arctic Gas Hydrate, Environment and Climate, Department of Geosciences, UiT The Arctic University of Norway, Tromsø, Norway, ²Alfred Wegener Institute, Helmholtz Centre for Polar and Marine Research, Bremerhaven, Germany, ³University of Bremen, Faculty of Geosciences, Bremen, Germany

Short duration events (SDEs) are reported worldwide from ocean-bottom seismometers (OBSs). Due to their high frequency (4–30 Hz) and short duration, they are commonly attributed to aseismic sources, such as fluid migration related processes from cold seeps, biological signals, or noise. We present the results of a passive seismic experiment that deployed an OBS network for 10-month (October 2015–July 2016) at an active seepage site on Vestnesa Ridge, West Svalbard continental margin. We characterize SDEs and their temporal occurrence using the conventional short-time-average over long-time-average approach. Signal periodograms show that SDEs have periodic patterns related to solar and lunar cycles. A monthly correlation between SDE occurrences and modelled tides for the area indicates that tides have a partial control on SDEs recorded over 10 months. The numbers of SDEs increase close to the tidal minima and maxima, although a correlation with tidal highs appears more robust. Large bursts of SDEs are separated by interim quiet cycles. In contrast, the periodicity analysis of tremors shows a different pattern, likely caused by the effect of tidally controlled underwater currents on the instrumentation. We suggest that SDEs at Vestnesa Ridge may be related to the dynamics of the methane seepage system which is characterized by a complex interaction between migration of deep sourced fluids, gas hydrate formation and seafloor gas advection through cracks. Our observation from this investigated area offshore west-Svalbard, is in line with the documentation of SDEs from other continental margins, where micro-seismicity and gas release into the water column are seemingly connected.

Keywords: ocean-bottom seismometer, micro-seismicity, short duration events, methane seepage, gas hydrates, tidal cycle

1 INTRODUCTION

Ocean-bottom seismometers (OBSs) are usually deployed in marine settings to investigate local seismicity of an area by monitoring earthquakes (e.g., Grevemeyer et al., 2015; Meier et al., 2021) or long-duration tremors (e.g., Monigle et al., 2009; Hsu et al., 2013; Franek et al., 2014).

In addition to earthquakes and tremors, OBSs often record signals commonly referred to as short duration events (SDEs) (e.g., Díaz et al., 2007; Tary et al., 2012; Franek et al., 2017). SDEs are characterized by a single pulse of a short (usually <1 s) duration with no discernible P and S phases, a relatively high (at least 4–30 Hz) frequency content, and a strong signal/noise ratio (Batsi et al., 2019). Although the general frequency range lies between 4–30 Hz, higher upper limits (reaching Nyquist frequency of the specific record—50 Hz), has been reported (Sgroi et al., 2014). Recorded SDEs also have variations in their signal characteristics, duration, periodicity and directionality, but similar types of signals have been recorded in different geological settings (Tary et al., 2012). The underlying mechanisms for variations in SDEs are not yet completely understood (e.g., Ugalde et al., 2019).

Recent experiments show the potential of using OBS recordings as a tool to study the long-term variability of the gas seepage and fluid movements through the analysis of SDEs (e.g., Franek et al., 2017; Batsi et al., 2019; Tsang-Hin-Sun et al., 2019). It is believed that there is a strong link between SDEs and fracture-controlled fluid migration. Laboratory experiments (Batsi et al., 2019), as well as several field studies (Sultan et al., 2011; Tary et al., 2012; Hsu et al., 2013; Embriaco et al., 2014; Franek et al., 2014; Liu et al., 2018; Ugalde et al., 2019), link SDEs in recorded signals to fluid movements in the subsurface.

Other existing and proposed origins of SDEs in marine environments include hydraulic fracturing and pressure transients in hydrothermal systems (Sohn et al., 1995; Bowman and Wilcock, 2013), pressure fluctuations in fluid pathways (Díaz et al., 2007), underwater currents (Chang et al., 2016; Ugalde et al., 2019), and fracture opening due to strong local earthquakes (Tsang-Hin-Sun et al., 2019). Some studies also hypothesize about biological sources of SDEs (e.g., fish and marine mammals) (Buskirk et al., 1981; Bowman and Wilcock, 2013; Batsi et al., 2019). In few cases, when SDE occurrences coincide with the initial stage of long-term experiments, mechanical coupling of the OBS at the sea bottom has been proposed as the source of SDEs (Ostrovsky, 1989).

The natural release of hydrocarbon gases from the seafloor at continental margins is widespread (e.g., Judd and Hovland, 2007; Römer et al., 2014; Mau et al., 2017). Factors such as changes in ice sheet thickness (Cremiere et al., 2016; Wallmann et al., 2018; Himmler et al., 2019), geological processes in the subsurface and local tectonic activity (Himmler et al., 2019; Plaza-Faverola and Keiding, 2019; Ciotoli et al., 2020), variations in the gas hydrate stability zone (Taylor et al., 2000; Crutchley et al., 2014; Mishra et al., 2020), changes in sea water temperature over geological times (Thomsen et al., 2012; Berndt et al., 2014; Cremiere et al., 2016) and sedimentation (Horozal et al., 2017; Karstens et al., 2018) create changes in seepage intensity and distribution over geological timescales (Etiope, 2015). Some studies attribute fluctuations in the seepage intensity to seasonal changes in the

seawater temperature (Berndt et al., 2014; Embriaco et al., 2014; Ferré et al., 2020). Other studies link small diurnal-scale variations in gas seepage to tides (Boles et al., 2001; Hsu et al., 2013; Römer et al., 2016; Riedel et al., 2018; Sultan et al., 2020).

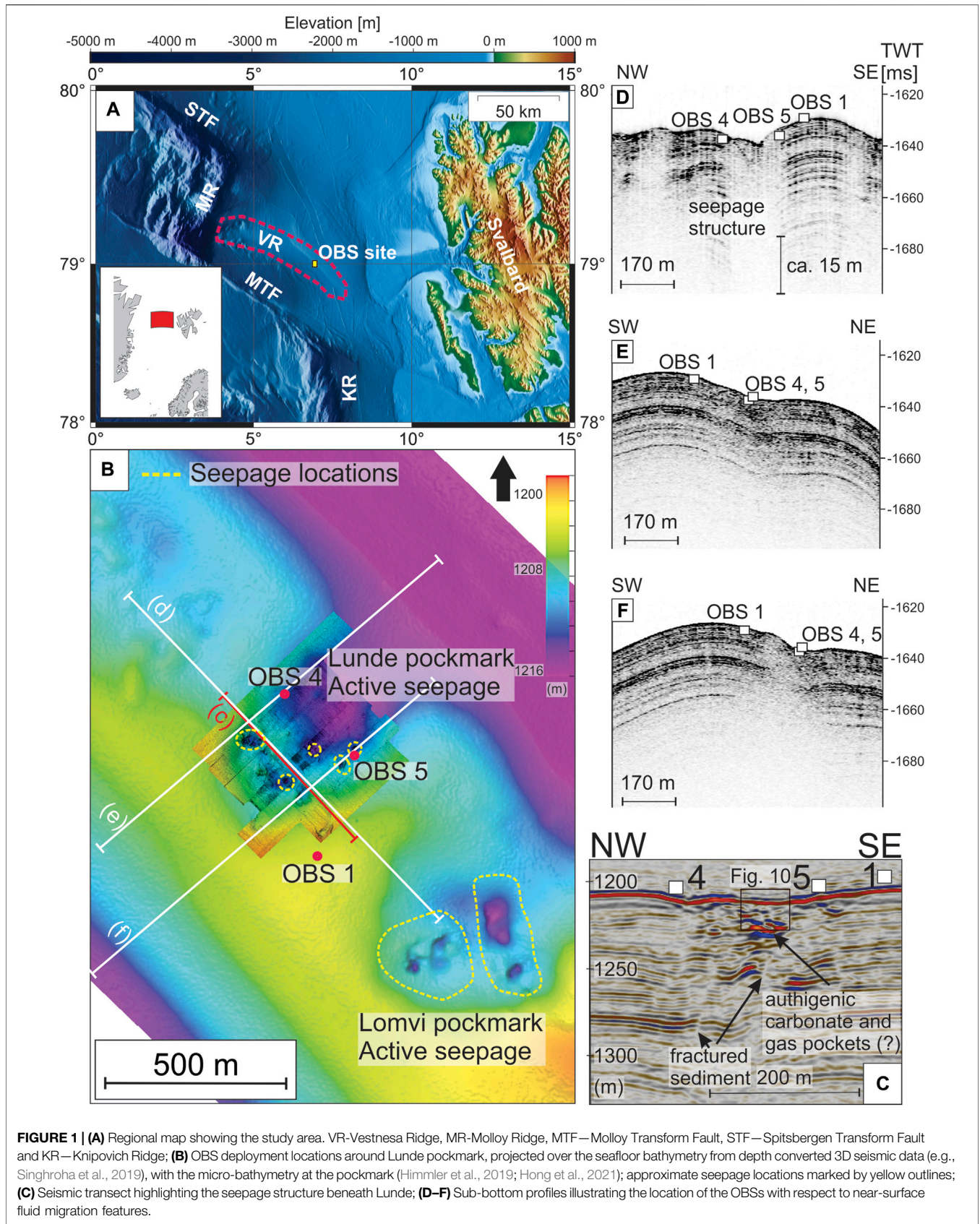
Seasonal and diurnal variations in the seepage activity have been primarily studied using backscattering from gas bubbles observed in sonar data (e.g., Veloso et al., 2015), direct *in-situ* observations using underwater cameras (e.g., Beccari et al., 2020; Di et al., 2020), and with sensors mounted at ocean-bottom observatories (e.g., Boles et al., 2001; Kvenvolden et al., 2001). Observations of the seepage periodicity using ship-mounted sonar data are dependent on the cruise time availability and therefore short-term and infrequent. Remotely operated vehicles (ROVs) for direct imaging are costly and not suitable for monitoring seepage activity for several hours. In contrast, long term OBS experiments can last more than a year and provide a continuous record of seismicity, allowing the investigation of the periodicity of SDE occurrences and their potential correlation to seepage activity.

In this study, we report on SDE occurrences in 10-month-long OBS recordings from an actively seeping pockmark on Vestnesa Ridge, a sedimentary ridge located offshore west-Svalbard. We study patterns of occurrence and intensity of SDEs in a deep marine Arctic geological setting and discuss their potential link with gas seepage dynamics.

1.1 Geological Setting

Vestnesa Ridge is a ca. 60 km long contourite drift located on west-Svalbard continental margin between North Atlantic mid-ocean ridge and Svalbard Archipelago (Eiken and Hinz, 1993; Howe et al., 2007; Hustoft et al., 2009) (**Figure 1A**). Molloy and Spitsbergen transform faults bound the ridge to the south and the north, respectively. The ridge consists of turbidites, hemipelagic and glaciomarine sediments (Eiken and Hinz, 1993; Ottesen et al., 2005) distributed along a northwest-southeast orientated eastern segment and an east-west orientated western segment (Vogt and Crane, 1994; Ritzmann et al., 2004; Plaza-Faverola et al., 2014).

Vestnesa Ridge hosts a broadly investigated gas hydrate system (Hustoft et al., 2009; Panieri et al., 2017; Pape et al., 2020; Plaza-Faverola et al., 2017). The presence of a bottom simulating reflection, a seismic boundary created by acoustic impedance contrast at the base of the gas hydrate stability zone (Shipley et al., 1979), establishes and constrains the gas hydrate system along the entire ridge (Bünz et al., 2012; Plaza-Faverola et al., 2017). Hydrocarbon gases seep through selected pockmarks in the eastern segment of the ridge (Bünz et al., 2012; Plaza-Faverola et al., 2015; Singhroha et al., 2019; Smith et al., 2014). Gas hydrate is not the main controller of the seepage at the site, however. Systems of faults and fractures control the underlying fluid migration pathways and chimneys, and thus, the distribution of pockmarks (**Figure 1C**) (Plaza-Faverola et al., 2015; Singhroha et al., 2019, 2020). The spatial and temporal distribution of seepage features along the sedimentary ridge has been linked to dynamic forcing from mid-ocean ridge spreading and from glacial isostatic rebound (Schneider et al., 2018; Himmler et al., 2019; Plaza-Faverola and Keiding, 2019). Studies based on sediment proxies suggest that there is a link



between seepage episodes and glacial cycles during the latest glaciations (Schneider et al., 2018; Himmler et al., 2019).

Annual multi-beam and single-beam sonar surveys show that acoustic flares in the water column (i.e., reaching heights of up to ~800 m) are restricted to the eastern Vestnesa Ridge segment (Bünz et al., 2012; Smith et al., 2014). The presence of seemingly dormant pockmarks on the ridge crest, especially towards the western segment, where there is no evidence of present-day advective seepage, suggests paleo-seepage at many locations along the ridge (Vogt and Crane, 1994; Petersen et al., 2010; Consolaro et al., 2015). Radio isotopic dating of authigenic carbonates extracted from shallow sediments shows three methane seepage episodes around ~160 to 133 ka, ~50 to 40 ka, and ~20 to 5 ka, that directly correspond to the episodes of glaciation and de-glaciation in the area (Himmler et al., 2019). Based on this information, it is suggested that glacial tectonics is one of the dominant forces driving the seepage on geological time scales.

Sonar data collected during numerous expeditions to the area show the presence of gas flares only from six pockmarks on the eastern side of the ridge (Smith et al., 2014). Pockmark Lunde is the one with the largest acoustic flare observed and it is in the near vicinity (<1 km) of another active pockmark (i.e., Lomvi (Panieri et al., 2017)). These pockmarks are ~300–400 m wide complex structures, containing both small-scale (<1 m) features and depressions up to 50 m in diameter (**Figure 1B**) that focus most of the seepage (Panieri et al., 2017). Diffusive gas release is likely to take place as well within the pockmarks, outside the pits. The presence of acoustic flares in the water column has been documented from three such pits at each pockmark (Panieri et al., 2017). Biological markers obtained from gravity cores indicate periodic variations in seepage on a scale of 1 ka years, possibly due to fault reactivation (Ambrose et al., 2015). Sampling of authigenic carbonate (Himmler et al., 2019) inside Lunde provided ground truth data for the widespread inference of past methane seepage events based on high resolution 3D seismic data (Plaza-Faverola et al., 2015).

2 DATA AND METHODS

2.1 Data

We deployed five LOBSTER type OBSs (Stähler et al., 2018) around the Lunde pockmark (**Figure 1**) to study the potential link between seismicity and seepage. Upon recovery of the OBSs we have lost one data unit to the sea and discovered that another unit has not recorded any data, leaving only 3 instruments for further study (OBSs 1, 4 and 5; **Figure 1**). The entire experiment lasted from October 2015 to July 2016. All OBSs were equipped with a three-component short-period seismometer (with 4.5 Hz corner frequency), and a hydrophone attached to the OBS frame at a ~0.5-m height from the sea bottom. Each seismometer was attached to a metal rod extending from the OBS frame, mechanically uncoupled and dropped directly onto the seafloor after approximately 1 h. By using this approach, we achieved direct contact with sediments and improved coupling of the seismometers.

The OBSs were deployed in with the free-fall approach at a water depth of ca. 1,200 m. Seismic lines were shot over the OBSs with the intention to precisely relocate the OBSs at the seafloor using times of direct wave arrivals (e.g., Plaza-Faverola et al., 2010). However, problems with the time records for the shots hampered improved relocation efforts. Thus, in this study, we used OBS positions registered during deployment. Since we did not attempt event location, the OBS position accuracy was not critical.

The instruments recorded with 20 ms (OBS-1) and 5 ms (OBS-4 and OBS-5) sampling intervals. This corresponds to the Nyquist frequency of 25 Hz for OBS-1 and 100 Hz for OBS-4 and OBS-5. All these data cover roughly the duration of the deployment (10.2015–07.2016), excluding the first two weeks of October 2015, when OBSs were settling on the sediment. Data quality of OBS-1 and OBS-4 is better than OBS-5. OBS-1 shows a consistent recorded signal throughout the entire deployment period. OBS-4 and OBS-5 have some periods (~up to week-long at times), where the recorded signal quality is unsatisfactory for analysis. During the first month of operation, OBS-5 recorded almost no signals of any kind, possibly due to poor coupling between the seismometer and the seafloor.

2.2 Preprocessing

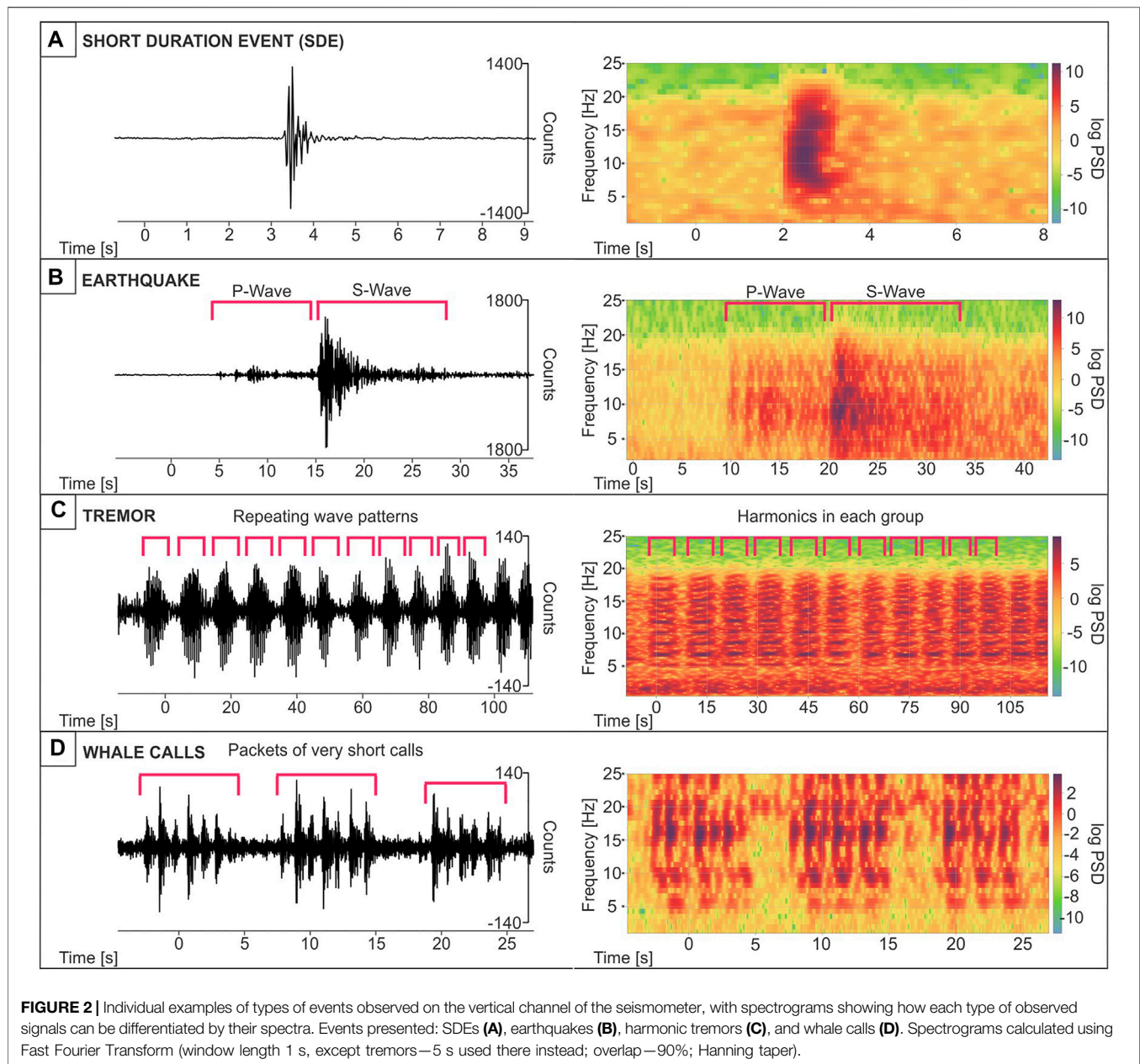
We converted the whole dataset into day-long mseed-format files and visually inspected the overall quality of the data. Subsequently we verified that known earthquakes (i.e., recorded by the nearby land stations at Svalbard) are present in the recording, that the signal quality is satisfactory and that most of the strong earthquakes have been recorded on all three stations.

2.3 Visual Recognition of Recorded Signals

By manual inspection of the datasets, we identify four dominant types of signals: SDEs, earthquakes, harmonic tremors and whale calls.

2.3.1 SDEs

From visual inspection of the data set, we noticed prominent signals (**Figure 2A**) that usually have amplitudes similar, if not stronger, than local earthquakes (**Figure 2B**). Their spectra cover almost the entire frequency range (up to 20 Hz in OBS-1 and 60–80 Hz in OBS-4 and OBS-5). Whereas the amplitude of these signals is highly variable, the frequency content between events remains more stable. Their average duration is between 1–2 s. On corresponding spectrograms, these signals appear as narrow “stripes” covering a large frequency band from 3–4 Hz to 20–25 Hz (OBS-1) or 60–65 Hz (OBS-4 and OBS-5), with similar energy levels for all frequencies they contain. We classify these signals as SDEs (**Figure 2A**). SDEs are usually observed on all channels of a seismometer, and sporadically, on a hydrophone record. One common characteristic they share is a lack of separate P and S wave arrivals, which clearly distinguishes them from local earthquakes (**Figures 2A,B**). The SDEs we document here follow the characteristics of SDEs described at Western Svalbard Shelf by Franek et al. (2017), and Sea of Marmara by Batsi et al. (2019).



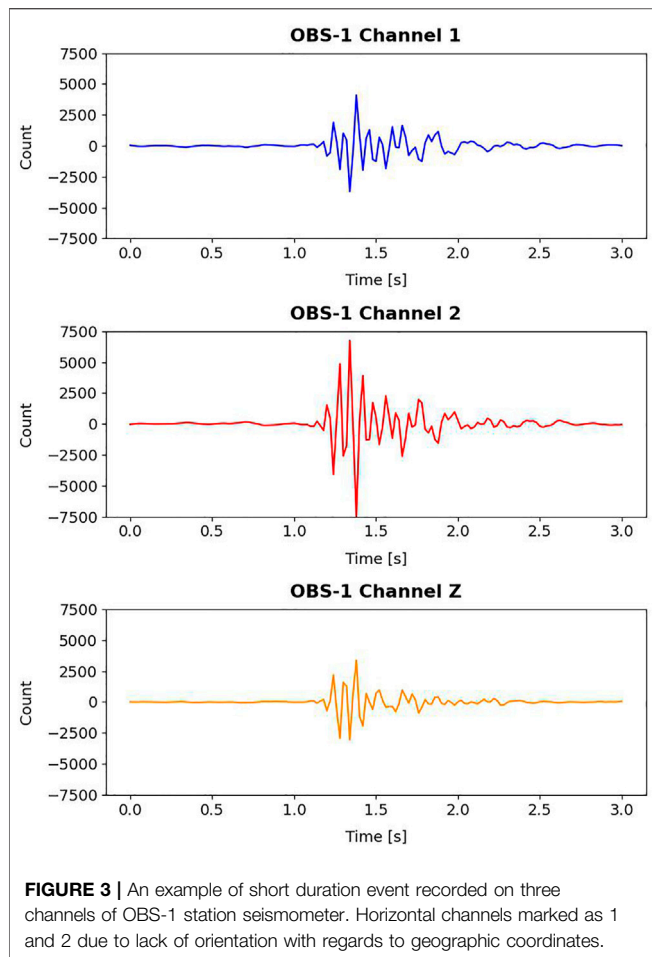
2.3.2 Earthquakes

The dominant sources of earthquakes in this dataset are ultra-slow spreading oceanic ridges (e.g., Molloy Ridge and Knipovich Ridge), that have been successfully studied by OBS deployments (e.g., Meier et al., 2021; Schlindwein et al., 2013). Earthquakes can be clearly distinguished from other signals by independent P and S waves arrivals and their overall length (**Figure 2B**). Usually, an individual earthquake is recorded on all three OBSs and on all channels of the seismometer. After an earthquake, a seismic wavefield propagating from the hypocenter reaches the seafloor and undergoes conversion at the water-sediment boundary. This process leads to the generation of acoustic waves in the water column that we have observed in our

hydrophone data, for particularly large earthquakes in the region with known, independently determined magnitudes. In this study, we observe events with the total duration of 8–10 s or more, for the most part, since our short-period seismometers (with a useful frequency range of 1 Hz upwards) are mainly suitable for studies of local and regional seismicity (Sutton et al., 1965; Webb, 1998).

2.3.3 Harmonic Tremors

A tremor is defined as a continuous signal of sustained amplitude recorded at frequencies within limited bandwidth (Chouet, 1992). By harmonic tremor, we refer to signals which beside the fundamental frequency contain one or more harmonics of this



frequency, as defined e.g., in Essing et al. (2021). This can be clearly seen on their spectra, with an energy pick for the fundamental frequency and subsequent energy levels for integer multiples of this frequency. We observe tremor on all seismometer channels, but not on the hydrophones. Tremors have ~1–5 Hz dominant frequency with at least one or more harmonics present (Figure 2C), and harmonic frequencies going up to 15–20 Hz in the case of strong tremors. Tremor events usually start with only the dominant frequency and one, sometimes two harmonics visible, but they increase in intensity quickly and the number of harmonics visible becomes larger. The opposite process is occurring towards the end of the tremor “window,” with number of harmonics decreasing, until only energy of the dominant frequency can be visible before tremor disappears completely. The usual duration of continuous presence of a tremor is counted in hours, but throughout these longer intervals, shorter (from few minutes upwards), “patchy” breaks can be randomly seen during the tremor events. They are observed on nearby instrumentation simultaneously, but there are small time differences between the start and the disappearance of tremor bursts between OBSs, with the variation between the onset and the disappearance time.

Approximately half of the dataset from each OBS is contaminated with the tremor noise of uniform characteristics

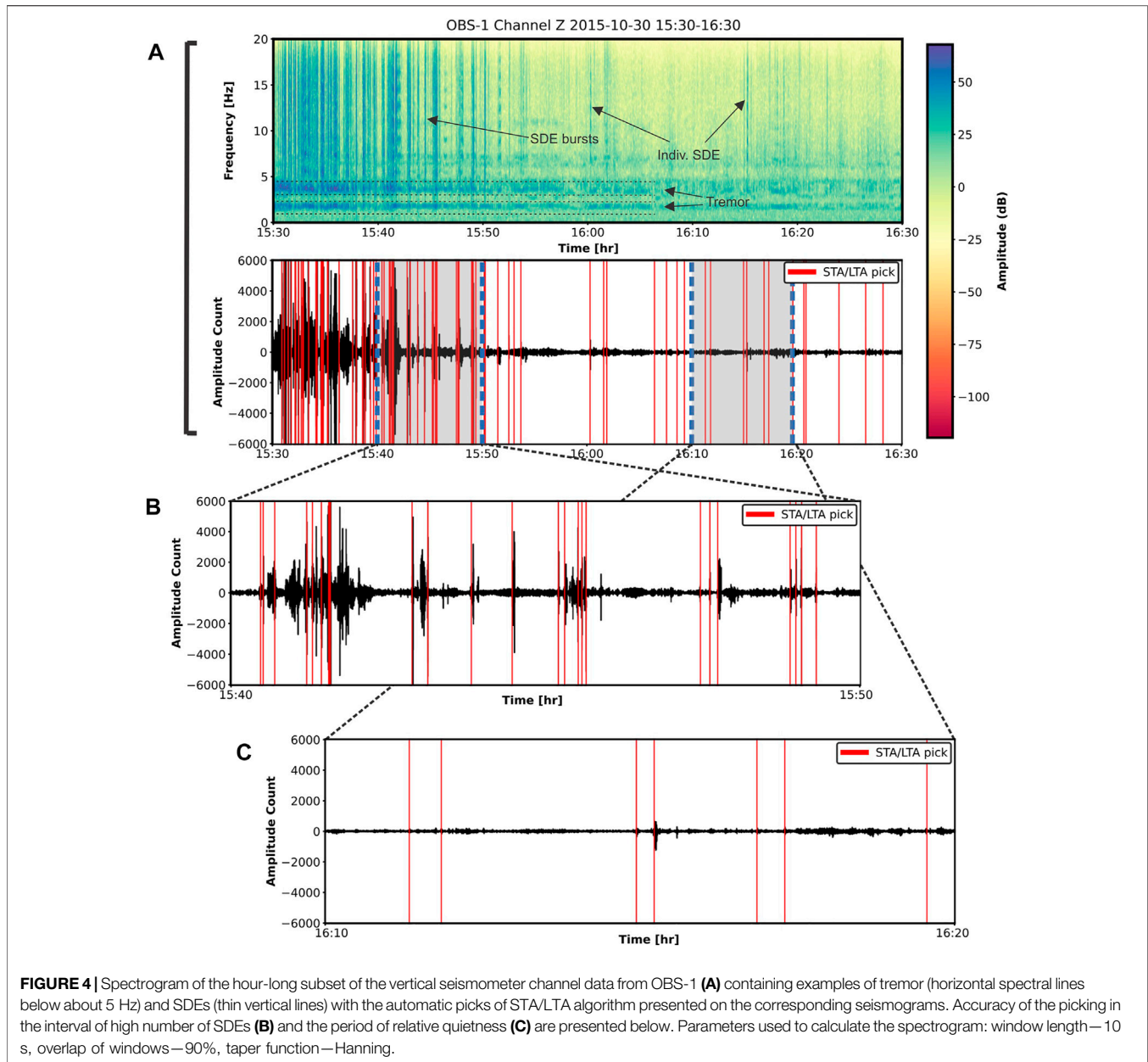
(Figure 2C). Instead of short, strong impulses, it consists of repeating patterns of a longer duration (few seconds and upwards) signal. Its amplitude is also much weaker in comparison to SDEs and most of the recorded earthquakes, which means that the signal to noise ratio is generally much lower. Unlike many whale calls, sporadic SDEs and stronger earthquakes, tremors are not present in the data of the hydrophone channel. These differences in signal’s strength over noise and individual packet duration allow for a distinction of tremor from other observed phenomena. However, due to its prevalence, tremors often coincide with SDEs and earthquakes. Owing to their frequency content up to 60 Hz and high amplitudes, SDEs are still recognizable during times of tremor (cf. Figure 4A).

Harmonic tremors are often interpreted as an effect of OBS instrumentation interacting with the deployment environment. Radio antenna used in OBS recovery has been suggested as a vibrating source of tremor controlled by underwater currents (Duennebieer et al., 1981). Underwater currents can excite the rope holding the head buoy used for post-deployment retrieval in LOBSTER design OBS instruments (Stähler et al., 2018). This excitation can give rise to a tremor-like signal with a fundamental frequency close to 1 Hz, in a process known as Karman vortex shedding. Tremor characteristics, similar to the ones discussed here, were also observed near Canary Islands and were attributed to underwater currents exciting the seismometers (Ugalde et al., 2019). This type of a harmonic noise exhibits strong correlation with tidal cycles (Ramakrushana Reddy et al., 2020; Essing et al., 2021). We therefore suggest that the observed harmonic tremor signals are likely caused by seafloor currents acting on the OBSs.

2.3.4 Whale Calls

We found numerous examples of fin whale calls in the sensitive frequency range of seismometers and hydrophones. They produce a repeating sequence of short (~1 s), down-sweeping pulses within the range of 5–40 Hz, with highest energy around 18 Hz (Figure 2D). The overall duration of an individual animal call lasts usually for more than 200 s (Gaspa Rebull et al., 2006). The duration of recorded calls is highly dependent on whether we observe a group of animals or just a single whale. Since the source of the signal is in the water column, it is predominantly recorded by the hydrophones, and depending on the distance, may also be seen on seismometer channels.

Many different marine mammal species produce vocalizations that can be recorded with a high frequency hydrophone, but numerous studies have shown it is possible to record fin and blue whale calls also on seismometers due to the low frequency of their calls (e.g., McDonald et al., 1995; Morano et al., 2012; Soule and Wilcock, 2013). Both species are seasonally present west of Svalbard (Edwards et al., 2015; Storrie et al., 2018; Løviknes et al., 2021). Blue whales’ songs have frequencies that also overlap with the bandwidth of OBS recordings, however their sounds are longer in duration (~8 s) and narrower in frequency (~20 Hz) for groups observed in North Atlantic (McDonald et al., 2006).



They can also produce a different type of call (D call), possibly related to feeding, that can resemble a fin whale down-sweeping pulse, but a single event is lasting several seconds, longer than a fin whale call (Mellinger and Clark, 2003; Rice et al., 2021).

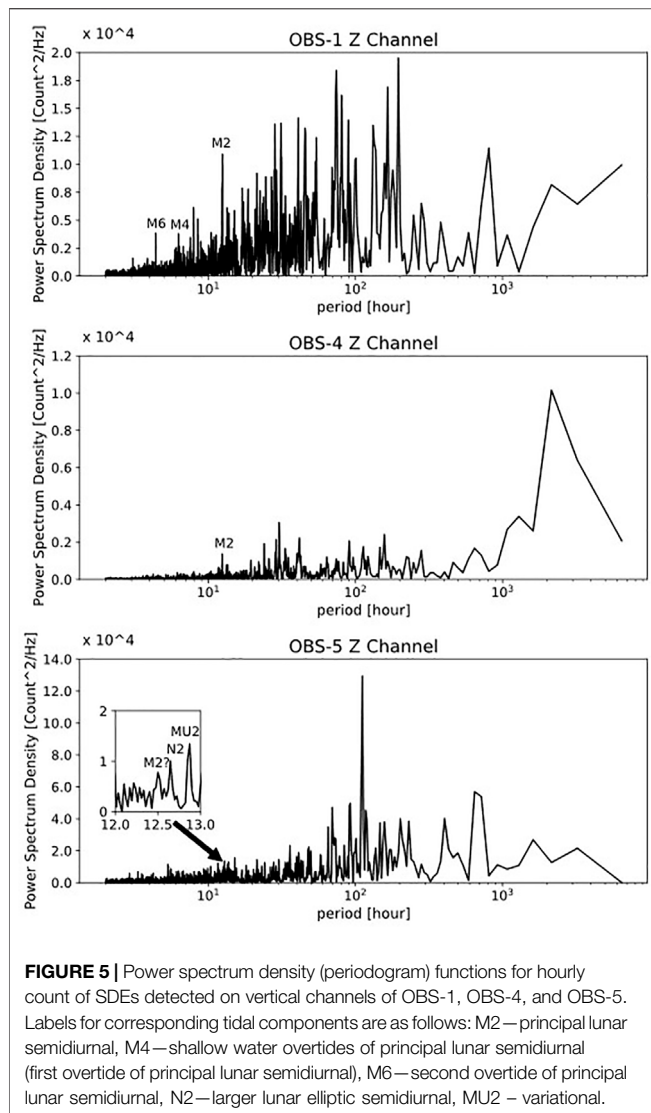
Call patterns of any of these species can clearly be distinguished from SDEs which lack down-sweep character and rhythmic sequences, they also have a longer duration.

Earthquakes, tremors and whale calls are beyond the scope of our study and will not be further discussed.

2.4 Automatic SDE Detection

We automatically extracted SDEs using the routine STA/LTA (short-term average/long-term average) algorithm implemented

in ObsPy toolbox (Beyreuther et al., 2010) following an approach adopted for several studies of SDEs (e.g., Tary et al., 2012; Embriaco et al., 2014; Franek et al., 2014; Franek et al., 2017; Batsi et al., 2019). First, we visually identified a large number of SDEs present in the data to gain an idea of the best search parameters for the STA/LTA detector, based on their signal characteristics (Figure 3). We conducted the search on vertical channels of all seismometers, because only the strongest SDEs were present on all channels of a seismometer (Figure 3). We have chosen arbitrary two-week long period of data and tested different detection parameters until we obtained satisfactory result. After a careful analysis and testing of STA/LTA trigger sensitivity, we set the following parameters: length of short-term window 0.35 s, length of long-term window 8 s, trigger threshold



ratio 5 and de-trigger threshold 2. We restricted the event duration to less than 2.5 s to make sure that local earthquakes from oceanic ridges and whale calls would not be included in the resulting dataset. The final output contained each picked SDE start time and its duration (defined as the difference between trigger and de-trigger time).

Overall, the STA/LTA automatic extraction is highly effective for periods with limited SDE activity (Figure 4C). However, in periods of intensive SDEs we notice that the STA/LTA identifies fewer SDEs than observed by visual inspection during the selected period (Figure 4B). Specifically, it fails to trigger detection more than once during longer periods of SDEs activity with practically no low-amplitude intervals in between. Therefore, the number of SDEs during phases of high activity is likely underestimated. Nevertheless, the presence of harmonic tremors does not affect the trigger sensitivity and SDEs are also detected during phases of intense tremor (15:30–15:50, Figure 4A). The use of the vertical seismometer channel for SDE detection further avoided triggering on whale calls.

3 RESULTS

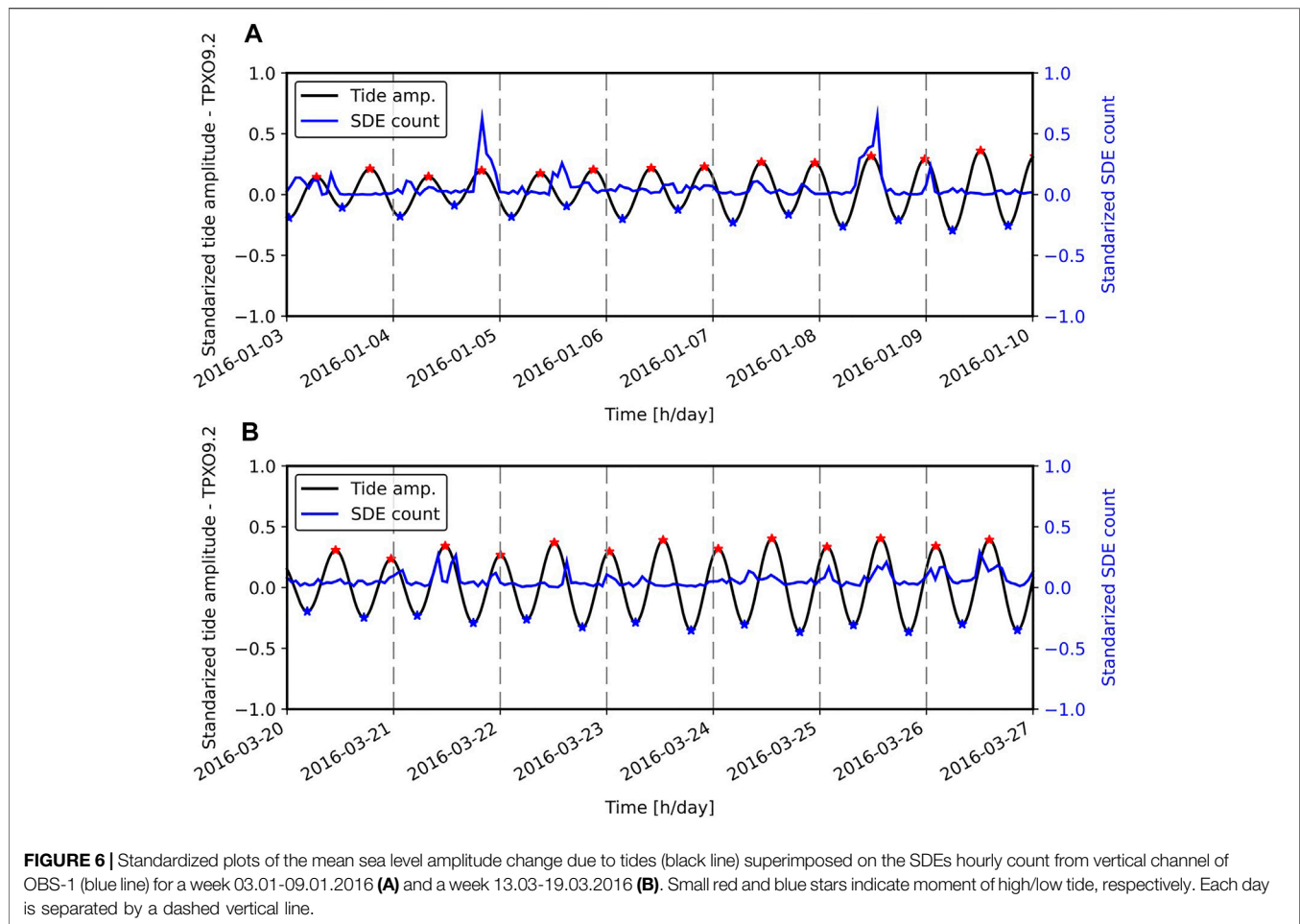
3.1 Occurrence and Periodicity of Observed SDEs

We detected more than 300,000 events using STA/LTA detector and more than 90,000 on OBS-1 alone throughout the deployment period. They occur as a single event or in bursts of dozens, sometimes hundreds, lasting several hours (Figure 4). We operated the STA/LTA detector on the vertical seismometer channel. However, SDEs are generally visible on all channels of a seismometer, and sometimes also on a hydrophone channel. We observe that the number of SDE occurrences varies with time along the records and these variations are not regular. Also, the observed bursts of SDEs do not occur simultaneously on the neighboring stations, despite their estimated distance of only 250–300 m. This indicates that the origin of the signal is very local, otherwise we would expect simultaneous detection on nearby stations. This is in line with other reports about their occurrence (e.g., Tary et al., 2012; Embriaco et al., 2014; Sgroi et al., 2021).

Periodogram plots reveal a periodic pattern of occurrence of SDEs that can be correlated with major tidal cycles. The SDE occurrence peaks in cycles of about 12.4 h (M2 in Figure 5) on OBSs 1 and 4, and to a lesser extent on OBS-5. There are also spectral peaks at 4.39 h (M6 in Figure 5) and 6.28 h (M4 in Figure 5) on OBS-1. M2, M4 and M6 correspond to the principal lunar semi-diurnal constituent and the first and the second overtide of principal lunar semi-diurnal constituent, respectively (Lopes and Tenreiro Machado, 2017). It can be argued that there are three small peaks related to M2 and other tidal constituents present on OBS-5 (M2? N2 and MU2 in Figure 5). In general, we also observe many more periodicity peaks greater than full-day on the spectra that cannot be assigned to the tides in a direct manner.

We conducted similar analysis of periodicity for the tremors to compare the strength of the tidal influence on both processes. We utilized the detection approach of Roman (2017) to obtain an hourly-binned dataset of tremor occurrence. This method uses the pitch detection approach from speech and music processing, due to their similar characteristics to harmonic tremors. It initially assumes that each individual sample has the tremor present. It first determines the fundamental frequency of a signal by consecutively decimating the Fourier transform of a signal and designating a frequency with the highest power as the fundamental one. Then, for the integer multiples of this frequency (harmonics), it measures the relative power ratios between the windows containing the fundamental frequency and its potential harmonics. If this ratio exceeds a predefined value, we can assume that the signal contains tremor, with a given fundamental frequency. We can also decide for how many harmonics the ratio has to be checked and met for a signal to be declared as a tremor.

In the resulting plots, we also observed clear spectral peaks corresponding to tidal cycles on OBS-1 and OBS-4 (Supplementary Figure S1), with the M2 peak more pronounced than in the SDE periodogram. In addition, longer



period tidal constituents (K1 and longer periods) are present in the tremor cyclicity. This underlines two points: that we could successfully discriminate SDE events and tremor signals with SDE occurrence patterns differing from tremor occurrence patterns; secondly, that different source mechanisms are responsible for producing tremors and SDEs.

3.2 Periodicity of SDEs and Comparison With Tidal Cycles

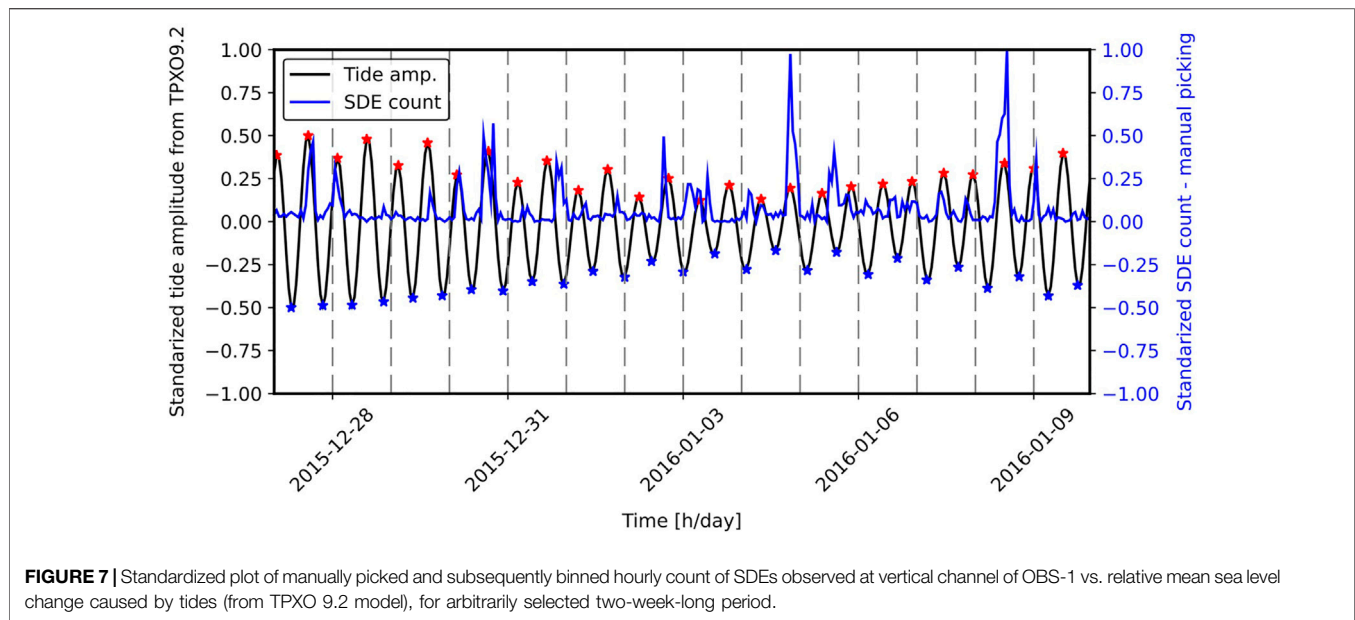
To further compare the observed periodicity of SDEs with the periodicity of diurnal tides, we used the models of expected mean sea level height changes for the months of the experiment using pyTMD (Sutterley et al., 2019). We calculated these values for the location of OBS-1 (6°54'30"E, 79°00'17"N) using TPXO 9.2 model (Egbert and Erofeeva, 2002). For this site, we obtained the maximum mean sea level height difference due to tides of about 1.2 m. We then compared the normalized modelled tidal response time series with normalized SDEs time series (Figure 6). Subsequently, we also noticed that occurrence of SDEs matches, albeit in not a consistent way, the pattern represented by tidal cycles calculated for Vestnesa Ridge. It appears that increased numbers of SDEs are usually visible near the peaks of sea level change, but SDEs are not present in every consecutive diurnal tide

cycle. More examples of observed SDEs intensity can be found in the supporting material (Supplementary Figures S2–S40). We performed manual picking of the SDEs on a smaller subset of the data and confirmed that the similar periodic pattern is present (Figure 7). Therefore, we can exclude those artefacts caused by the relative insensitivity of the STA/LTA detector in times of SDE bursts affect the SDE periodicity.

In general, these plots show that the observed relationship between tides and SDE occurrence is not very strong. This agrees with what is observed on periodograms, where peaks of spectral amplitude at the frequencies corresponding to tides are visible, but other, stronger periods are also present. Likewise, a prominent increase in SDE numbers is rarely observed on subsequent tidal cycles. We observe instead that at least a few days can pass with a lesser amount of SDEs. This pattern occurs through the entire dataset, with additional longer quiet periods (on a scale of weeks), where clear increases in SDEs are not observed (Supplementary Figures S2–S40).

3.3 Phase Relationship Between SDE Bursts and Tides

In order to quantify the strength of the relationship between SDEs and tides, we use cross-correlations (Appendix A) of the



normalized mean sea level change with the normalized SDE hourly count function as a quantitative measure of similarity. The cross-correlation allows calculation of the lag (i.e., the phase difference between the input time series), at which the relationship is potentially strongest. Since one of the functions used in the calculation has a clear periodic pattern (i.e., roughly 12-h periodicity in the case of the tides), we looked at the cross-correlation lag values only between -12 and 12 h (Figure 8). We detrended the time series prior to the correlation. In the next step, we split the data into monthly intervals and evaluated the relationship of SDE counts to both rising and falling tides. We then generated monthly plots for each OBS using the same approach, with the omission of July 2016, since we only had 5 full days of the record for this month (Figure 9).

The cross-correlation between the tidal time series and hourly SDE count time series shows a peak correlation in all three OBS stations between 0–1 h time lag. This indicates that rising tides close to the tidal maximum correspond to the highest likelihood of occurrence of SDEs (Figure 8). Additionally, each correlation peak has a corresponding minimum at roughly 6 h before and after the peak. This is a consequence of the periodic nature of one of the input functions (mean sea level change) for the correlation process, but it also indicates a weaker connection between SDEs and low tides. Shifting the tidal dataset back and forth by an arbitrary number of hours produces a cross correlation function with the maxima and minima shifted by the same number of hours, respectively.

We then study 27 individual samples representing correlation results for month-long subsets of SDE data for each of three OBS (Table 1). In most (17/27) of the cases, the peak correlation occurs either at 0 h lag or at 1 h lag. Since the input dataset is binned into hour-long intervals, this means that the actual peak occurs at the value between 0 and 1 h. In these cases, a maximum correlation value equal ~ 0.1 – 0.5 (Figure 9). This

indicates a stronger relationship between times of a rising tide and peaks in SDEs occurrence rather than between falling tides and peaks in SDE occurrence. The average correlation value for these periods is 0.17. For months where the correlation peak occurs at a time lag other than 0 h or 1 h, the correlation value is much lower (usually <0.05 , mean value 0.06), indicating weaker correlation/relationship between SDEs and relative wave height change due to tides. Additionally, among these 10 results with the correlation peak outside of 0–1 h range, only one correlation value is greater than 0.1 (i.e., for 2 h correlation lag in October for OBS-1), so the reliability of these 10 correlation results is poor. In general, the resultant correlation values are low, but there is a clear separation between values observed at lag 0–1 h in most of the months and the correlation results when peak is at different lag or barely recognizable.

It is worth remembering however, that the resulting coefficients are neither robust nor resistant (Wilks, 2011). This means that cross correlation may not recognize strong, but non-linear relationships (robustness), or its outcome value can be extremely sensitive to one or a few outlying points pairs (resistance). Relatively low coefficient values are caused partially by a high variance in the SDE dataset, where most of the observed counts during tide changes have relatively low value compared to extreme SDEs bursts that we observe sporadically in the data (median value of the normalized SDE occurrence is just 0.0259, 0.0185, and 0.0684 for OBS-1, OBS-4, and OBS-5, respectively). The aforementioned issues with the data quality for OBS-5 are likely the reason behind generally weak correlation for most of the months (with notable distinction of June (0.45), where the correlation is the strongest for the entire dataset from all recorders). In summary the results suggest that SDE peaks are more likely to happen at high and low tide but not at every tidal cycle and only sporadically. There is a stronger

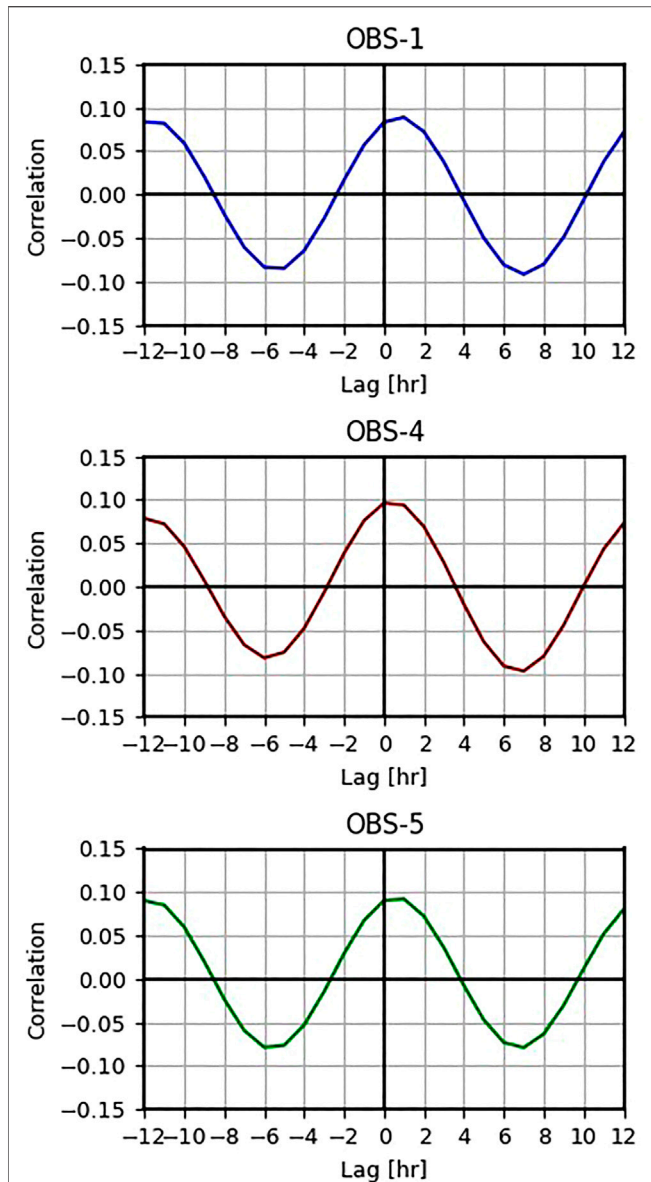


FIGURE 8 | Correlation of standardized SDEs hourly count (calculated for vertical channel of seismometer), with standardized tide amplitude for OBS-1, OBS-4, and OBS-5. For each plot the maximum positive correlation occurs at around +1 h (and repeat with periodicity of 12 h)—SDEs peak precedes the point of high tide by 1 h.

connection between high tides and peaks in SDE occurrence than between low tides and peaks in SDE occurrence.

4 DISCUSSION

4.1 Tidal Control on SDEs

The analyses above indicate that:

- SDEs at the investigated site on Vestnesa Ridge have a periodic pattern of distribution

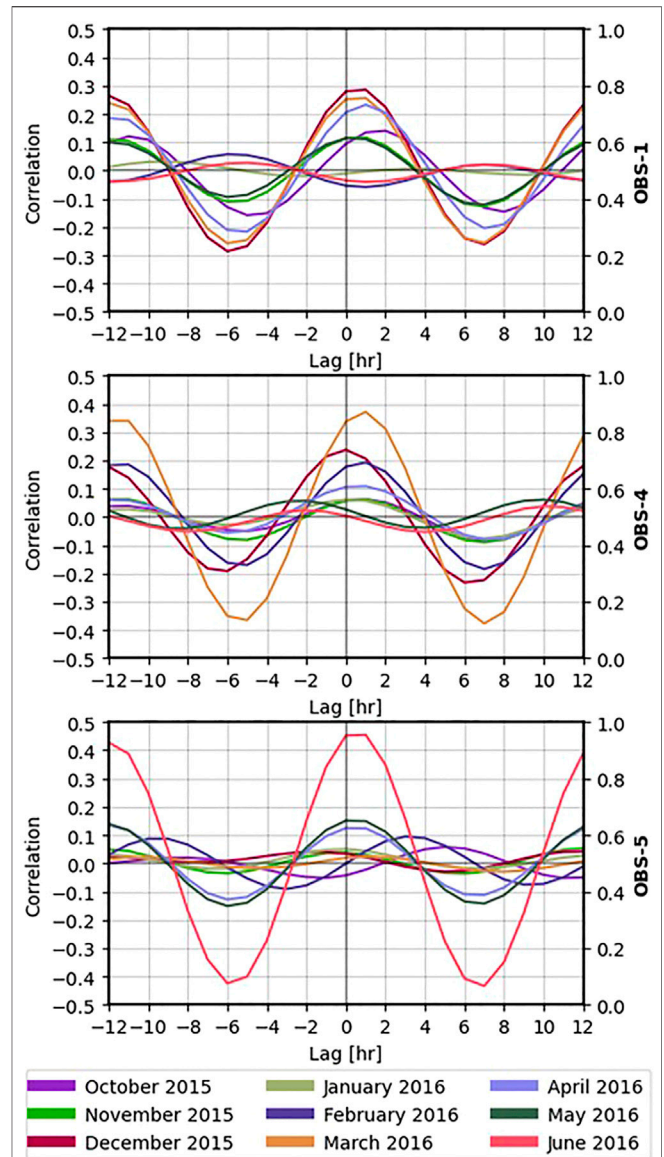


FIGURE 9 | Monthly correlation between standardized SDEs hourly count from vertical channels of OBS-1, OBS-4 and OBS-5, and standardized relative sea level change from TPXO 9.2 model.

- SDEs can be correlated with diurnal and longer-term periodicity sea level changes to some extent
- The correlation between SDE occurrences and tides is in average low, with a stronger connection between their increase at maximum sea level periods. In such an instance, increase in SDEs does not necessarily occur within each tidal cycle, but with the periods of lower activity in between

Our results reveal that although SDEs are not strongly correlated with sea level changes associated to ocean tides, observing their variability on a month-by-month basis still shows partial effect of tidal sea level oscillations on the intensity of SDE bursts.

TABLE 1 | Maximum peak correlation lag time (in h) and corresponding correlation coefficient values for every month of deployment of each OBS. For all peaks occurring outside of the lag window 0–2 h we observe very low, close to 0, values of correlation coefficient.

Month	Lag of peak [hr]			Correlation value		
	OBS-1	OBS-4	OBS-5	OBS-1	OBS-4	OBS-5
October	2	1	5	0.14	0.06	0.05
November	1	4	12	0.11	0.06	0.05
December	1	0	12	0.29	0.23	0.04
January	–9	0	0	0.03	0.06	0.05
February	–6	1	3	0.05	0.19	–0.9
March	1	1	1	0.26	0.37	0.02
April	1	1	0	0.23	0.1	0.12
May	0	10	0	0.11	0.06	0.15
June	1	10	1	0.12	0.03	0.45

While tremor periodicity indicates tidally modulated underwater currents (**Supplementary Figure S1**; Stähler et al., 2018; Ramakrushana Reddy et al., 2020; Essing et al., 2021), SDEs show a different periodic pattern, suggesting that their link to the sea level changes is via more complex near-seafloor processes.

Mean sea level changes represent pressure difference that impact near-surface geological processes. There are global observations that document a strong link between SDEs (i.e., micro-seismicity), and fluid movement through near seafloor sediments (Sultan et al., 2011; Tary et al., 2012; Embriaco et al., 2014; Franek et al., 2014; Franek et al., 2017; Batsi et al., 2019). Batsi et al. (2019) recreated in the lab (i.e., using a small amount of air and water injected into the sediments within a meter from the geophone) a signal characterized by high frequency content, strong amplitude and short duration that has a remarkable resemblance with SDEs.

All three SDE measurements documented here are concentrated near (<500 m) pockmark with proven gas hydrates and fracture-related seafloor seepage (**Figure 1**; Bünz et al., 2012; Panieri et al., 2017). The fact that SDEs are not recognized simultaneously on the three OBSs, together with strong relative amplitudes and no clear separation between the P and S wave signals (as in earthquakes), indicate local sources of SDEs that lose energy rapidly.

Discussions on the link between SDEs, tides and seepage dynamics at continental margins have gained significant attention following observations from various margins and geological settings. Several studies document tidal modulated seepage activity at continental margins (e.g., Boles et al., 2001; Torres et al., 2002; Hsu et al., 2013) and hydrothermal systems (e.g., Schultz et al., 1992; Plant et al., 2010). Along west-Svalbard continental margin, a potential effect of tides on the seepage intensity has been inferred from analyses of gas signatures on sonar (Veloso-Alarcon et al., 2019) and *in-situ* pore fluid pressure data (Sultan et al., 2020). Other studies document temporal relations between SDEs and enhanced methane release to the water column (e.g., Sea of Marmara; Embriaco et al., 2014). Bayrakci et al. (2014) noted a strong increase in the number of SDEs recorded on an OBS deployed directly at a seep location compared to other nearby devices. The polarization of SDEs

observed by Hsu et al. (2013) at a mud volcano off Taiwan indicated a source in the shallow subsurface. In their case, the tidal pattern in SDE occurrence matched the periodicity of the gas flux in the water column giving further direct evidence of a link between tidally controlled fluid flow systems and SDE generation.

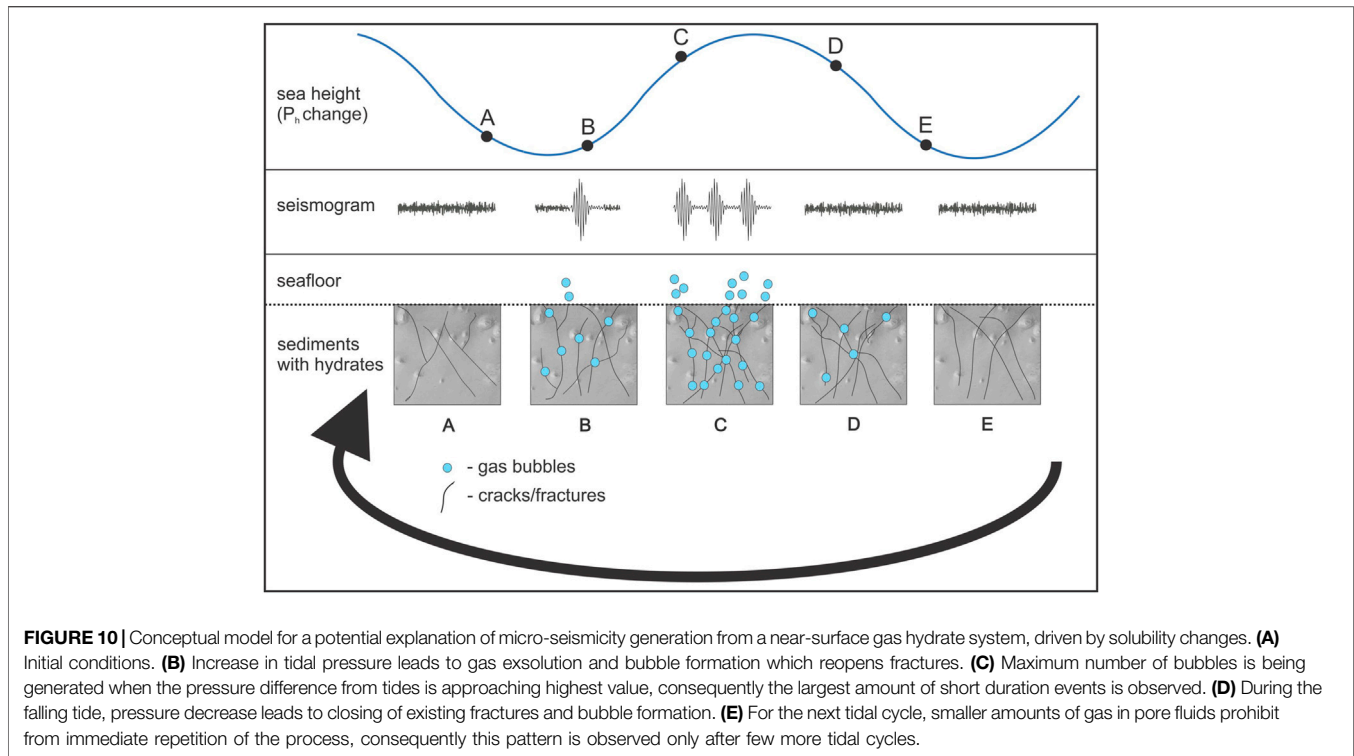
Very few studies discuss simultaneously mechanisms by which tides may affect seafloor seepage periodicity, which in turn may control the pattern of distribution of micro-seismic signals. Moreover, while a link between temporal modulation of gas release and occurrence of SDE events has been established based on data from various continental margins, the physical process behind this link is still the subject of the debate. We discuss hereafter physical mechanisms that can explain the link between SDE occurrences, sea level changes and seepage dynamics at Vestnesa Ridge gas hydrates and associated seepage system.

4.2 SDEs From a Fracture-controlled Gas Hydrate and Seepage System

Documented SDEs occurrences on Vestnesa Ridge are in line with observations from other margins, possibly reflecting sea level controlled dynamic changes on the seepage system from one or several of the surrounding pockmarks (**Figure 1**).

Soft, unconsolidated sediments create temporary pathways for migrating gas that undergo closure after the gas release (Boudreau et al., 2005). It has been suggested that SDEs could be the manifestation of opening new fractures allowing for gas expulsion or pockets of gas travelling upwards in the shallow sediment (Tary et al., 2012). Both modeling (Tary et al., 2012) and test in a sediment tank (Batsi et al., 2019), have shown that gas release from the surface would produce signals that resemble the SDEs recorded in the field.

Seepage over the monitored pockmark on Vestnesa Ridge has been documented over multiple yearly surveys since 2009 (e.g., Smith et al., 2014; Panieri et al., 2017). The pockmark is associated with one, among several, vertical fluid migration conduits along Vestnesa Ridge. These conduits are known as gas chimneys or gas pipes and are thought to be formed due to overpressured gas at the base of the gas hydrate stability zone (GHSZ) (Hustoft et al., 2009; Singhroha et al., 2016). The source of gas is both microbial and thermogenic (Pape et al., 2020) and seepage at the seafloor is sustained by pulses of gas migrating through fractured strata (**Figures 1C,D**) (Bünz et al., 2012; Plaza-Faverola et al., 2015; Singhroha et al., 2016). Buried authigenic carbonate accumulations within the pipes, characterized by high amplitude anomalies in 3D seismic data, indicate periods of enhanced methane release in the past (Himmeler et al., 2019; Plaza-Faverola et al., 2015; Schneider et al., 2018). These shallow authigenic carbonate concentrations and gas hydrates promote the entrapment of gas within the upper few meters below the seafloor (**Figure 1C**) (Plaza-Faverola et al., 2015; Himmeler et al., 2019). Over time, trapped gas bypasses local seals and continue through shallow fractures to sustain seafloor seepage at present day (Hong et al., 2021). Such fluid flow systems are known as self-sealed (Hovland et al., 2002).



The physical mechanism usually invoked to explain the modulation of seepage by tides is the forcing exerted by increasing and decreasing hydrostatic pressure on gas (i.e., a compressible fluid) present in the pore-fluids (Römer et al., 2016; Sultan et al., 2020). This change in pore-fluid pressure would also lead to changes in the state of pre-existing fractures in the subsurface, which would lead to enhanced or hindered gas migration. Such mechanical changes generate micro-seismicity (Hsu et al., 2013).

Observations of gas emissions into the water column (Boles et al., 2001; Torres et al., 2002; Plant et al., 2010; Römer et al., 2016; Riedel et al., 2018) at Cascadia margin and inferred from pore fluid pressure changes (Sultan et al., 2020) at Vestnesa Ridge point to the highest seepage activity during low tides, which would then lead to the largest number of SDEs also during low tides (i.e., assuming that the three processes: fracture opening, gas seepage, and generation of SDEs, occur simultaneously). This is not entirely consistent with the seismological SDE pattern we observe. We suggest that the key to understanding this apparent discrepancy is in the dynamics of the fluid migration system. The system monitored on Vestnesa Ridge has a constant supply of gas from the deeper sediments (e.g., Knies et al., 2018; Daszinnies et al., 2021) and seafloor seepage is continuous (Smith et al., 2014). Thus, it is possible that changes in pressure due to tides only modulate but do not control the seepage activity.

A constant input of gas (e.g., from the base of the gas hydrate stability zone; Singhroha et al., 2016) into the shallow sediment may result in overpressure-driven pulses of gas migration upwards (Hustoft et al., 2009). Micro-seismicity generation can happen both during high and low tides, provided there is enough gas present, and an effective stress of sediments is

overcome (Hsu et al., 2013). Hsu et al. (2013) points out, that for a specific location, the vertical stress of a rock stays more or less constant throughout the tidal cycle, leading to a greater pressure difference between gas-filled sediments and the water column at a high tide compared to at a low tide. This leads to larger observed micro-seismicity response during a tidal peak than during a tidal low, which is what they observed, and what we also have noticed during tidal cycles with micro-seismic activity present. In their case, the micro-seismic pattern is directly matched with the gas emission intensity measurement in the water column. Furthermore, in this study it is postulated that in a case of an insufficient methane replenishment (occurring on a scale larger than a single tidal cycle), there is a smaller gas charge, not strong enough to overcome the pressure difference when the influence of tides is largest (high tide). This mechanism can explain observations of increased gas emissions during low tide (e.g., Römer et al., 2016; Riedel et al., 2018; Sultan et al., 2020). Slower replenishment of the gas (on a scale of at least few tidal cycles), could also lead to gaps in the micro-seismic activity, which is what we have observed.

Complex thermodynamic behaviors of gas hydrates may be having an effect on the response of the seepage system to sea level changes and subsequently on the pattern of micro-seismicity generated in response to fluid migration. Normally, solubility of the methane in the pore water increases with the increase in pressure, but in a system supporting stable conditions for methane hydrate to form, the opposite situation is possible (Handa, 1990; Tishchenko et al., 2005; Sun and Duan, 2007; Liu and Flemings, 2011). This is especially true at low temperatures encountered at deep (>1200 m) seafloors. Specific pressure and

temperature conditions may favor exsolution of methane from the aqueous phase during high tides, leading to either formation of gas hydrate or generation of methane bubbles that fracture very shallow sediments and release in the form of bubbles. While the change in solubility will be very small, it has been shown that for shallow, unconsolidated sediments reopening of previously existing fractures and bubble generation is possible at a pressure difference provided by tides (Boudreau, 2012). This will not lead to a large change in the amount of methane seeping, but actually, the smaller the bubbles generated, the easier they move to the seafloor, either by initiating minor fractures (assuming linear elastic fracture mechanics) or through pre-existing fluid-filled cracks/pathways (Johnson et al., 2002; Boudreau et al., 2005; Algar et al., 2011a; Algar et al., 2011b; Boudreau, 2012). A conceptual model of such a cycle is presented in **Figure 10**. Such a change of release would probably not produce an observable difference in the acoustic flares observed in sonar data.

How gas hydrate thermodynamics affect seepage periodicity at continental margins is a largely understudied, yet highly relevant problem that deserves broader investigation.

5 CONCLUSION

Seismological data from three ocean bottom seismometers (OBS) obtained at Vestnesa Ridge reveals, in addition to information about local seismicity, continuous records of tremor-like signals and a large number of short duration events (SDEs). In line with observations from other margins, the tremors documented here are likely caused by the effect of tidal currents on the OBS instrumentation. These currents exhibit strong variability that can be linked to semi-diurnal tides and observed patterns of tremor occurrence match the periodicity of modelled tides for the site.

Comparably to other studies reporting SDEs, our analysis support local, near-surface origin of the observed events. Lack of simultaneous detections of SDEs on closely-spaced OBSs and no observations of SDEs in hydrophone channels point to shallow, subsurface SDE origin.

Our results indicate that both tremors and SDEs occurrences in the investigated setting have a periodic behavior, and their periodicity is comparable to tidal cycles. While the relationship between tides and tremors is through tide-generated currents at the sea-bottom, the relation between tides and SDEs reveals different periodic pattern, in addition to a clear tidal component. SDE bursts generally correlate better with local tide maxima.

SDE distribution, periodic behavior and signal characteristics from Vestnesa Ridge compare to reports from other seepage sites worldwide. A potential connection between SDEs, sea-level changes and seepage dynamics in this deep marine gas hydrate system is explained by:

- Sediment fracturing and gas release caused by small pressure changes due to tides
- Insufficient gas charge unable to overcome pressure difference at a high tide, leading to emission only during periods of low tide, whilst also explaining gaps between the tidal cycles with increased SDE bursts

- Alternatively, complex thermodynamic behavior of gas hydrate under pressure changes due to tides likely affects seepage periodicity and near-surface deformation. This is under-investigated, yet highly relevant problem for quantifying seafloor seepage at continental margins

More quantitative modelling of the gas hydrate behavior in the sediments influenced by tidal pressure variations is necessary to verify how it affects the seepage and shallow sediments.

DATA AVAILABILITY STATEMENT

The datasets presented in this study can be found at UiT's open research data repository (DataverseNO): <https://doi.org/10.18710/TCWUQN>.

AUTHOR CONTRIBUTIONS

SB, APF, and PF (former colleague at the Center) designed and conducted the ocean bottom seismic (OBS) experiment. PD conducted the processing and analysis of OBS records. SS and PD worked on the cross correlation with modelled tides. PD prepared the manuscript with significant contributions from APF, VS, and SS. HR contributed to the conceptualization of the proposed model and discussion.

FUNDING

This work is part of the SEAMSTRESS project, supported by the Tromsø Research Foundation (TFS) and the Research Council of Norway (grant nr. 287865). The work is also supported by the Research Council of Norway through its Centers of Excellence funding scheme grant 223259 (Centre for Arctic Gas Hydrate, Environment and Climate—CAGE).

ACKNOWLEDGMENTS

We thank the crew of R/V *Helmer Hanssen* for their help with deployment and recovery of OBSs. We also thank Peter Franek for his initial work with the datasets and valuable assistance at an early stage of data processing. We thank the Reviewers Kimihiro Mochizuki and Christopher Schmidt for the constructive feedback that helped to improve the final publication. We also thank the Associate Editor Mourad Bezzeghoud. Regional map was created using GMT (Wessel et al., 2019). Plotting waveforms and spectrograms was done using Pyrocko (Heimann et al., 2017).

SUPPLEMENTARY MATERIAL

The Supplementary Material for this article can be found online at: <https://www.frontiersin.org/articles/10.3389/feart.2022.831526/full#supplementary-material>

REFERENCES

- Algar, C. K., Boudreau, B. P., and Barry, M. A. (2011a). Initial Rise of Bubbles in Cohesive Sediments by a Process of Viscoelastic Fracture. *J. Geophys. Res.* 116 (B4). doi:10.1029/2010jb008133
- Algar, C. K., Boudreau, B. P., and Barry, M. A. (2011b). Release of Multiple Bubbles from Cohesive Sediments. *Geophys. Res. Lett.* 38 (8). doi:10.1029/2011gl046870
- Ambrose, W. G., Panieri, G., Schneider, A., Plaza-Faverola, A., Carroll, M. L., Åström, E. K. L., et al. (2015). Bivalve Shell Horizons in Seafloor Pockmarks of the Last Glacial-interglacial Transition: a Thousand Years of Methane Emissions in the Arctic Ocean. *Geochem. Geophys. Geosyst.* 16 (12), 4108–4129. doi:10.1002/2015gc005980
- Batsi, E., Tsang-Hin-Sun, E., Klingelhoefer, F., Bayrakci, G., Chang, E. T. Y., Lin, J. Y., et al. (2019). Nonseismic Signals in the Ocean: Indicators of Deep Sea and Seafloor Processes on Ocean-Bottom Seismometer Data. *Geochem. Geophys. Geosyst.* 20 (8), 3882–3900. doi:10.1029/2019gc008349
- Bayrakci, G., Scalabrin, C., Dupré, S., Leblond, I., Tary, J.-B., Lanteri, N., et al. (2014). Acoustic Monitoring of Gas Emissions from the Seafloor. Part II: a Case Study from the Sea of Marmara. *Mar. Geophys. Res.* 35 (3), 211–229. doi:10.1007/s11001-014-9227-7
- Beccari, V., Basso, D., Spezzaferri, S., Rüggeberg, A., Neuman, A., and Makovsky, Y. (2020). Preliminary Video-Spatial Analysis of Cold Seep Bivalve Beds at the Base of the continental Slope of Israel (Palmahim Disturbance). *Deep Sea Res. Part Topical Stud. Oceanography* 171, 104664. doi:10.1016/j.dsr.2.2019.104664
- Berndt, C., Feseker, T., Treude, T., Krastel, S., Liebetrau, V., Niemann, H., et al. (2014). Temporal Constraints on Hydrate-Controlled Methane Seepage off Svalbard. *Science* 343 (6168), 284–287. doi:10.1126/science.1246298
- Beyreuther, M., Barsch, R., Krischer, L., Megies, T., Behr, Y., and Wassermann, J. (2010). ObsPy: A Python Toolbox for Seismology. *Seismological Res. Lett.* 81 (3), 530–533. doi:10.1785/gssrl.81.3.530
- Boles, J. R., Clark, J. F., Leifer, I., and Washburn, L. (2001). Temporal Variation in Natural Methane Seep Rate Due to Tides, Coal Oil Point Area, California. *J. Geophys. Res.* 106 (C11), 27077–27086. doi:10.1029/2000jc000774
- Boudreau, B. P., Algar, C., Johnson, B. D., Croudace, I., Reed, A., and Furukawa, Y. (2005). Bubble Growth and Rise in Soft Sediments. *Geology* 33 (6). doi:10.1130/g21259.1
- Boudreau, B. P. (2012). The Physics of Bubbles in Surficial, Soft, Cohesive Sediments. *Mar. Pet. Geology* 38 (1), 1–18. doi:10.1016/j.marpetgeo.2012.07.002
- Bowman, D. C., and Wilcock, W. S. D. (2013). Unusual Signals Recorded by Ocean Bottom Seismometers in the Flooded Caldera of Deception Island Volcano: Volcanic Gases or Biological Activity? *Antarctic Sci.* 26 (3), 267–275. doi:10.1017/s0954102013000758
- Bünz, S., Polyakov, S., Vadakkepuliambatta, S., Consolaro, C., and Mienert, J. (2012). Active Gas Venting through Hydrate-Bearing Sediments on the Vestnesa Ridge, Offshore W-Svalbard. *Mar. Geology* 332–334, 189–197. doi:10.1016/j.margeo.2012.09.012
- Buskirk, R. E., Frohlich, C., Latham, G. V., Chen, A. T., and Lawton, J. (1981). Evidence that Biological Activity Affects Ocean Bottom Seismograph Recordings. *Mar. Geophys. Researches* 5 (2), 189–205.
- Chang, E. T. Y., Chao, B. F., Chen, G. Y., and Liao, J. M. (2016). Internal Tides Recorded at Ocean Bottom off the Coast of Southeast Taiwan. *J. Geophys. Res. Oceans* 121 (5), 3381–3394. doi:10.1002/2015jc011370
- Chouet, B. (1992). “A Seismic Model for the Source of Long-Period Events and Harmonic Tremor.” in *Volcanic Seismology*. Berlin, Heidelberg: Springer, 133–156. doi:10.1007/978-3-642-77008-1_11
- Ciotoli, G., Procesi, M., Etiope, G., Fracassi, U., and Ventura, G. (2020). Influence of Tectonics on Global Scale Distribution of Geological Methane Emissions. *Nat. Commun.* 11 (1), 2305. doi:10.1038/s41467-020-16229-1
- Consolaro, C., Rasmussen, T. L., Panieri, G., Mienert, J., Bünz, S., and Sztaybor, K. (2015). Carbon Isotope ($\delta^{13}\text{C}$) Excursions Suggest Times of Major Methane Release during the Last 14 Kyr in Fram Strait, the Deep-Water Gateway to the Arctic. *Clim. Past* 11 (4), 669–685. doi:10.5194/cp-11-669-2015
- Crémière, A., Lepland, A., Chand, S., Sahy, D., Condon, D. J., Noble, S. R., et al. (2016). Timescales of Methane Seepage on the Norwegian Margin Following Collapse of the Scandinavian Ice Sheet. *Nat. Commun.* 7, 11509. doi:10.1038/ncomms11509
- Crockett, R. (2019). *A Primer on Fourier Analysis for the Geosciences*. Cambridge: Cambridge University Press.
- Crutchley, G. J., Klaeschen, D., Planert, L., Bialas, J., Berndt, C., Papenberg, C., et al. (2014). The Impact of Fluid Advection on Gas Hydrate Stability: Investigations at Sites of Methane Seepage Offshore Costa Rica. *Earth Planet. Sci. Lett.* 401, 95–109. doi:10.1016/j.epsl.2014.05.045
- Daszinnies, M., Plaza-Faverola, A., Sylta, Ø., Bünz, S., Mattingsdal, R., Tømmerås, A., et al. (2021). The Plio-Pleistocene Seepage History off Western Svalbard Inferred from 3D Petroleum Systems Modelling. *Mar. Pet. Geology* 128, 105023. doi:10.1016/j.marpetgeo.2021.105023
- Di, P., Feng, D., Tao, J., and Chen, D. (2020). Using Time-Series Videos to Quantify Methane Bubbles Flux from Natural Cold Seeps in the South China Sea. *Minerals* 10 (3), 216. doi:10.3390/min10030216
- Díaz, J., Gallart, J., and Gaspà, O. (2007). Atypical Seismic Signals at the Galicia Margin, North Atlantic Ocean, Related to the Resonance of Subsurface Fluid-Filled Cracks. *Tectonophysics* 433 (1–4), 1–13. doi:10.1016/j.tecto.2007.01.004
- Duennebie, F. K., Blackinton, G., and Sutton, G. H. (1981). Current-generated Noise Recorded on Ocean Bottom Seismometers. *Mar. Geophys. Res.* 5 (1), 109–115. doi:10.1007/bf00310316
- Edwards, E. F., Hall, C., Moore, T. J., Sheredy, C., and Redfern, J. V. (2015). Global Distribution of Fin Whales Balaenoptera Physalus in the post-whaling Era (1980–2012). *Mammal Rev.* 45 (4), 197–214. doi:10.1111/mam.12048
- Egbert, G. D., and Erofeeva, S. Y. (2002). Efficient Inverse Modeling of Barotropic Ocean Tides. *J. Atmos. Oceanic Technol.* 19 (2), 183–204. doi:10.1175/1520-0426(2002)019<0183:eimobo>2.0.co;2
- Eiken, O., and Hinz, K. (1993). Contourites in the Fram Strait. *Sediment. Geology* 82 (1–4), 15–32. doi:10.1016/0037-0738(93)90110-q
- Embricaco, D., Marinaro, G., Frugoni, F., Monna, S., Etiope, G., Gasperini, L., et al. (2014). Monitoring of Gas and Seismic Energy Release by Multiparametric Benthic Observatory along the North Anatolian Fault in the Sea of Marmara (NW Turkey). *Geophys. J. Int.* 196 (2), 850–866. doi:10.1093/gji/ggt436
- Essing, D., Schlindwein, V., Schmidt-Aursch, M. C., Hadziioannou, C., and Stähler, S. C. (2021). Characteristics of Current-Induced Harmonic Tremor Signals in Ocean-Bottom Seismometer Records. *Seismological Res. Lett.* doi:10.1785/0220200397
- Etiope, G. (2015). “Gas Seepage and Past Climate Change,” in *Natural Gas Seepage: The Earth’s Hydrocarbon Degassing* (Cham: Springer International Publishing), 165–182. doi:10.1007/978-3-319-14601-0_8
- Ferré, B., Jansson, P. G., Moser, M., Serov, P., Portnov, A., Graves, C. A., et al. (2020). Reduced Methane Seepage from Arctic Sediments during Cold Bottom-Water Conditions. *Nat. Geosci.* 13 (2), 144–148. doi:10.1038/s41561-019-0515-3
- Franek, P., Mienert, J., Buenz, S., and Géli, L. (2014). Character of Seismic Motion at a Location of a Gas Hydrate-bearing Mud Volcano on the SW Barents Sea Margin. *J. Geophys. Res. Solid Earth* 119 (8), 6159–6177. doi:10.1002/2014jb010990
- Franek, P., Plaza-Faverola, A., Mienert, J., Buenz, S., Ferré, B., and Hubbard, A. (2017). Microseismicity Linked to Gas Migration and Leakage on the Western Svalbard Shelf. *Geochem. Geophys. Geosyst.* 18 (12), 4623–4645. doi:10.1002/2017gc007107
- Gaspà, O., Rebull, O., Cusí, J. D., Ruiz Fernández, M., and Muset, J. G. (2006). Tracking Fin Whale Calls Offshore the Galicia Margin, North East Atlantic Ocean. *The J. Acoust. Soc. America* 120 (4), 2077–2085. doi:10.1121/1.2336751
- Grevemeyer, I., Gràcia, E., Villaseñor, A., Leuchters, W., and Watts, A. B. (2015). Seismicity and Active Tectonics in the Alboran Sea, Western Mediterranean: Constraints from an Offshore-onshore Seismological Network and Swath Bathymetry Data. *J. Geophys. Res. Solid Earth* 120 (12), 8348–8365. doi:10.1002/2015jb012073
- Handa, Y. P. (1990). Effect of Hydrostatic Pressure and Salinity on the Stability of Gas Hydrates. *J. Phys. Chem.* 94 (6), 2652–2657. doi:10.1021/j100369a077
- Heimann, S., Kriegerowski, M., Isken, M., Cesca, S., Daout, S., Grigoli, F., et al. (2017). Pyrocko - an Open-Source Seismology Toolbox and Library. V. 0.3. *GFZ Data Serv.*
- Himmler, T., Sahy, D., Martma, T., Bohrmann, G., Plaza-Faverola, A., Bünz, S., et al. (2019). A 160,000-Year-Old History of Tectonically Controlled Methane Seepage in the Arctic. *Sci. Adv.* 5 (8), eaaw1450. doi:10.1126/sciadv.aaw1450
- Hong, W. L., Pape, T., Schmidt, C., Yao, H., Wallmann, K., and Plaza-Faverola, A. (2021). Interactions between Deep Formation Fluid and Gas Hydrate Dynamics Inferred from Pore Fluid Geochemistry at Active Pockmarks of the Vestnesa Ridge, West Svalbard Margin. *Mar. Pet. Geology* 127. doi:10.1016/j.marpetgeo.2021.104957

- Horozal, S., Bahk, J.-J., Urgeles, R., Kim, G. Y., Cukur, D., Kim, S.-P., et al. (2017). Mapping Gas Hydrate and Fluid Flow Indicators and Modeling Gas Hydrate Stability Zone (GHSZ) in the Ulleung Basin, East (Japan) Sea: Potential Linkage between the Occurrence of Mass Failures and Gas Hydrate Dissociation. *Mar. Pet. Geology*. 80, 171–191. doi:10.1016/j.marpetgeo.2016.12.001
- Hovland, M., Gardner, J. V., and Judd, A. G. (2002). The Significance of Pockmarks to Understanding Fluid Flow Processes and Geohazards. *Geofluids* 2, 127–136. doi:10.1046/j.1468-8123.2002.00028.x
- Howe, J. A., Shimmield, T. M., Harland, R. E. X., and Eyles, N. (2007). Late Quaternary Contourites and Glaciomarine Sedimentation in the Fram Strait. *Sedimentology* 55 (1), 179–200. doi:10.1111/j.1365-3091.2007.00897.x
- Hsu, S.-K., Wang, S.-Y., Liao, Y.-C., Yang, T. F., Jan, S., Lin, J.-Y., et al. (2013). Tide-modulated Gas Emissions and Tremors off SW Taiwan. *Earth Planet. Sci. Lett.* 369–370, 98–107. doi:10.1016/j.epsl.2013.03.013
- Hustoft, S., Bünnz, S., Mienert, J., and Chand, S. (2009). Gas Hydrate Reservoir and Active Methane-Venting Province in Sediments on < 20 Ma Young Oceanic Crust in the Fram Strait, Offshore NW-Svalbard. *Earth Planet. Sci. Lett.* 284 (1–2), 12–24. doi:10.1016/j.epsl.2009.03.038
- Johnson, B. D., Boudreau, B. P., Gardiner, B. S., and Maass, R. (2002). Mechanical Response of Sediments to Bubble Growth. *Mar. Geology*. 187 (3–4), 347–363. doi:10.1016/s0025-3227(02)00383-3
- Judd, A., and Hovland, M. (2007). *Seabed Fluid Flow: The Impact on Geology, Biology, and the marine Environment*. Cambridge: Cambridge University Press.
- Karstens, J., Hafliadason, H., Becker, L. W. M., Berndt, C., Rüpke, L., Planke, S., et al. (2018). Glacigenic Sedimentation Pulses Triggered post-glacial Gas Hydrate Dissociation. *Nat. Commun.* 9 (1), 635. doi:10.1038/s41467-018-03043-z
- Knies, J., Daszinnies, M., Plaza-Faverola, A., Chand, S., Sylta, Ø., Bünnz, S., et al. (2018). Modelling Persistent Methane Seepage Offshore Western Svalbard since Early Pleistocene. *Mar. Pet. Geology*. 91, 800–811. doi:10.1016/j.marpetgeo.2018.01.020
- Kvenvolden, K. A., Lorenson, T. D., and Reeburgh, W. S. (2001). Attention Turns to Naturally Occurring Methane Seepage. *Eos Trans. AGU* 82 (40), 457. doi:10.1029/01eo00275
- Liu, X., and Flemings, P. B. (2011). Capillary Effects on Hydrate Stability in marine Sediments. *J. Geophys. Res. Solid Earth* 116 (B7). doi:10.1029/2010jb008143
- Liu, Y., Tao, C., Liu, C., Qiu, L., Schlindwein, V., Zhang, H., et al. (2018). Seismic Activity Recorded by a Single OBS/H Near the Active Longqi Hydrothermal Vent at the Ultraslow Spreading Southwest Indian Ridge (49°39' E). *Mar. Georesources Geotechnology* 37 (2), 201–211. doi:10.1080/1064119x.2017.1420114
- Lopes, M. A., and Tenreiro Machado, J. (2017). Tidal Analysis Using Time-Frequency Signal Processing and Information Clustering. *Entropy* 19 (8). e19080390. doi:10.3390/e19080390
- Løviknes, S., Jensen, K. H., Krafft, B. A., Anthonypillai, V., and Nøttestad, L. (2021). Feeding Hotspots and Distribution of Fin and Humpback Whales in the Norwegian Sea from 2013 to 2018. *Front. Mar. Sci.* 8.
- Mau, S., Römer, M., Torres, M. E., Bussmann, I., Pape, T., Damm, E., et al. (2017). Widespread Methane Seepage along the continental Margin off Svalbard - from Bjørnøya to Kongsfjorden. *Sci. Rep.* 7, 42997. doi:10.1038/srep42997
- McDonald, M. A., Hildebrand, J. A., and Webb, S. C. (1995). Blue and Fin Whales Observed on a Seafloor Array in the Northeast Pacific. *J. Acoust. Soc. Am.* 98 (2 Pt 1), 712–721. doi:10.1121/1.153565
- McDonald, M. A., Mesnick, S. L., and Hildebrand, J. A. (2006). Biogeographic Characterization of Blue Whale Song Worldwide: Using Song to Identify Populations. *J. Cetacean Res. Manage.* 8 (1), 55–65.
- Meier, M., Schlindwein, V., Scholz, J. R., Geils, J., Schmidt-Aursch, M. C., and Kruger, F. (2021). Segment-Scale Seismicity of the Ultraslow Spreading Knipovich Ridge. *Geochem. Geophys. Geosystems* 22 (2), e2020GC009375. doi:10.1029/2020gc009375
- Mellinger, D. K., and Clark, C. W. (2003). Blue Whale (*Balaenoptera Musculus*) Sounds from the North Atlantic. *J. Acoust. Soc. America* 114 (2), 1108–1119. doi:10.1121/1.1593066
- Mishra, C. K., Dewangan, P., Sriram, G., Kumar, A., and Dakara, G. (2020). Spatial Distribution of Gas Hydrate Deposits in Krishna-Godavari Offshore basin, Bay of Bengal. *Mar. Pet. Geology*. 112. doi:10.1016/j.marpetgeo.2019.104037
- Monigle, P. W., Bohnenstiehl, D. R., Tolstoy, M., and Waldhauser, F. (2009). Seismic Tremor at the 9°50'N East Pacific Rise Eruption Site. *Geochem. Geophys. Geosystems* 10 (11). doi:10.1029/2009gc002561
- Morano, J. L., Salisbury, D. P., Rice, A. N., Conklin, K. L., Falk, K. L., and Clark, C. W. (2012). Seasonal and Geographical Patterns of Fin Whale Song in the Western North Atlantic Ocean. *J. Acoust. Soc. America* 132 (2), 1207–1212. doi:10.1121/1.4730890
- Ostrovsky, A. A. (1989). On the Nature of Microshocks Recorded by Ocean Bottom Seismographs. *Mar. Geophys. Res.* 11 (2), 113–118. doi:10.1007/bf00285662
- Ottesen, D., Dowdeswell, J. A., and Rise, L. (2005). Submarine Landforms and the Reconstruction of Fast-Flowing Ice Streams within a Large Quaternary Ice Sheet: The 2500-Km-Long Norwegian-Svalbard Margin (57°–80°N). *GSA Bull.* 117 (7–8), 1033–1050. doi:10.1130/b25577.1
- Panieri, G., Bünnz, S., Fornari, D. J., Escartin, J., Serov, P., Jansson, P., et al. (2017). An Integrated View of the Methane System in the Pockmarks at Vestnesa Ridge, 79°N. *Mar. Geology*. 390, 282–300. doi:10.1016/j.margeo.2017.06.006
- Pape, T., Bünnz, S., Hong, W. L., Torres, M. E., Riedel, M., and Panieri, G. (2020). Origin and Transformation of Light Hydrocarbons Ascending at an Active Pockmark on Vestnesa Ridge, Arctic Ocean. *J. Geophys. Res. Solid Earth* 125 (1). doi:10.1029/2018jb016679
- Petersen, C. J., Bünnz, S., Hustoft, S., Mienert, J., and Klaeschen, D. (2010). High-resolution P-Cable 3D Seismic Imaging of Gas Chimney Structures in Gas Hydrated Sediments of an Arctic Sediment Drift. *Mar. Pet. Geology*. 27 (9), 1981–1994. doi:10.1016/j.marpetgeo.2010.06.006
- Plant, J. N., Johnson, K. S., Fitzwater, S. E., Sakamoto, C. M., Coletti, L. J., and Jannasch, H. W. (2010). Tidally Oscillating Bisulfide Fluxes and Fluid Flow Rates Observed with *In Situ* Chemical Sensors at a Warm spring in Monterey Bay, California. *Deep Sea Res. Oceanographic Res. Pap.* 57 (12), 1585–1595. doi:10.1016/j.dsr.2010.10.001
- Plaza-Faverola, A., Bünnz, S., Johnson, J. E., Chand, S., Knies, J., Mienert, J., et al. (2015). Role of Tectonic Stress in Seepage Evolution along the Gas Hydrate-Charged Vestnesa Ridge, Fram Strait. *Geophys. Res. Lett.* 42 (3), 733–742. doi:10.1002/2014gl062474
- Plaza-Faverola, A., Bünnz, S., and Mienert, J. (2010). Fluid Distributions Inferred from P-Wave Velocity and Reflection Seismic Amplitude Anomalies beneath the Nyegga Pockmark Field of the Mid-Norwegian Margin. *Mar. Pet. Geology*. 27 (1), 46–60. doi:10.1016/j.marpetgeo.2009.07.007
- Plaza-Faverola, A., and Keiding, M. (2019). Correlation between Tectonic Stress Regimes and Methane Seepage on the Western Svalbard Margin. *Solid Earth* 10 (1), 79–94. doi:10.5194/se-10-79-2019
- Plaza-Faverola, A., Pecher, I., Crutchley, G., Barnes, P. M., Bünnz, S., Golding, T., et al. (2014). Submarine Gas Seepage in a Mixed Contractural and Shear Deformation Regime: Cases from the Hikurangi Oblique-Subduction Margin. *Geochem. Geophys. Geosyst.* 15 (2), 416–433. doi:10.1002/2013gc005082
- Plaza-Faverola, A., Vadakkupuliyambatta, S., Hong, W.-L., Mienert, J., Bünnz, S., Chand, S., et al. (2017). Bottom-simulating Reflector Dynamics at Arctic Thermogenic Gas Provinces: An Example from Vestnesa Ridge, Offshore West Svalbard. *J. Geophys. Res. Solid Earth* 122 (6), 4089–4105. doi:10.1002/2016jb013761
- Ramakrushana Reddy, T., Dewangan, P., Arya, L., Singha, P., and Raju, K. A. (2020). Tidal Triggering of the Harmonic Noise in Ocean-Bottom Seismometers. *Seismological Res. Lett.* 91 (2A), 803–813. doi:10.1785/0220190080
- Rice, A., Širović, A., Trickey, J. S., Debich, A. J., Gottlieb, R. S., and Wiggins, S. M. (2021). Cetacean Occurrence in the Gulf of Alaska from Long-Term Passive Acoustic Monitoring. *Mar. Biol.* 168 (5). doi:10.1007/s00227-021-03884-1
- Riedel, M., Scherwath, M., Römer, M., Veloso, M., Heesemann, M., and Spence, G. D. (2018). Distributed Natural Gas Venting Offshore along the Cascadia Margin. *Nat. Commun.* 9 (1), 3264. doi:10.1038/s41467-018-05736-x
- Ritzmann, O., Jokat, W., Czuba, W., Guterch, A., Mjelde, R., and Nishimura, Y. (2004). A Deep Seismic Transect from Hovgård Ridge to Northwestern Svalbard across the continental-ocean Transition: A Sheared Margin Study. *Geophys. J. Int.* 157 (2), 683–702. doi:10.1111/j.1365-246x.2004.02204.x
- Roman, D. C. (2017). Automated Detection and Characterization of Harmonic Tremor in Continuous Seismic Data. *Geophys. Res. Lett.* 44 (12), 6065–6073. doi:10.1002/2017gl073715
- Römer, M., Riedel, M., Scherwath, M., Heesemann, M., and Spence, G. D. (2016). Tidally Controlled Gas Bubble Emissions: A Comprehensive Study Using Long-Term Monitoring Data from the NEPTUNE Cabled Observatory Offshore Vancouver Island. *Geochem. Geophys. Geosyst.* 17 (9), 3797–3814. doi:10.1002/2016gc006528
- Römer, M., Torres, M., Kasten, S., Kuhn, G., Graham, A. G. C., Mau, S., et al. (2014). First Evidence of Widespread Active Methane Seepage in the Southern Ocean, off the Sub-antarctic Island of South Georgia. *Earth Planet. Sci. Lett.* 403, 166–177. doi:10.1016/j.epsl.2014.06.036

- Schindwein, V., Demuth, A., Geissler, W. H., and Jokat, W. (2013). Seismic gap beneath Logachev Seamount: Indicator for Melt Focusing at an Ultralow Mid-ocean ridge? *Geophys. Res. Lett.* 40 (9), 1703–1707. doi:10.1002/grl.50329
- Schneider, A., Panieri, G., Lepland, A., Consolaro, C., Crémère, A., Forwick, M., et al. (2018). Methane Seepage at Vestnesa Ridge (NW Svalbard) since the Last Glacial Maximum. *Quat. Sci. Rev.* 193, 98–117. doi:10.1016/j.quascirev.2018.06.006
- Schultz, A., Delaney, J. R., and McDuff, R. E. (1992). On the Partitioning of Heat Flux between Diffuse and point Source Seafloor Venting. *J. Geophys. Res.* 97 (B9). doi:10.1029/92jb00889
- Sgroi, T., Monna, S., Embriaco, D., Giovanetti, G., Marinaro, G., and Favali, P. (2014). Geohazards in the Western Ionian Sea: Insights from Non-earthquake Signals Recorded by the NEMO-SN1 Seafloor Observatory. *Oceanog* 27 (2), 154–166. doi:10.5670/oceanog.2014.51
- Sgroi, T., Polonia, A., Beranzoli, L., Billi, A., Bosman, A., Costanza, A., et al. (2021). One Year of Seismicity Recorded through Ocean Bottom Seismometers Illuminates Active Tectonic Structures in the Ionian Sea (Central Mediterranean). *Front. Earth Sci.* 9, 643. doi:10.3389/feart.2021.661311
- Shipley, T. H., Houston, M. H., Buffler, R. T., Shaub, F. J., McMillen, K. J., Laod, J. W., et al. (1979). Seismic Evidence for Widespread Possible Gas Hydrate Horizons on Continental Slopes and Rises. *AAPG Bull.* 63 (12), 2204–2213. doi:10.1306/2f91890a-16ce-11d7-8645000102c1865d
- Singhroha, S., Bünz, S., Plaza-Faverola, A., and Chand, S. (2020). Detection of Gas Hydrates in Faults Using Azimuthal Seismic Velocity Analysis, Vestnesa Ridge, W-Svalbard Margin. *J. Geophys. Res. Solid Earth* 125 (2). doi:10.1029/2019jb017949
- Singhroha, S., Bünz, S., Plaza-Faverola, A., and Chand, S. (2016). Gas Hydrate and Free Gas Detection Using Seismic Quality Factor Estimates from High-Resolution P-cable 3D Seismic Data. *Interpretation* 4 (1), SA39–SA54. doi:10.1190/int-2015-0023.1
- Singhroha, S., Chand, S., and Bünz, S. (2019). Constraints on Gas Hydrate Distribution and Morphology in Vestnesa Ridge, Western Svalbard Margin, Using Multicomponent Ocean-Bottom Seismic Data. *J. Geophys. Res. Solid Earth* 124 (5), 4343–4364. doi:10.1029/2018jb016574
- Smith, A. J., Mienert, J., Bünz, S., and Greinert, J. (2014). Thermogenic Methane Injection via Bubble Transport into the Upper Arctic Ocean from the Hydrate-Charged Vestnesa Ridge, Svalbard. *Geochem. Geophys. Geosyst.* 15 (5), 1945–1959. doi:10.1002/2013gc005179
- Sohn, R. A., Hildebrand, J. A., Webb, S. C., and Fox, C. G. (1995). Hydrothermal microseismicity at the megaplume site on the southern Juan de Fuca Ridge. *Bull. Seismological Soc. America* 85 (3), 775–786.
- Soule, D. C., and Wilcock, W. S. D. (2013). Fin whale tracks recorded by a seismic network on the Juan de Fuca Ridge, Northeast Pacific Ocean. *J. Acoust. Soc. America* 133 (3), 1751–1761. doi:10.1121/1.4774275
- Stähler, S. C., Schmidt-Aursch, M. C., Hein, G., and Mars, R. (2018). A Self-Noise Model for the German DEPAS OBS Pool. *Seismological Res. Lett.* 89 (5), 1838–1845. doi:10.1785/0220180056
- Storrie, L., Lydersen, C., Andersen, M., Wynn, R. B., and Kovacs, K. M. (2018). Determining the Species Assemblage and Habitat Use of Cetaceans in the Svalbard Archipelago, Based on Observations from 2002 to 2014. *Polar Res.* 37 (1). doi:10.1080/17518369.2018.1463065
- Sultan, N., Plaza-Faverola, A., Vadakkepuliambatta, S., Buenz, S., and Knies, J. (2020). Impact of Tides and Sea-Level on Deep-Sea Arctic Methane Emissions. *Nat. Commun.* 11 (1), 5087. doi:10.1038/s41467-020-18899-3
- Sultan, N., Riboulot, V., Ker, S., Marsset, B., Géli, L., and Tary, J. B. (2011). Dynamics of Fault-Fluid-Hydrate System Around a Shale-Cored Anticline in deepwater Nigeria. *J. Geophys. Res.* 116 (B12). doi:10.1029/2011jb008218
- Sun, R., and Duan, Z. (2007). An Accurate Model to Predict the Thermodynamic Stability of Methane Hydrate and Methane Solubility in marine Environments. *Chem. Geology*. 244 (1–2), 248–262. doi:10.1016/j.chemgeo.2007.06.021
- Sutterley, T. C., Markus, T., Neumann, T. A., van den Broeke, M., van Wessem, J. M., and Ligtenberg, S. R. M. (2019). Antarctic Ice Shelf Thickness Change from Multisensor Lidar Mapping. *The Cryosphere* 13 (7), 1801–1817. doi:10.5194/tc-13-1801-2019
- Sutton, G. H., McDonald, W. G., Prentiss, D. D., and Thanos, S. N. (1965). Ocean-bottom Seismic Observatories. *Proc. IEEE* 53 (12), 1909–1921. doi:10.1109/proc.1965.4468
- Tary, J. B., Géli, L., Guennou, C., Henry, P., Sultan, N., Çağatay, N., et al. (2012). Microevents Produced by Gas Migration and Expulsion at the Seabed: a Study Based on Sea Bottom Recordings from the Sea of Marmara. *Geophys. J. Int.* 190 (2), 993–1007. doi:10.1111/j.1365-246x.2012.05533.x
- Taylor, M. H., Dillon, W. P., and Pecher, I. A. (2000). Trapping and Migration of Methane Associated with the Gas Hydrate Stability Zone at the Blake Ridge Diapir: New Insights from Seismic Data. *Mar. Geology*. 164 (1), 79–89. doi:10.1016/s0025-3227(99)00128-0
- Thomsen, L., Barnes, C., Best, M., Chapman, R., Pirenne, B., Thomson, R., et al. (2012). Ocean Circulation Promotes Methane Release from Gas Hydrate Outcrops at the NEPTUNE Canada Barkley Canyon Node. *Geophys. Res. Lett.* 39 (16). doi:10.1029/2012gl052462
- Tishchenko, P., Hensen, C., Wallmann, K., and Wong, C. S. (2005). Calculation of the Stability and Solubility of Methane Hydrate in Seawater. *Chem. Geology*. 219 (1–4), 37–52. doi:10.1016/j.chemgeo.2005.02.008
- Torres, M. E., McManus, J., Hammond, D., De Angelis, M., Heeschen, K., and Colbert, S. (2002). Fluid and Chemical Fluxes in and Out of Sediments Hosting Methane Hydrate Deposits on Hydrate Ridge, OR, I: Hydrological Provinces. *Earth Planet. Sci. Lett.* 201 (3–4), 525–540. doi:10.1016/s0012-821x(02)00733-1
- Tsang-Hin-Sun, E., Batsi, E., Klingelhoefer, F., and Géli, L. (2019). Spatial and Temporal Dynamics of Gas-Related Processes in the Sea of Marmara Monitored with Ocean Bottom Seismometers. *Geophys. J. Int.* 216 (3), 1989–2003. doi:10.1093/gji/ggy535
- Ugalde, A., Gaité, B., Ruiz, M., Villaseñor, A., and Ranero, C. R. (2019). Seismicity and Noise Recorded by Passive Seismic Monitoring of Drilling Operations Offshore the Eastern Canary Islands. *Seismological Res. Lett.* doi:10.1785/0220180353
- Veloso, M., Greinert, J., Mienert, J., and De Batist, M. (2015). A New Methodology for Quantifying Bubble Flow Rates in Deep Water Using Splitbeam Echosounders: Examples from the Arctic Offshore NW- S Valbard. *Limnol. Oceanogr. Methods* 13 (6), 267–287. doi:10.1002/lom3.10024
- Veloso-Alarcon, M. E., Janson, P., De Batist, M., Minshull, T. A., Westbrook, G. K., and Palikes, H. (2019). Variability of Acoustically Evidenced Methane Bubble Emissions Offshore Western Svalbard. *Geophys. Res. Lett.* 46 (15), 9072–9081.
- Vogt, P. R., and Crane, K. (1994). Methane-generated () Pockmarks on Young, Thickly Sedimented Oceanic Crust in the Arctic. Vestnesa ridge, Fram Strait. *Geology* 22 (3). doi:10.1130/0091-7613(1994)022<0255:mgpoyt>2.3.co;2
- Wallmann, K., Riedel, M., Hong, W. L., Patton, H., Hubbard, A., Pape, T., et al. (2018). Gas Hydrate Dissociation off Svalbard Induced by Isostatic Rebound rather Than Global Warming. *Nat. Commun.* 9 (1), 83. doi:10.1038/s41467-017-02550-9
- Webb, S. C. (1998). Broadband Seismology and Noise under the Ocean. *Rev. Geophys.* 36 (1), 105–142. doi:10.1029/97rg02287
- Wessel, P., Luis, J. F., Uieda, L., Scharroo, R., Wobbe, F., Smith, W. H. F., et al. (2019). The Generic Mapping Tools Version 6. *Geochem. Geophys. Geosyst.* 20, 5556–5564. doi:10.1029/2019gc008515
- Wilks, D. S. (2011). *Statistical Methods in the Atmospheric Sciences (Vol. 100)*. San Diego, CA: Academic Press.

Conflict of Interest: The authors declare that the research was conducted in the absence of any commercial or financial relationships that could be construed as a potential conflict of interest.

Publisher's Note: All claims expressed in this article are solely those of the authors and do not necessarily represent those of their affiliated organizations, or those of the publisher, the editors and the reviewers. Any product that may be evaluated in this article, or claim that may be made by its manufacturer, is not guaranteed or endorsed by the publisher.

Copyright © 2022 Domel, Singhroha, Plaza-Faverola, Schindwein, Ramachandran and Bünz. This is an open-access article distributed under the terms of the Creative Commons Attribution License (CC BY). The use, distribution or reproduction in other forums is permitted, provided the original author(s) and the copyright owner(s) are credited and that the original publication in this journal is cited, in accordance with accepted academic practice. No use, distribution or reproduction is permitted which does not comply with these terms.

APPENDIX A CROSS-CORRELATION

For two N-element equal-interval (1 h) time series $SDE(t) = \{SDE(t_n)\}$ and $Tide(t) = \{Tide(t_n)\}$ with the lag value k such as $-\max_lag \leq k \leq \max_lag$, lagged cross-correlation coefficient (Pearson product-moment coefficient of linear correlation) is given by (Crockett, 2019):

$$R_{xy}(k) = \frac{cov(SDE_k, Tide_k)}{\sigma(SDE_k) \sigma(Tide_k)}$$

where the covariance and standard deviations (σ) apply to the segments SDE_k and $Tide_k$ that overlap at lag k and $-1 \leq R_{xy}(k) \leq 1$. Covariance (joint variance) between two N-element

discrete variables $SDE(n) = \{SDE_n\}$ and $Tide(n) = \{Tide_n\}$, where $n = 0, 1, \dots, N-1$ is defined as:

$$cov(SDE, Tide) = \frac{1}{N} \sum_{n=0}^{N-1} (SDE_n - \overline{SDE})(Tide_n - \overline{Tide})$$

where \overline{SDE} , \overline{Tide} are arithmetic means of normalized SDEs counts and normalized tidal height values, respectively. Lastly, the standard deviation of discrete variable $SDE(n)$ is defined as (definition for $Tide$ is analogous):

$$\sigma(SDE) = \sqrt{\frac{1}{N} \sum_{i=1}^N (SDE_i - \overline{SDE})^2}$$

Article 2

Event recognition in marine seismological data using Random Forest machine learning classifier

Przemyslaw Domel¹, Clément Hibert², Vera Schlindwein^{3,4} and Andrea Plaza-Faverola¹

¹*Department of Geosciences, UiT The Arctic University of Norway, Dramsvegen 201, 9010 Tromsø, Norway. E-mail: przemyslaw.domel@uit.no*

²*ITES/Institut Terre et Environnement de Strasbourg, CNRS UMR7063 CNRS – Université de Strasbourg, 5 rue Descartes, F-67084 Strasbourg, France*

³*Alfred Wegener Institute, Helmholtz Centre for Polar and Marine Research, Am Alten Hafen 26, 27568 Bremerhaven, Germany*

⁴*Faculty of Geosciences, University of Bremen, Klagenfurter Straße 2-4, 28359 Bremen, Germany*

Accepted 2023 June 9. Received 2023 June 5; in original form 2023 February 20

SUMMARY

Automatic detection of seismic events in ocean bottom seismometer (OBS) data is difficult due to elevated levels of noise compared to the recordings from land. Popular deep-learning approaches that work well with earthquakes recorded on land perform poorly in a marine setting. Their adaptation to OBS data requires catalogues containing hundreds of thousands of labelled event examples that currently do not exist, especially for signals different than earthquakes. Therefore, the usual routine involves standard amplitude-based detection methods and manual processing to obtain events of interest. We present here the first attempt to utilize a Random Forest supervised machine learning classifier on marine seismological data to automate catalogue screening and event recognition among different signals [i.e. earthquakes, short duration events (SDE) and marine noise sources]. The detection approach uses the short-term average/long-term average method, enhanced by a kurtosis-based picker for a more precise recognition of the onset of events. The subsequent machine learning method uses a previously published set of signal features (waveform-, frequency- and spectrum-based), applied successfully in recognition of different classes of events in land seismological data. Our workflow uses a small subset of manually selected signals for the initial training procedure and we then iteratively evaluate and refine the model using subsequent OBS stations within one single deployment in the eastern Fram Strait, between Greenland and Svalbard. We find that the used set of features is well suited for the discrimination of different classes of events during the training step. During the manual verification of the automatic detection results, we find that the produced catalogue of earthquakes contains a large number of noise examples, but almost all events of interest are properly captured. By providing increasingly larger sets of noise examples we see an improvement in the quality of the obtained catalogues. Our final model reaches an average accuracy of 87 per cent in recognition between the classes, comparable to classification results for data from land. We find that, from the used set of features, the most important in separating the different classes of events are related to the kurtosis of the envelope of the signal in different frequencies, the frequency with the highest energy and overall signal duration. We illustrate the implementation of the approach by using the temporal and spatial distribution of SDEs as a case study. We used recordings from six OBSs deployed between 2019 and 2020 off the west-Svalbard coast to investigate the potential link of SDEs to fluid dynamics and discuss the robustness of the approach by analysing SDE intensity, periodicity and distance to seepage sites in relation to other published studies on SDEs.

Key words: Machine learning; Arctic region; Computational seismology; Seismic noise; Wave propagation; Time-series analysis.

1 INTRODUCTION

Detecting seismicity in ocean bottom seismometer (OBS) data has additional challenges when compared to the seismicity recorded on land. In a marine setting a wide range of signals not encountered on land is present (e.g. ship noise, mammal calls and ocean current tremor). In addition, the general level of ambient noise is much higher. In the low frequency band (0.05–0.1 Hz), persistent signals are related to Rayleigh waves created by ocean surface waves interacting with both shallow and deep ocean floor (primary and secondary micro seismic peak, e.g. Sutton *et al.* 1965; Barstow *et al.* 1989; Hilmo & Wilcock 2020). In the higher frequency band (above 1 Hz), noise can be generated by underwater currents (e.g. Stähler *et al.* 2018; Ramakrushana Reddy *et al.* 2020; Essing *et al.* 2021), marine mammals vocalizations (e.g. McDonald *et al.* 1995; Soule & Wilcock 2013; Løviknes *et al.* 2021), active seismic exploration and marine traffic, especially on shipping routes (Hildebrand 2009). Spurious signals caused by electronic malfunction, mass centring and tilt correction for broadband sensors also generate unwanted signals on the seismogram (Sutton & Latham 1964).

Additionally, there is a type of signal reported from OBS data that often outnumber the recorded earthquakes by a large margin. These signals consist of a short duration, high amplitude pulses with no discernible seismic phases and have been referred in literature as short duration events (SDE). Some studies associate SDEs with fluid migration and sedimentary fracturing processes in shallow sediments (e.g. Tary *et al.* 2012; Hsu *et al.* 2013; Batsi *et al.* 2019). However, what exactly is at the origin of SDEs remains a matter of debate (Tary *et al.* 2012). An interesting observation comes from the review of the currently available SDE studies, namely the ubiquitous use of either manual picking or classical short-term/long-term average (STA/LTA) ratio described by Allen in 1982 (e.g. Buskirk *et al.* 1981; Sohn *et al.* 1995; Díaz *et al.* 2007; Embriaco *et al.* 2014; Franek *et al.* 2014; Ugalde *et al.* 2019; Sgroi *et al.* 2021).

The problem of microseismicity detection has been studied in great detail over several decades and the non-exhaustive list includes methods based on: energy-ratios (e.g. Allen 1982; Baer & Kradolfer 1987), autoregression modelling (e.g. Sleeman & van Eck 1999), statistical parameters of the signal (e.g. Saragiotis *et al.* 2004; Baillard *et al.* 2013), fuzzy logic theory (e.g. Chu & Mendel 1994), shallow neural networks (e.g. McCormack *et al.* 1993; Gentili, & Michelini 2006), cross correlation (e.g. Molyneux & Schmitt 1999; De Meersman *et al.* 2009) wavelet transforms (e.g. Anant & Dowla 1997; Bogiatzis, & Ishii 2015; Mousavi *et al.* 2016) or combinations of methods (e.g. Gelchinsky & Shtivelman 1983; Diehl *et al.* 2009; Nippres *et al.* 2010). Many of these approaches are sensitive to the high noise level which is a case for a marine setting (Withers *et al.* 1998; Mousavi *et al.* 2016; Guan & Niu 2017). Other, such as polarity analysis (e.g. Vidale 1986; Jurkevics 1988), rely on the knowledge of the horizontal component geographical orientation which not always can be established for OBS data. Network based methods cannot be deployed to systematically detect SDEs since their signal is typically seen only locally on individual stations and not across a network. Impulsive nature of the SDEs makes the detection using relatively simple STA/LTA possible and justified in the past studies, however the detector itself does not allow to separate SDEs from other signal sources. Constructing reliable event catalogues that discriminate between earthquakes and SDEs from STA/LTA alone is challenging and require manual verification of the entire data set or specific time intervals of interest (e.g. Meier

et al. 2021; Jeddi *et al.* 2021; Domel *et al.* 2022). The need of reducing the amount of manual processing makes SDEs an interesting case study for the classification problem now commonly addressed by the use of machine learning.

Recent years led to a rapid development of the earthquake detection and phase picking methods based on deep learning (e.g. Mousavi *et al.* 2020; Ross *et al.* 2018a, b; Zhu & Beroza 2018). Many of these methods rely on the training of the corresponding models using very large databases (thousands of examples and more) of manually curated earthquakes. Several such models exist for land recordings (e.g. Münchmeyer *et al.* 2022a), and in some scenarios they can be applied to OBS data without retraining (Chen *et al.* 2022). However, differences in the noise sources and levels can lead to a poor performance of the land-based earthquake detectors in marine records (we demonstrate the performance of popular machine learning models on our data in the text S1 in the electronic supplement).

When it comes to the recognition of other signals, such as SDEs, the detection and classification problem remains underdeveloped. STA/LTA method can be fine-tuned to detect SDEs but still either misses signals at high detection thresholds or contains false detections upon sensitive tuning due to the abundance of stochastically varying over time noise in marine settings (e.g. Tary *et al.* 2012; Batsi *et al.* 2019; Ugalde *et al.* 2019; Domel *et al.* 2022). The number of false detections in the catalogues created with this approach can outnumber the signal of interest by orders of magnitude and require time-consuming quality control, which is simply not feasible for large data sets. Previously described machine learning based approaches could not be used yet for SDE detection, as no large enough, curated SDE catalogues exist for model training. Models specifically trained for earthquake detection consider SDEs as a noise and do not trigger on them (see electronic supplement). Moreover, a careful comparison between the signals from different data sets would need to be made to properly define the common characteristics of SDEs that still can vary in between the publications.

Supervised machine learning-driven approaches based on the Random Forest classifier (Breiman 2001) have shown over the years to be highly efficient in the recognition of different types of signals, ranging from earthquakes to volcanic tremors, avalanches, and landslides (e.g. Hibert *et al.* 2017, 2019; Provost *et al.* 2017; Chmiel *et al.* 2021; Wenner *et al.* 2021). These methods usually rely on curated databases of events to extract the necessary amount of information that would allow the separation between distinct categories of signals. Compared to the mentioned deep learning approaches, Random Forest can provide similar or even better results with dozens to hundreds of examples to train from per signal type (Hibert *et al.* 2017, 2019; Provost *et al.* 2017). This makes it well suited to microseismic studies, where there is a need of recognizing new signals with a limited set of examples to train from. It is also shown to work well in finding rare events of interests in very large data sets dominated by noise or superfluous signals (Wenner *et al.* 2021). To our knowledge, Random Forest has not yet been tested in marine seismological records.

Here, we propose a new approach based on the Random Forest supervised machine learning algorithm that reduces the amount of data processing and manual verification needed compared to manual screening of STA/LTA detections. The aim of the study is to test whether the method introduced in Provost *et al.* (2017) and Hibert *et al.* (2017), for rockfalls, landslides and volcanic earthquakes on land is suitable for classifying earthquakes, SDEs and noise present in marine seismograms. We use data from six OBSs deployed in 2019 to study microseismicity and seafloor seepage off the west

coast of Svalbard (Bünz 2023a). We show the initial training process for a new data set that relies on preparation of a small number of manual examples. We study the trained model performance on one station and subsequently progress with the data processing on other OBSs, extending the training data set to properly accommodate the variation of observed noisy signals. We discuss the observed variation in the method performance and provide the metrics of the classification accuracy where feasible. Finally, we demonstrate the method validity by using the trained model to obtain a catalogue of SDEs on all OBS stations and briefly discuss their periodicity, intensity and potential link to the gas seepage sites in the area.

2 DATA

2.1 Deployment

As part of a study on seafloor seepage dynamics off the west coast of Svalbard (Bünz 2023a), we deployed seven long-term OBSs along the length of Vestnesa Ridge (Fig. 1) to monitor potential micro seismicity. We positioned most devices within an area of a known, active methane seepage on the ridge crest (OBS25-29), with two seismometers located further away: one of them at the ridge bend separating western and eastern part of Vestnesa ridge (OBS-24) and another at the south-eastern termination of the structure (OBS-30). Three of them (OBS25, 28 and 29) surrounded a seabed pockmark broadly investigated due to repeated methane release observations in the water column (e.g. Panieri *et al.* 2017; Himmler *et al.* 2019). Stations in the pockmark area were separated by 800–900 m (around the pockmark), up to 2–2.5 km (OBS-26 and OBS-27). The distance between OBS-24 and the closest station (OBS-26) was 14.8 km, and for station OBS-30, the distance from OBS-29 was 18.3 km (Fig. 1). The experiment began in early July 2019 and ended with the successful recovery of all instruments in August 2020 (Bünz 2023b).

Deployment by free fall took place from H/V Helmer Hanssen at water depths of roughly 1200 m (Table 1). To establish their true location on the seafloor, we conducted an active source seismic experiment, acquiring several seismic lines within the area. Most of the OBSs drifted in either NW or NE direction with an average horizontal drift of 223 m.

Each OBS recorded seismicity using a short-period three-channel geophone with a corner frequency of 4.5 Hz. Two types of recorders were used: KUM ‘6d6’ for OBS-24 and OBS-25, and Geomar ‘Geolog’ for the remaining instruments. We set the sampling frequency to 250 Hz for OBS-24 and OBS-25.

OBS-24 and OBS-25 recorded a full year of data until July 2020 (Table 1). However, we encountered several problems with the data on other stations. OBS-29 stopped recording after one day of deployment. The data on OBS-26, OBS-27, OBS-28 and OBS-30 was sampled erroneously at 500 Hz due to an internal error, leading to a much quicker storage use and shorter duration of the recording. For OBS-26, OBS-27 and OBS-30 this led to a stop of the record approximately 3 months after the deployment (4–7.10.2019). We had equipped OBS-28 with a twice as big memory card (128 GB), therefore its recording lasted roughly twice as long, until middle of January 2020.

2.2 Most frequently observed event types

Earthquakes

Most of the seismicity in the area comes from the nearby oceanic ridges (Fig. 1, inset). The earthquakes originating from there have most of their energy in the frequency range below 10–15 Hz and have a P–S phase separation of >8 s for our station positions (Fig. 2a). Their duration is relatively short (30–60 s on average) and there is often a *T*-wave train visible in the data.

SDEs

Short duration events in this data set are characterized by a single, strong impulse with energy from 5 Hz up to 25 Hz and more (Fig. 2b). P and S phases cannot be recognized. Most of the SDE events last about 1–2 s. They occur in groups of several SDEs or as single events (Fig. 2b). Their relative amplitude can be stronger than even the largest of local earthquakes. Unlike earthquakes, they are visible mostly only on the vertical channel of the geophone. Only for the stronger ones, we see energy on horizontal components and even hydrophone records in some cases.

Undesired signals

In an underwater setting, it is difficult to list all the possible types of noise present. The most prevalent one in our case, is most likely related to current-induced instrument shaking and is referred to as harmonic tremor (Fig 2c; Stähler *et al.* 2018; Ramakrushana Reddy *et al.* 2020; Essing *et al.* 2021). We consider this type of signal as a noise occurring in repeating patterns lasting up to several hours. Even though it is usually less prominent from the background noise than other signals, individual wave ‘packets’ can easily exceed the amplitude threshold in the STA/LTA detector. Unlike earthquakes and SDEs, tremors are not observed in hydrophone data. This type of noise is likely the largest factor in lowering the number of earthquake records (both visible and detected) on different OBSs in this study.

In addition to this signal, different high-amplitude events can be included in the noise category. Some of them are related to instrumentation problems, others to marine mammals, seismic acquisition or marine traffic and some do not have an explanation and may simply be stochastic in nature. For the purposes of the study, we do not make a specific differentiation between different origins of the noise and do not try to make different subcategories of it.

3 METHODS

3.1 Detection and extraction of signals for classification

We are interested in separating local earthquakes from SDEs and different types of noise present in the data set. We aim to improve and build upon the classically used search routine based on the STA/LTA detector (Allen 1982). We do it by using STA/LTA as a tool to extract time slices from continuous data and then assign them to different classes of events based on their signal characteristics. To account for differences between SDEs and earthquakes, we used STA/LTA detector twice and adjusted the parameters to improve its sensitivity to SDEs (short, abrupt signals) and earthquakes (long, more emergent signals). Even with finely tuned settings, the STA/LTA detector will trigger on noise and other sources of signal, and in a typical processing workflow, events of interest have to be manually extracted. We down sampled all data sets to 50 Hz to equalize the data from different stations. We used an STA window

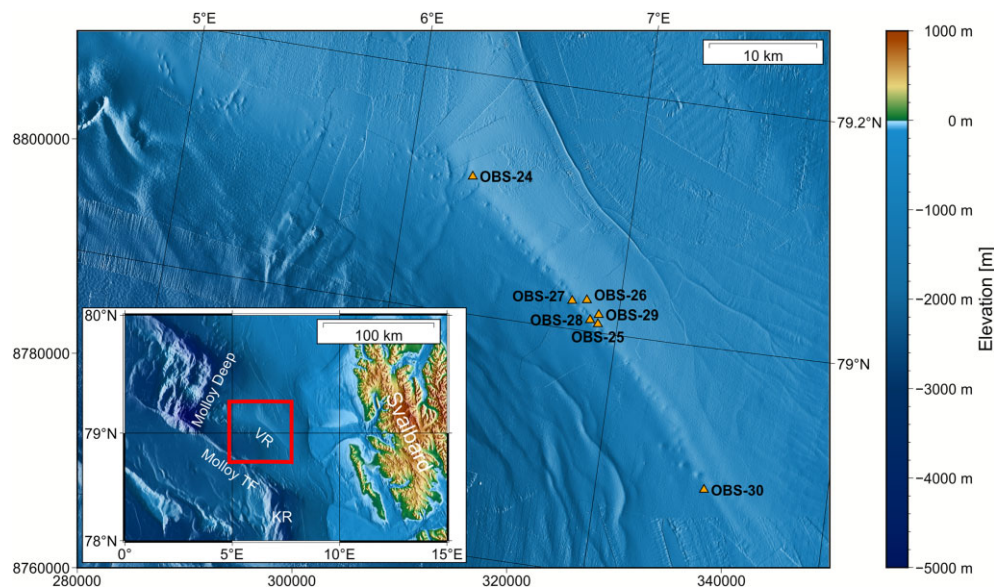


Figure 1. Map of the study area and location of the instrumentation. The triangles represent true ocean bottom seismometer (OBS) positions (after relocation) deployed at Vestnesa Ridge. Inset: Overview map of the Fram Strait with location of Vestnesa Ridge, off the west Svalbard margin and major tectonic features labelled. Regional bathymetry from the IBCAO (International Bathymetric Chart of the Arctic Ocean) (Jakobsson *et al.* 2020), see Data Availability. VR-Vestnesa Ridge; Molloy TF-Molloy Transform Fault; KR- Knipovich Ridge.

Table 1. Overview of all the stations in the experiment, with their calculated position at the sea bottom, respective water depth, duration of the recording, sampling frequency and drift (difference between the calculated and deployed location) with its direction.

Station	Longitude [°E]	Latitude [°N]	Water depth [m]	Data record start [dd/mm/yyyy]	Data record end [yyyy/mm/dd]	Sampling frequency [Hz]	Drift [m]/direction
OBS-24	6.2790	79.1141	1243	07/07/2019	09/07/2020	250	202/NE
OBS-25	6.9153	79.0073	1207	07/07/2019	09/07/2020	250	271/NW
OBS-26	6.8532	79.0258	1230	07/07/2019	07/10/2019	500	286/NW
OBS-27	6.7899	79.0236	1210	07/07/2019	07/10/2019	500	238/NW
OBS-28	6.8790	79.0097	1203	07/07/2019	19/01/2020	500	226/NW
OBS-29	6.9134	79.0150	1223	07/07/2019	08/07/2019	500	238/NW
OBS-30	7.4681	78.8821	1135	07/07/2019	04/10/2019	500	101/SW

length of 0.8 s with an LTA window length of 45 s for earthquakes, and an STA window length of 0.35 s with an LTA window length of 8 s for SDEs. With the STA/LTA detection ratio set at 7, we ran the detector on the 1 Hz high pass filtered vertical channels of the geophones. Each detection was set to end at the ratio of 1.5 (Fig. 3b). We selected the lowest possible value of the trigger threshold that would not lead to continuous detections of the noise of the data set. In the earthquake-adjusted search, we removed all the detections with a duration shorter than 4 s (value determined empirically, Fig 3a). Conversely, for the SDE-adjusted search, we only kept the detections shorter than or equal to 4 s. Additionally in earthquake-adjusted search, to reduce the number of separate detections of P and S phases from the same earthquake we merged the detections that were less than 10 s from each other. We also used a kurtosis-based picker (Baillard *et al.* 2014; Hibert *et al.* 2014) to automatically improve the initial onset of all earthquakes found in this run. This method relies on the fact that while random noise and seismic signal have, statistically speaking, a normal amplitude distribution, the change between them does not. By computing a characteristic function based on the kurtosis (4th moment) of the signal provided by Baillard *et al.* (2014), the onset of the event can be found. We computed the function in several sliding windows for

different frequency ranges and then determined the onset from the sum of all functions. We used the sliding windows of 1, 2, 3 and 5 s, and computed characteristic functions in the frequency bands of: 1–5 Hz, 5–10 Hz, 10–20 Hz and 20–25 Hz. In our case, the picker was used on a window from -10 to $+1$ s relative to original pick (window range determined by trial and error; Fig. 3c). In the test we noted that the detection of many earthquakes ended too abruptly, hence for each detection, we also calculated a new end time based on a mean signal amplitude in the window from the start of STA/LTA detection to 60 s after the pick. When the amplitude of the current sample dropped below 1.5 of this mean amplitude (for samples after initial detection end), we shifted the end time to this position (Fig. 3d). As the final step, we merged the detections from earthquake-adjusted and SDE-adjusted runs and kept only one copy of the detection in the case of overlapping. We subsequently used the created catalogue to cut the windows around the signals in question and use them as an input to the subsequent classification.

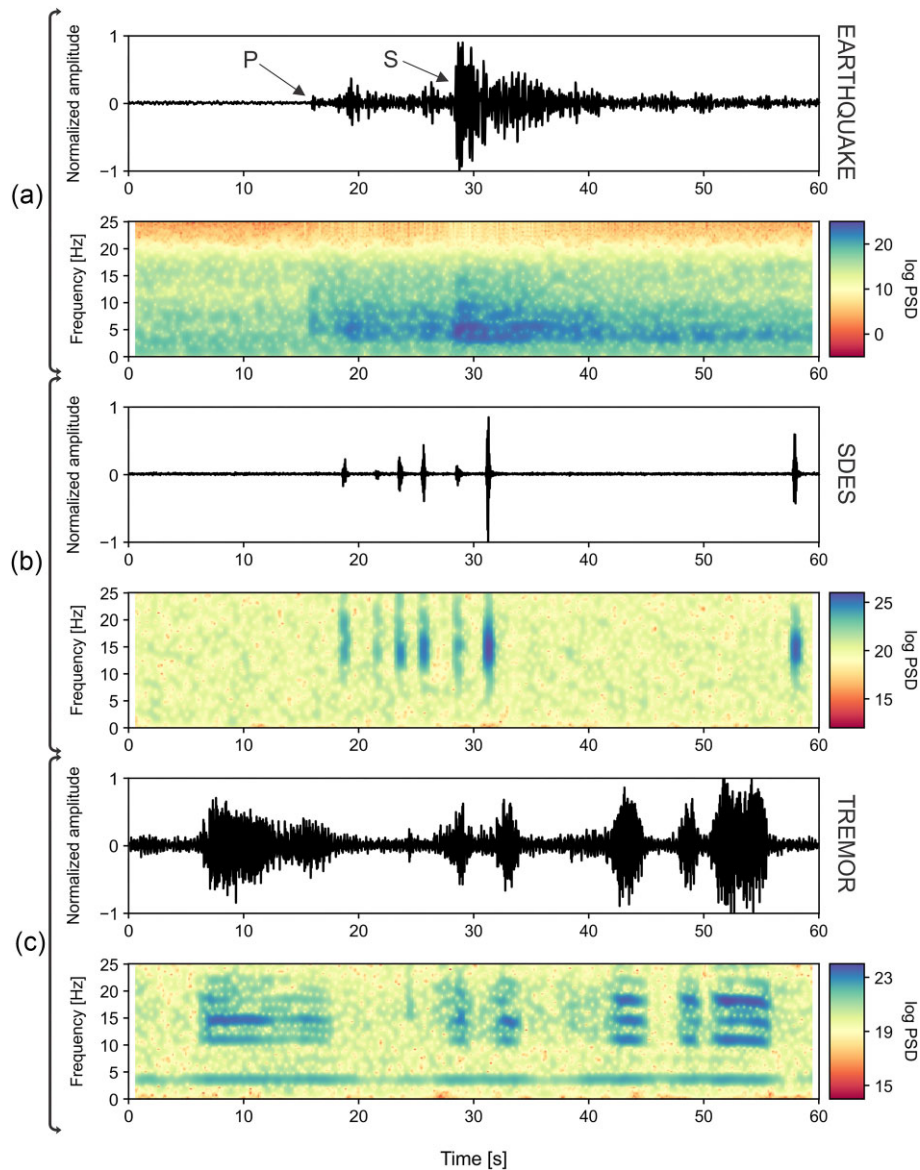


Figure 2. Examples of distinct types of events present in data belonging to different classes used in the machine learning classification approach with their corresponding spectrograms (window length: 1 s, overlap 90 per cent, Hanning taper). All examples from the vertical channel of a geophone. (a) Local ridge earthquake. (b) SDEs. (c) Harmonic tremor.

3.2 Random forest and seismic signal features

After extraction of each example, we use the Random Forest algorithm to differentiate between events of interest and noises. The implementation is provided by the scikit-learn python library (Pedregosa *et al.* 2011). This approach is based on computing a large number (1000 in our case) of decision trees, where each decision tree takes a random subset of parameters used in training to conduct a vote assigning an event to a class (Breiman 2001). Based on the majority of votes from all trees, the final decision of the outcome class of event is made. We specifically use the approach previously applied successfully to classify environmental sources (Hibert *et al.* 2017; Provost *et al.* 2017; Chmiel *et al.* 2021; Wenner *et al.* 2021) and volcanic seismicity (Hibert *et al.* 2014; Maggi *et al.* 2017; Malfante *et al.* 2018; Falcin *et al.* 2021). With the exception of the number of trees used, we retain the default parameters of the method provided by scikit-learn (see electronic supplement).

We trained a model with a purpose of recognizing three classes: EQ (earthquakes), SDE and NOISE.

Supervised machine learning algorithms such as the Random Forest require that each event is described by the same features. To do so, we transform each seismic signal in the data set into an array of curated features that are designed to extract information that is similar to what human operators use in distinguishing between different classes of seismic sources. For the features used as an input for the training, we provided 24 waveform-based features, 17 related to the frequency content and 17 pseudo-spectrogram features calculated for single channel data, plus four parameters related to the polarity computed from all three channels. We followed the approach and features proposed by Provost *et al.* (2017) (excluding the network-based features included there). We worked on the signals filtered down to 50 Hz sampling rate (Nyquist frequency of 25 Hz) and we modified the frequency windows used to calculate the parameters accordingly. Instead of calculating the features only on the

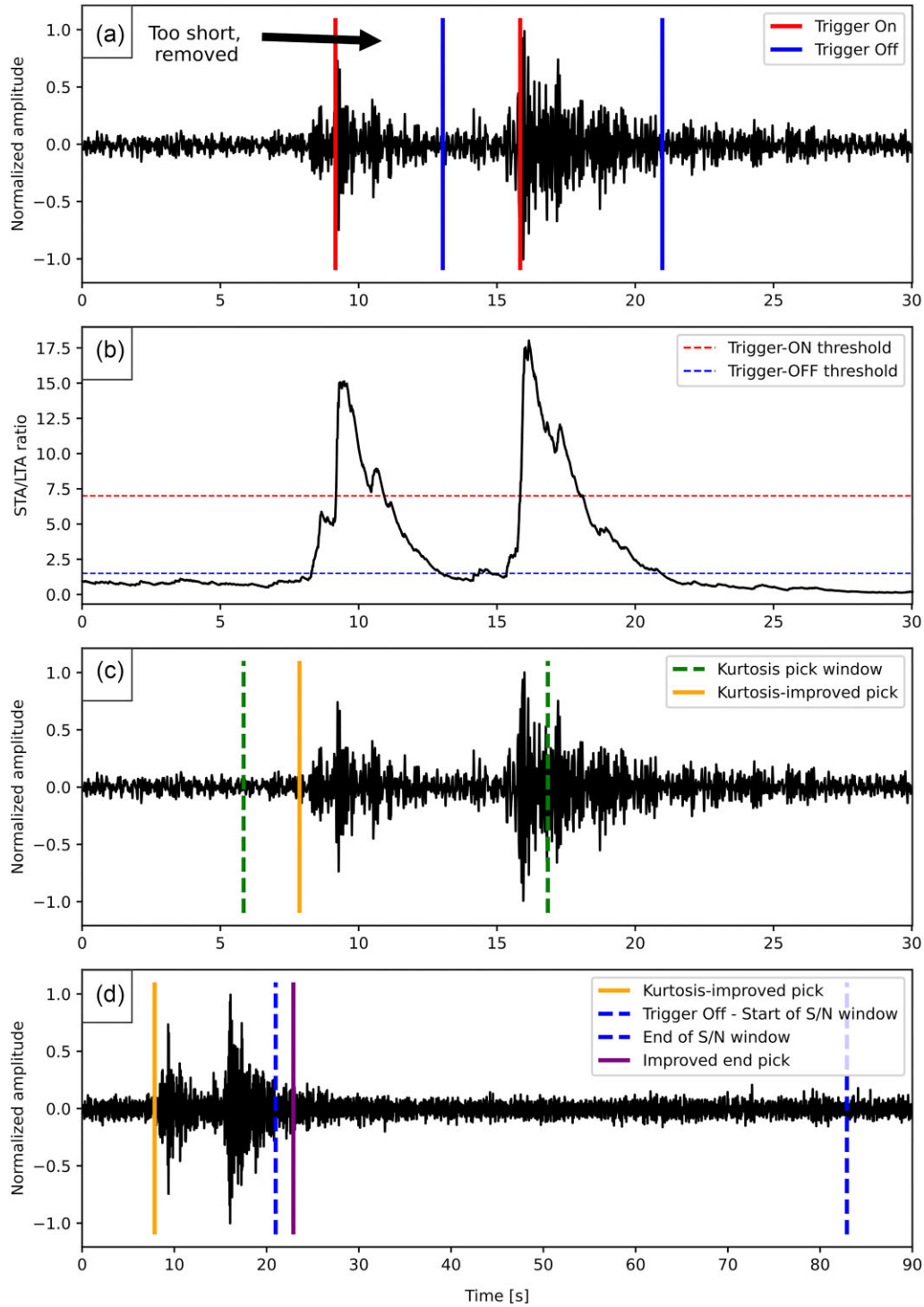


Figure 3. Graphical explanation of the steps taken to obtain detection time windows used later in the classification. (a) An example earthquake on which STA/LTA detector triggered twice, with the first detection removed due to the length s (b) STA/LTA ratio for the event in (a) with the thresholds used for onsets and terminations of detections used in this study. (c) Time window for the kurtosis-based pick with the final improved onset pick for the remaining detection from (a). (d) Time window used to estimate the background amplitude of the signal and adjust the end pick when the ratio drops below certain threshold (1.5 in this case), with the improved onset pick from step (c) and a new position of the detection end.

channel with highest signal-to-noise ratio (SNR), we computed the features on three components of each OBS. This gives in total 174 features computed on single channel data, plus four features using three channels simultaneously. We provide the list of features with corresponding formulae in Table A1.

3.3 Iterative model building

We manually screened the catalogue to prepare the initial set of examples used in training the machine learning classification. From all stations, we selected 100 earthquakes representing a class EQ, 100 SDEs representing a class SDE and 100 examples of different

types of noise that triggered the STA/LTA detector that were together grouped into one class labelled NOISE. We used all the samples in the training step and assessed the performance of the model on the continuous data detections. We present the results of the training phase in the form of a confusion matrix (Fig. 4). We define an accuracy of model as a total number of correct predictions in a class divided by all predictions in said class. Throughout the text we also use precision as a measure of the amount of false positive detections in each corresponding class. We compute it as a ratio between correct detections in the class versus the sum of correct (true positive) and incorrect (false positive) detections. In an ideal model scenario, all training samples should end up on the diagonal of the matrix.

Initial training set—model A

The initial classification test performed well with only one example in the entire test data set being mislabelled. This shows that the differences between types of signals are potentially easily recognizable with this approach (Fig. 4, Model A). Encouraged by the results, we decided to check the model performance on a full data set from one of the stations. Based on the results, we intended to either directly transfer the model to analyse the subsequent stations or iteratively increase the training data set with incorrectly labelled examples, retrain the model and then verify how well the model transfers between different OBSs. We followed the numbering order of the stations, starting with OBS-24 and concluding with OBS-30.

OBS-24—model B

We used the Reviewed Bulletin of the International Seismological Centre (ISC; www.isc.ac.uk) to list all earthquakes recorded at the closest land stations on Svalbard and Greenland. This catalogue subsequently served as a reference to which we compared the results obtained from our detector. We downloaded all records of earthquakes located between 70°N and 90°N in latitude and 25°W to 40°E in longitude that occurred during the duration of the survey. Not all events seen on land were recorded by the OBS and vice versa. We manually verified 206 earthquakes on OBS-24 from the 393 reported in the reviewed version of the ISC catalogue. Out of these 206 earthquakes, our method detected 191 and labelled 181 as an earthquake. All the remaining visible events had a low SNR, and it would be impossible to correctly pick P and S phases for location purposes. We manually screened 5 months of data to see how many additional detections were properly labelled as earthquakes. We found that 117 new earthquakes have been detected (bringing the total amount of earthquakes to 298), but also 406 detections labelled as an earthquake turned out to be incorrect (Table 2). Due to the very large number of detections for SDE (16 442) and NOISE (2677) classes, we were not able to check all of them individually, but we observed that while there are some events classified as SDE that we consider noise and vice versa, there were no immediately visible earthquakes that were attributed to these classes. To improve the model performance, we added the cleanest examples of the different classes of events into the training set (137 EQ, 41 SDE and 109 NOISE), and obtained an updated model, which had a slightly lower accuracy during training (99 per cent for EQ class, 99 per cent for SDE class, 98 per cent for NOISE class; Fig. 4, Model B). After this procedure, we ran the detector again on OBS-24 and ended up

with 324 correctly identified earthquakes and only 18 false positives (caused by noise) during the entire duration of the experiment (precision of 94.7 per cent; Table 2).

OBS-25—model C

After using this newly trained model (Model B) on a next station, OBS-25, we observed that new distinct types of noisy signal led to much a lower accuracy of the approach. While in the subset of earthquakes seen simultaneously at OBS-24, we have found no incorrectly labelled earthquakes (102 earthquakes seen in total for OBS-25), a large number of false picks of noise (220) led to an overall precision of 31.7 per cent for this data set (Table 2). In an effort to train the model to correctly identify wrongly classified examples, we added all correct and wrong examples from the EQ and NOISE classes to the appropriate groups in the training data set, with additional examples of SDEs included as well (Fig. 4, Model C). We found remarkably similar, high performance in recognition of all training events compared to previous models, with all SDEs from this data set recognized properly. After testing the new model on continuous data from OBS-25, we again found that providing additional events, specifically new examples of noise from OBS-25, leads to drastically improved results compared to the first attempt on this station. This iteration resulted in 98 correctly labelled earthquakes (4 seen previously have been wrongly classified) and 14 incorrect detections labelled as earthquakes (EQ class precision of 87.5 per cent; Table 2). We retained almost all correctly labelled earthquakes while removing 206 false positive earthquake detections.

OBS-26—model D

Due to the overall shorter duration of the OBS-26 data set (roughly 3 months in total), we decided to manually verify all detections and labels after the classification with the current version of the model (Fig. 4, Model C). We found that 452 earthquakes had a correct label, but 2253 noise-type signals were also present in the EQ category (precision equal to 16.7 per cent; Table 2). On the other hand, we confirmed our observations of correct recognition between SDEs and noise. Out of 97 SDE detections, 7 of them were incorrectly labelled earthquakes, with 4 additional events difficult to assign manually (precision equal to 89.8 per cent). We found 452 correctly marked noise events, with 9 examples of SDEs and only two earthquakes in the NOISE class (precision of 97.6 per cent). Since, we checked all detections on this data set manually, we were also able to compute how many true detections for the class we actually missed (recall). We use the definition of recall that it is a ratio between the true positive detections divided by the sum of true positive and false negative detections. The recall value for each class on OBS-26 is as following: EQ—98.0 per cent, SDE—90.9 per cent and NOISE—16.7 per cent). This confirmed our observations from previous inspections that almost all earthquakes and SDEs are being labelled correctly and the only outstanding problem is a large number of noisy events that are labelled as earthquakes or SDEs. As with previous stations, we took the verified examples and added them to the training data set, providing another iteration of the model (Fig. 4, Model D).

Model training results

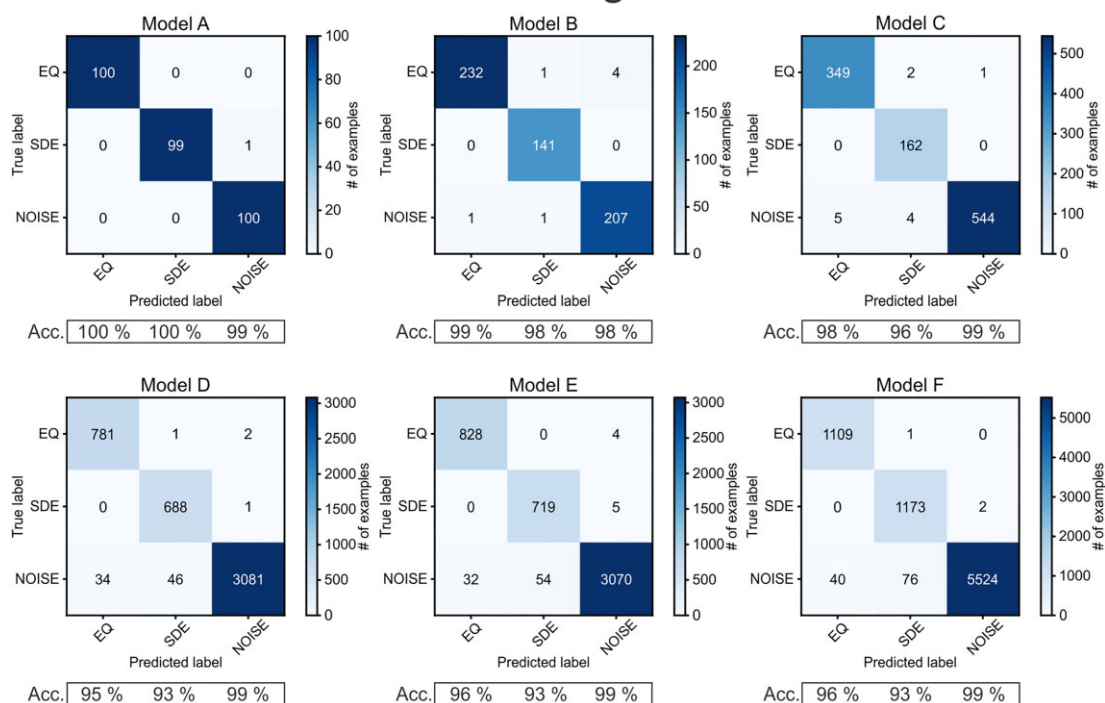


Figure 4. Confusion matrices showing how well the classification algorithm recognized events used in the training after subsequent additions of new waveforms to the training data set. Accuracy given below is the number of correct predictions in each class divided by the total number of predictions assigned to this class.

Table 2. Performance of the trained models on the continuous data—classifier precision for all events assigned to EQ class.

Model/station	Correct detections—EQ class	Incorrect detections—EQ class	Precision [true positives / (true positives + false positives)]
Model A/OBS-24	298	406	42.3 per cent
Model B/OBS-24	324	18	94.7 per cent
Model B/OBS-25	102	220	31.7 per cent
Model C/OBS-25	98	14	87.5 per cent
Model C/OBS-26	452	2253	16.7 per cent
Model D/OBS-27	264	562	31.9 per cent
Model D/OBS-28	346	601	36.5 per cent
Model F/OBS-30	236	94	71.5 per cent

OBS-27 and OBS-28—model E

Observations up until this point indicated that a relatively small number of earthquakes and SDEs is improperly classified, even if there is a large number of false events in EQ class. Due to the large amount of data and detections remaining, we only checked events in the EQ class from this point onward. Results for the next two stations are as follows: 346 correctly recognized earthquakes and 601 incorrectly labelled signals (precision of 36.5 per cent) for OBS-28, and 264 earthquakes and 562 cases of noise (precision of 31.9 per cent) for OBS-27 (Table 2). After this step, we again provided the highest quality examples as an additional input to recompute the machine learning model (Fig. 4, Model E).

OBS-30—model F

For the last station (OBS-30), we wanted to test whether the training data set is robust enough to be applied on a new station without having any prior knowledge about the types of signals present. For this

purpose, we removed all examples of signals from OBS-30 present in the initial training data set and all subsequent iterations. This meant the removal of 19 earthquakes from Model E. There were no examples of NOISE and SDE class from OBS-30 used in any iteration so far. This final model (Fig 4, Model F) correctly recognized 236 earthquakes on OBS-30 while also outputting 94 false detections (precision of 71.5 per cent; Table 2). Additionally, for 32 events we had a difficulty in manually assigning them to any of the classes. In the final comparison with the ISC land-based detections, out of 132 earthquakes listed for the OBS-30 survey duration, the STA/LTA detector triggered on 62 of them and the classifier subsequently correctly labelled 57. We checked the remaining ISC earthquakes listed, and they were either not present in the data at all or their quality was too low for further investigation. This concluded the training process of the classifier.

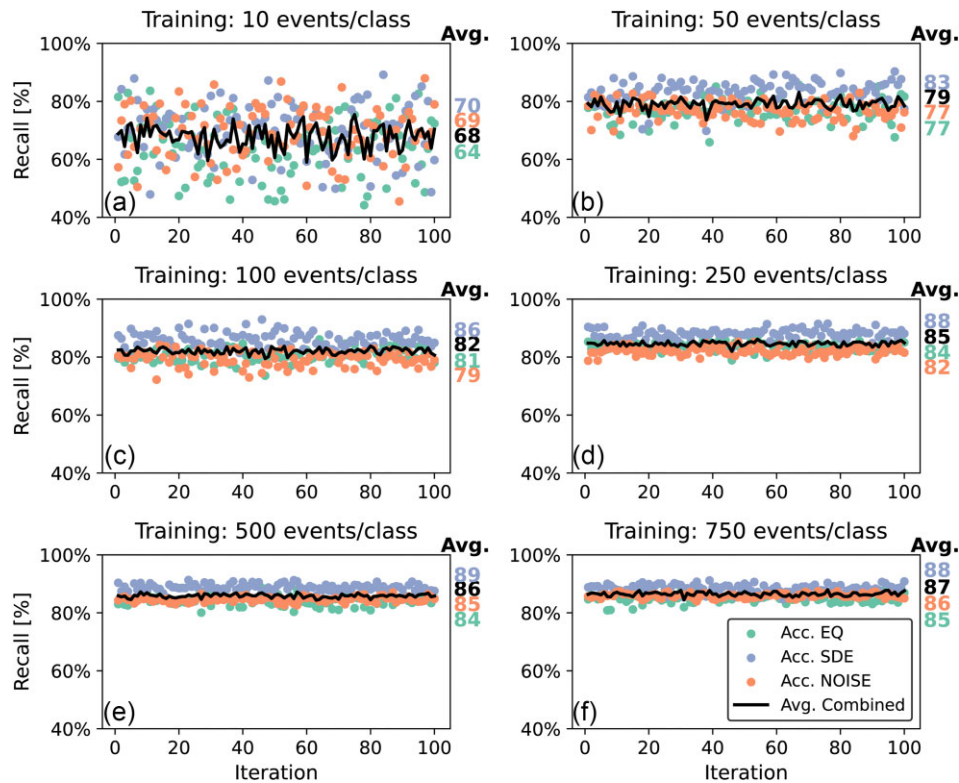


Figure 5. Recall value of the Random Forest classifier for recognizing events belonging to EQ, SDE and NOISE class for 100 iterations of training and validating of the model, when training data set equals: (a) 10 events/class, (b) 50 events/class, (c) 100 events/class, (d) 250 events/class, (e) 500 events/class and (f) 750 events/class. The validation of the model is conducted on the remainder of the events from final training data set. Average recall from all iterations per class presented in corresponding colour on the right side. The black line shows average values for all classes per iteration and the black number on the right total average for all iterations.

3.4 Performance of the model

To evaluate how well the Random Forest algorithm is suited to recognize different classes of the events, we repeated the training using 10, 50, 100, 250, 500 and 750 events per each class from all event examples used to train final model (Model F). We established the performance of each attempt using each corresponding model on the remaining samples from the data set. For each size of training data set, we repeated the procedure 100 times and calculated the overall average recall value and the average recall value per class. As previously mentioned, recall informs about the percentage of the samples from each class labelled correctly by the model (true positive rate, sensitivity).

We also investigated how well the model performs when we have a training data set with a large difference of event examples per class (i.e. as it is in our case, with strongly overfitted NOISE class). To do so, we performed two rounds of testing, one in which all classes are represented by the same number of examples and one in which the ratio between the samples in each class reflects the ratio of examples in our final model. We took randomly between 1–30 per cent of all samples from the final model for each class (which means between 79 and 2337 events for each category) and trained the model while verifying its recall value on all remaining examples. For classes EQ and SDE this leads to using the same examples multiple times, since the final model contains 1110 and 1175 examples for these classes, respectively. The data set for the final model contains 5640 examples for NOISE class. For each percentage, we repeated the training 100 times and averaged the results. In the second scenario, we repeated the same training process, but we used the percentage

of all samples belonging to their respective class. This means taking between 11 and 333 examples for the EQ class, between 12 and 352 examples for the SDE class and between 56 and 1692 examples for the NOISE class. This way, the ratio between the samples in each class remained constant and equal to the ratio in the final model.

3.5 Importance of features

With all the signal features provided, it is important to determine which of the selected features were most important during the classification of events. The Random Forest approach allows to calculate the importance of each feature, obtained by comparing the performance and the error of the model with given features randomly permuted for all the examples versus the classification result without the permutation (Breiman 2001). Arbitrary swapping of values of the selected feature allows to estimate how critical this parameter was in achieving the final result. We used the built-in `feature_importances_` function within the scikit-learn library for this purpose (Pedregosa *et al.* 2011).

4 RESULTS/BUILDING A RELIABLE CLASSIFICATION MODEL

4.1 Testing of the final model (model F)

The results of repeated training using increasingly larger number of events show that even with only 10 events per class the average recall reaches 68 per cent (Fig. 5a). Gradually increasing a number of examples leads to less varying results per iteration and overall

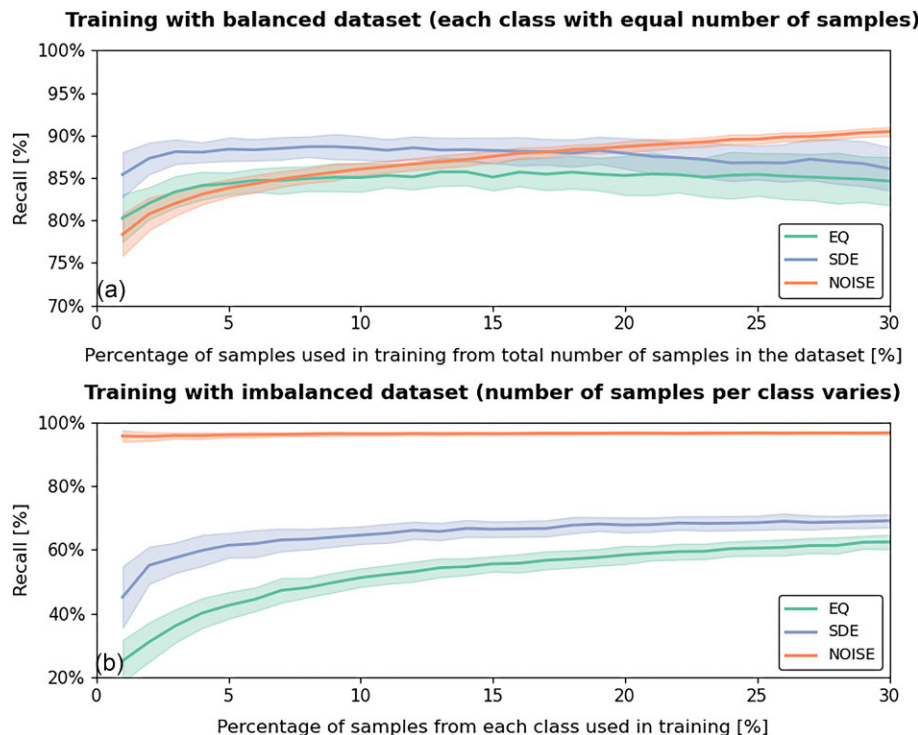


Figure 6. Recall value of the Random Forest classifier in recognizing different classes with the increase in the number of samples included in the training data set depending on whether the training data sets for each class are equal (i.e. balanced model, a) or some classes are overfitted (as NOISE in the final model, i.e. unbalanced model, b). Training was done on a given percentage of balanced or unbalanced data set and verified on the remainder of all samples. For each percentage, the model was trained 100 times and recall values were averaged. Shaded areas denote standard deviation obtained from 100 iterations of training and validation.

higher recall value in each of the classes (Figs 5b–f). The SDE class seems to be the least dependent on the number of samples needed for training, reaching a recall value of 86 per cent already with 100 examples (Fig. 5c), and increasing only by 2–88 per cent recall value when 750 examples were used (Fig. 5f). On the other hand, the NOISE class requires more examples overall in training to reach a similar performance (86 per cent recall value at 750 events used for training) (Fig. 5f). The results for the EQ class indicate that with 100 events the recall value is already at 81 per cent (Fig. 5c), there is no larger increase in the performance of the model and the overall recall value at 750 examples is high (85 per cent), but the lowest of all the classes (Fig. 5f). The final average recall value for all classes is equal to 87 per cent at 750 examples per class used in training, but it is already at 85 per cent with much smaller subset of 250 events per class (Figs 5d and f).

When using the same number of events per class for the training process, the recall value in detecting earthquakes and SDEs is already high with 1 per cent of total examples used for each class (80 and 85 per cent, respectively, Fig. 6a), whereas the NOISE class benefits the most on the increase in the number of samples used for training (accuracy of 78 per cent at 1 per cent of total data used, 90 per cent when using 30 per cent of total training samples available, Fig. 6a). The recall values of classes EQ and SDE began to decrease, when the model was trained with the same examples used multiple times. The entire training data set consists of 7925 examples (1149 EQ, 1250 SDE and 5526 for NOISE; Model F in Fig. 4). When we use the percentage of all 7925 examples to train the model and compute the recall, the number of examples for EQ and SDE class becomes greater than the actual number of examples available for these classes at the value of around 15 per cent. Above that number,

an increasing number of examples from the EQ and SDE classes is used more than once for the training.

Testing the model with the ratio between classes similar to the one for the entire training data set we have leads to a very high recall value for NOISE class that remains constant regardless of the number of samples used (ca. 95 per cent from 1 to 30 per cent of NOISE class examples used, Fig. 6b). Due to the much lower numbers of examples used initially for classes EQ and SDE (only 11 and 12 examples at 1 per cent of each class, respectively), the initial recall value is low (25 per cent for earthquakes, 45 per cent for SDEs, Fig. 6b). It increases steadily, however, reaching 62 per cent for EQ class and 69 per cent for SDE class when 30 per cent of examples from each class are used (Fig. 6b).

4.2 Importance of features for the final model

The ten most important features during the training of the final model are presented in Fig. 7 (all the features with their corresponding importance can be found in a text file provided with the electronic supplement to this article). Seven out of ten features are from the vertical channel of the geophone. Out of them, four of the five most important are related to the kurtosis of the signal computed for different frequency ranges. The remaining one from the top five, on the third place, is the frequency with the maximum energy in the frequency spectrum. Three of the top ten features are related to the duration of the signal (on the seventh, eighth and tenth place), and all of them have equal values, since the signal in each sample is cut into even-length windows on all channels. The remaining features on the list are the root-mean-square (RMS) difference between the decreasing part of the signal and the straight-line approximation (on the sixth place) and the energy in the first quarter of frequency band

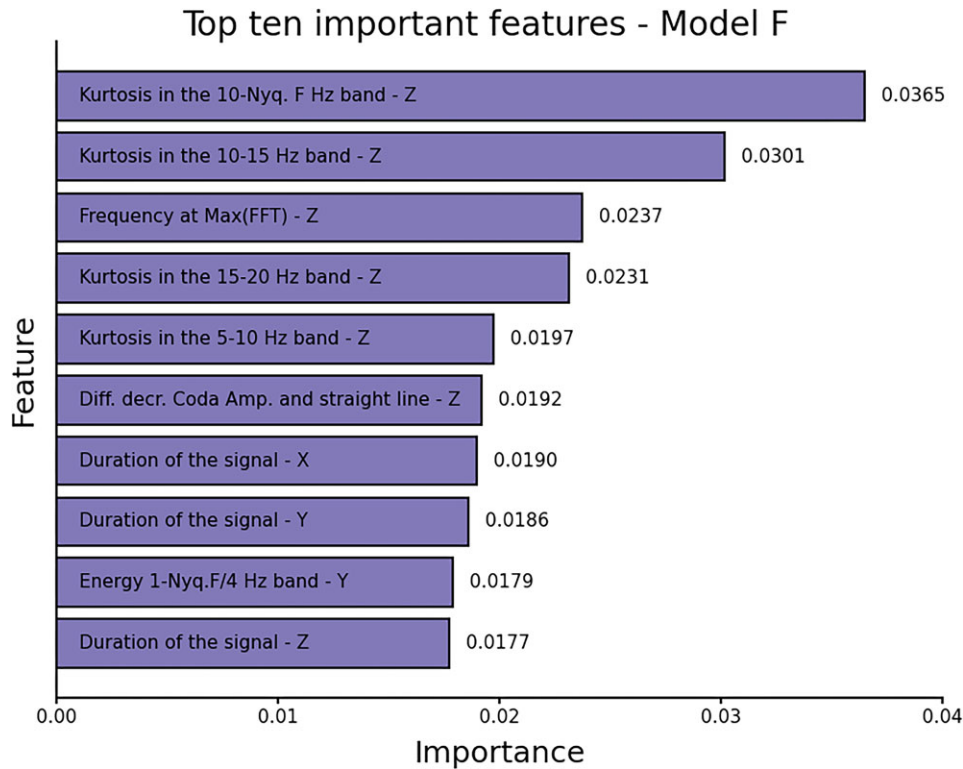


Figure 7. Top 10 most important features from the final trained model with their corresponding importance, based on the mean and the standard deviation of accumulation of the impurity decrease within each tree in the trained model (1000 trees used), obtained by randomly permuting values of all features and comparing results with the results without permutation (Pedregosa *et al.* 2011).

from 1 Hz to the Nyquist Frequency (25 Hz in this case) on one of the horizontal channels (on the ninth place).

5 DISCUSSION

5.1 Training process for the new model and its transferability between data sets

The detection and classification approach presented in this study aimed to improve the processing of OBS data sets which, due to the much higher noise levels than in data recorded on land, poses a more difficult challenge. To properly classify different types of signals, we needed to ensure that the time windows extracted using an STA/LTA detector correctly encapsulated and separated different types of signals. By testing and adjusting the parameters of the STA/LTA detector separately for SDEs and earthquakes, we were able to capture two types of events with the same method, but at the expense of the overall detection number. We found that SDEs, due to their high SNR, are usually correctly detected and extracted from the continuous data, but earthquake extraction proved more problematic.

Adjusting STA/LTA parameters alone does not ensure a proper detection of full earthquake signals. We often observed a presence of two separate detections for P and S phases and in the case of weaker signals, the STA/LTA detector responded only to the S phase, usually the strongest part of a waveform. It was therefore important to adjust the onset of each detection to properly capture the full signal if the detection contained an earthquake. Using the kurtosis-based picker designed to recognize slowly emergent signal in a noisy data set (Baillard *et al.* 2014; Hibert *et al.* 2014) proved satisfactory for this purpose. While not always the exact onset of the *P*-wave arrival was

selected, the Random Forest classifier very rarely had a difficulty with correctly labelling an event as an earthquake even with an only partially present *P*-wave phase (Fig. 8).

The initial verification of our approach using a curated catalogue of events (Model A, Fig. 4) showed that the method is very well suited to the problem and features computed from the extracted windows provide enough information to discriminate between earthquakes, SDEs and noisy signals. The test on the continuous data set from OBS-24 using publicly available ISC catalogue showed that 95 per cent of the detections made by the STA/LTA detector were assigned correctly to the EQ category and the remaining earthquakes listed in the catalogue were either not present or too weak to be recognized by automatic detection. We also found that SDE classification is working correctly, but we were not able to manually verify all of the detections due to the large size of the resulting catalogue.

This step also made us realize that the data set containing examples of noise is likely lacking examples of many different spurious signals that we can encounter in the OBS data. These signals can be sometimes traced to the issues with the instrumentation itself, but can be related, for example to the ocean currents inducing shaking on the frame (e.g. Stähler *et al.* 2018; Essing *et al.* 2021), marine mammals (e.g. McDonald *et al.* 1995; Soule & Wilcock 2013; Løviknes *et al.* 2021) or can include seismic operations at sea, which we also conducted during the first days of the survey. Providing the additional examples to the model allowed us to not only find 200 more local earthquakes, but also regain high level of correct detections in EQ class (94.7 per cent, Table 2; Model B, Fig. 4).

We repeatedly observed that applying the Random Forest model trained on one set of data to a new OBS requires retraining to

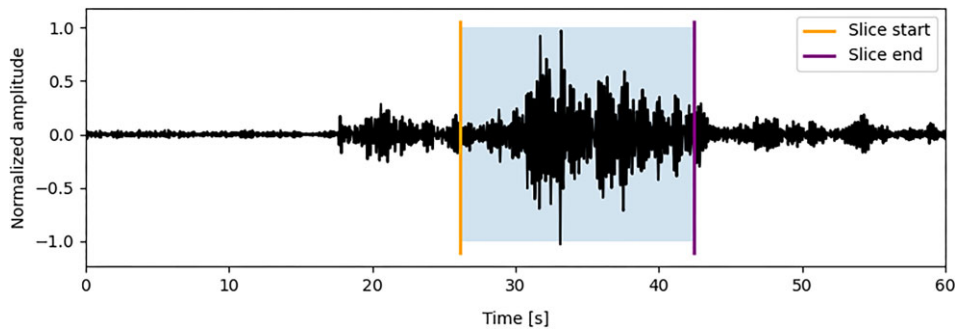


Figure 8. An example of the correct classification of an earthquake recorded on OBS-30 by the final model (Model F) for a slice that do not encompasses the earthquake waveform fully. Blue outline shows the part of the signal used in the classification, which lacks a majority of the P-phase within.

achieve high accuracy in the earthquake detections, but our classifier correctly recognizes between earthquakes and SDEs. On all subsequently trained and verified iterations of the model (Model C-F, Fig. 4), new types of noise examples were present and labelled as earthquake signals. We attribute these issues to the random nature and/or very localized origin of the noise and the differences in the signal characteristics between the different stations (separated by up to 30 km between the farthest OBS positions). Different recorders used in experiment also could have influenced the results. After making sure that the amount of improperly labelled earthquakes remains small, we found that even with the manual processing involved, checking additional few hundreds of examples leads to a significant speed-up of the data processing compared to the laborious scanning through the tens of thousands of the STA/LTA detections in the database. As for resulting SDE detections, even if the manual verification is still not a feasible task, our observations indicate that the resulting catalogue already is a notable improvement over the STA/LTA detection studies without any subsequent processing steps, which was the routine approach so far (e.g. Franek *et al.* 2017; Batsi *et al.* 2019; Domel *et al.* 2022).

By gradually increasing the number of examples in the training set for the NOISE class, we hoped to achieve a high enough level of completeness that would lead to a small number of incorrect detections for the subsequent OBS stations we checked. While starting from station OBS-26, we found a larger number (452, Table 2) of correctly labelled earthquakes present (OBS-25 had small number of earthquakes compared to other data sets; 102, Table 2), the overall accuracy of detections when reapplying a model to a new data set was decreasing. It is important to mention that each station can pose unique challenges. In the example of OBS-26 we found an order of magnitude higher number of incorrect detections, which is probably explained by the disproportionately large amount of noise on this station. We suspect the strength of underwater currents for this OBS was much larger than in any other station possibly due to its location with respect to the seafloor morphology. For stations OBS-27 and OBS-28, a third of detections in the EQ category were retained as correct, same as for OBS-25 when using the model without including additional examples for a given station after manual checking (Table 2). For the last data set (OBS-30), we found that the final model (Fig. 4, Model F), with the five times more examples of noise than samples in the other two categories, shows a significant improvement in the reduction of incorrect detections in EQ category. With the precision of 71.5 per cent for EQ class (Table 2), the majority of distinct types of noise were properly recognized by this approach. We intend to use the final model in future processing of different OBS data sets to reduce the amount of manual labour needed.

5.2 Final model performance and its training data set

The results shown in confusion matrices inform us whether the model is well suited to recognize events using the features provided (Fig. 4), however by training the model on all examples available, these plots do not tell us about the robustness of the model in recognizing new, unknown samples (generalization). Therefore, it was important to conduct rigorous testing using even, increasingly large training sets and verify the model performance on samples of different types of events that were not included in the training phase (Fig. 5). We see that it takes a small number of 50 examples per class to reach the average recall value of 79 per cent and that a gradual increase of training sets leads to a smaller performance improvement. The recall value of detecting SDEs remains highest among all the categories throughout the testing process, which is confirmed by the verification of the SDE class content for OBS-26. With 750 events per class used for training, the recall value of independent recognition of both earthquakes and noise is high (85 and 86 per cent, respectively). In the manual verification we observed a higher recall in the recognition of earthquakes (with only two earthquakes labelled as noise and 452 correctly labelled examples of noise in OBS-26), but a lower recall value for the recognition of noise (2253 noise examples in EQ category for the same OBS). We attribute this discrepancy to a significant portion of noise being mislabelled due to the data set not fully capturing the broad range of types and features noise that a marine setting can exhibit. At this point in the model development, we opted against the creation of separate categories for different noise sources.

By providing more examples for the NOISE class (that has the largest expected variability of sources and signal shapes), we attempted to counteract the generalization of event types in this class and enforce correct recognition of most of the noise sources. Training with the increased percentage of the overall data set highlights that the NOISE class benefits the most with the provision of additional samples (Fig. 6a). The perceived drop of the recall for the remaining classes by 15 per cent mark is caused by reusing examples in these classes during the testing phase. When we train the model keeping the relative ratio between the number of examples in each category the same as for the entire, final training data set, we see that the recall value in recognizing noise is excellent regardless of the percentage of samples used for training (Fig. 6b). Therefore, we believe that when one category consists of a variety of signals with different origins, unbalancing the model to compensate for this diversity is a valid, but not necessarily the best approach. It would be beneficial to spend more time in differentiating between signals that obscure the events of interest in OBS data sets and potentially train the model using separate categories of different noise types.

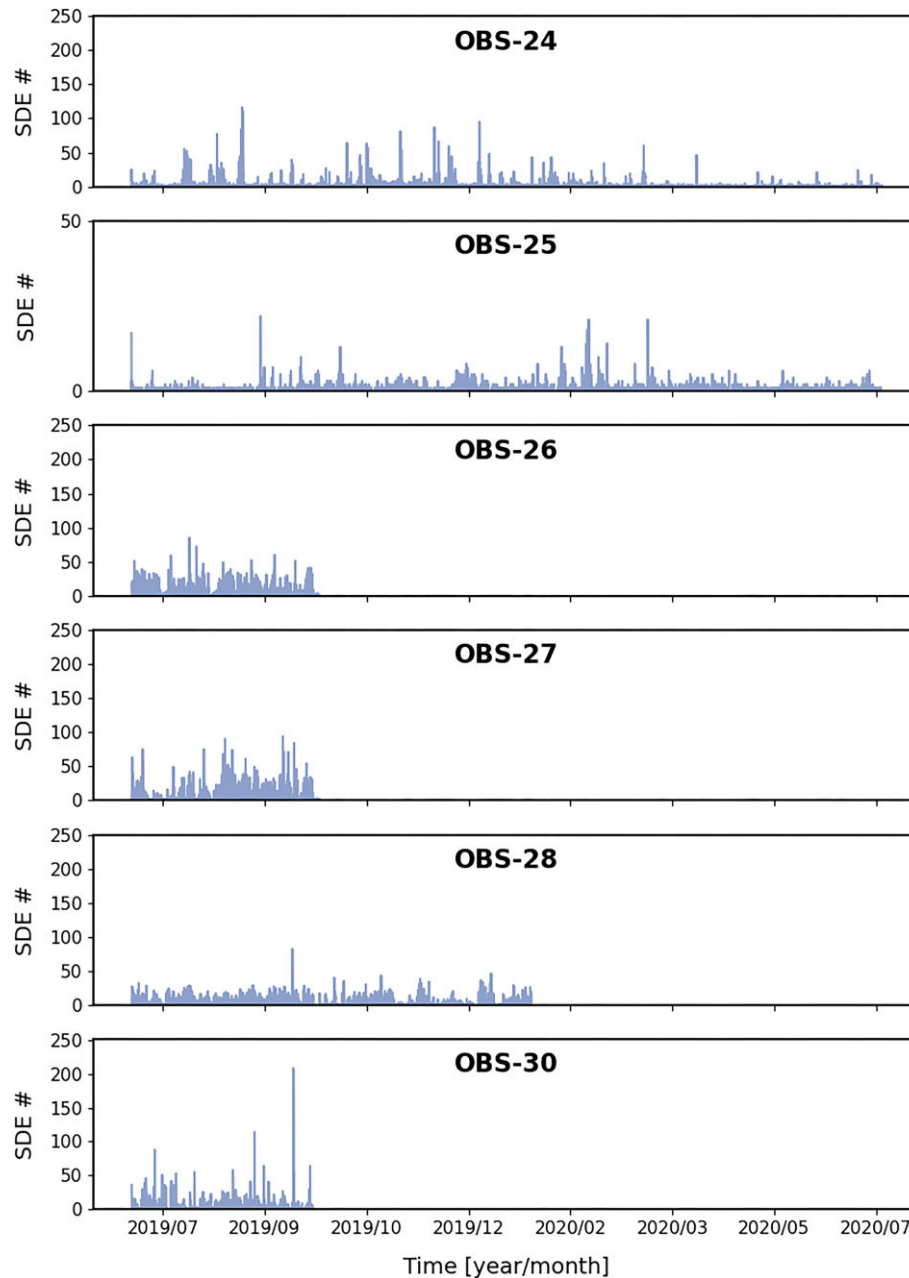


Figure 9. Time-series of hourly SDE occurrence on OBS stations obtained using random forest classification with Model F. Note the difference in vertical axis for OBS-25. The difference in the duration of data sets is explained in more detail in Sections 2 and 3.

5.3 Most important signal characteristics

In the recognition of earthquakes, SDEs and noise, the kurtosis of the signal and signal duration played a key role, judging by their prevalence in the top ten most important features (Fig. 7). This is expected, based on observed differences between the different signal waveforms generated by each source, as explained below. Kurtosis informs about the deviation of the random variable distribution from normal distribution (Hibert *et al.* 2014) and the curve for different frequency ranges will have different shapes depending on the event type. We have initially a low amplitude signal (P-phase), followed by an increase (S-phase) and slow decay for earthquakes that in our data set usually not exceeds one minute of duration. SDEs on the other hand, generally show sharp spikes with an immediate termination of the signal and the usual individual duration under 5 s. In the NOISE

class, we contained an assortment of both longer and shorter events, some continuous, emergent signal as in ocean current tremor, but generally more varied than two other classes. The differences in their length and shape of the kurtosis proved to be significant enough for a high level of recognition from the remaining two classes. The importance of the way in which amplitude decreases towards the end of the signal is also reflected by the presence of feature related to the coda of the signal deviating from the straight line (feature 24 in Table 2; on sixth place in Fig. 7).

SDEs are high amplitude events, with most of their energy in the upper part of the studied spectrum (10–25 Hz, Fig. 2), similar to tremor noise present in the NOISE class. Therefore, the frequency at which maximum energy was found (third most important feature, Fig. 7), also proved useful in discerning these classes from the earthquakes, for which we expect highest amounts of energy below

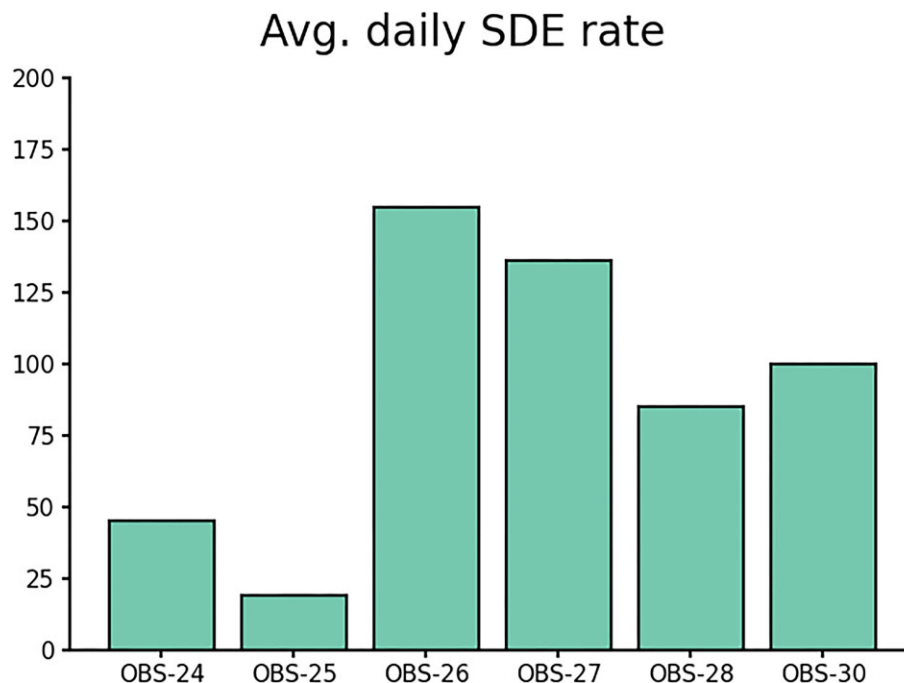


Figure 10. Average daily rate of SDE occurrence obtained from the Random Forest classification method using the final trained model (model F) for all OBS stations used in this study.

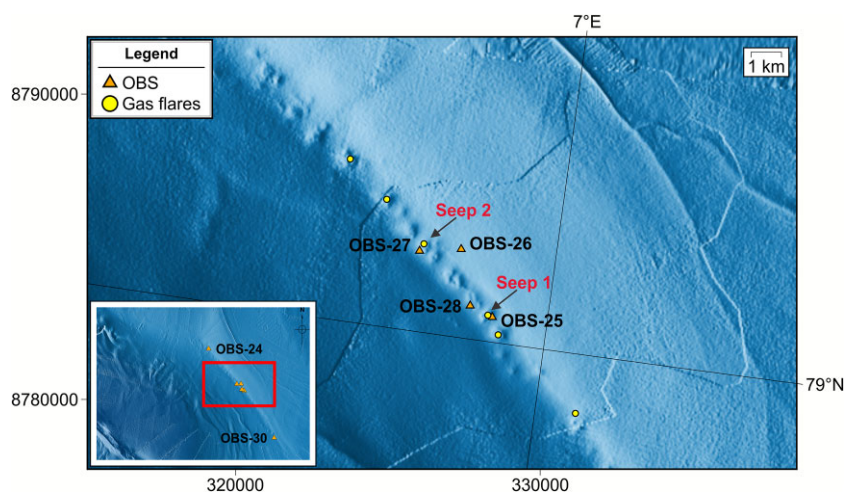


Figure 11. Positions of OBS-25, OBS-26, OBS-27 and OBS-28 at the crest of Vestnesa Ridge with relation to proven, continuous gas seepage sites. Seep sites discussed in the text labelled in red with the arrows. Inset shows which part of the map from Fig. 1 is presented here in a greater detail, with positions of OBS-24 and OBS-30 further away from seep sites.

10 Hz. This differentiation is linked with the energy in the lower quarter of spectrum used (1–6.25 Hz in this case), which is also present on the list of the most important features (on the ninth position, Fig. 7).

6 APPLICATION OF THE TRAINED MODEL ON SDE TIME SERIES ANALYSIS

With the Model F established to classify between event types with high accuracy on all stations, we have tested the capability of the method to build a SDE catalogue useful for subsequent analysis, alongside its earthquake detecting capability. Out of a total number of 180 000 STA/LTA triggers on all seven stations of the network,

model F classified 2374 as earthquakes, almost 73 000 as SDEs and the remainder as noise.

These numbers clearly underline the importance of SDEs in marine environments where they can outnumber earthquake detections, in our deployment setting by a factor of 30. We present their hourly occurrence throughout the duration of the experiment (Fig. 9). The overall intensity varies greatly between the stations, with OBS-25 having the least amount of the detections (3580—4.9 per cent of total SDE count), despite one of the longest duration of recordings. OBS-28 recorded the greatest amount of SDEs total over its roughly five-month-long record—16 822 (23 per cent of total SDE count). The total detection numbers for remaining stations are: OBS-24—16 425 (22.5 per cent of total SDE count), OBS-26—14 431 (19.8 per cent of total SDE count), OBS-27—12 674 (17.4

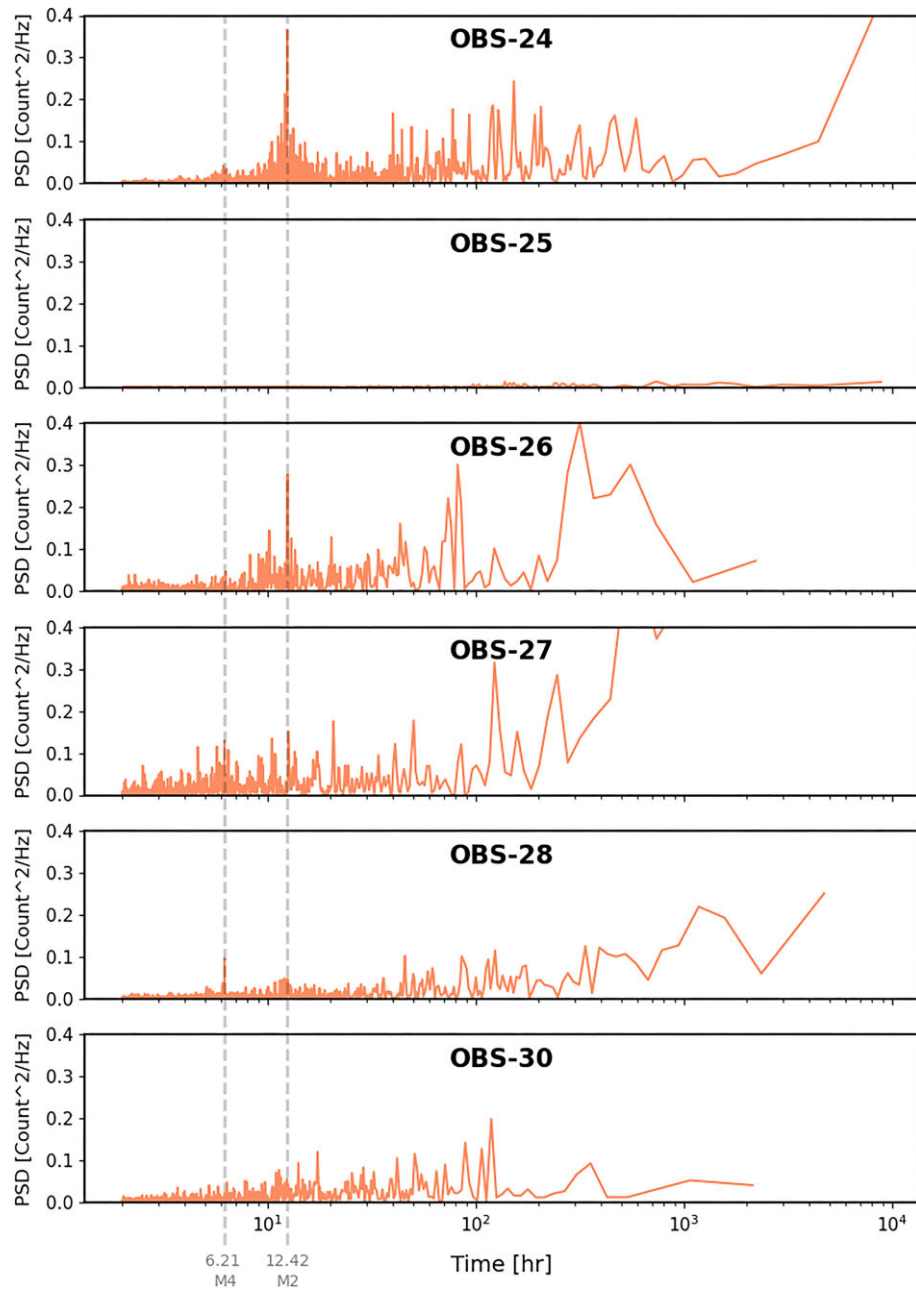


Figure 12. Periodograms (power spectrum density) plots of hourly SDE occurrences at investigated OBS stations. Two dashed lines correspond to principal lunar semidiurnal tidal component (M2–12.42 hr) and first overtide of M2 component (M4–6.31 hr).

per cent of total SDE count), and OBS-30–9032 (12.4 per cent of total SDE count). To better reflect the SDE occurrence intensity across the stations with different data set lengths, we computed their average daily rate of SDE occurrence, which is as follows: 45 for OBS-24, 19 for OBS-25, 155 for OBS-26, 136 for OBS-27, 85 for OBS-28 and 100 for OBS-30 (Fig. 10). SDEs typically occur in a form of seemingly irregular bursts, separated by periods of relative quiescence, with a varying frequency between stations.

The OBS data we use for the testing of Random Forest machine learning approach in a marine environment was collected as part of a study on fracture-controlled seepage dynamics along Vestnesa Ridge (e.g. Singhroha *et al.* 2020; Plaza-Faverola *et al.* 2015). SDEs documented along continental margins globally have been linked

to fluid migration and gas release from the seafloor via cracking of subseabed sediment in response to external factors (e.g. tides, e.g. Hsu *et al.* 2013; Bayrakci *et al.* 2014; Embriaco *et al.* 2014; Hilmo & Wilcock 2020; Domel *et al.* 2022).

The origin of SDEs is a matter of ongoing debate and goes beyond the scope of the present study. However, with the classification approach presented in this study we were able to quickly produce a data set of SDE detections that should be a more accurate depiction of SDE intensity than unfiltered STA/LTA picker results utilized so far (e.g. Tary *et al.* 2012; Batsi *et al.* 2019; Domel *et al.* 2022; Ugalde *et al.* 2019). The resulting catalogue of SDEs includes six OBS stations distributed at varying distances from gas seepage pits and underlying structures of gas migration (Bunz *et al.* 2012; Panieri *et al.* 2017; Fig 11).

Preliminary analyses of SDE counts with respect to their distribution along Vestnesa Ridge fluid migration system reveal interesting observations with implications for advancing knowledge on SDEs:

(i) We observe the absolute lowest daily rate of SDEs at OBS-25, which is the station closest to one of the gas pits in the area (*ca.* 150 m from Seep 1 in Fig. 11). OBS-28 located 650 m away from the same seep has higher, but lower than other nearby stations, daily rate of SDE occurrence (85 per day; Fig. 10).

(ii) The two stations with the highest average daily count of SDEs (OBS-26 and OBS-27; Fig. 10) are located *ca.* 1200 and 650 m, respectively, from another seep site (Seep 2 in Fig. 11).

(iii) Two OBSs located *ca.* 11 and 14 km west and east from the cluster of seeps (OBS-24 and OBS-30, respectively; Fig. 11), recorded a sustained number of SDEs throughout the experiment duration.

Overall, this data shows that SDE intensity does not necessarily increase with the decreasing distance to the active seepage pits. On one hand, these observations challenge the perception that SDEs are associated with gas bubble rise at the seafloor (e.g. Tary *et al.* 2012; Hsu *et al.* 2013; Batsi *et al.* 2019). On the other hand, an increase of SDEs in a closed fluid flow system (shallow gas accumulations without an active gas release at the seafloor) supports observations from piezometer data where sub-seabed excess pore pressures fluctuate in response to the sea level changes in the region (Sultan *et al.* 2020).

A correlation between SDEs and tidal cycles is partially visible in periodograms of hourly counts of SDEs (Fig. 12). There are visible peaks of the SDE periodicity corresponding to semidiurnal tide component M2 (12.42 hr period) in the case of stations OBS-24 and OBS-26, and potentially a small peak of the first overtide of this component (M4–6.21 h period) in the case of OBS-28 (Fig. 12). Since this group represents the stations both within the area with an active seepage (OBS-26 and OBS-28) and away from it (OBS-24), no conclusive links can be established between seepage, tides and intensity of SDEs for the results of this experiment.

7 CONCLUSION

We applied a Random Forest classifier used previously in seismology on land to recognize signals in marine data from OBSs. We focused specifically on recognition of earthquakes and signals referred to as short duration events from the noise. These events are an interesting case study due to their high incidence rate, relatively similar characteristic between events, high/signal to noise ratio and a prevalence of STA/LTA based research with only some degree of manual verification in literature. to recognize between earthquakes, short duration events and noise present in the data from OBSs. We used the set of features previously tested on seismological data from land and found it robust enough to differentiate between the distinct classes of events with high accuracy during the training phase. During the verification on the continuous data sets, we encountered two major challenges. First, the resulting earthquake catalogues contained a large number of non-earthquake events. This is due to the high percentage of noise present. We attempted to mitigate this by including a progressively larger number of noise examples during the training phase for the noise class. This led to an eventual improvement with the percentage of correct earthquake detections rising, but not reaching the high recall values suggested by the initial testing of the recognition between the classes. The second challenge

lies in the categorization of noise in a marine realm. Combining different types of signals into a single NOISE category hampers the possibility of applying the same training model to data sets from different instruments. This can be potentially solved by creating separate categories for noisy signals of different origin (e.g. bottom currents, ship noise, instrument vibrations and mammal signals).

Overall, we achieved a mean accuracy of 87 per cent for event classification (final model; after training using examples from six OBS stations). The final results show that the signal characteristics that play the most important role in training the algorithm match the features we use in visual differentiation of events. Using the final iteration of the model we were able to compile a catalogue of 73 000 SDEs, close to two orders of magnitude larger than the amount of SDE examples used for training. With this new catalogue, we studied the variability of SDE between the stations during the duration of experiment. The data set we obtained shows an apparent relation between the daily SDE rate and the distance of active seep pits. We also observe some of the same periodic patterns reported from other studies about SDEs. This reinforces the approach presented as an efficient and potentially more precise method of SDE event detection and recognition in the absence of large enough SDE databases to train deep-learning models.

Additionally, this supervised machine learning method can potentially be used to discern other sources of signal in the marine seismological data, such as mammal vocalizations, volcanic tremors or ship noises. This requires further investigation and compilation of a larger database of different types of events to achieve a better generalization of the approach.

ACKNOWLEDGMENTS

This work is conducted as a part of the SEAMSTRESS project, supported by the Tromsø Research Foundation (TFS) and the Research Council of Norway (grant nr. 287865). The work is also supported by the Research Council of Norway through its Centers of Excellence funding scheme grant 223259 (Centre for Arctic Gas Hydrate, Environment and Climate—CAGE). We thank the crew of R/V Helmer Hanssen, chief scientist Stefan Bünz from CAGE and Anke Dannowski & Bettina Schramm from GEOMAR, Helmholtz Centre for Ocean Research Kiel, for making the deployment and recovery of OBSs possible.

DATA AVAILABILITY

Raw OBS data will be uploaded to University of Tromsø open research repository (DataverseNO; <https://dataverse.no/>) in 2023. The land data earthquake catalogue was obtained from the International Seismological Centre (ISC) Seismological Dataset Repository (<https://doi.org/10.31905/6TJZECEY>). The ObsPy package was used for processing of the seismological data (Krischer *et al.* 2015). Plotting waveforms and spectrograms was done using Pyrocko (Heimann *et al.* 2017). Figs 1 and 11 were created using Generic Mapping Tools (GMT; Wessel *et al.* 2019). Bathymetry of the region provided by the International Bathymetric Chart of the Arctic Ocean (IBCAO) (Jakobsson *et al.* 2020). Supplemental material for this article includes a text describing the performance of popular machine learning approaches in discussed data set with figures showing examples of their performance. Additional text file contains information about the final model, with the order of importance of the signal characteristics after training.

REFERENCES

- Allen, R., 1982. Automatic phase pickers: their present use and future prospects, *Bull. seism. Soc. Am.*, **72**(6B), S225–S242.
- Anant, K.S. & Dowla, F.U., 1997. Wavelet transform methods for phase identification in three-component seismograms, *Bull. seism. Soc. Am.*, **87**(6), 1598–1612.
- Baer, M. & Kradolfer, U., 1987. An automatic phase picker for local and teleseismic events, *Bull. seism. Soc. Am.*, **77**(4), 1437–1445.
- Baillard, C., Crawford, W.C., Ballu, V., Hibert, C. & Mangeney, A., 2013. An Automatic Kurtosis-Based P- and S-Phase Picker Designed for Local Seismic Networks, *Bull. seism. Soc. Am.*, **104**(1), 394–409.
- Baillard, C., Crawford, W.C., Ballu, V., Hibert, C. & Mangeney, A., 2014. An automatic kurtosis-based P- and S-phase picker designed for local seismic networks, *Bull. seism. Soc. Am.*, **104**(1), 394–409.
- Barstow, N., Sutton, G.H. & Carter, J.A., 1989. Particle motion and pressure relationships of ocean bottom noise: 3900 M depth; 0.003 to 5 Hz. *Geophys. Res. Lett.*, **16**(10), 1185–1188.
- Batsi, E. et al., 2019. Nonseismic signals in the ocean: indicators of deep sea and seafloor processes on ocean-bottom seismometer data. *Geochem. Geophys. Geosyst.*, **20**(8), 3882–3900.
- Bayrakci, G. et al., 2014. Acoustic monitoring of gas emissions from the seafloor. Part II: a case study from the Sea of Marmara, *Mar. Geophys. Res.*, **35**(3), 211–229.
- Bogiatzis, P. & Ishii, M., 2015. Continuous wavelet decomposition algorithms for automatic detection of compressional- and shear-wave arrival times, *Bull. seism. Soc. Am.*, **105**(3), 1628–1641.
- Breiman, L., 2001. Random forests, *Mach. Learn.*, **45**(1), 5–32.
- Bünz, S., 2023a. CAGE19-1 cruise report: passive and active ocean-bottom seismic surveys at Vestnesa Ridge, west-Svalbard margin within the framework of the SEAMSTRESS project, CAGE – Centre for Arctic Gas Hydrate, Environment and Climate Report Series 7.
- Bünz, S., 2023b. CAGE20-5 cruise report: tectonic stress studies and seismic surveys on the West-Svalbard margin, CAGE – Centre for Arctic Gas Hydrate. Environment and Climate Report Series 8.
- Bünz, S., Polyakov, S., Vadakkepuliambatta, S., Consolaro, C. & Mienert, J., 2012. Active gas venting through hydrate-bearing sediments on the Vestnesa Ridge, offshore W-Svalbard, *Mar. Geol.*, **332–334**, 189–197.
- Buskirk, R.E., Frohlich C. Latham G.V. Chen, A.T. & Lawton J. 1981. Evidence that biological activity affects ocean bottom seismograph recordings, *Marine Geophysical Researches*, **5**(1), 189–205.
- Chen, H., Yang, H., Zhu, G., Xu, M., Lin, J. & You, Q., 2022. Deep outer-rise faults in the Southern Mariana Subduction Zone indicated by a machine-learning-based high-resolution earthquake catalog, *Geophys. Res. Lett.*, **49**, e2022GL097779.
- Chmiel, M., Walter, F., Wenner, M., Zhang, Z., McArdell, B.W. & Hibert, C., 2021. Machine learning improves debris flow warning, *Geophys. Res. Lett.*, **48**(3), e2020GL090874.
- Chu, C. K. & Mendel, J., 1994. First break refraction event picking using fuzzy logic systems: IEEE Transaction on Fuzzy Systems, **2**, 255–266.
- De Meersman, K., Kendall, J.M. & van der Baan, M., 2009. The 1998 Valhall microseismic data set: an integrated study of relocated sources, seismic multiplets, and S-wave splitting, *Geophysics*, **74**(5), B183–B195.
- Díaz, J., Gallart, J. & Gaspà, O., 2007. Atypical seismic signals at the Galicia Margin, North Atlantic Ocean, related to the resonance of subsurface fluid-filled cracks, *Tectonophysics*, **433**(1–4), 1–13.
- Diehl, T., Deichmann, N., Kissling, E. & Husen, S., 2009. Automatic S-wave picker for local earthquake tomography, *Bull. seism. Soc. Am.*, **99**(3), 1906–1920.
- Domel, P., Singhroha, S., Plaza-Faverola, A., Schlindwein, V., Ramachandran, H. & Bünz, S., 2022. Origin and periodic behavior of short duration signals recorded by seismometers at Vestnesa Ridge, an active seepage site on the West-Svalbard continental margin, *Front. Earth Sci.*, **10**, doi:10.3389/feart.2022.831526.
- Embricco, D. et al., 2014. Monitoring of gas and seismic energy release by multiparametric benthic observatory along the North Anatolian Fault in the Sea of Marmara (NW Turkey), *Geophys. J. Int.*, **196**(2), 850–866.
- Essing, D., Schlindwein, V., Schmidt-Aursch, M.C., Hadziioannou, C. & Stähler, S.C., 2021. Characteristics of current-induced harmonic tremor signals in ocean-bottom seismometer records, *Seismol. Res. Lett.*, **92**, 3100–3112.
- Falcin, A. et al., 2021. A machine-learning approach for automatic classification of volcanic seismicity at La Soufrière Volcano, Guadeloupe, *J. Volc. Geotherm. Res.*, **411**, doi:10.1016/j.jvolgeores.2020.107151.
- Franek, P., Mienert, J., Buenz, S. & Géli, L., 2014. Character of seismic motion at a location of a gas hydrate-bearing mud volcano on the SW Barents Sea margin, *J. geophys. Res.: Solid Earth*, **119**(8), 6159–6177.
- Franek, P., Plaza-Faverola, A., Mienert, J., Buenz, S., Ferré, B. & Hubbard, A., 2017. Microseismicity linked to gas migration and leakage on the Western Svalbard Shelf, *Geochem. Geophys. Geosyst.*, **18**(12), 4623–4645.
- Gelchinsky, B. & Shtivelman, V., 1983. Automatic picking of first arrivals and parametrization of traveltimes curves, *Geophys. Prospect.*, **31**(6), 915–928.
- Gentili, S. & Michelini, A., 2006. Automatic picking of P and S phases using a neural tree, *J. Seismol.*, **10**(1), 39–63.
- Guan, Z. & Niu, F., 2017. An investigation on slowness-weighted CCP stacking and its application to receiver function imaging, *Geophys. Res. Lett.*, **44**(12), 6030–6038.
- Heimann, S. et al., 2017. Pyrocko - an Open-Source Seismology Toolbox and Library. V. 0.3. GFZ Data Serv.
- Hibert, C. et al., 2014. Automated identification, location, and volume estimation of rockfalls at Piton de la Fournaise volcano, *J. geophys. Res.*, **119**(5), 1082–1105.
- Hibert, C., Michéa, D., Michéa, D., Provost, F., Malet, J. P. & Geertsema, M., 2019. Exploration of continuous seismic recordings with a machine learning approach to document 20 yr of landslide activity in Alaska, *Geophys. J. Int.*, **219**(2), 1138–1147.
- Hibert, C., Provost, F., Malet, J.-P., Maggi, A., Stumpf, A. & Ferrazzini, V., 2017. Automatic identification of rockfalls and volcano-tectonic earthquakes at the Piton de la Fournaise volcano using a Random Forest algorithm, *J. Volc. Geotherm. Res.*, **340**, 130–142.
- Hildebrand, J.A., 2009. Anthropogenic and natural sources of ambient noise in the ocean, *Mar. Ecol. Prog. Ser.*, **395**, 5–20.
- Hilmo, R. & Wilcock, W.S.D., 2020. Physical sources of high-frequency seismic noise on cascadia initiative ocean bottom seismometers, *Geochem. Geophys. Geosyst.*, **21**(10), doi:10.1029/2020GC009085.
- Himmeler, T., Sahy, D., Martma, T., Bohrmann, G., Plaza-Faverola, A., Bünz, S., et al., 2019. A 160,000-year-old history of tectonically controlled methane seepage in the Arctic, *Science Advances*, **5**(8), eaaw1450.
- Hsu, S.-K., Wang, S.-Y., Liao, Y.-C., Yang, T.F., Jan, S., Lin, J.-Y. & Chen, S.-C., 2013. Tide-modulated gas emissions and tremors off SW Taiwan, *Earth planet. Sci. Lett.*, **369–370**, 98–107.
- Jakobsson, M. et al., 2020. The International Bathymetric Chart of the Arctic Ocean Version 4.0, *Sci Data*, **7**(1), 176.
- Jeddi, Z., Ottemöller, L., Sørensen, M. B., Rezaei, S., Gibbons, S. J. & Strømme, M. L., 2021. Improved Seismic Monitoring with OBS Deployment in the Arctic: A Pilot Study from Offshore Western Svalbard, *Seismol. Res. Lett.*, **92**(5), 2705–2717.
- Jurkevics, A., 1988. Polarization analysis of three-component array data, *Bull. seism. Soc. Am.*, **78**(5), 1725–1743.
- Krischer, L., Megies, T., Barsch, R., Beyreuther, M., Lecocq, T., Caudron, C. & Wassermann, J., 2015. ObsPy: a bridge for seismology into the scientific Python ecosystem, *Comput. Sci. Discov.*, **8**(1), doi:10.1088/1749-4699/8/1/014003.
- Løviknes, S., Jensen, K.H., Krafft, B.A., Anthonypillai, V. & Nøttestad, L., 2021. Feeding hotspots and distribution of fin and humpback whales in the Norwegian Sea from 2013 to 2018, *Front. Mar. Sci.*, **8**, doi:10.3389/fmars.2021.632720.
- Maggi, A., Ferrazzini, V., Hibert, C., Beauducel, F., Boissier, P. & Amemoutou, A., 2017. Implementation of a multistation approach for automated event classification at Piton de la Fournaise Volcano, *Seismol. Res. Lett.*, **88**(3), 878–891.

- Malfante, M., Dalla Mura, M., Mars, J.I., Métaixian, J.-P., Macedo, O. & Inza, A., 2018. Automatic classification of volcano seismic signatures, *J. geophys. Res.*, **123**(12), 10 645–10 658.
- McCormack, M.D., Zaucha, D.E. & Dushek, D.W., 1993. First-break refraction event picking and seismic data trace editing using neural networks, *Geophysics*, **58**(1), 67–78.
- McDonald, M.A., Hildebrand, J.A. & Webb, S.C., 1995. Blue and fin whales observed on a seafloor array in the northeast Pacific, *J. acoust. Soc. Am.*, **98**(2 Pt 1), 712–721.
- Meier, M., Schlindwein, V., Scholz, J.R., Geils, J., Schmidt-Aursch, M.C., Kruger, F., Czuba, W. & Janik, T., 2021. Segment-scale seismicity of the ultraslow spreading Knipovich Ridge, *Geochem. Geophys. Geosyst.*, **22**(2), e2020GC009375, doi:10.1029/2020GC009375.
- Molyneux, J.B. & Schmitt, D.R., 1999. First-break timing; arrival onset times by direct correlation, *Geophysics*, **64**(5), 1492–1501.
- Mousavi, S.M., Ellsworth, W.L., Zhu, W., Chuang, L.Y. & Beroza, G.C., 2020. Earthquake transformer—an attentive deep-learning model for simultaneous earthquake detection and phase picking, *Nat. Commun.*, **11**(1), 3952. <https://www.ncbi.nlm.nih.gov/pubmed/32770023>.
- Mousavi, S.M., Langston, C.A. & Horton, S.P., 2016. Automatic microseismic denoising and onset detection using the synchrosqueezed continuous wavelet transform, **81**(4), V341–V355.
- Münchmeyer, J. et al., 2022a. Which picker fits my data? A quantitative evaluation of deep learning based seismic pickers, *J. geophys. Res.*, **127**(1), doi:10.1029/2021JB023499.
- Nippres, S.E.J., Rietbrock, A. & Heath, A.E., 2010. Optimized automatic pickers: application to the ANCORP data set, *Geophys. J. Int.*, **181**(2), 911–925.
- Panieri, G. et al., 2017. An integrated view of the methane system in the pockmarks at Vestnesa Ridge, 79 degrees N, *Mar. Geol.*, **390**, 282–300.
- Pedregosa, F. et al., 2011. Scikit-learn: machine learning in Python, *J. Mach. Learn. Res.*, **12**, 2825–2830.
- Plaza-Faverola, A., Bünz, S., Johnson, J. E., Chand, S., Knies, J., Mienert, J. & Franek, P., 2015. Role of tectonic stress in seepage evolution along the gas hydrate-charged Vestnesa Ridge, Fram Strait, *Geophys. Res. Lett.*, **42**(3), 733–742.
- Provost, F., Hibert, C. & Malet, J.P., 2017. Automatic classification of endogenous landslide seismicity using the Random Forest supervised classifier, *Geophys. Res. Lett.*, **44**(1), 113–120.
- Ramakrushana Reddy, T., Dewangan, P., Arya, L., Singha, P. & Kamesh Raju, K.A., 2020. Tidal triggering of the harmonic noise in ocean-bottom seismometers, *Seismol. Res. Lett.*, **91**(2A), 803–813.
- Ross, Z.E., Meier, M.-A. & Hauksson, E., 2018b. P-wave arrival picking and first-motion polarity determination with deep learning, *J. geophys. Res.*, **123**(6), 5120–5129.
- Ross, Z.E., Meier, M.A., Hauksson, E. & Heaton, T.H., 2018a. Generalized seismic phase detection with deep learning, *Bull. seism. Soc. Am.*, **108**(5A), 2894–2901.
- Saragiotis, C.D., Hadjilentiadis, L.J., Rekanos, I.T. & Panas, S.M., 2004. Automatic P phase picking using maximum kurtosis and κ -statistics criteria, *IEEE Geosci. Remote Sens. Lett.*, **1**(3), 147–151.
- Sgroi, T., Polonia, A., Beranzoli, L., Billi, A., Bosman, A., Costanza, A. et al., 2021. One Year of Seismicity Recorded Through Ocean Bottom Seismometers Illuminates Active Tectonic Structures in the Ionian Sea (Central Mediterranean), *Front. Earth Sci.*, **9**.
- Singhroha, S., Bünz, S., Plaza-Faverola, A. & Chand, S., 2020. Detection of gas hydrates in faults using azimuthal seismic velocity analysis, Vestnesa Ridge, W-Svalbard Margin, *J. geophys. Res.*, **125**(2), doi:10.1029/2019JB017949.
- Sleeman, R. & van Eck, T., 1999. Robust automatic P-phase picking: an online implementation in the analysis of broadband seismogram recordings, *Phys. Earth planet. Inter.*, **113**(1), 265–275.
- Sohn, R.A., Hildebrand, J.A., Webb, S.C. & Fox, C.G., 1995. Hydrothermal microseismicity at the megaplume site on the southern Juan de Fuca Ridge, *Bull. seism. Soc. Am.*, **85**(3), 775–786.
- Soule, D.C. & Wilcock, W.S., 2013. Fin whale tracks recorded by a seismic network on the Juan de Fuca Ridge, Northeast Pacific Ocean, *J. acoust. Soc. Am.*, **133**(3), 1751–1761.
- Stähler, S.C., Schmidt-Aursch, M.C., Hein, G. & Mars, R., 2018. A self-noise model for the German DEPAS OBS pool, *Seismol. Res. Lett.*, **89**(5), 1838–1845.
- Sultan, N., Plaza-Faverola, A., Vadakkepuliambatta, S., Buenz, S. & Knies, J., 2020. Impact of tides and sea-level on deep-sea Arctic methane emissions, *Nat. Commun.*, **11**(1), doi:10.1038/s41467-020-18899-3.
- Sutton, G.H. & Latham, G.V., 1964. Analysis of a feedback-controlled seismometer, *J. geophys. Res.*, **69**(18), 3865–3882.
- Sutton, G.H., McDonald, W.G., Prentiss, D.D. & Thanos, S.N., 1965. Ocean-bottom seismic observatories, *Proc. IEEE*, **53**(12), 1909–1921.
- Tary, J.B., Géli, L., Guennou, C., Henry, P., Sultan, N., Çağatay, N. & Vidal, V., 2012. Microevents produced by gas migration and expulsion at the seabed: a study based on sea bottom recordings from the Sea of Marmara, *Geophys. J. Int.*, **190**(2), 993–1007.
- Ugalde, A., Gaité, B., Ruiz, M., Villaseñor, A. & Ranero, C.R., 2019. Seismicity and noise recorded by passive seismic monitoring of drilling operations offshore the eastern Canary Islands, *Seismol. Res. Lett.*, **90**(4), 1565–1576.
- Vidale, J.E., 1986. Complex polarization analysis of particle motion, *Bull. seism. Soc. Am.*, **76**(5), 1393–1405.
- Wenner, M., Hibert, C., van Herwijnen, A., Meier, L. & Walter, F., 2021. Near-real-time automated classification of seismic signals of slope failures with continuous random forests, *Nat. Haz. Earth Syst. Sci.*, **21**(1), 339–361.
- Wessel, P., Luis, J.F., Uieda, L., Scharroo, R., Wobbe, F., Smith, W.H.F. & Tian, D., 2019. The Generic Mapping Tools version 6, *Geochem. Geophys. Geosyst.*, **20**, 5556–5564.
- Withers, M., Aster, R., Young, C., Beiriger, J., Harris, M., Moore, S. & Trujillo, J., 1998. A comparison of select trigger algorithms for automated global seismic phase and event detection, *Bull. seism. Soc. Am.*, **88**(1), 95–106.
- Zhu, W. & Beroza, G.C., 2018. PhaseNet: a deep-neural-network-based seismic arrival time picking method, *Geophys. J. Int.*, **216**(1), doi:10.1093/gji/ggy423.

SUPPORTING INFORMATION

Supplementary data are available at *GJI* online.

FigureS1. Example 1 of the earthquake detection on data recorded in a marine setting. The upper plot shows a waveform from the vertical channel of a seismometer used for the detection (all methods use three-component data). Below presented are characteristic functions computed by each approach (Detection, P and S phase probability for EQTransformer; P and S phase probability for the remaining two).

FigureS2. Example 2 of the earthquake detection on data recorded in a marine setting. The upper plot shows a waveform from the vertical channel of a seismometer used for the detection (all methods use three-component data). Below presented are characteristic functions computed by each approach (Detection, P and S phase probability for EQTransformer; P and S phase probability for the remaining two).

Figure S3. Example 3 of the earthquake detection on data recorded in a marine setting. The upper plot shows a waveform from the vertical channel of a seismometer used for the detection (all methods use three-component data). Below presented are characteristic functions computed by each approach (Detection, P and S phase probability for EQTransformer; P and S phase probability for the remaining two).

Figure S4. Example 4 of the earthquake detection on data recorded in a marine setting. The upper plot shows a waveform from the

vertical channel of a seismometer used for the detection (all methods use three-component data). Below presented are characteristic functions computed by each approach (Detection, P and S phase probability for EQTransformer; P and S phase probability for the remaining two).

Figure S5. Example 5 of the earthquake detection on data recorded in a marine setting. The upper plot shows a waveform from the vertical channel of a seismometer used for the detection (all methods use three-component data). Below presented are characteristic functions computed by each approach (Detection, P and S phase probability for EQTransformer; P and S phase probability for the remaining two).

Figure S6. Example 5 of the earthquake detection on data recorded in a marine setting. The upper plot shows a waveform from the vertical channel of a seismometer used for the detection (all methods use three-component data). Below presented are characteristic functions computed by each approach (Detection, P and S phase probability for EQTransformer; P and S phase probability for the remaining two).

Figure S7. Example 1 of the SDE detection on data recorded in a marine setting. The upper plot shows a waveform from the vertical channel of a seismometer used for the detection (all methods use three-component data). Below presented are characteristic functions computed by each approach (Detection, P and S phase probability for EQTransformer; P and S phase probability for the remaining two).

Figure S8. Example 2 of the SDE detection on data recorded in a marine setting. The upper plot shows a waveform from the vertical channel of a seismometer used for the detection (all methods use three-component data). Below presented are characteristic functions computed by each approach (Detection, P and S phase probability for EQTransformer; P and S phase probability for the remaining two).

Figure S9. Example 3 of the SDE detection on data recorded in a marine setting. The upper plot shows a waveform from the vertical channel of a seismometer used for the detection (all methods use three-component data). Below presented are characteristic functions computed by each approach (Detection, P and S phase probability for EQTransformer; P and S phase probability for the remaining two).

Figure S10. Example 4 of the SDE detection on data recorded in a marine setting. The upper plot shows a waveform from the vertical channel of a seismometer used for the detection (all methods use three-component data). Below presented are characteristic functions computed by each approach (Detection, P and S phase probability for EQTransformer; P and S phase probability for the remaining two).

Figure S11. Example 5 of the SDE detection on data recorded in a marine setting. The upper plot shows a waveform from the vertical channel of a seismometer used for the detection (all methods use three-component data). Below presented are characteristic functions computed by each approach (Detection, P and S phase probability

for EQTransformer; P and S phase probability for the remaining two).

Figure S12. Example 6 of the SDE detection on data recorded in a marine setting. The upper plot shows a waveform from the vertical channel of a seismometer used for the detection (all methods use three-component data). Below presented are characteristic functions computed by each approach (Detection, P and S phase probability for EQTransformer; P and S phase probability for the remaining two).

Figure S13. Example 1 of the detections recorded in noise examples for data from a marine setting. The upper plot shows a waveform from the vertical channel of a seismometer used for the detection (all methods use three-component data). Below presented are characteristic functions computed by each approach (Detection, P and S phase probability for EQTransformer; P and S phase probability for the remaining two).

Figure S14. Example 2 of the detections recorded in noise examples for data from a marine setting. The upper plot shows a waveform from the vertical channel of a seismometer used for the detection (all methods use three-component data). Below presented are characteristic functions computed by each approach (Detection, P and S phase probability for EQTransformer; P and S phase probability for the remaining two).

Figure S15. Example 3 of the detections recorded in noise examples for data from a marine setting. The upper plot shows a waveform from the vertical channel of a seismometer used for the detection (all methods use three-component data). Below presented are characteristic functions computed by each approach (Detection, P and S phase probability for EQTransformer; P and S phase probability for the remaining two).

Figure S16. Example 4 of the detections recorded in noise examples for data from a marine setting. The upper plot shows a waveform from the vertical channel of a seismometer used for the detection (all methods use three-component data). Below presented are characteristic functions computed by each approach (Detection, P and S phase probability for EQTransformer; P and S phase probability for the remaining two).

Figure S17. Example 5 of the detections recorded in noise examples for data from a marine setting. The upper plot shows a waveform from the vertical channel of a seismometer used for the detection (all methods use three-component data). Below presented are characteristic functions computed by each approach (Detection, P and S phase probability for EQTransformer; P and S phase probability for the remaining two).

supplement_attribute_importances.txt

Please note: Oxford University Press is not responsible for the content or functionality of any supporting materials supplied by the authors. Any queries (other than missing material) should be directed to the corresponding author for the paper.

APPENDIX

Table A1. Signal features calculated from the examples used to train machine learning classifier [features calculation following Provost *et al.* (2017) and Hibert *et al.* (2017)]. Numbers-channel pairs represent order of the features in the array used for classification. DFT stands for discrete Fourier transform.

Number-seismometer channel	Description	Formula
Waveform-based features		
1-Z, 63-Y, 121-X	Duration of the signal	$t_j - t_i$, where t_i and t_j : start and end of the signal
2-Z, 64-Y, 122-X	Ratio of the max and the mean of the normalized envelope	$\max[e(t)]/\text{mean}[e(t)]$
3-Z, 65-Y, 123-X	Ratio of the max and the mean of the normalized envelope	$\max[e(t)]/\text{median}[e(t)]$
4-Z, 66-Y, 124-X	Ascending time/decreasing time of the envelope	$\frac{t_{\max} - t_i}{t_j - t_{\max}}$, t_{\max} : time of the largest amplitude
5-Z, 67-Y, 125-X	Kurtosis (peakness) of the raw signal	$\frac{m_4}{\sigma^4}$, m_4 : fourth moment, σ : standard deviation
6-Z, 68-Y, 126-X	Kurtosis of the signal envelope	see 5
7-Z, 69-Y, 127-X	Skewness of the raw signal	$\frac{m_3}{\sigma^3}$, m_3 : third moment
8-Z, 70-Y, 128-X	Skewness of the signal envelope	see 7
9-Z, 71-Y, 129-X	Number of peaks in the autocorrelation function of the raw signal	-
10-Z, 72-Y, 130-X	Energy in the first 1/3 of the autocorrelation function	$\int_0^{\frac{T}{3}} C(\tau) d\tau$, T : signal duration, C : autocorrelation function
11-Z, 73-Y, 131-X	Energy in the remaining part of the autocorrelation function	See 10
12-Z, 74-Y, 132-X	Ratio of the 10 and 11	-
13-17-Z, 75-79-Y, 133-137-X	Energy of the signal in: 1-5 Hz, 5-10 Hz, 10-15 Hz, 15-20 Hz, 10-Nyquist frequency	$ES_i = \log_{10} \int_0^T y_f(t) dt$, y_f : filtered signal in the frequency range
18-22-Z, 80-84-Y, 138-142-X	Kurtosis of the signal in: 1-5 Hz, 5-10 Hz, 10-15 Hz, 15-20 Hz, 10-Nyquist frequency	see 5
23-Z, 85-Y, 143-X	RMS between the coda of the signal and the straight line $l(t) = Y_{\max} - \frac{Y_{\max}}{t_f - t_{\max}} t$	$\sqrt{Y(t) - l(t)^2}$, Y : envelope of the signal
24-Z, 86-Y, 144-X	Ratio between maximum of the envelope of the signal and signal duration	-
Frequency-related features		
25-Z, 87-Y, 145-X	Mean of the DFT	DFT: discrete Fourier transform
26-Z, 88-Y, 146-X	Maximum of the DFT	-
27-Z, 89-Y, 147-X	Frequency at the maximum of DFT	-
28-Z, 90-Y, 148-X	Frequency of the spectral centroid	$f(\gamma_1)$, see 39
29-Z, 91-Y, 149-X	Central frequency of the 1st quartile	-
30-Z, 92-Y, 150-X	Central frequency of the 3rd quartile	-
31-Z, 93-Y, 151-X	Median of the normalized DFT	-
32-Z, 94-Y, 152-X	Variance of the normalized DFT	-
33-Z, 95-Y, 153-X	Number of peaks ($>0.75 \text{ DFT}_{\text{MAX}}$)	DFT_{MAX} : maximum of the DFT
34-Z, 96-Y, 154-X	Mean peaks value from 33	-
35-38-Z, 97-100-Y, 155-158-X	Energy in $0-0.25 \cdot \text{Nyq.}$, $0.25-0.5 \cdot \text{Nyq.}$, $0.5-0.75 \cdot \text{Nyq.}$, $0.75-1 \cdot \text{Nyq.}$, where Nyq. - Nyquist frequency of the signal	$\int_{f_1}^{f_2} \text{DFT}(f) df$, f_1, f_2 : corresponding frequency range
39-Z, 101-Y, 159-X	Spectral centroid	$\gamma_1 = \frac{m_2}{m_1}$, m_1, m_2 : first and second moment
40-Z, 102-Y, 160-X	Spectral gyration radius	$\gamma_2 = \sqrt{\frac{m_3}{m_2}}$, m_3 : third moment
41-Z, 103-Y, 161-X	Spectral centroid width	$\sqrt{\gamma_1^2 - \gamma_2^2}$
Pseudo spectrogram features (calculated with DFTs of 10-s length and an overlap of 90 per cent)		
42-Z, 104-Y, 162-X	Kurtosis of the envelope of the maximum energy on the spectrograms	Kurtosis $[\gamma = 0, \dots, T](\text{SPEC}(t, f))$, $\text{SPEC}(t, f)$: spectrogram
43-Z, 105-Y, 163-X	Kurtosis of the envelope of the median energy on all spectrograms	see 42
44-Z, 106-Y, 164-X	Mean ratio between the maximum and the mean of all DFTs	$\text{mean} \left[\frac{\max(\text{SPEC})}{\text{mean}(\text{SPEC})} \right]$
45-Z, 107-Y, 165-X	Mean ratio between the maximum and the median of all DFTs	see 44
46-Z, 108-Y, 166-X	Number of the peaks in the curve showing the temporal evolution of the DFTs maximum	-
47-Z, 109-Y, 167-X	Number of the peaks in the curve showing the temporal evolution of the DFTs mean	-
48-Z, 110-Y, 168-X	Number of the peaks in the curve showing the temporal evolution of the DFTs median	-
49-Z, 111-Y, 169-X	Ratio between 46 and 47	-
50-Z, 112-Y, 170-X	Ratio between 46 and 48	-
51-Z, 113-Y, 171-X	Number of peaks in the curve of the temporal evolution of the DFTs central frequency	-

Table A1. Continued

Number-seismometer channel	Description	Formula
52-Z, 114-Y, 172-X	Number of peaks in the curve of the temporal evolution of the DFTs maximum frequency	-
53-Z, 115-Y, 173-X	Ratio between 51 and 52	-
54-Z, 116-Y, 174-X	Mean distance between the curves of the temporal evolution of the DFTs maximum frequency and mean frequency	-
55-Z, 117-Y, 175-X	Mean distance between the curves of the temporal evolution of the DFTs maximum frequency and median frequency	-
56-Z, 118-Y, 176-X	Mean distance between the 1st quartile and the median of all DFTs as a function of time	-
57-Z, 119-Y, 177-X	Mean distance between the 3rd quartile and the median of all DFTs as a function of time	-
58-Z, 120-Y, 178-X	Mean distance between the 3rd quartile and the 1st quartile of all DFTs as a function of time	-
Polarity features (all channels used)		
59	Rectilinearity	$1 - \frac{\lambda_{11} + \lambda_{22}}{2\lambda_{33}}, \lambda_{33} \gg \lambda_{22} \gg \lambda_{11}$
60	Azimuth	$\arctan(\lambda_{23}/\lambda_{13}) \times 180/\pi$
61	Dip	$\arctan(\lambda_{33}/\sqrt{\lambda_{23}^2 + \lambda_{13}^2}) \times 180/\pi$
62	Planarity	$1 - \frac{2\lambda_{11}}{\lambda_{33} + \lambda_{22}}$

Manuscript 3

1 **Local seismicity and sediment deformation in the west Svalbard margin: Implications**
2 **of neotectonics for seafloor seepage**

3

4 **P. Domel¹, A. Plaza-Faverola², V. Schlindwein^{3,4}, and S. Bünz²**

5 ¹Department of Geosciences, UiT – The Arctic University of Norway, Tromsø, Norway

6 ²iC3: Centre for ice, Cryosphere, Carbon and Climate, Department of Geosciences, UiT – The
7 Arctic University of Norway, Tromsø, Norway

8 ³Alfred Wegener Institute, Helmholtz Centre for Polar and Marine Research, Bremerhaven,
9 Germany

10 ⁴Faculty of Geosciences, University of Bremen, Bremen, Germany

11

12 Corresponding author: Przemyslaw Domel (przemyslaw.domel@uit.no)

13

14 **Key Points:**

- 15 • Earthquakes located predominantly S-SW from the Molloy Transform Fault outline, as
16 evidenced by faulted shallow sediments in seismic data
- 17 • Seismicity and seismic line at the corner between the Molloy Transform Fault and the
18 Knipovich Ridge suggest buried spreading center
- 19 • Two earthquakes at the Vestnesa Ridge seepage system may indicate reactivation of crustal
20 faults, but no link with present ridge spreading

21 **Abstract**

22 In the Fram Strait, mid-ocean ridge spreading is represented by the ultra-slow system of the Molloy
23 Ridge, the Molloy Transform Fault and the Knipovich Ridge. Sediments on oceanic and
24 continental crust are gas charged and there are several locations with documented seafloor seepage.
25 Sedimentary faulting shows recent stress release in the sub-surface, but the drivers of stress change
26 and its influence on fluid flow are not entirely understood. We present here the results of an 11-
27 month-long ocean bottom seismometer survey conducted over the highly faulted sediment drift
28 northwards from the Knipovich Ridge to monitor seismicity and infer the regional state of stress.
29 We obtain a detailed earthquake catalog that improves the spatial resolution of mid-ocean ridge
30 seismicity compared to published data. Seismicity at the Molloy Transform Fault is occurring
31 southwards from the bathymetric imprint of the fault, as supported by seismic profiles.
32 Earthquakes in the northern termination of the Knipovich Ridge extend eastwards from the ridge
33 valley, which together with syn-rift faulting identified in seismic reflection data, suggests that a
34 portion of the currently active spreading center is buried under sediments away from the
35 bathymetric expression of the rift valley. This hints at the direct link between crustal rifting
36 processes and faulting in shallow sediments. Two earthquakes occur close to the seepage system
37 of the Vestnesa Ridge further north from the network. We suggest that deeper rift structures,
38 reactivated by gravity and/or post-glacial subsidence, may lead to accommodation of stress
39 through shallow extensional faults, therefore impacting seepage dynamics.

40 Plain Language Summary

41 In the Fram Strait, between Greenland and Svalbard, the ocean floor is slowly spreading due to the
42 plate motion and this process generates most of the seismicity in the region and is also responsible
43 for sediment faulting. In this area, sediments are known to contain gas accumulations and gas is
44 being released into the ocean. It is still not well understood whether sediment deformation and gas
45 release are controlled by the plate motion and crustal changes following deglaciation of the
46 continents. To capture weak seismicity, it is necessary to have seismometers deployed locally on
47 the ocean floor. This study uses the data from a network of ocean bottom seismometers, which
48 were placed at the seafloor and recorded seismicity for 11 months. Local seismicity and high-
49 resolution seismic data showed regions of present-day tectonic deformation and help to better
50 identify major active faults in the rift valley. At the Molloy Transform Fault, earthquakes occur

51 further south than expected, and seismic lines show shallow sediment faulting. Our results suggest
52 that thick sediment deposits adjacent to the mid-ocean ridges may reactivate deep rift structures
53 and accommodate stress through extensional faults that leaked methane over geological time.

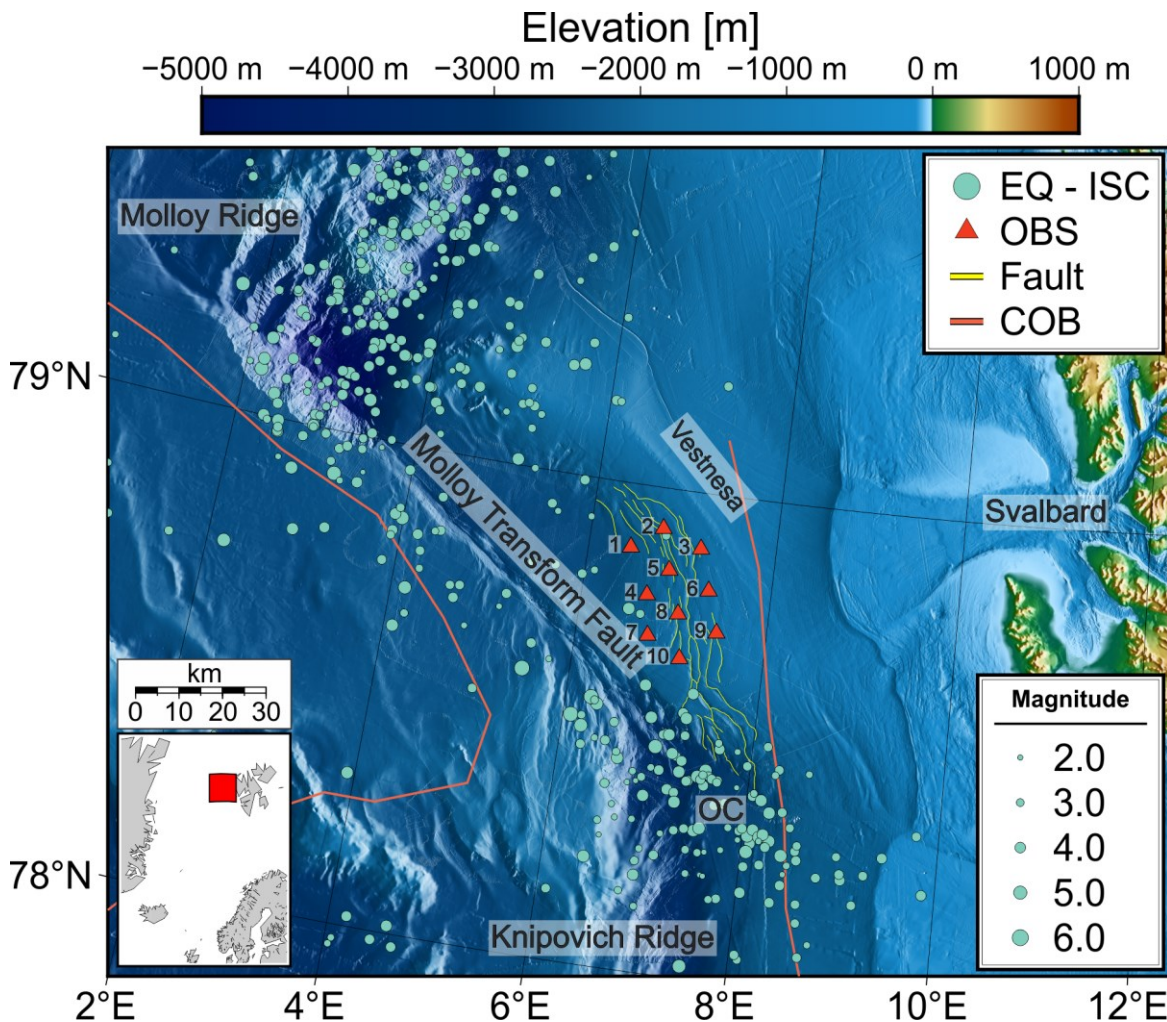
54 **1. Introduction**

55 Sedimentary structures in ocean margin settings are controlled by the local stress field. This field
56 is influenced by external (e.g., tectonic, glaciotectonic) and internal factors (e.g., pore fluid
57 pressure). Constraining the forces exerted on the sedimentary column along continental margins
58 is crucial to understand seismicity, fault development, structural deformation, and fluid transfer to
59 the ocean (e.g., England et al., 1987; Judd & Hovland, 2007). This knowledge is important in the
60 risk assessment of tsunami hazard and landslide generation with implications on both the
61 submarine (e.g., fiber telecommunication cables) and coastal infrastructures (e.g., Gardner et al.,
62 2001; Carter et al., 2014). It also improves our understanding of natural hydrocarbon seepage (e.g.,
63 Etiope et al., 2015), and aids in risk assessment of potential carbon capture and storage (CCS)
64 projects (e.g., Solomon et al., 2008).

65
66 As its name implies, “passive” margins are classically considered to be inactive, with no plate
67 tectonic influence on the present-day change in the stress field (indicated by seismological activity)
68 away from the spreading ridge zones or transform faults (Miall, 2013). It is generally assumed that
69 deformation within the sedimentary cover along rifted margins is related to gravitational processes
70 such as sliding, slumping, listric faulting, mud diapirism, focused fluid flux, and potentially salt
71 tectonics (Allen & Allen, 2005). However, recent observations at divergent continental margins
72 (e.g., along the N and S Atlantic Ocean), indicate that the assumption of tectonic quiescence of
73 these regions during the post-rift phase does not match observations in seismic profiles and heat
74 flow measurements (Paton, 2011). Some passive margins remain in structural balance over long
75 periods of time until small changes in the overall conditions drive them into instability (Hudec &
76 Jackson, 2004). The mechanisms driving changes in the local stress field in shallow sediments
77 remain poorly understood.

78 Several factors contribute to the local state of stress. Plate tectonics is one of the major forces
79 behind the current stress regime in the lithosphere (Zoback et al., 1989). In the Arctic Ocean, plate
80 tectonics is associated with mid-ocean ridge spreading, which is responsible for the majority of

81 the seismological activity observed in the region. In the Fram Strait, between Greenland and
82 Svalbard, the ridge system consists of the Molloy Ridge (MR) and the Knipovich Ridge (KR),
83 connected by the Molloy Transform Fault (MTF) (e.g., Crane et al., 1991; Figure 1). The MR is
84 connected to the Gakkel Ridge in the north and the KR to the Mohns Ridge in the south. Both the
85 MR and KR are classified as ultra-slow spreading systems (Dick et al., 2003). Spreading rates at
86 the MR are about 6.5 mm/y for the western side and 6.3 mm/y for the eastern part (Ehlers & Jokat,
87 2009). The northern part of the KR spreads more asymmetrically, with rates of 7.1 mm/y and 5.9
88 mm/y for the west and east blocks, respectively (Dumais et al., 2021). Opening of the north
89 Atlantic initiated from the south to the north around 56 Ma (Talwani & Eldholm, 1977; Crane et
90 al., 1988). The beginning of spreading process at the MR is estimated to start in the Early Miocene
91 (10-20 Ma; Engen et al., 2008). For the KR, the most recent interpretation puts the opening of the
92 northern part of the KR at ca. 20 Ma with the possibility of a ridge jump at around 18 Ma (Dumais
93 et al., 2021).



94

95 **Figure 1.** Overview map of the area investigated in this study. Red triangles represent the position
 96 of deployed ocean bottom seismometers over the investigated fault structures (yellow lines).
 97 Circles represent earthquake locations for the area provided by the International Seismological
 98 Centre (ISC) for years between 1960 and 2020. Orange lines outline most recent estimates of
 99 continent-ocean crust boundary (Dumais et al., 2021). Bathymetry provided by the International
 100 Bathymetric Chart of the Arctic Ocean (IBCAO).

101

102 Glacial isostasy is another important component of the current state of stress in the Fram Strait.
 103 The entirety of Fennoscandia, the Barents Sea and Svalbard experienced an isostatic response to
 104 the glacial load up to 800 m in the last million years (Fjeldskaar & Amantov, 2018). The transition
 105 zone between the uplift and subsidence due to glacial isostasy may be responsible for high seismic
 106 activity offshore mid Norway and in SW Barents Sea (Fjeldskaar et al., 2000; Olesen et al., 2013).

107 The area to the east of the MR along the shelf edge was under the influence of glaciations at least
108 for the past 3.6 Ma (Knies et al., 2009), with a local intensification of glacial-interglacial cycles
109 occurring around 2.7 Ma (e.g., Faleide et al., 1996; Mattingsdal et al., 2014). Glacial stress
110 modeling suggests that the area between the MR and the west-Svalbard margin shelf break is
111 within the merged Greenland and Barents Sea forebulge zone (Vachon et al., 2022). The changes
112 in stress field over the glacial cycles have potentially influenced fault kinematics and fluid
113 migration processes in the entire region.

114

115 Large amounts of sediments deposited within the west-Svalbard continental margin make
116 gravitational loading a potential source of local stress field perturbations. In addition to varying
117 extent of ice since the Late Pliocene, large amounts of hemipelagic sediments were deposited along
118 the continental margin (e.g., Faleide et al., 1996). Strong deep-water currents drive the sediment
119 transport and deposition in the form of contourites (Eiken & Hinz, 1993). Along the northern part
120 of the KR valley, there is a 600 m height (seafloor depth) asymmetry between the eastern and
121 western ridge flanks interpreted as the result of sediment loading in the eastern portion (Kvarven
122 et al., 2014; Engen et al., 2003, 2008; Crane 2001, Faleide et al., 1996), with at least 850-950 m
123 of sediments deposited on this flank and within the valley (Amundsen et al., 2011; Kvarven et al.,
124 2014). The thickest sequence of sediments formed the Vestnesa Ridge contourite drift to the NE
125 from the MTF, with the estimated thickness of more than 5 km in places (Eiken & Hinz, 1993).

126

127 One way of constraining the current state of stress in the region is by earthquake monitoring. The
128 influence of the rift system on the current tectonic regime has been reported from seismological
129 observations for decades in the area using land stations (e.g., Engen et al., 2003; Gibbons et al.,
130 2017). Sparse station coverage and large distances (>100 km) from nearest land hamper the
131 monitoring of both ridge system and intraplate seismicity, which in turn could inform about current
132 tectonic processes affecting contourite deposits (e.g., the Vestnesa Ridge) and the fault structures
133 outcropping north of the KR northward termination. For this reason, there is a large uncertainty in
134 the location of earthquakes and their hypocentral depths, leading to an imprecise seismological
135 image of the region (Figure 1; Bondár & Storchak, 2011). Temporary deployments of ocean
136 bottom seismometers (OBS) allow the detection of lower magnitude earthquakes in targeted

137 investigations along Arctic ridge boundaries (e.g., Schlindwein et al., 2015; Meier et al., 2021;
138 Jeddi et al., 2021).

139

140 In this study we document the results of a long-term (11 months) OBS survey that targeted the
141 area of bathymetric scarps characterized by thick sedimentary deposits over oceanic and
142 continental crust off the north-west Svalbard coast. This area is wedged between the intersection
143 of the KR and the MTF from the south, and the Vestnesa Ridge contourite drift to the north, north-
144 east. With this study our aim was to investigate the present-day stress regime and the influence of
145 oblique spreading on sedimentary faulting, fluid flow within the sedimentary cover and seafloor
146 seepage. At the same time, the network placement allowed us to better constrain the spreading
147 ridge system seismicity, particularly at the Molloy Transform Fault and the northern part of the
148 Knipovich Ridge.

149 **2. Deep marine fluid flow systems in the Fram Strait**

150 One of the most investigated gas hydrate and seepage systems in the Arctic is that of the Vestnesa
151 Ridge. Vestnesa Ridge is a contourite drift that continuously seeps methane through sedimentary
152 faults and fractures at the crest of its eastern segment (e.g., Bünz et al., 2012, Plaza-Faverola et al.,
153 2015; Panieri et al., 2017). The system was predominantly created from sediments deposited by
154 the contourite currents driven by the deep-water exchange between Arctic and Atlantic oceans that
155 started between 17-10 Ma ago (Eiken & Hinz, 1993; Jakobsson et al., 2007; Ehlers & Jokat, 2009).
156 The N-S oriented pattern of current sediment deposition along the west-Svalbard shelf edge was
157 influenced by the spreading direction of the oceanic seafloor leading to the NW turn of the ridge
158 crest (Johnson et al., 2015: Figure 1). The youngest seismic facies consist of glaciomarine
159 contourites with a component of turbidites close to the shelf edge, reflecting the onset of
160 Pleistocene glaciations (Eiken & Hinz, 1993; Mattingsdal et al., 2014). To the southwest, major
161 contourite drift deposits are characterized by scarps/faults visible on bathymetry data. These scarps
162 extend from the northern termination of the ultra-slow spreading Knipovich Ridge towards north,
163 north-west (Figure 1).

164

165 Along the NW-SE oriented portion of the Vestnesa Ridge crest, systems of pockmarks point to the
166 past and present episodes of methane seepage (Vogt & Crane, 1994; Bunz et al., 2012). Gas

167 hydrates with the underlying free gas accumulations are identified from seismic reflection data
168 along the entire length of the Vestnesa Ridge (Hustoft et al., 2009; Petersen et al., 2010; Goswami
169 et al., 2015; Plaza-Faverola et al., 2017; Singhroha et al., 2016, 2019). Presently documented
170 seepage is contained within the eastern part of the ridge crest, but past seepage activity on the
171 western segment of the system is well documented in sediments, seismic data, and bathymetry
172 (Vogt & Crane, 1994; Consolaro et al., 2015; Plaza-Faverola et al., 2015; Cooke et al., 2023).
173 Current seepage activity from pockmarks occurs at the termination of subseafloor fluid flow fault
174 systems (Plaza-Faverola et al., 2015). Orientation of the faults (from 3D high-resolution seismic
175 data) is similar to the bathymetric scarps propagating northward from the Knipovich Ridge;
176 therefore, a potential link has been suggested (Plaza-Faverola et al., 2015). The creation of the
177 bathymetric scarps itself was postulated to be an indication of the present-day northward
178 propagation of the spreading Knipovich Ridge (Crane et al., 2001).

179

180 The presence of gas hydrate deposits and free gas accumulations has also been documented for
181 almost the entire area with the bathymetric scarps between the Vestnesa Ridge and KR using
182 seismic interpretation (Vanneste et al., 2005; Madrussani et al., 2010). Tidally modulated seafloor
183 gas emissions have been inferred from pressure and temperature data about 20 km to the east-
184 southeast from the area presented in this study (Sultan et al., 2020). Active seafloor seepage
185 observed on hydroacoustic measurements was recently documented at one of the seafloor
186 pockmarks adjacent to sedimentary faults north of the KR (Plaza-Faverola, 2022).

187

188 The process behind spatial variation in currently observed seepage is still a matter of debate. In
189 the past (< 160 ka), seepage intensification episodes at the Vestnesa Ridge have been directly
190 linked to the time shortly after glacial maxima, placing the highest emphasis on glacially induced
191 stress as a factor driving fault activation and seepage activity (Schneider et al., 2018; Himmler et
192 al. 2019). Seepage activity here has also been proposed to be associated with an extensional stress
193 regime generated from the northward propagation of the KR (e.g., Vanneste et al., 2005; Plaza-
194 Faverola & Keiding 2019). At present day, the extensional forcing from ridge spreading, glacial
195 isostatic adjustment and gravitational stress due to the sediment loading are all considered as a
196 potential culprit controlling deep marine seepage activity in the region (Plaza-Faverola et al., 2015;
197 Plaza-Faverola & Keiding, 2019; Vachon et al., 2022).

198 **3. Data and Methods**

199 3.1 OBS network deployment and recovery

200 The data we used for this study is part of an experiment intended to constrain the stress regime and
201 its role on fault-controlled seepage in the west-Svalbard margin. A network of closely spaced
202 OBSs (10 instruments separated within 10 km from its closest neighbor) was intended to record
203 any potential earthquake associated with sedimentary faults to the north of the KR termination
204 (Figure 1). The aim was to infer the dominant tectonic stress regime locally, based on focal
205 mechanisms from recorded earthquakes.

206
207 The instruments were dropped freely to the seafloor in August 2020 and recovered in July 2021
208 during cruises CAGE20-5 (Bünz, 2023) and CAGE21-3 (Plaza-Faverola et al., 2022a), onboard
209 R/V Helmer Hanssen. Each station was located approximately 10 km apart from all of its nearest
210 neighbors. All stations except VSN02 and VSN10 were equipped with a Trillium Compact
211 broadband seismometer (sensitive to periods of 120 s). These OBSs were provided by the German
212 Instrument Pool for Amphibian Seismology DEPAS (Schmidt-Aursch & Haberland, 2017).
213 Stations VSN02 and VSN10 used instrumentation from UiT – The Arctic University of Norway.
214 These consisted in short-period geophones with 4.5 Hz corner frequency commonly used for active
215 source high resolution experiments (e.g., Singhroha et al., 2020). Additionally, each unit had a
216 hydrophone attached to its frame. Each OBS recorded data continuously with a sampling
217 frequency of 100 Hz.

218 3.2 Preprocessing

219 3.2.1 Relocation

220 We established the true position of each OBS on the seafloor (red triangles in Figure 1) using
221 active seismic surveys conducted directly after the deployment. We used the direct arrival of the
222 P wave from hundreds of seismic shots with known positions and inverted the travel-time equation
223 for the OBS location with the smallest root-mean-square (RMS) error. For the calculations, we
224 assumed an average P wave velocity in the water column of 1500 m/s. We estimated the average
225 error in positioning stations to be smaller than 10 m.

226 3.2.2 Time correction of data

227 We synchronized the internal clock of each OBS recording unit with the GPS signal prior to
228 deployment and after recovery, and thus established the absolute clock drift (skew) for all stations
229 except VSN03, VSN04, VSN06 and VSN09 (Table S1). For these stations, a synchronization of
230 the clocks after recovery was not possible. Prior experience with the clocks of the recording units
231 showed that the assumption of a linear drift of the clock is not always valid. We followed the cross-
232 correlation procedure described by Hannemann et al. (2014) to independently determine the time-
233 dependent clock drift for each station. We filtered the data in the frequency range of 0.1 – 1 Hz
234 and correlated the recorded signal daily between station pairs using a window of 250 s length with
235 50% overlap (a subset of the plots is presented in Figures S1-S2). Based on the results, we assumed
236 that station VSN01 had a linear drift and the absolute skew value for it was known from the clock
237 synchronization after recovery (Table S1). We therefore selected it as a reference station and
238 applied a linear skew correction to it. We then repeated cross-correlations between VSN01 and all
239 other stations to determine the time-dependent clock drift for other instruments (Figures S3-S11).
240 We found that only for stations VSN04 and VSN06 (in addition to VSN01), a linear skew
241 correction would be correct. We subsequently fitted a third-degree polynomial to all established
242 skew curves and applied daily, linear corrections approximating the fitted curve for each station.
243 In the final step, we verified the correct skew adjustment by a final round of pair-wise cross-
244 correlations (Figures S12-S13). We found the residual skew being lower than the expected
245 accuracy of the manual picking of seismic phases of about 0.2 s, thus acceptable for further data
246 analysis (Figure S14).

247 3.3 Earthquakes recorded by the OBS network

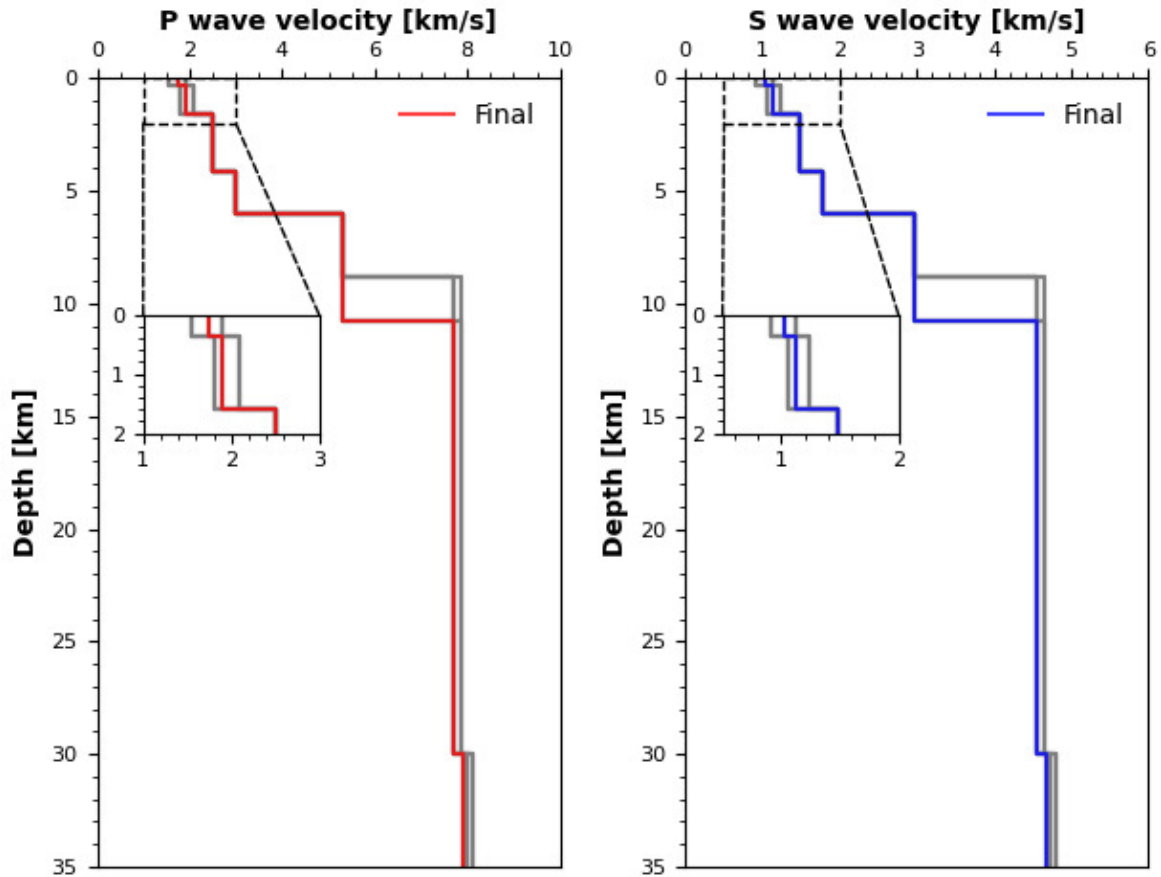
248 3.3.1 Detection and phase picking

249 We conducted a search for earthquakes on each station using the short-term average/long-term
250 average (STA/LTA) picker (Allen, 1982), and we subsequently identified actual earthquake
251 detections using a Random Forest classifier on time windows around each potential event (Hibert
252 et al., 2014, 2017; Provost et al., 2017). We adjusted the parameters of the STA/LTA detector to
253 the expected local seismicity in the area in the following fashion: STA window length – 0.8 s, LTA
254 window length – 45 s, detection start ratio – 7 and detection end ratio – 1.5. For event classification,

255 we used a model trained previously on events recorded by a different experiment at the Vestnesa
256 Ridge (Domel et al., 2023). We manually verified all detections recognized as earthquakes and
257 found 358 events with a signal-to-noise ratio high enough to manually pick seismic phases for at
258 least one station. We subsequently picked P and S wave arrival times of events (where possible)
259 for all stations using the SEISAN software package (Havskov & Ottemöller, 1999; Havskov et al.,
260 2020). Pick uncertainty is about 0.2 s.

261 3.3.2 Earthquake location procedure

262 Initial locations showed that the seismicity is present mostly outside of the seismic network, which
263 makes the estimation of a minimum 1D velocity model difficult using common procedures such
264 as VELEST (Kissling et al., 1995). We therefore used the following forward approach, applying
265 the HYPOSAT location algorithm for estimating earthquake locations (Schweitzer, 2001). Instead
266 of inverting for seismic velocities from our earthquake records, we used seismic velocity
267 constraints from a nearby seismic refraction study (Ritzmann et al., 2004). Seismic velocities
268 within the shallow sediments (up to 1600 m below the seafloor) were obtained from a P-wave
269 reflection tomography available in the study area (Madrussani et al., 2010). In the initial testing,
270 we tried different V_p/V_s ratios and chose 1.69 for the final model evaluation. We represented the
271 shallow sediments as two layers with fixed layer boundary depths at 350 m and 1600 m below the
272 seafloor. For the upper layer we tested V_p velocities between 1.5 – 1.9 km/s for V_p (Figure 2).
273 Similarly, for the bottom layer we tested velocities between 1.8 – 2.1 km/s. The section of the
274 model below 1600 m depth was derived from the refraction study (Ritzmann et al., 2004), and
275 remained mostly fixed in the analysis. We tried different depths of the crust-mantle boundary to
276 better match the parts of the refraction profile closest to our study area and varied slightly the P-
277 wave velocity in the upper mantle (between 7.9 – 8.1 km/s). All individual variations of velocity
278 resulted in 18 different models tested model (Figure 2).



279

280 **Figure 2.** Overview of all velocity models tested for relocation in HYPOSAT software. Color lines
 281 represent the final models using to obtain earthquake locations for P and S waves, red and blue,
 282 respectively.

283

284 To compare the effect of the different velocity functions on event relocation, we first located all
 285 events using a regional velocity model (BAREY; Hicks et al., 2004) with a fixed hypocenter depth
 286 of 10 km and selected a small subset of earthquakes meeting the following criteria: RMS error <
 287 0.8 s, number of used seismic phases > 20, average error ellipse size < 10 km, and maximum
 288 distance from the center of the network < 50 km.

289

290 The resulting subset of 46 earthquakes was repeatedly located with all 18 different versions of our
 291 local velocity model for fixed hypocenter depths of 8,10,12,15,25, and 30 km, respectively. To
 292 obtain a location solution for each pair of model variant and fixed hypocenter depth, three iterations
 293 with HYPOSAT were performed, using the average station residual of all earthquakes as a station

294 correction term in the subsequent iteration. It is important to keep in mind that we cannot reliably
295 establish depths of earthquakes located further than twice the focal depth from the station and
296 without dense azimuthal coverage (e.g., Havskov et al., 2011), which in our case means outside
297 the deployed network. For thin oceanic crust in spreading zones, earthquakes usually originate at
298 depths of about 0-30 km (e.g., Schlindwein et al., 2016). The fixed earthquake depths used in
299 relocation were selected to minimize errors in the positioning of the events but cannot be
300 interpreted in a meaningful way. Consequently, we refrained from the discussion on the
301 hypocentral depth of earthquakes.

302

303 For each event, we selected the fixed-depth location with the lowest RMS error and lowest average
304 error ellipse size as a final solution for the respective velocity model variant. We then computed
305 average values of the RMS error and the error ellipse size for all events within each velocity model
306 variant. This way, we could compare the performance of the different velocity models. We selected
307 the model that had both lowest average RMS error and average error ellipse (red line in Figure 2).
308 In the testing, we found that the differences between different models were ultimately very small
309 and obtained earthquake locations very similar (max. 0.01 s for the average RMS error, less than
310 0.2 km for the average error ellipse). The final 1D velocity model was used by HYPOSAT up to
311 an epicentral distance of 1 degree (approx. 111 km) from each station. Events at larger distance
312 were located using the regional velocity model BAREY (Hicks et al., 2004).

313

314 We subsequently located all 358 earthquakes using the final velocity model and for each event we
315 retained the result with the fixed depth that produced the smallest RMS error. For further analysis,
316 we only used events that met the following criteria: RMS error < 0.4 s, minimum number of
317 stations with seismic phases used ≥ 3 and average error ellipse < 10 km. The resulting dataset
318 contained 254 earthquakes. We include the plots of residual times for P and S phase picks (the
319 difference between computed and observed travel times of waves) in the supplement (Figures S15
320 & S16).

321

3.3.3 Local magnitude estimation

322 We calculated local magnitudes based on manual picks of the maximum amplitude of the S wave
323 train on the horizontal channels of the Wood-Anderson simulated OBS data (e.g., Kanamori &

324 Jennings, 1978; Hutton & Boore, 1987). We used the formula of Hutton and Boore with the default
325 parameters (Hutton & Boore, 1987). Using the maximum curvature method (Wyss et al., 1999;
326 Wiemer & Wyss, 2000), we estimated a magnitude of completeness M_c of 2.5 for our earthquake
327 dataset.

328 3.4 Other earthquake catalogs

329 For the general overview of the regional seismicity in the past decades we used the International
330 Seismological Centre (ISC) Reviewed Bulletin that compiles phase picks from all seismological
331 networks in the area and provides its own hypocenter solutions (Bondár & Storchak, 2011). We
332 plotted all events in the area from years 1980-2020 that have an RMS error < 3 s, contributed
333 phases of at least 10 stations to the location solution, and had magnitudes ≥ 2.0 (Figure 1). These
334 selection criteria resulted in 580 earthquakes.

335

336 We further searched for earthquakes that occurred during our experiment and were detected both
337 on land and by our network. For that purpose, we referred to the bulletin of the Norwegian National
338 Seismic Network (NNSN) (Ottemöller et al., 2018). In addition to the stations on Svalbard and in
339 Norway, it routinely incorporates the phase picks from the Danish seismological stations in
340 Greenland. We used all locations with an RMS error ≤ 2 s for our analysis, resulting in a total of
341 293 earthquakes.

342

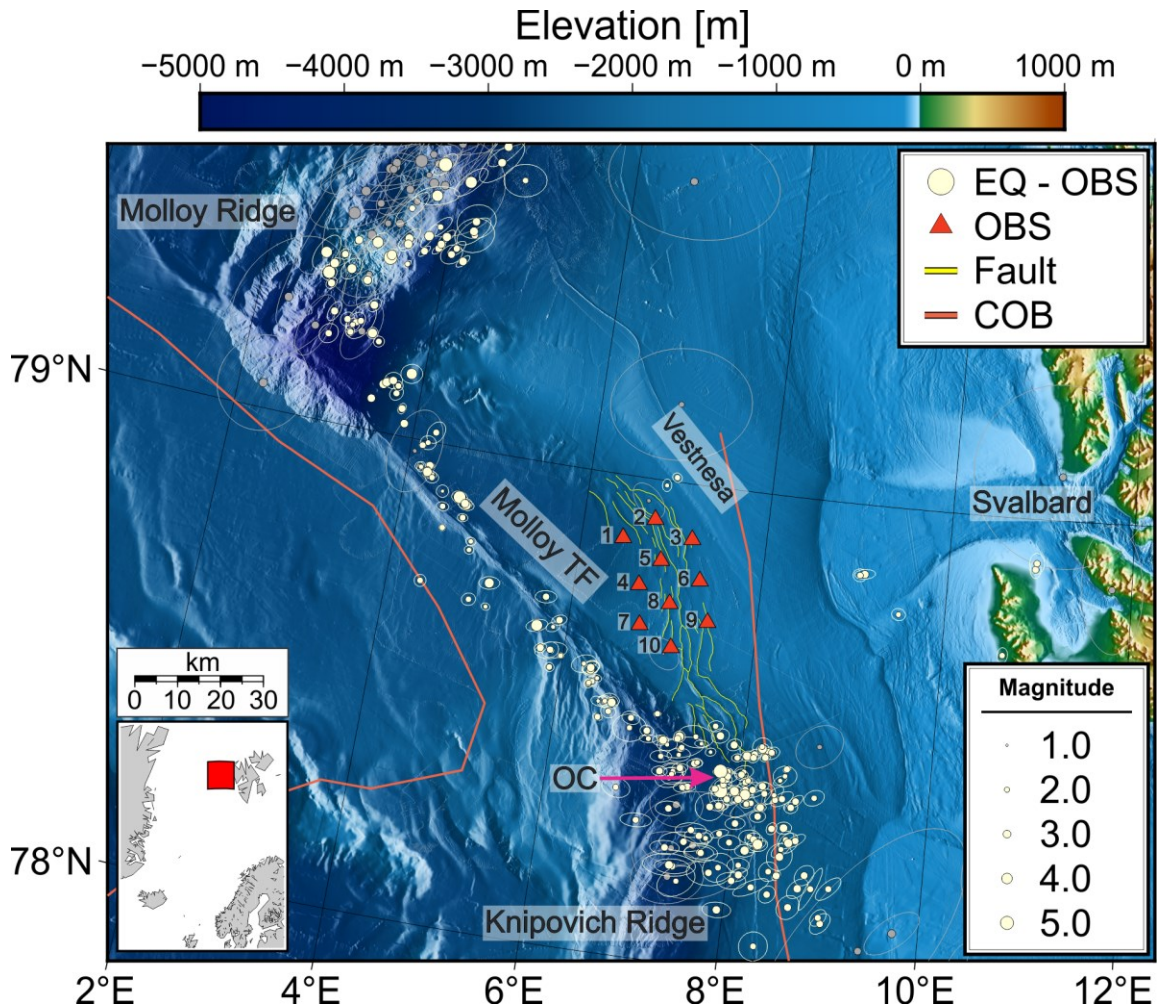
343 Out of 358 earthquakes detected and located by the OBS network, we identified 170 that were also
344 recorded on land and included in the NNSN bulletin. For these events, we additionally obtained
345 the phase picks of the land stations. We manually matched each individual event between the
346 catalogs and combined the phase picks from land stations and OBS stations to relocate the events
347 using HYPOSAT. Our goal was to determine the best constrained location for each earthquake
348 and therefore we compared the locations results and errors from using the OBS network only, the
349 NNSN reported locations, and finally, a relocation combining the phase picks of both networks.
350 For the relocation with combined phase picks, we repeated the same procedure as when using only
351 OBS observations. Locating earthquakes using phase picks from stations in vastly different
352 geological conditions with large differences of crustal thickness to be accommodated in a 1D
353 velocity model led to overall higher location errors. We therefore considered earthquakes as well

354 located when an RMS error < 1 s (compared to 0.4 s when using OBS data only). With this criterion
355 we retained 85 of the 170 earthquakes as well located for further analysis.

356 **4. Results**

357 4.1 Regional seismicity

358 Our OBS network detected and reliably located the regional seismicity in an area comprising the
359 nearby oceanic ridges: the Molloy Ridge (MR), and the northernmost part of the Knipovich Ridge
360 (KR), the Molloy Transform Fault (MTF) and the coast of Svalbard (Figure 3). Almost all
361 seismicity is concentrated along the North American and the Eurasian plate boundaries and is
362 related to plate motion. Events at the MR seem to occur well within the bathymetric outline of the
363 ridge axis. Along the MTF, earthquakes are closely aligned with the fault outline in the north-
364 western part and positioned slightly to the southwest in the south-eastern part of the fault (Figure
365 3). We notice a large number of earthquakes originating from the KR but spread out in the easterly
366 direction. There is an obvious clustering of events at the outside corner, away from what seems to
367 be the rift valley of the KR based on bathymetry data. This area is bounded toward the north by a
368 fault, the prolongation of the MTF that extends past the KR rift valley toward Svalbard (Figure 3).
369 Here, we refer to this area as the outside corner between the MTF and the KR (Figure 3). We do
370 not observe seismicity propagating northwards from the KR and no earthquakes were detected
371 within the deployed network. We detect two weak earthquakes of magnitudes 1.2 and 2.0,
372 respectively, close to the crest of the Vestnesa Ridge to the north from the OBS network (Figure
373 3). Additional three weak ($M < 3$) events occurred close to the shelf edge on the west coast of
374 Svalbard and a few similarly small earthquakes are visible near to and at the mainland of the
375 archipelago.



376

377 **Figure 3.** Regional map of the seismicity with all earthquakes locations obtained during ocean
 378 bottom seismometer (OBS) deployment (August 2020 – July 2021). Circles around each location
 379 represent the error ellipse for each earthquake. Earthquakes and circles in gray are locations below
 380 the accuracy criteria selected (RMS error < 0.4 s, minimum number of stations with seismic phases
 381 used ≥ 3 and average error ellipse < 10 km). OC marks the location of the outside corner of the
 382 Knipovich Ridge – Molloy Transform Fault intersection discussed more in the text. Rest of the
 383 labels and bathymetry the same as in Figure 1.

384

385 Throughout the duration of the survey, earthquakes occurred in all the described areas without any
 386 larger temporal clusters of seismicity like earthquake swarms or prominent main shock – after
 387 shock sequences, apart from a few sporadic small clusters in the rift valleys. The magnitudes of
 388 the well-located events from Figure 3 are between 0.9 and 5.3. Among the strongest $M > 4$ events,

389 most are contained within the rift valley of the MR. Two out of four events with magnitudes $M >$
390 5 originate there as well, but the other two are observed in the outside corner between the MTF
391 and KR (Figure 3).

392 4.2 Quality assessment of the obtained seismicity map

393 We do not observe earthquakes occurring within the network; hence we focus on the analysis of
394 the recorded earthquake epicenter distribution. The residual times of P and S phase picks used in
395 earthquake location show good reliability of the results (Figures S15 & S16). The majority of the
396 picks is distributed narrowly around zero, with a symmetric distribution indicating correct phase
397 identification. The P phase picks are mostly contained in a range between -0.2 s and 0.2 s for all
398 the stations (between -0.4 s and 0.4 s for S phase picks). The largest deviation from the symmetric
399 pattern and above ranges of residuals is for stations VSN02 and VSN10, and because of the
400 generally larger residuals, these are also the stations utilized the least in the relocation process. The
401 elongation of our network in NW-SE direction (Figures 1 & 3) leads to a preferred orientation of
402 the semi-major axis of the error ellipses in SW-NE direction for the earthquakes in the northern
403 part of the KR. Therefore, it is especially important to critically assess the accuracy of earthquake
404 locations from the MTF and the outside corner between the MTF and KR before suggesting any
405 geological interpretation for the area. We accomplish this by comparison of OBS derived
406 earthquake locations to well constrained ISC results since 1960, one-to-one comparisons of the
407 earthquake locations obtained using OBS data and NNSN bulletin, and relocations of the observed
408 events using combined phase picks from the OBS network and provided by the NNSN bulletin.

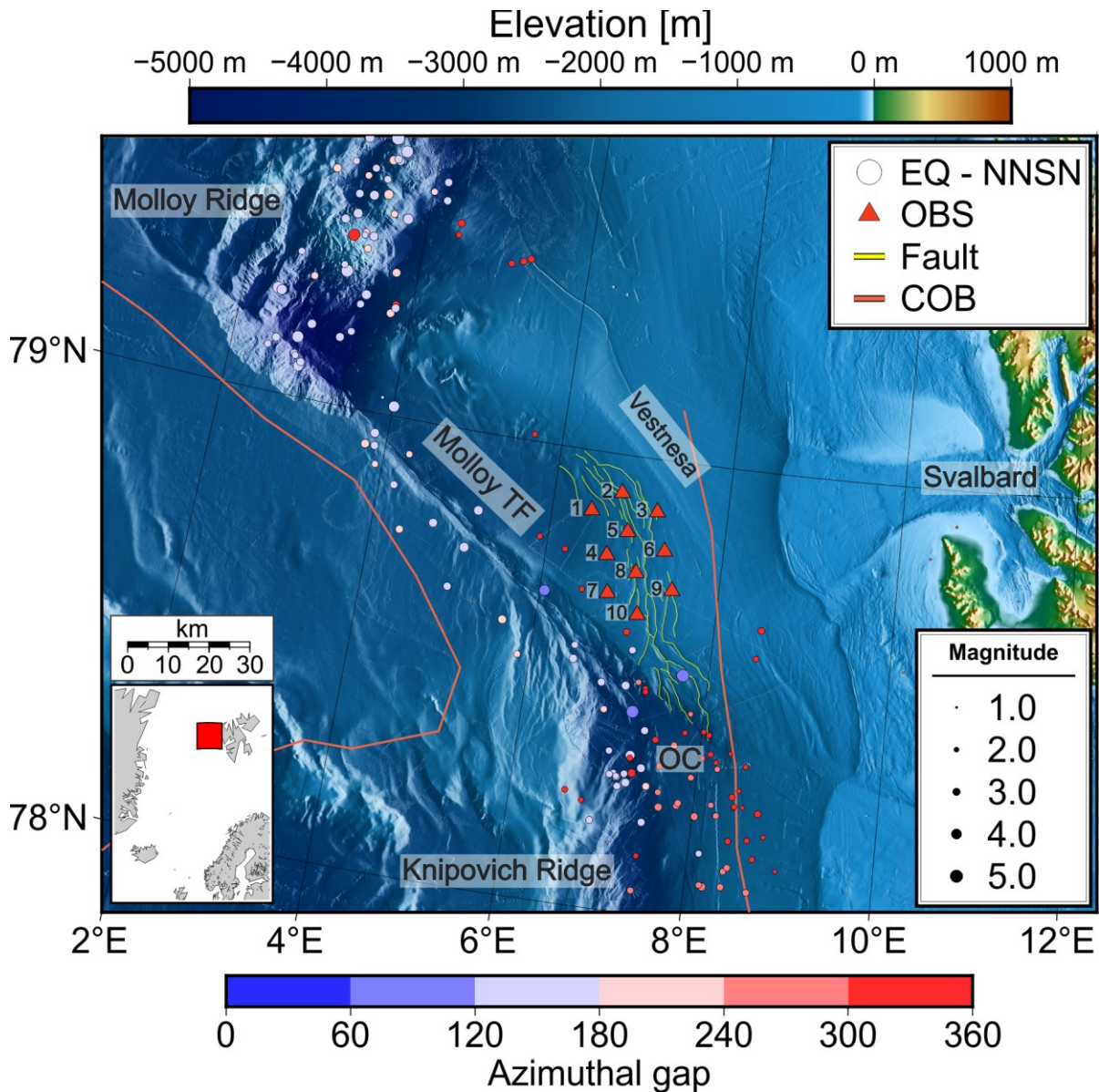
409 4.2.1 Comparison with the ISC Reviewed Bulletin

410 The observed seismicity in the ISC Reviewed Bulletin in the last 40 years appears to be much more
411 spread out along the plate boundaries, especially along the MTF (Figure 1). Most of the
412 earthquakes are located southwest of the bathymetric expression of the fault outline. Some events
413 are also reported in the area of the fault scarps on the Vestnesa Ridge flanks within our OBS
414 network. Seismicity in the vicinity of the MR is dispersed in the eastern direction, with many
415 events located in the west part of the Vestnesa Ridge sedimentary drift. The presence of seismicity
416 in the outside corner between the MTF and KR (OC in Figure 1) is clearly visible here, in the same
417 manner as in our study (Figure 3). Events with magnitudes ≥ 5 are located within the bathymetric

418 outline of this feature. Likewise, a similar shift of the earthquake locations eastward in the northern
419 part of the KR can be observed. Overall, we see that the seismicity pattern recorded by our OBS
420 network is in a good agreement with the longer-term observations provided by the ISC Bulletin,
421 but our network yields a sharper image of the seismicity with less scatter and more focused
422 earthquake locations along the plate boundaries.

423 4.2.2 Comparison with the regional NNSN bulletin for the duration of the OBS 424 survey

425 The results of the observations by the NNSN regional network during the time period of the OBS
426 deployment do not differ drastically from the seismicity map obtained from the OBS data (Figure
427 4). We plot the NNSN earthquake locations color-coded by the azimuthal gap of observations,
428 which can help determine which events are observed from many different directions and for which
429 the observations are limited mostly to seismic stations on Svalbard. We see that well-recorded
430 events with a low azimuthal gap are located in close vicinity of the plate boundaries. Earthquakes
431 along the MTF are more spread out compared to our OBS data, and again a large portion of them
432 is situated to the southwest of the fault outline. As in our survey, there is seismicity present at the
433 outside corner between the MTF and KR intersection (OC in Figure 4), however most observations
434 by the NNSN have limited azimuthal coverage, lacking phase arrivals west of the KR, mainly from
435 Greenland. Since some of the events there have a magnitude as high as 4.0, we suspect that the
436 ridge prevents wave propagation toward the west. Two strong ($M \geq 5.0$) events, which are located
437 by our OBS network close to each other in the outside corner between the MTF and KR, have
438 locations in the KR ridge valley and north of the corner, toward the fault scarps of the Vestnesa
439 Ridge (outlined in yellow in Figure 4). NNSN locates two earthquakes close to the shelf edge,
440 southeast of our OBS network. These events are visible in the OBS data, but the noise levels are
441 too high to make accurate phase picks. In general, we can say that despite the confined nature
442 of our OBS network, the recorded seismicity seems to be better aligned with the dominant tectonic
443 structures of the region than the earthquakes located in the same time period by the NNSN regional
444 network.



445

446 **Figure 4.** Earthquakes recorded and located in the study area by Norwegian National Seismic
 447 Network (NNSN) using observations from permanent land stations. Color of the circle represent
 448 the azimuthal gap of seismic phase observations. All other information and data used are the same
 449 as Figures 1 & 3.

450

4.2.3 Joint observations of seismicity with the OBS data and NNSN phase picks

451

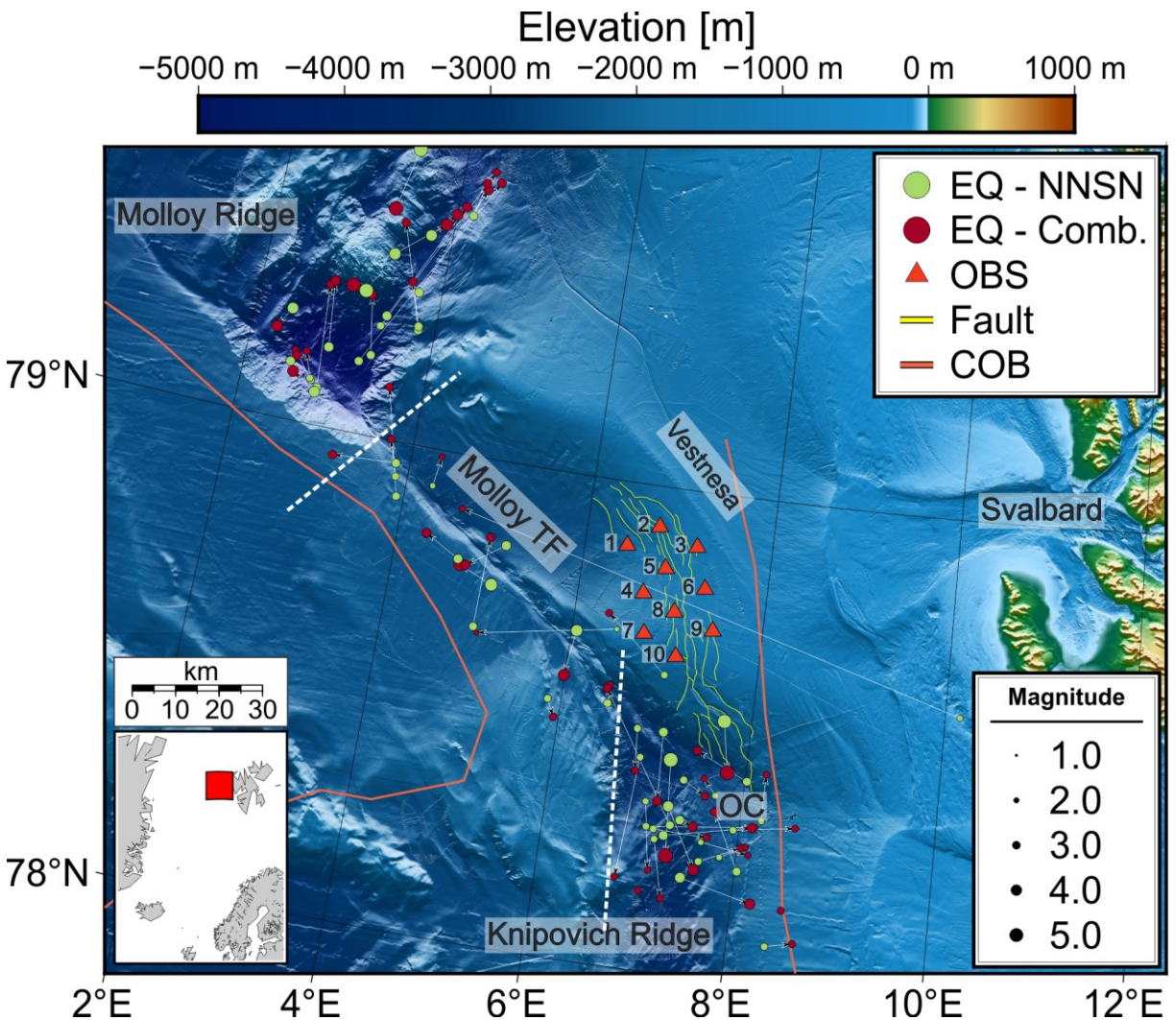
Merging the phase observations from the NNSN network with our marine data leads to a large
 452 rearrangement of originally NNSN-reported locations (Figure 5). We split the seismicity map into
 453 three regions, approximately separating the KR, MTF and MR to compute the average epicenter

454 shift and median azimuth of it (Table 1; dashed lines in Figure 5). Weak events with small
455 azimuthal coverage experience the largest shift and become positioned closer to the plate
456 boundaries and their newly determined locations are very close to the results from OBS data only
457 (Figure 3). The median amount of the distance that epicenters shifted is very similar for all regions
458 (Table 1). Across the MR, there is a noticeable trend of moving hypocenters towards NW and NE
459 directions (circular mean of epicenter shift azimuth of 332; Table 1), however the new locations
460 are still following the bathymetric outline of the rift valley. The seismicity along the MTF exhibits
461 a similar shift of epicenter distance and the circular mean of epicenter shift azimuth is similar to
462 the MR (Table 1). The overall image of seismicity does not change there between the maps, with
463 the exception of an event reported close to the mainland being relocated to the MTF and a number
464 of events being moved either from southwards of the fault outline northwards or vice versa.
465 Overall, the locations obtained from combining the datasets are more closely aligned along the
466 MTF than the positions reported in NNSN bulletin and do not greatly differ from the locations
467 obtained from OBS data. At the outside corner between the MTF and KR and on the northern part
468 of the KR itself the events are generally moved eastward when seismic phases from OBS data are
469 included (circular mean of epicenter shift azimuth of 89 in Table 1). Some events exhibit a large
470 shift southward, including one earthquake of a magnitude $M > 5.0$ that is now positioned much
471 further south and not anymore on the extension of the MTF propagating southeast. Inversely, a
472 second similarly large event that was located north of the outside corner between the MTF and KR
473 is now placed directly on the large fault outline and its location is almost identical to the position
474 obtained from only the OBS data (Figures 3 & 5). Inversely, it can be said that combining phase
475 picks from OBS and NNSN catalog generally shifts the epicenters westward compared to
476 seismicity map from only OBS data (Figure S17). Combining the phase observations from OBS
477 and NNSN data leads to smaller azimuthal gaps for earthquakes, particularly in the KR area, but
478 the overall RMS errors of resulting locations are higher (0.46 s versus 0.16 s, compared to the
479 locations of these events from OBS data). Therefore, at least for the earthquakes close to the OBS
480 network, the obtained locations using the combined datasets are likely less accurate. Ultimately,
481 in all of the discussed catalogs the occurrence of seismicity in the outside corner between the MTF
482 and KR is clearly visible.
483

484 **Table 1.** Median epicenter shift of earthquake locations and circular mean of epicenter shift
 485 azimuth between the observations of NNSN network (land data) and locations for the same events
 486 when phase picks from OBS data are included (combined observations). Earthquakes are split into
 487 three separate groups, roughly encompassing the Molloy Deep, the Molloy Transform Fault and
 488 the Knipovich Ridge (separation shown on Figure 5).

Region	Median epicenter shift [km]	Circular mean of epicenter shift azimuth [°]
Molloy Ridge	12.7	332
Molloy Transform Fault	12.2	346
Knipovich Ridge	13.1	89

489



490

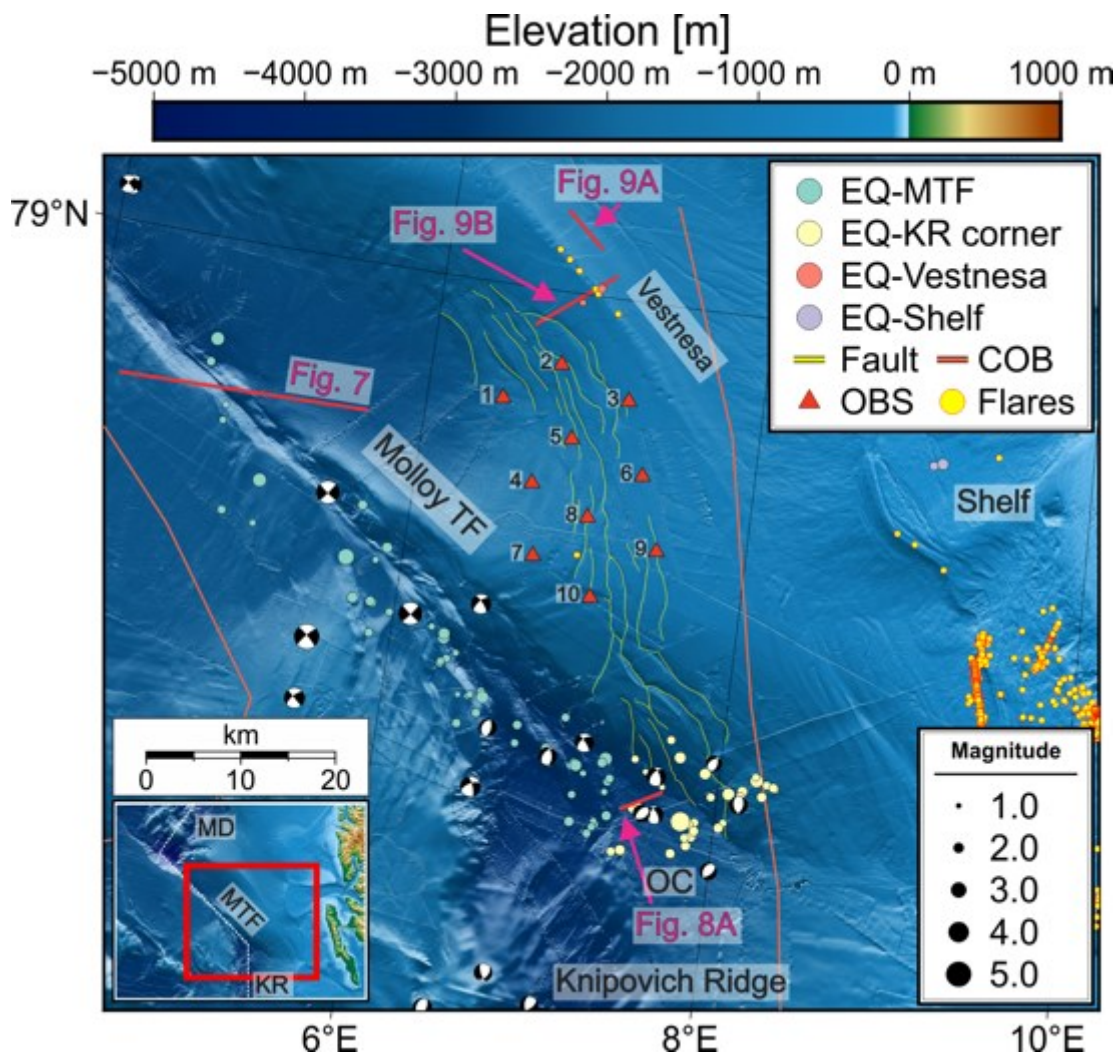
491 **Figure 5.** Regional map of seismicity showing the difference between observations from
492 Norwegian National Seismic Network (NNSN; green circles) and earthquake locations when phase
493 picks from OBS data are included (Combined; red circles), with arrows showing the change in
494 each individual event position. Other labels and symbols the same as in Figures 1,3 & 4).

495 4.2.4 Rationale for an interpretable local seismicity catalog

496 Since all of the earthquakes located by our OBS stations are outside the designed network, it is
497 important to determine for how big of an area the obtained local seismicity catalog provides more
498 accurate results compared to regional and global bulletins and can be interpreted with regards to
499 the local geology. The general seismicity pattern is similar to decadal observations provided by
500 the ISC, but with a better alignment to the plate boundaries. We focus on two important
501 observations in the later sections. First is a presence of seismicity in the outside corner between
502 the MTF and KR, visible as a spread-out cloud of earthquakes on ISC data (OC in Figure 1).
503 Observations from the nearby OBS network confirm it and with the relocation combining OBS
504 phases with NNSN land observations we verify that events with a low azimuthal coverage in the
505 NNSN catalog, while rearranged, are still present in this corner (Figures 3, 4 & 5). In this process,
506 we also position a $M > 5.0$ earthquake directly on the bathymetric outline of the MTF extension in
507 a location almost identical to the one obtained from just OBS data (Figures 3 & 5). Secondly, there
508 is a visible shift of earthquake locations to the southwest of the MTF outline. It is seen as more
509 earthquakes located there in all of the catalogs discussed (Figures 3, 4 & 5). Overall, the observed
510 pattern does not change by much when we combine land and marine observations.

511
512 We put a conservative limit of 50 km from the geographic midpoint of the OBS network as an area
513 for which we interpret the earthquake catalog (Figure 6). This value is based on the average RMS
514 error of the calculated hypocenters and the larger amount of weak events observed compared to
515 those reported in land NNSN catalog (Figures 3 & 4). The magnitude $M > 5.0$ earthquake in the
516 outside corner between the MTF and KR within this limit has an RMS error of 1.7 s in the NNSN
517 catalog and 0.4 s when adding OBS phases and relocating. For the same event, location from OBS
518 data has the RMS error decreased to 0.22 s. For all of the events reported in the NNSN catalog and
519 seen on OBS data within this radius, locations from OBS data show a decrease of the average RMS
520 error from 1.05 s to 0.17 s. For the given radius, the NNSN catalog provides only 15 earthquake

521 locations compared to a total of 68 observed on OBS data during the same time period. Therefore,
 522 at least for events located at the MTF and northern portion of the KR, we believe the OBS-based
 523 hypocenter locations are more reliable and the overall image of seismicity is more detailed. The
 524 resulting catalog includes in addition two earthquakes on the Vestnesa Ridge sedimentary drift and
 525 two events on the shelf edge, none of them reported on land (Figure 6).



526

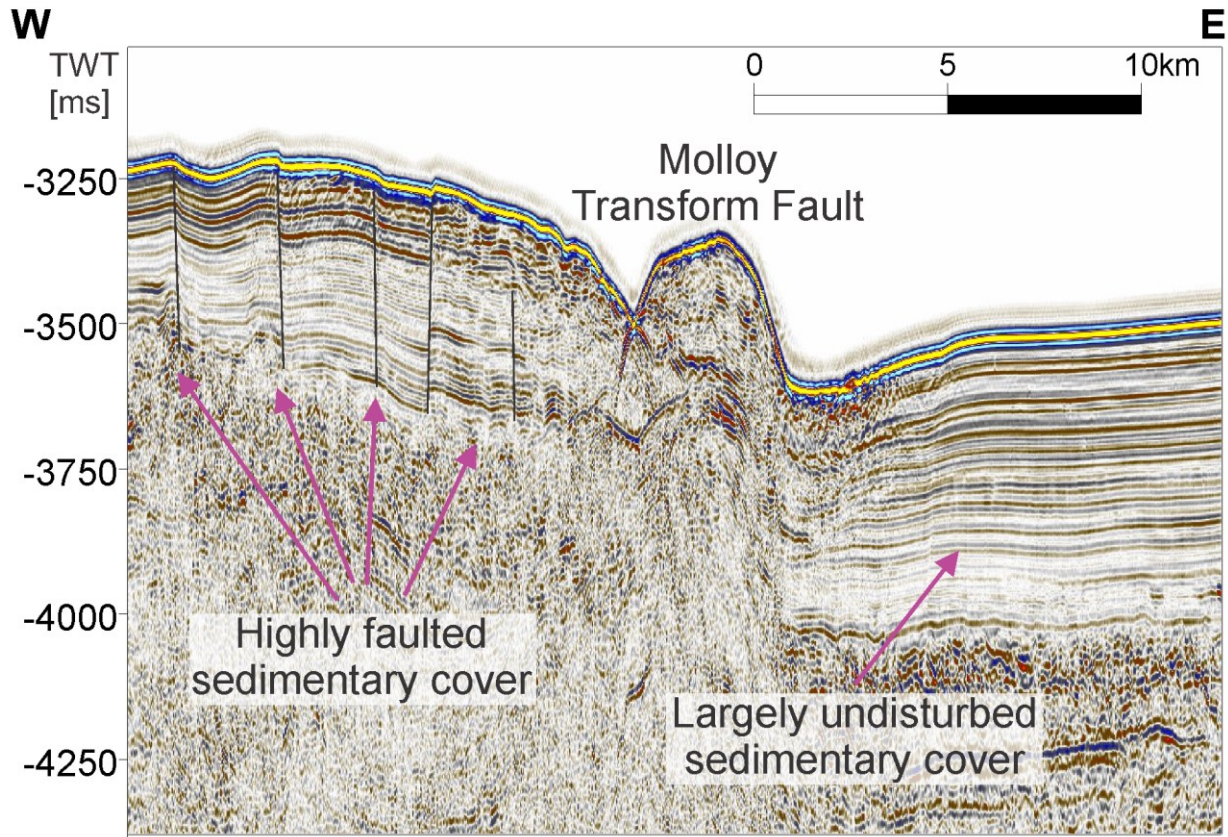
527 **Figure 6.** A close-up map of the area in the vicinity of OBS network, with the earthquake locations
 528 computed using only OBS data. Earthquakes are differentiated by different colors into groups that
 529 are individually discussed in the text. In addition, all available earthquakes with focal mechanisms
 530 between 1980 and 2020 provided by the International Seismological Centre (ISC) are plotted. Pink
 531 lines show the locations of seismic profiles discussed in the text, with the corresponding figure

532 number. Yellow circles with the red outline indicate all currently documented seepage sites in the
533 area (e.g., Smith et al., 2014; Panieri et al., 2017). Other labels the same as in Figures 1,3,4 & 5.

534 **5. Discussion**

535 5.1 Tectonic activity at the plate boundary

536 Our observations, in agreement to land seismological bulletins, show continuous energy release
537 (stress drop) along the transform boundary at the MTF. The obtained dataset of seismic locations
538 shows a misalignment between the earthquake activity and the bathymetric outline of the MTF
539 (blue events in Figure 6), that can be observed on decadal observations of ISC and 2020-2021
540 observations from NNSN but could be interpreted as a hypocenter uncertainty due to limitations
541 of the 1D velocity modeling. We suggest that the shift of the earthquakes in the southeastern part
542 of the MTF is a real phenomenon and the majority of earthquake energy release is happening to
543 the southwest of the MTF outline (at the North American Plate). This is supported by high
544 resolution seismic data available in the area (location on the Figure 6; Figure 7) showing a highly
545 faulted sedimentary cover with the fault outlines reaching the seafloor south of the MTF and
546 largely undisturbed sedimentary cover north of it (Figure 7). The presence of both shallow faults
547 in sediments and larger structures potentially reaching the crust is documented for the same side
548 from the bathymetric outline further northwest along the MTF (Waghorn et al., 2018).



549

550 **Figure 7.** Seismic profile crossing the Molloy Transform Fault (location marked on the Figure 6).
 551 Areas to the west from the transform fault have highly sedimented cover with faults reaching
 552 almost to the seafloor, whereas sediments to the east are largely undisturbed.

553

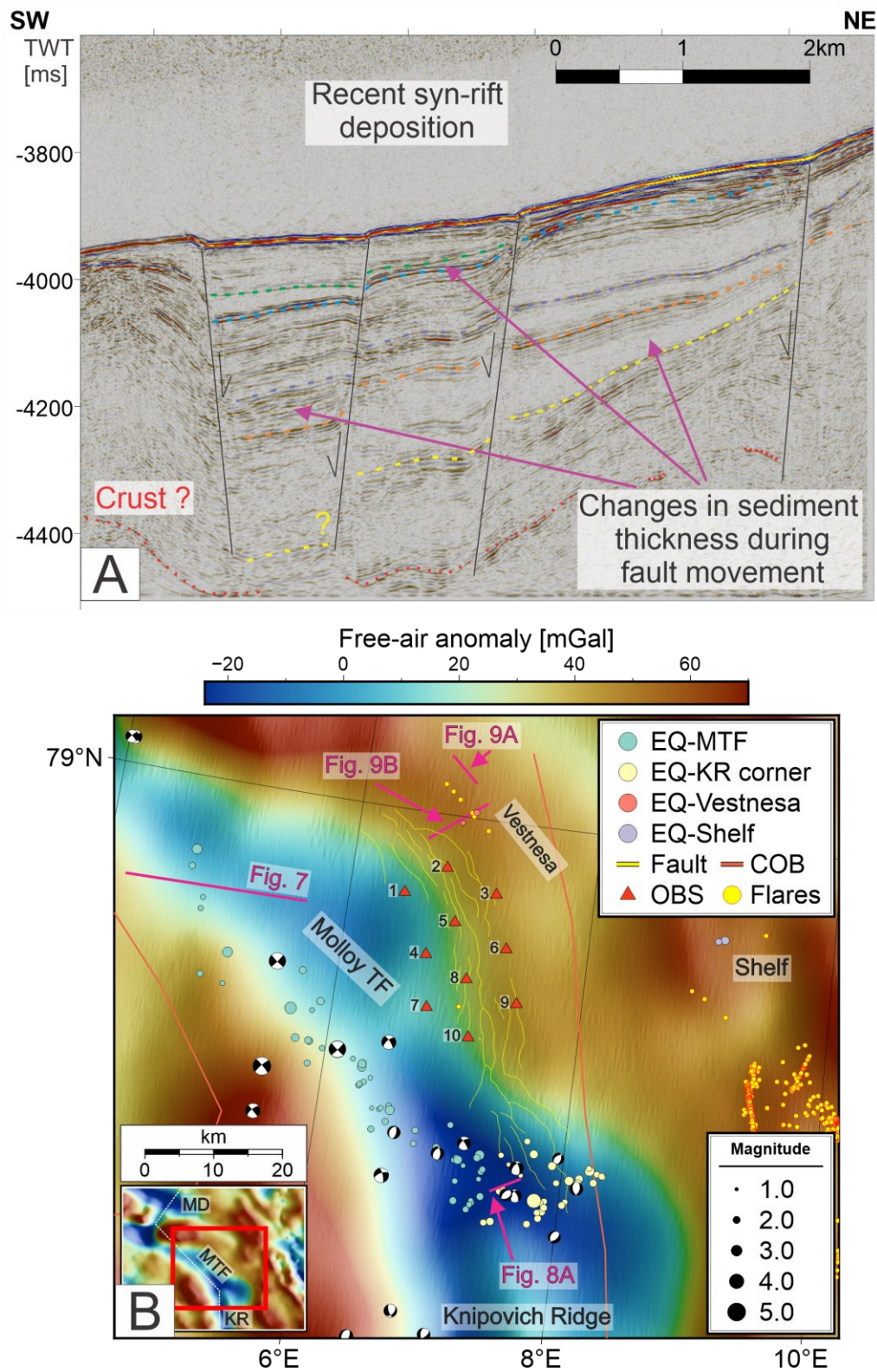
554 We do not observe any seismic activity in the targeted area of the bathymetric scarps (Figure 6).
 555 These scarps were previously interpreted as a sign of northwards propagation of the KR (Crane, et
 556 al., 2001), following the previous early Cenozoic structures of Spitsbergen Shear Zone (Crane et
 557 al., 1991), and this rationale was assumed in several further studies in the area (Vanneste et al.,
 558 2005; Hustoft et al., 2009, Plaza-Faverola et al., 2015). This interpretation was based only on
 559 bathymetric data and so far, no deep-reaching faults with potential connection to the crust have
 560 been observed on the seismic lines in the area of bathymetric scarps (Dumke et al., 2016). Past
 561 seismic studies for this location were estimated to image only the youngest sediments up to 0.78
 562 Ma (Vanneste et al., 2005). During our OBS deployment, we have not detected signs of seismicity
 563 at these fault scarps or beneath them, with the exception of the flanks in the vicinity of the outside
 564 corner between the MTF and KR (Figure 6). With the network specifically designed to monitor

565 seismicity within the scarps area, we were unable to record any earthquakes within the network,
566 thus we conclude that the faults do not accommodate seismically any large tectonic movement. In
567 this area the estimated thickness of the sediments is about 4-5 km (Ritzmann et al., 2004). We
568 follow the previous suggestion from the refraction study of Ritzmann et al., (2004), that the
569 basement subsidence due to the heavy sedimentary load might be a mechanism behind the
570 generation of gravitational faults outcropping on the seafloor. Their presence may also be the result
571 of the gravitational forcing at the steep edges of the sediment pile (Plaza-Faverola & Keiding,
572 2019), deposited steadily through the deep-water currents along the margin boundary since post
573 Late Miocene (Eiken & Hinz, 1993; Hustoft et al., 2009).

574

575 Within the interpretable seismicity map, we see a number of earthquakes originating eastward from
576 the northernmost part of the KR, beyond the rift valley into the outside corner between the MTF
577 and KR, and partially in the location of southernmost bathymetric scarps targeted by the survey
578 (Figure 6). Generally, fracture zones outside of the ridge-transform fault intersection have been
579 classically considered inactive, however several zones worldwide have major earthquake activity
580 in these zones documented (Bohnenstiehl et al., 2004; Lay, 2019). The observed activity in the
581 corner is frequent, and with at least one earthquake of $M > 5$, comparable in energy to the strongest
582 earthquakes recorded in the region. It is also visible in both the ISC catalog between 1980-2020 as
583 well as in NNSN catalog during the duration of our survey. The corner area is characterized by
584 gently sloping seafloor toward the KR rift valley. Recent interpretation of aeromagnetic data
585 indicates the rift jump at 18 Ma in this section of the KR eastward, with the failed rift segment
586 identified more than 100 km to the west at the present day (Dumais et al., 2021). The valley itself
587 in this part is estimated to be covered by up to 950 m of sediments (Amundsen et al., 2011), and
588 currently spreading at a rate of 7.1 mm/y and 5.9 mm/y for the west and east section, respectively
589 (Dumais et al., 2021). The total thickness of the sediments at the eastern flank of the KR ridge
590 valley is around 850-950 m here (Kvarven et al., 2014), with the thickness at the corner likely
591 greater due to shallower water depth (therefore larger sediment thickness measured from the crust).
592 The sediments in the flank were previously determined to be predominantly glacial-hemipelagic
593 deposits sourced from the western-Svalbard margin (Kvarven et al., 2014; Amundsen et al., 2011),
594 not older than Late Pliocene – Pleistocene age (Amundsen et al., 2011). The rapid sedimentation
595 from the eastern direction modulated by glacial and inter-glacial periods since Late Pliocene

596 (Knies et al., 2009) led to greater amount of sediments deposited on the eastern flank compared to
597 the western one at the northern portion of the KR due to sediment load (Kvarven et al., 2014;
598 Engen et al., 2003, 2008; Crane 2001, Faleide 1996). This corresponds to water depths greater in
599 the west part by about 600 m on average (Kvarven et al., 2014). A section of the seismic line
600 recorded over the outside corner between the MTF and KR shows a clear indication of recent syn-
601 rift deposition (i.e., increase in the thickness of sedimentary layers towards active fault planes)
602 over a potential crustal ridge structure (Figure 8A). We propose therefore that the outside corner
603 between the KR and MTF represents a sediment filled continuation of the rift valley and the
604 inactive fracture zone is located further eastward. The ridge valley is generally oriented in the
605 north-east direction along the entire length of the KR, following documented orientation of
606 magmatic centers' axial high trends (Crane et al., 2001). This interpretation is supported by the
607 available focal mechanism solutions provided by the ISC bulletin (Bondár & Storchak, 2011),
608 showing a gradual change from the strike-slip pattern along the MTF all the way to normal faulting
609 in the outside corner (Figure 6 & 8B). Additionally, a strong low-gravity free-air anomaly is visible
610 in this corner (Figure 8B), which can correspond either to the spreading center as seen along the
611 MR, MTF and along the KR to the south, but also reflect the sedimentary infill (Dumais et al.,
612 2022; gravity data from Sandwell et al., 2014). The earthquake activity ceases roughly at the newly
613 revised continental-oceanic margin boundary (Dumais, et al., 2022; COB line in Figures 6 & 8B)
614 and is most likely limited to the oceanic portion of the crust.



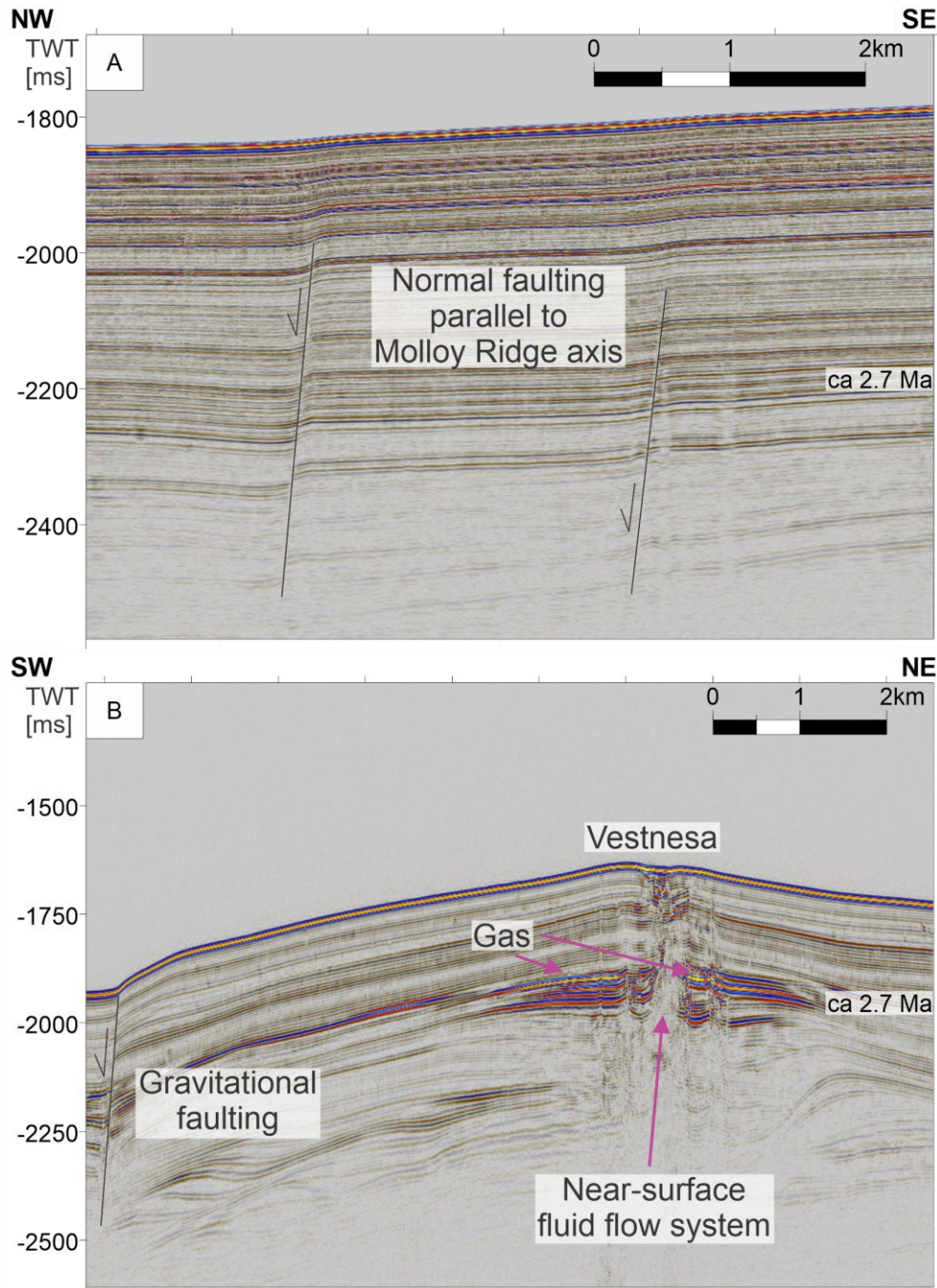
615

616 **Figure 8.** (a) Seismic profile located in the outside corner between the Molloy Transform Fault
 617 and the Knipovich Ridge (location in the Figure 6). Several young normal faults that show

618 difference in the layer thickness indicating syn-rift deposition (b) Free-air gravity anomaly map of
619 the same area as in Figure 6 (Sandwell et al., 2014), showing negative gravity anomaly extending
620 eastwards from the Knipovich Ridge bathymetric outline. All other features labelled in the same
621 way as in Figure 6.

622 5.2 Seismicity along the Vestnesa Ridge sedimentary drift

623 During the 11-month survey we recorded only two earthquakes close to the Vestnesa Ridge
624 sedimentary drift crest (Figures 6 and 8B). These have local magnitudes of 1.2 and 2.0, therefore
625 we assume that the detection sensitivity was about $M=1.0$ for this area. High resolution seismic
626 data across and along the ridge crest, show evidence of normal faulting through the Quaternary
627 sedimentary cover (Figure 9). Two major sedimentary fault planes are oriented parallel or nearly
628 parallel to the MR spreading axis (Figure 9A). In the direction perpendicular to the ridge crest, we
629 see the top of the ridge with documented near-surface fluid flow system and the gas accumulations
630 related to seepage, but also one of the bathymetric scarps on the south-western flank of the ridge
631 that we interpret as a gravitational fault (Figure 9B). No spatial changes in layer thickness indicate
632 recent faulting, markedly different from the example from the outside corner between the MTF
633 and the KR (Figure 7). Based on the fault geometry, the age constraint of one of the reflections at
634 2.7 Ma (Plaza-Faverola et al., 2015; Mattingsdal et al., 2014), and the opening time of the MR
635 dated currently at 10-20 Ma (Engen et al., 2008), we consider the direct influence of present-day
636 drift at the MR on the generation of these two normal faults unlikely (Figure 9A). It is however
637 possible, that the orientation of these faults (parallel or near parallel to the MR spreading axis) is
638 a result of the dominant orientation of stresses in the shallow subsurface established during the
639 seafloor spreading (namely that underlying crustal faults may be accommodating stress generated
640 by the sedimentary weight). It is unlikely that the present-day tectonic faulting at the MTF would
641 influence the fault generation in both seismic profiles due to the lack of observed seismicity
642 northwards from its bathymetric outline in the OBS data (Figure 6) and the general paucity of
643 earthquakes reported for this part of the region (Figure 1).



644

645 **Figure 9.** Two high resolution seismic profiles in the area of the Vestnesa Ridge contourite drift:
 646 one parallel to the ridge crest (a), and one perpendicular, crossing the well-studied fluid flow
 647 system (b). Faults in the profile (a) are parallel or near parallel to the orientation of ultraslow
 648 spreading Molloy Ridge. In the profile (b), one of the bathymetric features investigated with OBS
 649 dataset (yellow lines in e.g., Figure 6), is interpreted as a gravitational fault.

650 Vestnesa Ridge lies close to the inferred continental-oceanic crust boundary. However, most recent
651 (Dumais, 2020; COB line in Figures 6 and 8B), and previous estimations (Engen et al., 2008)
652 locate the earthquakes at the crest of the Vestnesa at least 15 km from the boundary, reducing the
653 probability of any potential interactions between the oceanic and continental crust as a factor in
654 earthquake generation.

655

656 In the past 3.6 Ma the shelf area to the east of the Vestnesa was under cyclic influence of
657 propagating and retreating ice masses (Knies et al., 2009). The changes in the regional stress
658 regime due to glacial processes in the past can be a factor influencing current tectonic processes
659 with the potential for even large magnitude earthquakes (e.g., Thorson, 2000; Steffen et al., 2021).
660 Recent modelling of the lithospheric response to the past glaciation cycles suggests that the glacial
661 processes contribute to the current day stress regime and can influence existing fault structures,
662 but the degree of the influence has to be further quantified (Vachon et al., 2022). Therefore, post
663 glacial subsidence along the continental slope and rise may be a factor contributing to the
664 generation of earthquakes at the Vestnesa and near the shelf break (purple events in Figures 6 &
665 8).

666 5.3 Implications of neotectonics for fault-controlled fluid seepage in the Fram Strait

667 We observe that two of the earthquakes from the Vestnesa Ridge are in a vicinity of the ridge
668 portion that is currently seeping methane from the seafloor (yellow dots in Figures 6 & 8B, e.g.,
669 Smith et al., 2014; Panieri et al., 2017). Plausible determination of the mechanism responsible for
670 the two observed events is therefore especially important in the context of the current and past gas
671 seepage that is reported and studied there (e.g., Hustoft et al., 2009; Bünz et al., 2012, Plaza-
672 Faverola et al., 2015; Panieri et al., 2017). There is strong evidence for modulations of gas seepage
673 during the recent glacial and interglacial periods in the seismic data (Plaza-Faverola et al., 2015).
674 Dating of sedimentary cores links to a correlation between the glacial cycles and increased seepage
675 directly after the glacial maxima, therefore several authors proposed glacial tectonics as the
676 dominant force behind the seepage activity cycles (Schneider et al., 2018, Himmler et al., 2019).
677 These observations cannot however explain why a similar group of seafloor structures
678 (pockmarks), further west on the crest of the ridge, connected to the recent (> 8000 years ago)
679 seepage activity, is presently dormant (Consolaro et al., 2015; Plaza-Faverola et al., 2015; Cooke

680 et al., 2023). It was previously suggested that the spatial variation in seepage activity is driven
681 predominantly by the tectonic forces from seafloor spreading at the MR and KR (Plaza-Faverola
682 et al., 2015; Plaza-Faverola & Keiding, 2019). Our observations of seismicity at the Vestnesa
683 Ridge (or lack of thereof) imply little or no rifting influence at present time. The orientation of
684 normal faults visible in the profile parallel to the Vestnesa (Figure 9A) can however point to a
685 reactivation of deeper, crustal faults established in the normal fault spreading regime under the
686 sediment weight. The connection to the deeper structures cannot be however established using the
687 high-resolution seismic data available for this study. Nevertheless, it is perhaps not casual that the
688 only two earthquakes recorded near the crest of the VR by the OBS array discussed here are located
689 proximal to the most prominent seepage activity along the sedimentary ridge (Figures 6 & 8B).
690 Moreover, recent seepage activity documented southward (Figures 6 & 8B) is also proximal to a
691 zone seismologically active (i.e., the MTF/KR outside corner; Figures 6 & 8B).

692

693 Two observed earthquakes occurred close to the ridge crest, where the overall sediment thickness
694 is greatest and the flanks of the crest are steepest (e.g., Eiken & Hinz, 1993). We do not observe
695 seismic activity where sediment thickness is lower and/or their deposition is close to horizontal, in
696 the area between the Vestnesa Ridge and MTF, but also to the north (Figure 3). Therefore, we
697 propose that the sediment loading driven by the depositional pattern is playing an important role
698 for the seepage distribution in the area. The stress orientation and the main fault structures in the
699 crust for this area should under normal circumstances be established near the spreading centers in
700 the past and remain extensional while the crust progressively is moved towards the continental
701 margin. It is possible that the observed seismicity and reported seepage activity are related to the
702 reactivation of deeper tectonic structures oriented parallel to the spreading MR by the gravitational
703 weight of the sediments and the process can be selective dependent on the direction of older faults
704 and the shape of deposited sedimentary structures (e.g., Dubois et al., 2002; Bellahsen & Daniel,
705 2005; Brandes et al., 2011). This reactivation can be influenced by isostatic rebalancing after the
706 glaciations (e.g., Redfield et al., 2005; Steffen et al., 2014; Vachon et al., 2022), Alternatively, it
707 is entirely possible that the difference in the glacial stress field between now and the last glacial
708 maximum (23 ka ago) is significant enough to reactivate faults and influence seepage activity in
709 the region (Vachon et al., 2022). These observations support what has been inferred in previous

710 studies; namely that sedimentary faults to the north of the KR termination are prone to dilation and
711 favor fluid migration and seepage (Plaza-Faverola et al., 2015; Vachon et al., 2022).

712

713 While we do not observe present day seismicity and therefore a direct link between the ridge
714 system and the fluid flow system at the Vestnesa, the rift structures indirectly control sedimentary
715 faulting. Since the initial opening of the Fram Strait, the systems of current circulation developed
716 along the newly forming KR rift valley and started depositing sediments on young ocean floor
717 (e.g., Eiken & Hinz, 1993; Engen et al., 2008; Amundsen et al.; 2011). The intensification of
718 Northern Hemisphere glaciation and the resulting influx of hemipelagic deposits, together with the
719 differential motion of plates between the MTF caused offshore extension of sediment deposition
720 and the westward facing progression of the Vestnesa Ridge crest (Johnson et al., 2015). This means
721 that the plate motion between the MTF was partially responsible for the shift in sediment
722 deposition direction from roughly north-south to the east-west visible today, therefore influencing
723 the gravitational faulting direction along the flanks of the created sedimentary rift. This change in
724 the faulting orientation can be followed looking at the bathymetric outline of the faults along the
725 structure (yellow lines in Figures 6 & 8A) and the current day W-E orientation can be seen in the
726 seismic data perpendicular to the ridge crest (Figure 9B). Therefore, even if the faulting, and by
727 extension, the seepage currently occurring at the Vestnesa Ridge are not controlled by the present-
728 day ocean spreading, the direction of fault planes and the location of observed, sparse seismicity
729 may be the aftermath of the sediment drift depositional history, strongly influenced by the very
730 same plate motion.

731 **6. Conclusions**

732 We investigated the local stress regime at the oblique spreading ridge setting of the eastern Fram
733 Strait using seismological observations. We used data from an ocean bottom seismometer (OBS)
734 network with 10 instruments that recorded over 11 months between August 2020 and July 2021.
735 We studied earthquakes to understand regional distribution of present-day tectonic processes and
736 their connection to shallow fault systems, for some of which seafloor gas seepage has been
737 previously documented. This temporary OBS survey between the northern termination of the
738 Knipovich Ridge and the Vestnesa Ridge contourite drift led to the following observations and
739 potential explanations for the spatial patterns of seismicity observed:

740
741
742
743
744
745
746
747
748
749
750
751
752
753
754
755
756
757
758
759
760
761
762
763
764
765
766
767
768
769

- Along the MTF, most of the seismicity is located to the south-southwest in relation to the bathymetric outline of the fault zone. This observation is supported by the long-term observations of the seismicity in the region and seismic data indicating recent faulting of sediments to the south-southwest from the MTF and undisturbed shallow sediments in the north-northeastern direction.
- The outside corner between the MTF and KR, seen as an extension of the MTF eastwards from the KR ridge valley is an active tectonic area with the reported normal-faulting and frequent, large magnitude earthquakes. We propose that this region represents a sediment-covered northernmost portion of the active spreading zone, indicated by the syn-rift deposition of recent sedimentary deposits and the observed frequent seismic activity in OBS data, but also in long-term studies.
- We do not observe any local earthquakes within the bathymetric faults (“scarps”) to the north of the northward termination of the KR and the earthquake activity seems to be constrained to the vicinity of the KR termination. We suggest that therefore structures visible on the seafloor are likely gravitational faults created due to the sediment load and gravitational sliding, possibly influenced by the glacial subsidence modelled for the area at present. There seem to be no connection between the faults and northward propagation of the KR, suggested in the past.
- The observations at the MTF and the outside corner between the MTF and KR indicate potential connection between deeper crustal faults (as evidenced by earthquakes) and shallow sediments (as indicated by near-surface fault structures in seismic data). We observe two weak (M 1.2 & 2.0) earthquakes close to the Vestnesa Ridge crest, that are likely caused by the similar processes as bathymetric scarps further south. High-resolution seismic data indicates that some of the buried sedimentary faults perpendicular to the Vestnesa Ridge crest have comparable orientation to the rift structures at the Molloy Ridge. Observed earthquakes may suggest crustal fault reactivation, and stress accommodation in the form of extensional sedimentary faults that promote gas leakage. The direct link to deeper structures cannot be established without seismic data with greater penetration depth. Sparse seismic activity without a direct connection to the MR, MTF and KR makes a

770 propagation of present-day spreading from the plate boundaries into the sedimentary
771 deposits on the Eurasian plate unlikely.

772 **Acknowledgments**

773 This work is conducted as a part of the SEAMSTRESS project, supported by the Tromsø Research
774 Foundation (TFS) and the Research Council of Norway (grant nr. 287865). The work was also
775 supported by the Research Council of Norway through its Centers of Excellence funding scheme
776 grant 223259 (Centre for Arctic Gas Hydrate, Environment and Climate—CAGE). We thank the
777 crew of R/V Helmer Hanssen, Mechita Schmidt--Aursch and Henning Kirk for their support
778 during deployment and recovery of OBSs. We additionally thank Mechita Schmidt-Aursch for the
779 help with processing and data management of OBS dataset. We are grateful for machine learning
780 classification codes provided by Clément Hibert. We also thank Marie Dumais for sharing the
781 outline of the revised continent-ocean margin boundary for plotting. Authors report no real or
782 perceived conflicts of interest.

783 **Open Research**

784 The raw dataset is archived at PANGAEA (Plaza-Faverola et al., 2022b;
785 <https://doi.pangaea.de/10.1594/PANGAEA.952424>) and available in GEOFON repository under
786 the network code Y9 (<https://geofon.gfz-potsdam.de/>). The data is under embargo until
787 31.12.2024. The land data earthquake catalogue was obtained from the International Seismological
788 Centre (ISC) Seismological Dataset Repository (<https://doi.org/10.31905/6TJZECEY>) and
789 Norwegian National Seismic Network (NNSN; Ottemöller et al., 2018). The ObsPy package was
790 used for processing of the seismological data (Krischer et al. 2015). All maps were created using
791 Generic Mapping Tools - GMT (Wessel et al. 2019). Bathymetry of the region provided by the
792 International Bathymetric Chart of the Arctic Ocean (IBCAO) (Jakobsson et al. 2020). Free-air
793 gravity anomaly map provided by Sandwell et al., (2014). An estimate of continental-oceanic
794 transition boundary obtained from Norwegian Geological Institute (Dumais et al., 2021).

795 **References**

- 796 Allen, P. A., & Allen, J. R. (2013). *Basin analysis: Principles and application to petroleum play*
797 *assessment*: John Wiley & Sons.
- 798 Allen, R. (1982). Automatic phase pickers: Their present use and future prospects. *Bulletin of the*
799 *Seismological Society of America*, 72(6B), S225-S242.
- 800 Amundsen, I. M. H., Blinova, M., Hjelstuen, B. O., Mjelde, R., & Haflidason, H. (2011). The
801 Cenozoic western Svalbard margin: sediment geometry and sedimentary processes in an area of
802 ultraslow oceanic spreading. *Marine Geophysical Research*, 32(4), 441-453.
- 803 Bellahsen, N., & Daniel, J. M. (2005). Fault reactivation control on normal fault growth: an
804 experimental study. *Journal of Structural Geology*, 27(4), 769-780.
- 805 Bohnenstiehl, D. R., Tolstoy, M., & Chapp, E. (2004). Breaking into the plate: A 7.6 Mw fracture-
806 zone earthquake adjacent to the Central Indian Ridge. *Geophysical Research Letters*, 31(2).
- 807 Bondár, I., & Storchak, D. (2011). Improved location procedures at the International Seismological
808 Centre. *Geophysical Journal International*, 186(3), 1220-1244.
- 809 Brandes, C., Polom, U., & Winsemann, J. (2011). Reactivation of basement faults: interplay of
810 ice-sheet advance, glacial lake formation and sediment loading. *Basin Research*, 23(1), 53-64.
- 811 Bünz, S., Polyanov, S., Vadakkepuliambatta, S., Consolaro, C., & Mienert, J. (2012). Active gas
812 venting through hydrate-bearing sediments on the Vestnesa Ridge, offshore W-Svalbard. *Marine*
813 *Geology*, 332, 189-197.
- 814 Bünz, S. (2023). CAGE20-5 Cruise Report: Tectonic stress studies and seismic surveys on the
815 West-Svalbard margin. *CAGE – Centre for Arctic Gas Hydrate, Environment and Climate Report*
816 *Series*, 8.
- 817 Carter, L., Gavey, R., Talling, P. J., & Liu, J. T. (2014). Insights into Submarine Geohazards from
818 Breaks in Subsea Telecommunication Cables. *Oceanography*, 27(2), 58-67.
- 819 Consolaro, C., Rasmussen, T. L., Panieri, G., Mienert, J., Bunz, S., & Sztybor, K. (2015). Carbon
820 isotope ($\delta C-13$) excursions suggest times of major methane release during the last 14 kyr in
821 Fram Strait, the deep-water gateway to the Arctic. *Climate of the Past*, 11(4), 669-685.
- 822 Cooke, F., Plaza-Faverola, A., Bünz, S., Sultan, N., Ramachandran, H., Bedle, H., et al. (2023).
823 Sedimentary deformation relating to episodic seepage in the last 1.2 million years: a multi-scale
824 seismic study from the Vestnesa Ridge, eastern Fram Strait. *Frontiers in Earth Science*, 11.

- 825 Crane, K., Sundvor, E., Foucher, J. P., Hobart, M., Myhre, A. M., & LeDouaran, S. (1988).
826 Thermal evolution of the western Svalbard margin. *Marine Geophysical Researches*, 9(2), 165-
827 194.
- 828 Crane, K., Sundvor, E., Buck, R., & Martinez, F. (1991). Rifting in the northern Norwegian-
829 Greenland Sea: Thermal tests of asymmetric spreading. *Journal of Geophysical Research: Solid*
830 *Earth*, 96(B9), 14529-14550.
- 831 Crane, K., Doss, H., Vogt, P., Sundvor, E., Cherkashov, G., Poroshina, I., & Joseph, D. (2001).
832 The role of the Spitsbergen shear zone in determining morphology, segmentation and evolution of
833 the Knipovich Ridge. *Marine Geophysical Researches*, 22(3), 153-205.
- 834 Dick, H. J. B., Lin, J., & Schouten, H. (2003). An ultraslow-spreading class of ocean ridge. *Nature*,
835 426(6965), 405-412.
- 836 Domel, P., Hibert, C., Schlindwein, V., & Plaza-Faverola, A. (2023). Event recognition in marine
837 seismological data using Random Forest machine learning classifier. *Geophysical Journal*
838 *International*, 235(1), 589-609.
- 839 Dubois, A., Odonne, F., Massonnat, G., Lebourg, T., & Fabre, R. (2002). Analogue modelling of
840 fault reactivation: tectonic inversion and oblique remobilisation of grabens. *Journal of Structural*
841 *Geology*, 24(11), 1741-1752.
- 842 Dumais, M. A., Gernigon, L., Olesen, O., Johansen, S. E., & Brønner, M. (2021). New
843 interpretation of the spreading evolution of the Knipovich Ridge derived from aeromagnetic data.
844 *Geophysical Journal International*, 224(2), 1422-1428.
- 845 Dumais, M. A., Gernigon, L., Olesen, O., Lim, A., Johansen, S. E., & Brønner, M. (2022). Crustal
846 and Thermal Heterogeneities Across the Fram Strait and the Svalbard Margin. *Tectonics*, 41(10).
- 847 Dumke, I., Burwicz, E. B., Berndt, C., Klaeschen, D., Feseker, T., Geissler, W. H., & Sarkar, S.
848 (2016). Gas hydrate distribution and hydrocarbon maturation north of the Knipovich Ridge,
849 western Svalbard margin. *Journal of Geophysical Research: Solid Earth*, 121(3), 1405-1424.
- 850 Ehlers, B.-M., & Jokat, W. (2009). Subsidence and crustal roughness of ultra-slow spreading
851 ridges in the northern North Atlantic and the Arctic Ocean. *Geophysical Journal International*,
852 177(2), 451-462.
- 853 Eiken, O., & Hinz, K. (1993). Contourites in the Fram Strait. *Sedimentary Geology*, 82(1-4), 15-
854 32.

- 855 Engen, Ø., Eldholm, O., & Bungum, H. (2003). The Arctic plate boundary. *Journal of Geophysical*
856 *Research: Solid Earth*, 108(B2).
- 857 Engen, Ø., Faleide, J. I., & Dyreng, T. K. (2008). Opening of the Fram Strait gateway: A review
858 of plate tectonic constraints. *Tectonophysics*, 450(1-4), 51-69.
- 859 England, W. A., Mackenzie, A. S., Mann, D. M., & Quigley, T. M. (1987). The movement and
860 entrapment of petroleum fluids in the subsurface. *Journal of the Geological Society*, 144(2), 327-
861 347.
- 862 Etiope, G. (2015). *Natural Gas Seepage: The Earth's Hydrocarbon Degassing*: Springer.
- 863 Faleide, J. I., Solheim, A., Fiedler, A., Hjelstuen, B. O., Andersen, E. S., & Vanneste, K. (1996).
864 Late Cenozoic evolution of the western Barents Sea-Svalbard continental margin. *Global and*
865 *Planetary Change*, 12(1-4), 53-74.
- 866 Fjeldskaar, W., Lindholm, C., Dehls, J. F., & Fjeldskaar, I. (2000). Postglacial uplift, neotectonics
867 and seismicity in Fennoscandia. *Quaternary Science Reviews*, 19(14), 1413-1422.
- 868 Fjeldskaar, W., & Amantov, A. (2018). Effects of glaciations on sedimentary basins. *Journal of*
869 *Geodynamics*, 118, 66-81.
- 870 Gardner, J. V., van den Aamele, E. J., Gelfenbaum, G., Barnhardt, W., Lee, H., & Palmer, S.
871 (2001). Mapping southern Puget Sound delta fronts after 2001 earthquake. *Eos, Transactions*
872 *American Geophysical Union*, 82(42), 485-489.
- 873 Gibbons, S. J., Harris, D. B., Dahl-Jensen, T., Kværna, T., Larsen, T. B., Paulsen, B., & Voss, P.
874 H. (2017). Locating seismicity on the Arctic plate boundary using multiple-event techniques and
875 empirical signal processing. *Geophysical Journal International*, 211(3), 1613-1627.
- 876 Goswami, B. K., Weitemeyer, K. A., Minshull, T. A., Sinha, M. C., Westbrook, G. K., Chabert,
877 A., et al. (2015). A joint electromagnetic and seismic study of an active pockmark within the
878 hydrate stability field at the Vestnesa Ridge, West Svalbard margin. *Journal of Geophysical*
879 *Research: Solid Earth*, 120(10), 6797-6822.
- 880 Hannemann, K., Krüger, F., & Dahm, T. (2014). Measuring of clock drift rates and static time
881 offsets of ocean bottom stations by means of ambient noise. *Geophysical Journal International*,
882 196(2), 1034-1042.
- 883 Havskov, J., Bormann, P., & Schweitzer, J. (2011). Seismic source location. In P. Bormann (Ed.),
884 *New Manual of Seismological Observatory Practice 2 (NMSOP-2)*, Potsdam: Deutsches
885 GeoForschungszentrum GFZ, 1-36.

- 886 Havskov, J., & Ottemöller, L. (1999). SEISAN earthquake analysis software. *Seismological*
887 *Research Letters*, 70(5), 532-534.
- 888 Havskov, J., Voss, Peter H., & Ottemöller, L. (2020). Seismological Observatory Software: 30 Yr
889 of SEISAN. *Seismological Research Letters*, 91(3), 1846-1852.
- 890 Hibert, C., Mangeney, A., Grandjean, G., Baillard, C., Rivet, D., Shapiro, N. M., et al. (2014).
891 Automated identification, location, and volume estimation of rockfalls at Piton de la Fournaise
892 volcano. *Journal of Geophysical Research: Earth Surface*, 119(5), 1082-1105.
- 893 Hibert, C., Provost, F., Malet, J.-P., Maggi, A., Stumpf, A., & Ferrazzini, V. (2017). Automatic
894 identification of rockfalls and volcano-tectonic earthquakes at the Piton de la Fournaise volcano
895 using a Random Forest algorithm. *Journal of Volcanology and Geothermal Research*, 340, 130-
896 142.
- 897 Hicks, E. C., Kvaerna, T., Mykkeltveit, S., Schweitzer, J., & Ringdal, F. (2004). Travel-times and
898 Attenuation Relations for Regional Phases in the Barents Sea Region. *pure and applied*
899 *geophysics*, 161(1), 1-19.
- 900 Hudec, M. R., & Jackson, M. P. A. (2004). Regional restoration across the Kwanza Basin, Angola:
901 Salt tectonics triggered by repeated uplift of a metastable passive margin. *AAPG Bulletin*, 88(7),
902 971-990.
- 903 Hustoft, S., Bunz, S., Mienert, J., & Chand, S. (2009). Gas hydrate reservoir and active methane-
904 venting province in sediments on < 20 Ma young oceanic crust in the Fram Strait, offshore NW-
905 Svalbard. *Earth and Planetary Science Letters*, 284(1-2), 12-24.
- 906 Jeddi, Z., Ottemöller, L., Sørensen, M. B., Rezaei, S., Gibbons, S. J., Strømme, M. L., et al. (2021).
907 Improved Seismic Monitoring with OBS Deployment in the Arctic: A Pilot Study from Offshore
908 Western Svalbard. *Seismological Research Letters*, 92(5), 2705-2717.
- 909 Judd, A., & Hovland, M. (2007). *Seabed fluid flow : the impact on geology, biology, and the*
910 *marine environment*. Cambridge: Cambridge University Press.
- 911 Kissling, E., Kradolfer, U., & Maurer, H. (1995). Program VELEST user's guide-Short
912 Introduction. Institute of Geophysics, ETH Zurich.
- 913 Knies, J., Matthiessen, J., Vogt, C., Laberg, J. S., Hjelstuen, B. O., Smelror, M., et al. (2009). The
914 Plio-Pleistocene glaciation of the Barents Sea–Svalbard region: a new model based on revised
915 chronostratigraphy. *Quaternary Science Reviews*, 28(9-10), 812-829.

- 916 Krischer, L., Megies, T., Barsch, R., Beyreuther, M., Lecocq, T., Caudron, C., & Wassermann, J.
917 (2015). ObsPy: a bridge for seismology into the scientific Python ecosystem. *Computational*
918 *Science & Discovery*, 8(1), 014003.
- 919 Kvarven, T., Hjelstuen, B. O., & Mjelde, R. (2014). Tectonic and sedimentary processes along the
920 ultraslow Knipovich spreading ridge. *Marine Geophysical Research*, 35(2), 89-103.
- 921 Lay, T. (2019). Reactivation of Oceanic Fracture Zones in Large Intraplate Earthquakes? In
922 *Transform Plate Boundaries and Fracture Zones* (pp. 89-104).
- 923 Madrussani, G., Rossi, G., & Camerlenghi, A. (2010). Gas hydrates, free gas distribution and fault
924 pattern on the west Svalbard continental margin. *Geophysical Journal International*, 180(2), 666-
925 684.
- 926 Mattingsdal, R., Knies, J., Andreassen, K., Fabian, K., Husum, K., Grøsfjeld, K., & De Schepper,
927 S. (2014). A new 6 Myr stratigraphic framework for the Atlantic–Arctic Gateway. *Quaternary*
928 *Science Reviews*, 92, 170-178.
- 929 Meier, M., Schlindwein, V., Scholz, J. R., Geils, J., Schmidt-Aursch, M. C., Kruger, F., et al.
930 (2021). Segment-Scale Seismicity of the Ultraslow Spreading Knipovich Ridge. *Geochemistry*
931 *Geophysics Geosystems*, 22(2), e2020GC009375.
- 932 Miall, A. D. (2013). *Principles of sedimentary basin analysis*: Springer Science & Business Media.
- 933 Olesen, O., Bungum, H., Dehls, J., Lindholm, C., Pascal, C., & Roberts, D. (2013). Neotectonics,
934 seismicity and contemporary stress field in Norway—mechanisms and implications. *Quaternary*
935 *Geology of Norway, Geological Survey of Norway Special Publication*, 13, 145-174.
- 936 Ottemöller, L., Strømme, M., & Storheim, B. (2018). Seismic Monitoring and Data Processing at
937 the Norwegian National Seismic Network. *Summary of the Bulletin of the International*
938 *Seismological Centre*, 52(I), 27 – 40.
- 939 Panieri, G., Bunz, S., Fornari, D. J., Escartin, J., Serov, P., Jansson, P., et al. (2017). An integrated
940 view of the methane system in the pockmarks at Vestnesa Ridge, 79 degrees N. *Marine Geology*,
941 390, 282-300.
- 942 Paton, D. (2011). Post-Rift Deformation of the North East and South Atlantic Margins: Are
943 “Passive Margins” Really Passive? In *Tectonics of Sedimentary Basins* (pp. 249-269).
- 944 Petersen, C. J., Bünz, S., Hustoft, S., Mienert, J., & Klaeschen, D. (2010). High-resolution P-Cable
945 3D seismic imaging of gas chimney structures in gas hydrated sediments of an Arctic sediment
946 drift. *Marine and Petroleum Geology*, 27(9), 1981-1994.

- 947 Plaza-Faverola, A., Bünz, S., Johnson, J. E., Chand, S., Knies, J., Mienert, J., & Franek, P. (2015).
948 Role of tectonic stress in seepage evolution along the gas hydrate-charged Vestnesa Ridge, Fram
949 Strait. *Geophysical Research Letters*, *42*(3), 733-742.
- 950 Plaza-Faverola, A., Vadakkepuliambatta, S., Hong, W. L., Mienert, J., Bunz, S., Chand, S., &
951 Greinert, J. (2017). Bottom-simulating reflector dynamics at Arctic thermogenic gas provinces:
952 An example from Vestnesa Ridge, offshore west Svalbard. *Journal of Geophysical Research-Solid*
953 *Earth*, *122*(6), 4089-4105.
- 954 Plaza-Faverola, A., & Keiding, M. (2019). Correlation between tectonic stress regimes and
955 methane seepage on the western Svalbard margin. *Solid Earth*, *10*(1), 79-94.
- 956 Plaza-Faverola, A. (2022). CAGE21-5 Cruise Report: Test of offshore instrumentation for in-situ
957 sediment pressure measurements, west-Svalbard continental margin. *CAGE – Centre for Arctic*
958 *Gas Hydrate, Environment and Climate Report Series*, *9*.
- 959 Plaza-Faverola, A., Schlindwein, V., Domel, P., Schmidt-Aursch, M., Cooke, F. A., Holm, T., &
960 Jensen, S. A. (2022a). CAGE21-3 Cruise Report: Ocean bottom seismics and acoustic surveys on
961 the West-Svalbard margin – a study of local seismicity and its effect on methane seepage. *CAGE*
962 *– Centre for Arctic Gas Hydrate, Environment and Climate Report Series*, *9*.
- 963 Plaza-Faverola, A., Domel, P., Bünz, S., Schmidt-Aursch, M., Schlindwein, V. (2022b): Project
964 SEAMSTRESS: DEPAS ocean-bottom seismometer operations on Vestnesa Ridge in 2020-2021.
965 *PANGAEA*. <https://doi.pangaea.de/10.1594/PANGAEA.952424>
- 966 Provost, F., Hibert, C., & Malet, J. P. (2017). Automatic classification of endogenous landslide
967 seismicity using the Random Forest supervised classifier. *Geophysical Research Letters*, *44*(1),
968 113-120.
- 969 Ritzmann, O., Jokat, W., Czuba, W., Guterch, A., Mjelde, R., & Nishimura, Y. (2004). A deep
970 seismic transect from Hovgård Ridge to northwestern Svalbard across the continental-ocean
971 transition: A sheared margin study. *Geophysical Journal International*, *157*(2), 683-702.
- 972 Sandwell, D. T., Müller, R. D., Smith, W. H. F., Garcia, E., & Francis, R. (2014). New global
973 marine gravity model from CryoSat-2 and Jason-1 reveals buried tectonic structure. *Science*,
974 *346*(6205), 65-67.
- 975 Schlindwein, V., Demuth, A., Korger, E., Läderach, C., & Schmid, F. (2015). Seismicity of the
976 Arctic mid-ocean Ridge system. *Polar Science*, *9*(1), 146-157.

- 977 Schlindwein, V., & Schmid, F. (2016). Mid-ocean-ridge seismicity reveals extreme types of ocean
978 lithosphere. *Nature*, 535(7611), 276-279.
- 979 Schmidt-Aursch, M., & Haberland, C. (2017). DEPAS (Deutscher Geräte-Pool für amphibische
980 Seismologie): German Instrument Pool for Amphibian Seismology. *Journal of largescale
981 research facilities*, 3, A122.
- 982 Schneider, A., Panieri, G., Lepland, A., Consolaro, C., Crémière, A., Forwick, M., et al. (2018).
983 Methane seepage at Vestnesa Ridge (NW Svalbard) since the Last Glacial Maximum. *Quaternary
984 Science Reviews*, 193, 98-117.
- 985 Schweitzer, J. (2001). HYPOSAT – An Enhanced Routine to Locate Seismic Events. *pure and
986 applied geophysics*, 158(1), 277-289.
- 987 Singhroha, S., Bünz, S., Plaza-Faverola, A., & Chand, S. (2016). Gas hydrate and free gas
988 detection using seismic quality factor estimates from high-resolution P-cable 3D seismic data.
989 *Interpretation*, 4(1), SA39-SA54.
- 990 Singhroha, S., Chand, S., & Bünz, S. (2019). Constraints on Gas Hydrate Distribution and
991 Morphology in Vestnesa Ridge, Western Svalbard Margin, Using Multicomponent Ocean-Bottom
992 Seismic Data. *Journal of Geophysical Research: Solid Earth*, 124(5), 4343-4364.
- 993 Solomon, S., Carpenter, M., & Flach, T. A. (2008). Intermediate storage of carbon dioxide in
994 geological formations: A technical perspective. *International Journal of Greenhouse Gas Control*,
995 2(4), 502-510.
- 996 Steffen, R., Steffen, H., Wu, P., & Eaton, D. W. (2014). Stress and fault parameters affecting fault
997 slip magnitude and activation time during a glacial cycle. *Tectonics*, 33(7), 1461-1476.
- 998 Steffen, H., Olesen, O., & Sutinen, R. (2021). *Glacially-triggered faulting*: Cambridge University
999 Press.
- 1000 Talwani, M., & Eldholm, O. (1977). Evolution of the Norwegian-Greenland Sea. *GSA Bulletin*,
1001 88(7), 969-999.
- 1002 Thorson, R. M. (2000). Glacial tectonics: a deeper perspective. *Quaternary Science Reviews*,
1003 19(14), 1391-1398.
- 1004 Vachon, R., Schmidt, P., Lund, B., Plaza-Faverola, A., Patton, H., & Hubbard, A. (2022). Glacially
1005 Induced Stress Across the Arctic From the Eemian Interglacial to the Present—Implications for
1006 Faulting and Methane Seepage. *Journal of Geophysical Research: Solid Earth*, 127(7).

- 1007 Vanneste, M., Guidard, S., & Mienert, J. (2005). Bottom-simulating reflections and geothermal
1008 gradients across the western Svalbard margin. *Terra Nova*, *17*(6), 510-516.
- 1009 Vogt, P. R., & Crane, K. (1994). Methane-generated() pockmarks on young, thickly sedimented
1010 oceanic crust in the Arctic. Vestnesa ridge, Fram strait. *Geology*, *22*(3).
- 1011 Waghorn, K. A., Vadakkepuliambatta, S., Plaza-Faverola, A., Johnson, J. E., Bunz, S., & Waage,
1012 M. (2020). Crustal processes sustain Arctic abiotic gas hydrate and fluid flow systems. *Sci Rep*,
1013 *10*(1), 10679.
- 1014 Wolfson-Schwehr, M., & Boettcher, M. S. (2019). Chapter 2 - Global Characteristics of Oceanic
1015 Transform Fault Structure and Seismicity. In J. C. Duarte (Ed.), *Transform Plate Boundaries and*
1016 *Fracture Zones* (pp. 21-59): Elsevier.
- 1017 Wyss, M., Hasegawa, A., Wiemer, S., & Umino, N. (1999). Quantitative mapping of precursory
1018 seismic quiescence before the 1989, M 7.1 off-Sanriku earthquake, Japan. *Annals of Geophysics*,
1019 *42*(5).
- 1020 Zoback, M. L., Zoback, M. D., Adams, J., Assumpção, M., Bell, S., Bergman, E. A., et al. (1989).
1021 Global patterns of tectonic stress. *Nature*, *341*(6240), 291-298.

Local seismicity and sediment deformation in the west Svalbard margin: Implications of neotectonics for seafloor seepage

P. Domel¹, A. Plaza-Faverola², V. Schlindwein^{3,4}, and S. Bünz²

¹Department of Geosciences, UiT, The Arctic University of Norway, Tromsø, Norway

²iC3: Centre for ice, Cryosphere, Carbon and Climate, Department of Geosciences, UiT – The Arctic University of Norway, Tromsø, Norway

³Alfred Wegener Institute, Helmholtz Centre for Polar and Marine Research, Bremerhaven, Germany

⁴Faculty of Geosciences, University of Bremen, Bremen, Germany

Contents of this file

Figures S1 to S17

Table S1

Introduction

This supporting material contains figures presenting the cross-correlation procedure utilized for fixing the clock drift in ocean bottom dataset used in this study. Figures S1 and S2 show the results of daily cross-correlation between the reference station (VSN01) and other stations prior to corrections. Figures S3 to S11 show these plots individually for each station pair and the established clock drift curve that was later used for correction. Figures S11 and S12 show the resultant cross-correlations after the drift correction was applied to the data. Figure S13 shows the residual clock drift that remained after the correction presented in Figures S11 and S12. Figures S14 and S15 show the residual travel times from earthquakes location used in the study for the P and S waves, respectively. Figure S17 shows how the earthquake location varies between the hypocenters obtained using only OBS data and when the picks from Norwegian National Seismic Network are included in the calculations. Table S1 lists the most important parameters about the ocean bottom seismometers, including their true position on the seafloor, water depth, recording duration, clock drift from synchronization before and after deployment, and clock drift obtained from the cross-correlations.

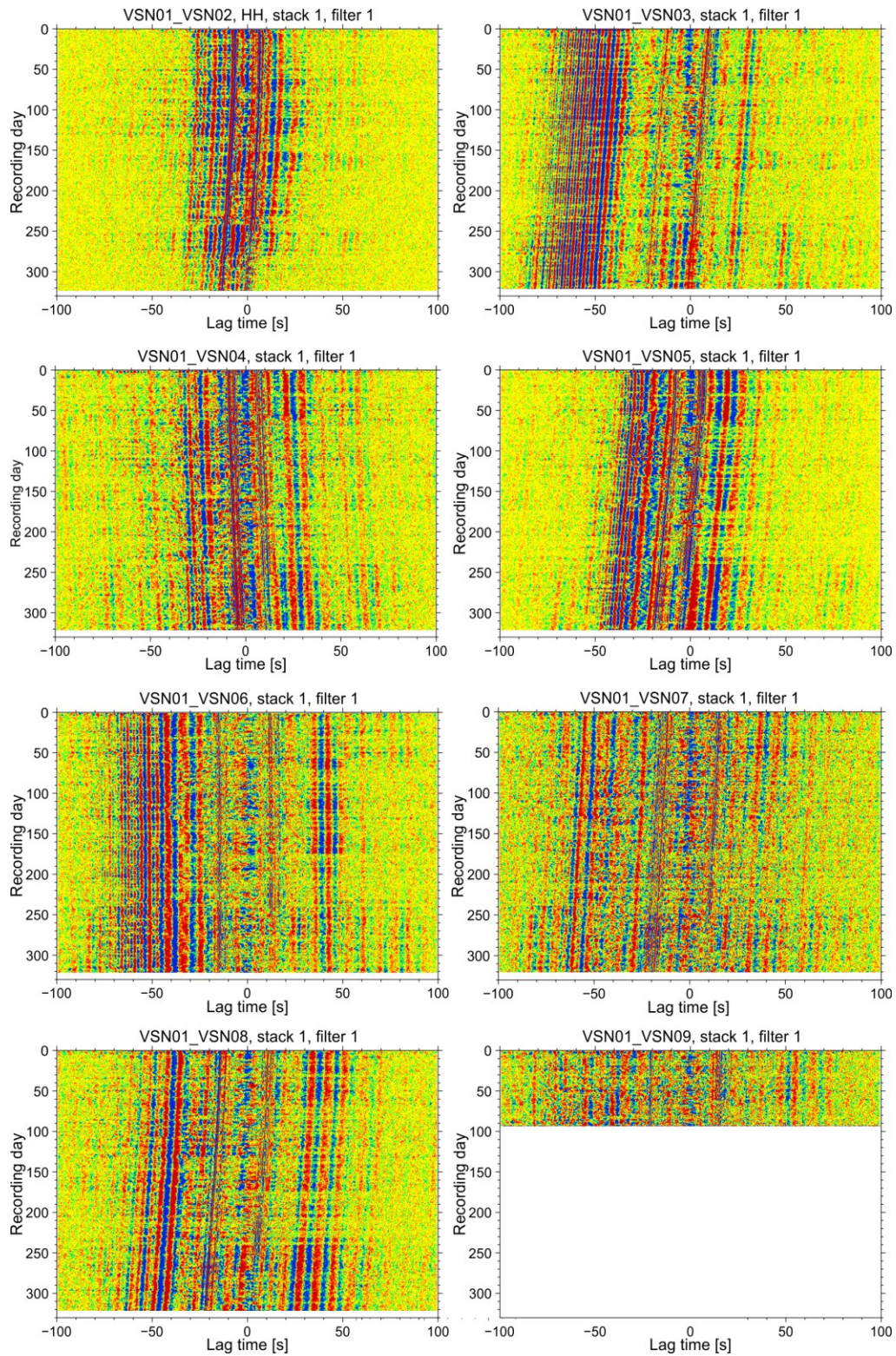


Figure S1. Daily cross-correlation plots between reference station VSN01 and stations VSN02-VSN09.

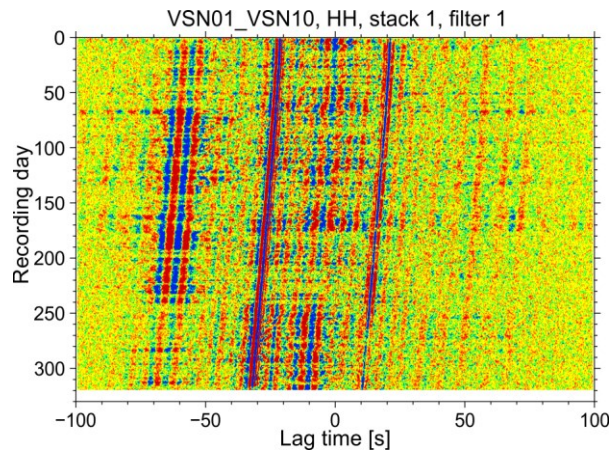


Figure S2. Daily cross-correlation plot between reference station VSN01 and station VSN10.

VSN02_VSN01, HH, Bandpass 1–10 s

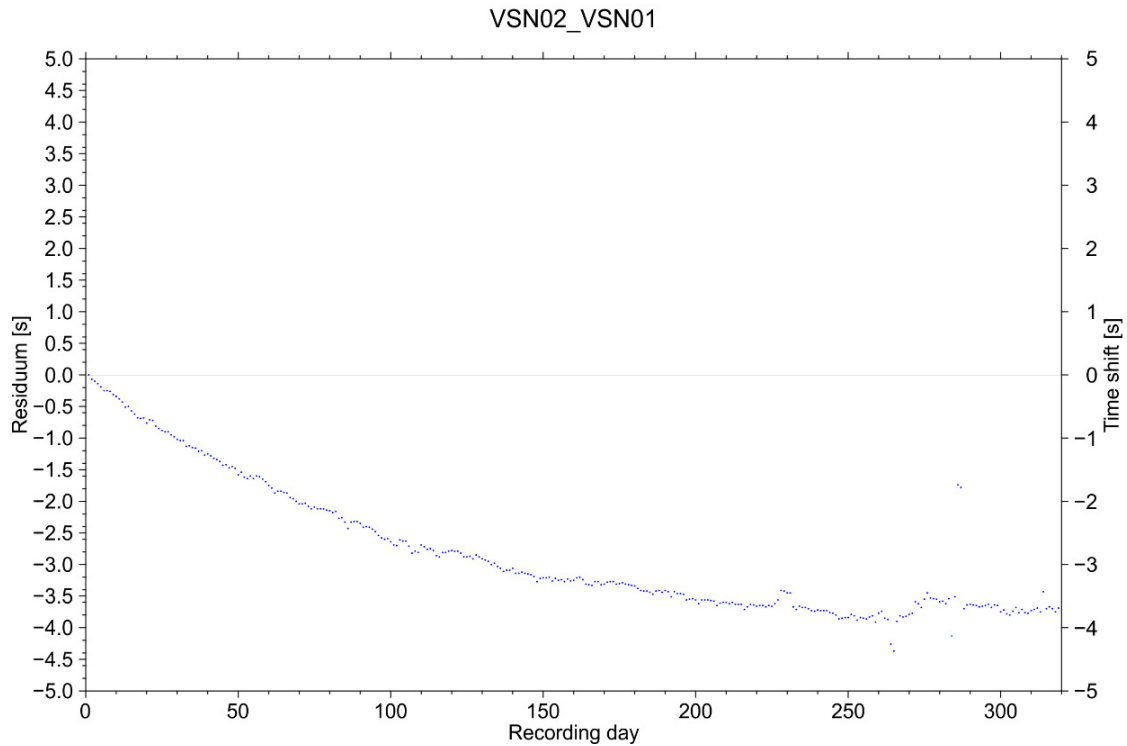
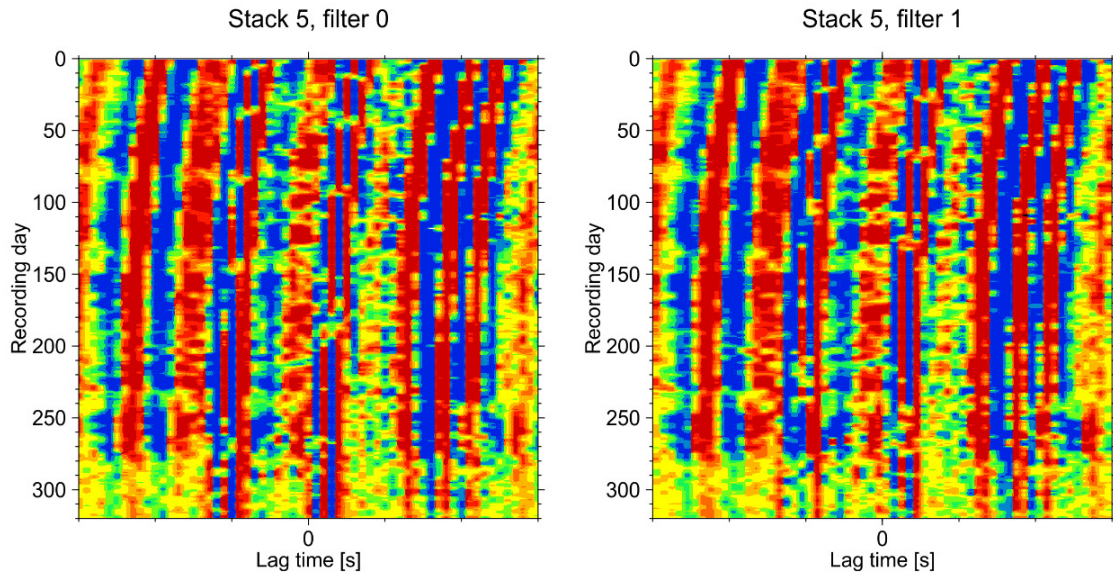


Figure S3. Daily cross-correlation plots (with and without bandpass filter of between 0.1-1.0 Hz) for the reference station VSN01 and the station VSN02 and the estimated clock drift curve for this station.

VSN03_VSN01, ZZ, Bandpass 1–10 s

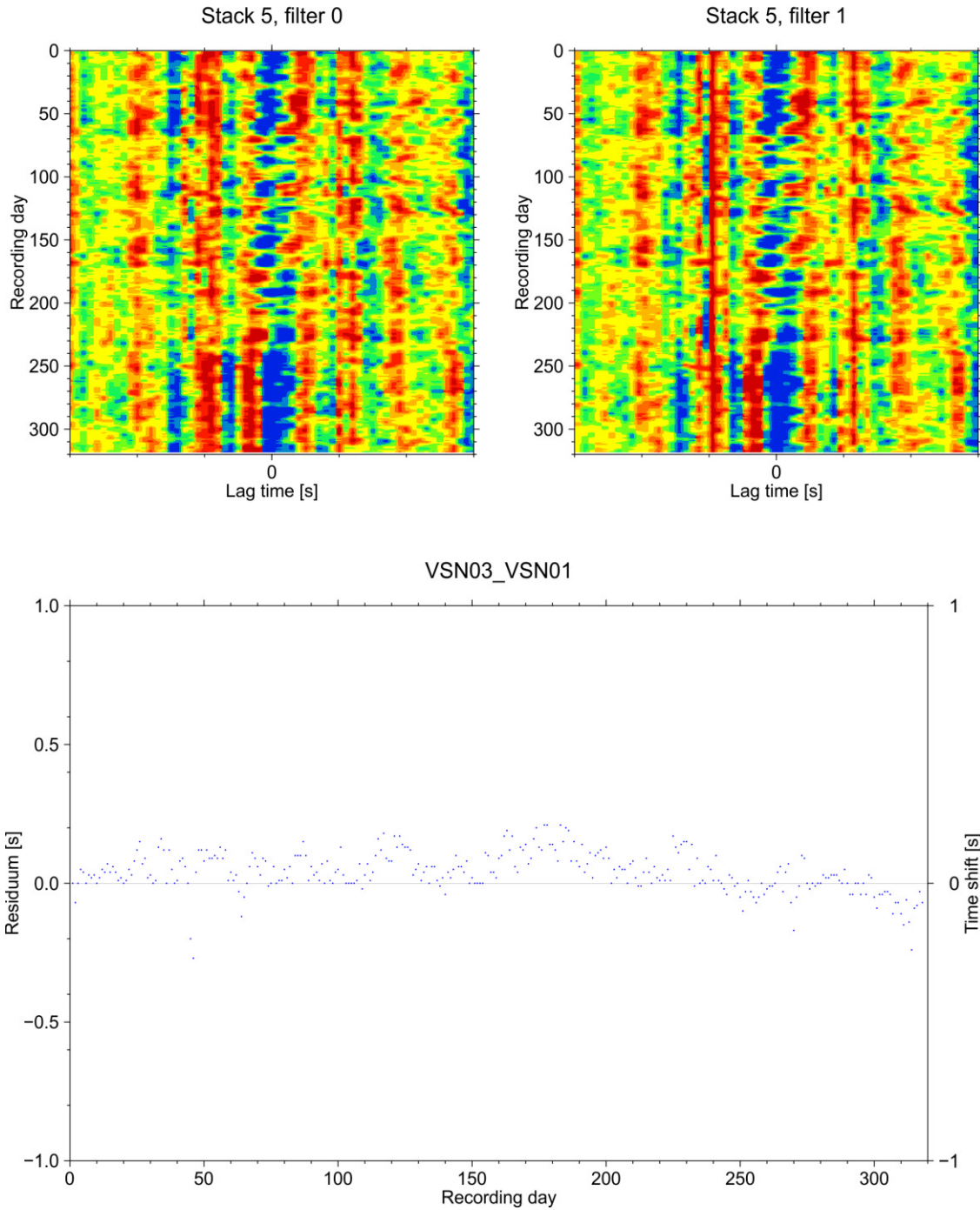


Figure S4. Daily cross-correlation plots (with and without bandpass filter of between 0.1-1.0 Hz) for the reference station VSN01 and the station VSN03 and the estimated clock drift curve for this station.

VSN04_VSN01, ZZ, Bandpass 1-10 s

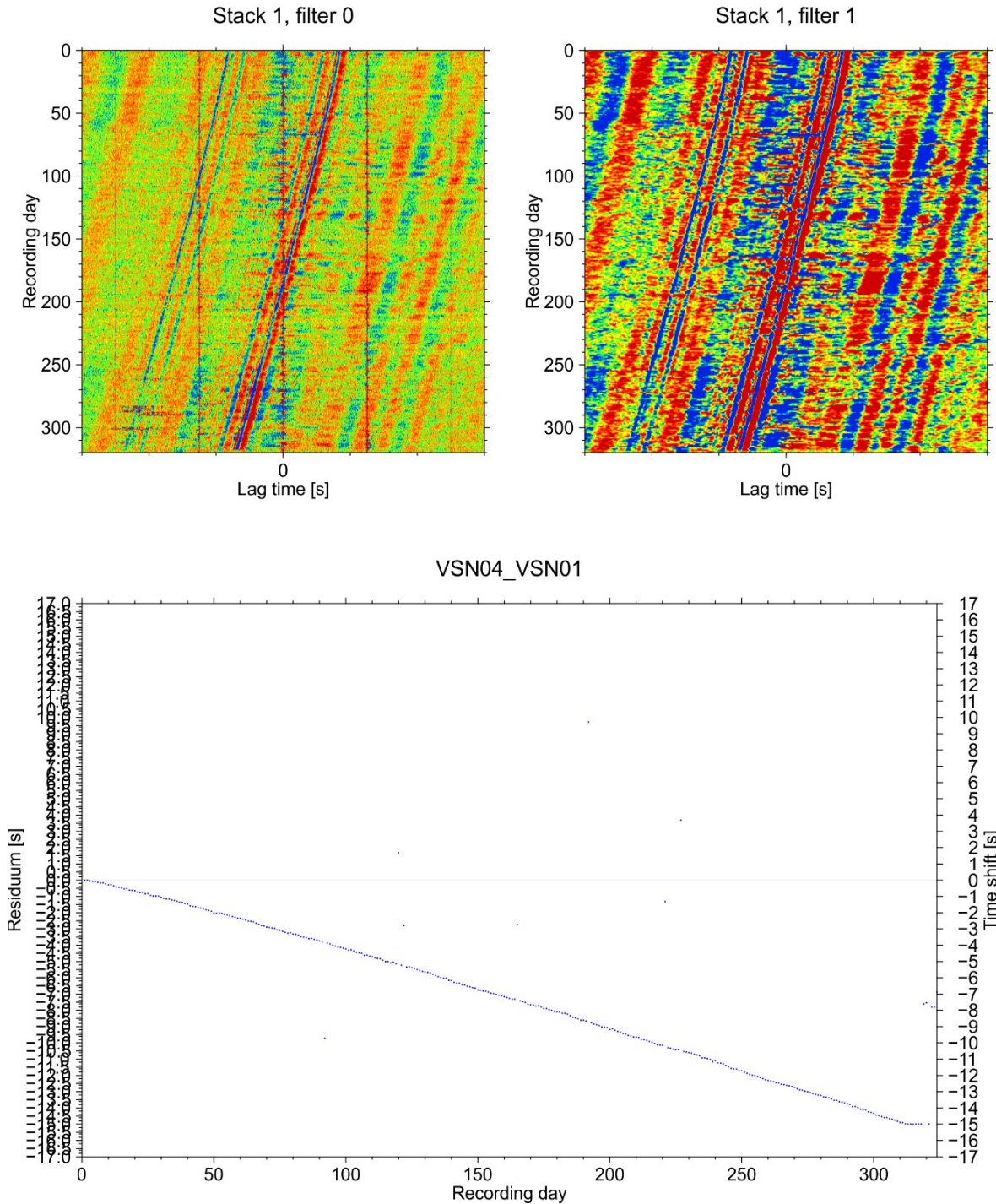


Figure S5. Daily cross-correlation plots (with and without bandpass filter of between 0.1-1.0 Hz) for the reference station VSN01 and the station VSN04 and the estimated clock drift curve for this station.

VSN05_VSN01, ZZ, Bandpass 1-10 s

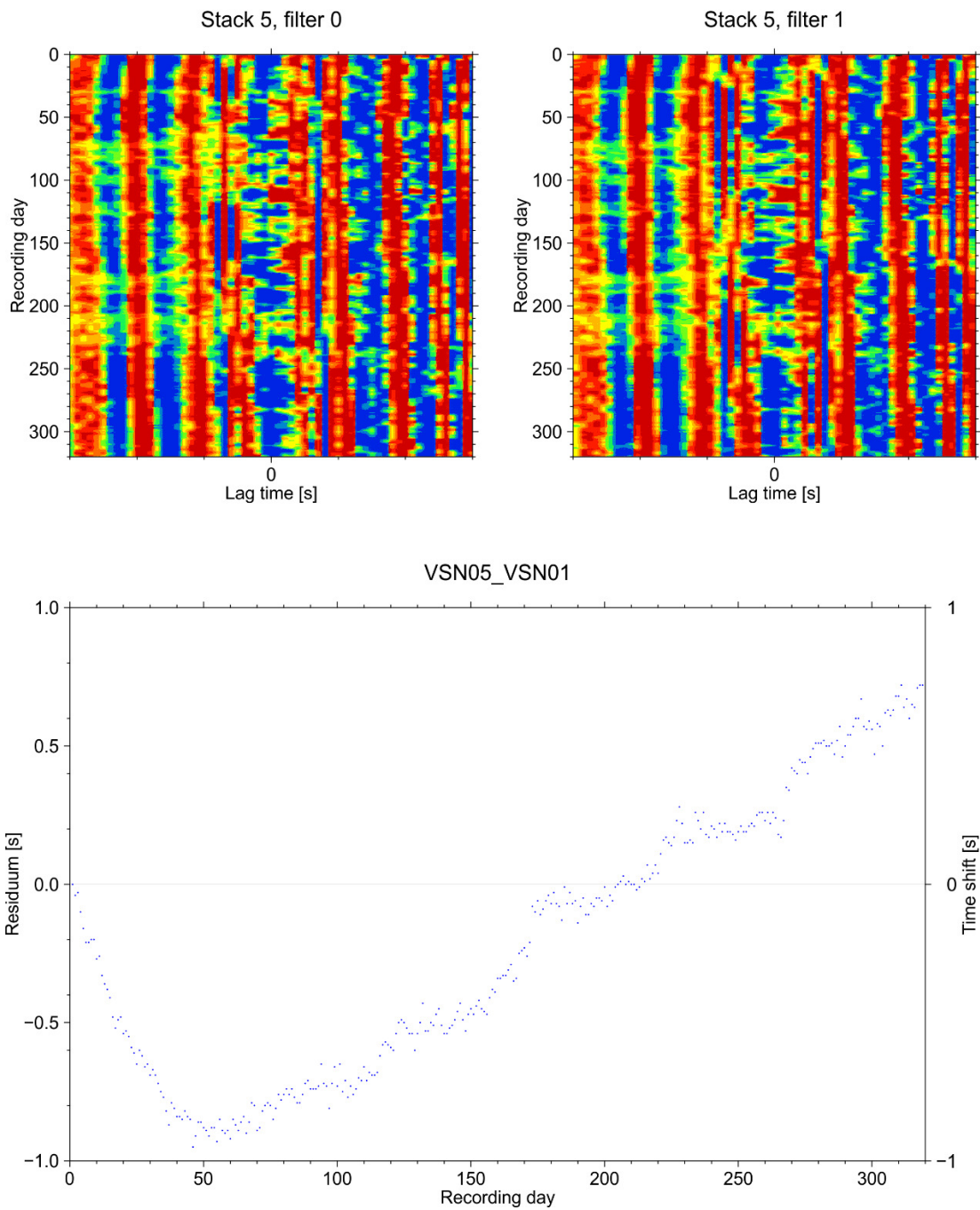


Figure S6. Daily cross-correlation plots (with and without bandpass filter of between 0.1-1.0 Hz) for the reference station VSN01 and the station VSN05 and the estimated clock drift curve for this station.

VSN06_VSN01, ZZ, Bandpass 1-10 s

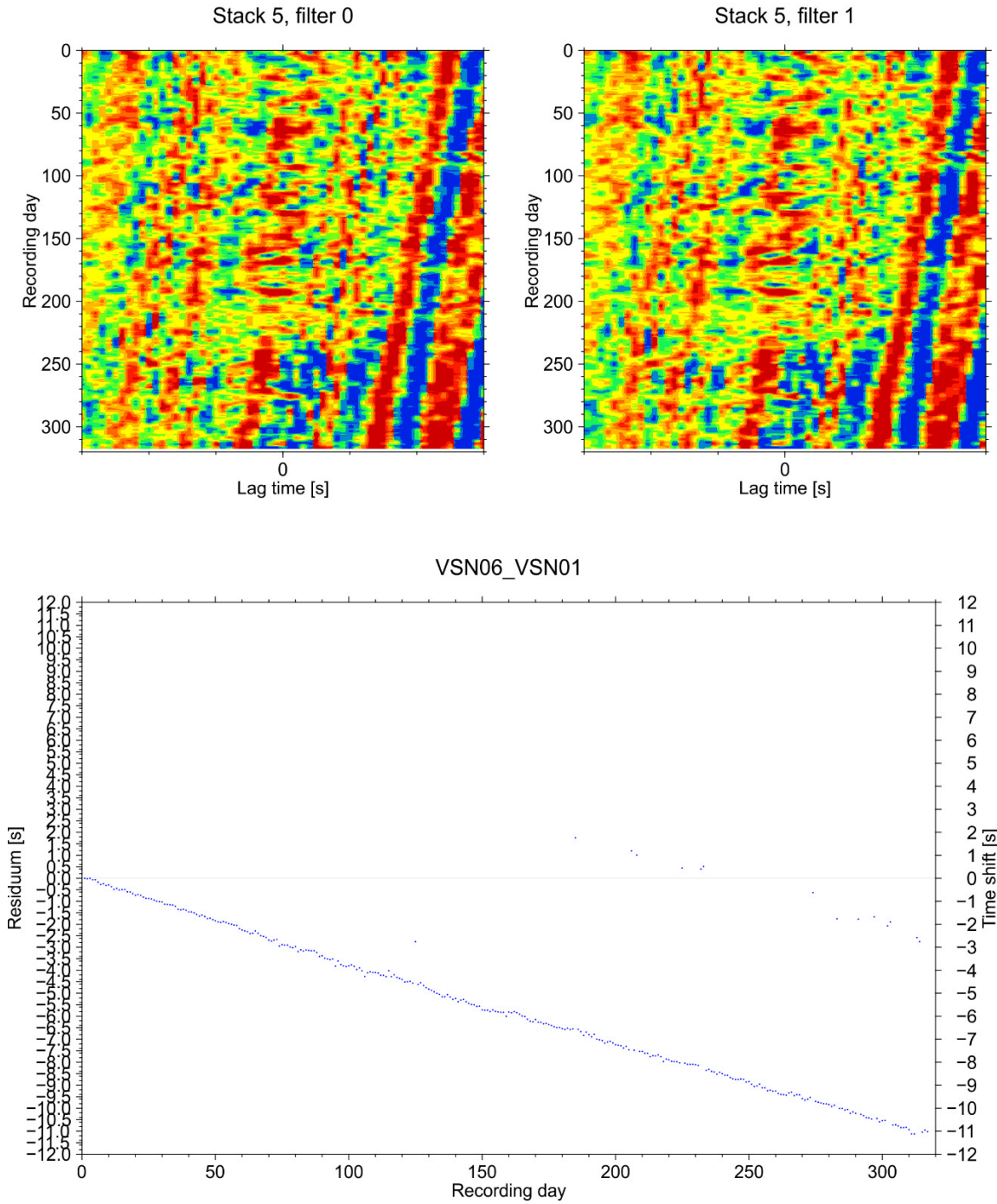


Figure S7. Daily cross-correlation plots (with and without bandpass filter of between 0.1-1.0 Hz) for the reference station VSN01 and the station VSN06 and the estimated clock drift curve for this station.

VSN07_VSN01, ZZ, Bandpass 1-10 s

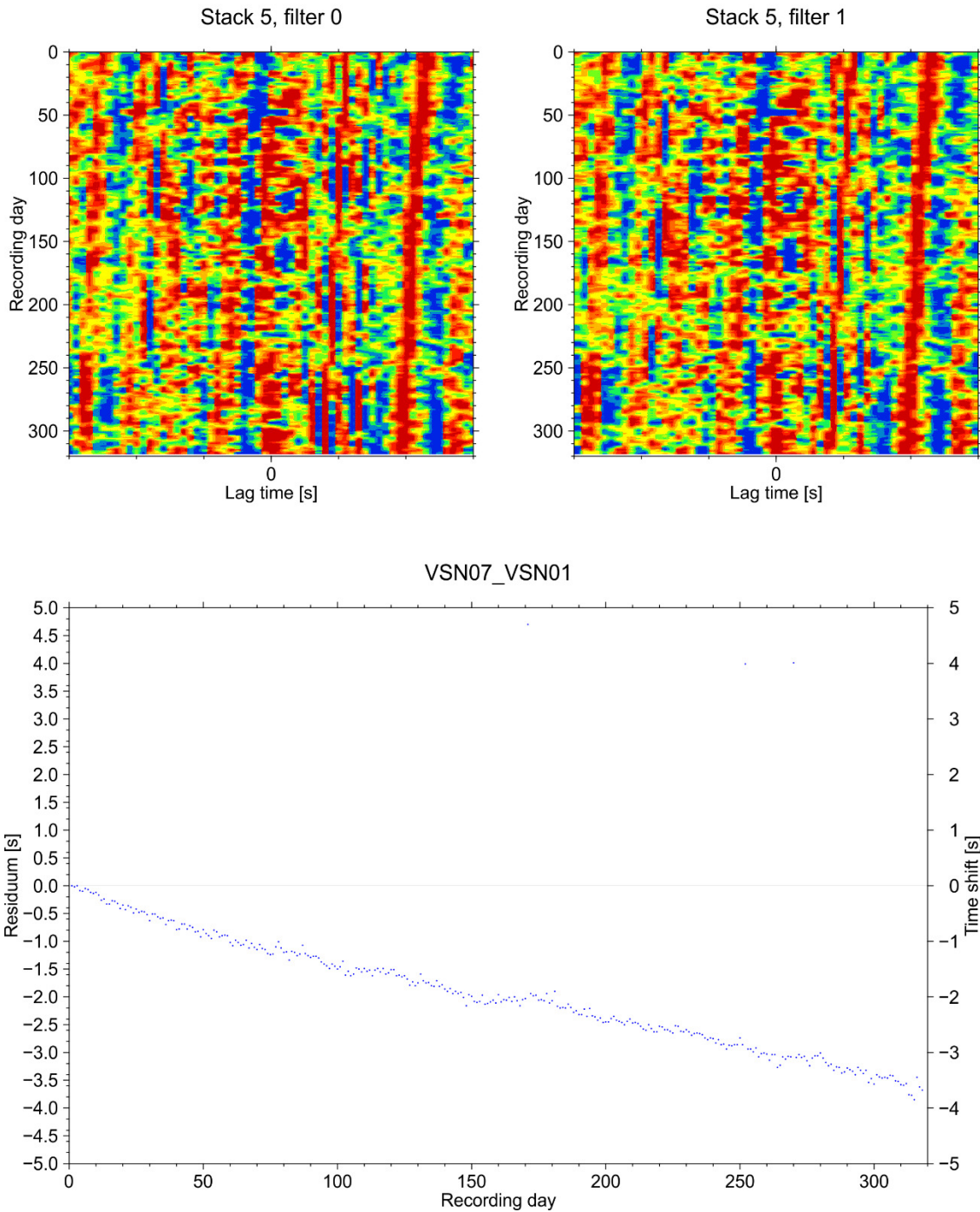


Figure S8. Daily cross-correlation plots (with and without bandpass filter of between 0.1-1.0 Hz) for the reference station VSN01 and the station VSN07 and the estimated clock drift curve for this station.

VSN08_VSN01, ZZ, Bandpass 1-10 s

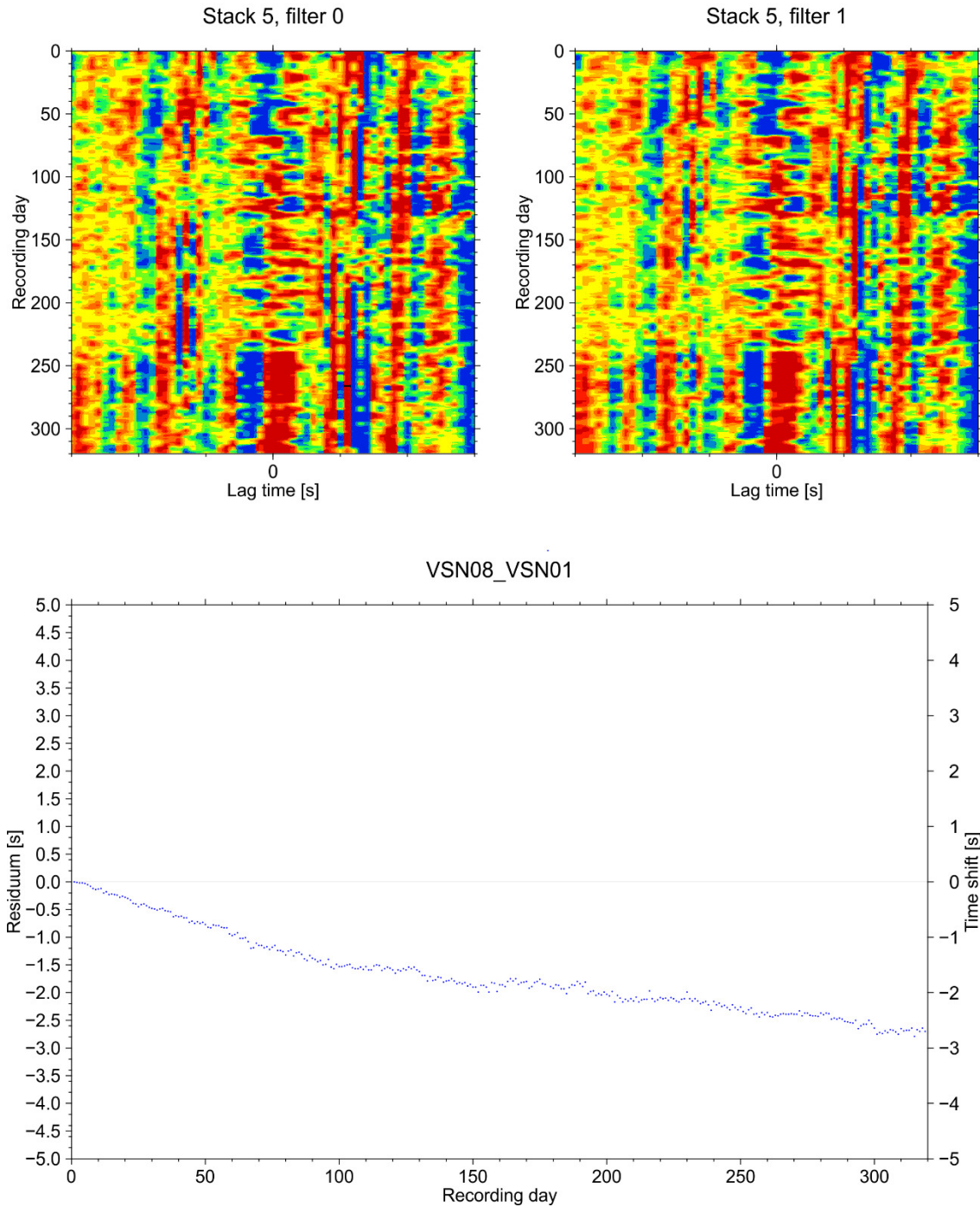


Figure S9. Daily cross-correlation plots (with and without bandpass filter of between 0.1-1.0 Hz) for the reference station VSN01 and the station VSN08 and the estimated clock drift curve for this station.

VSN09_VSN01, ZZ, Bandpass 1-10 s

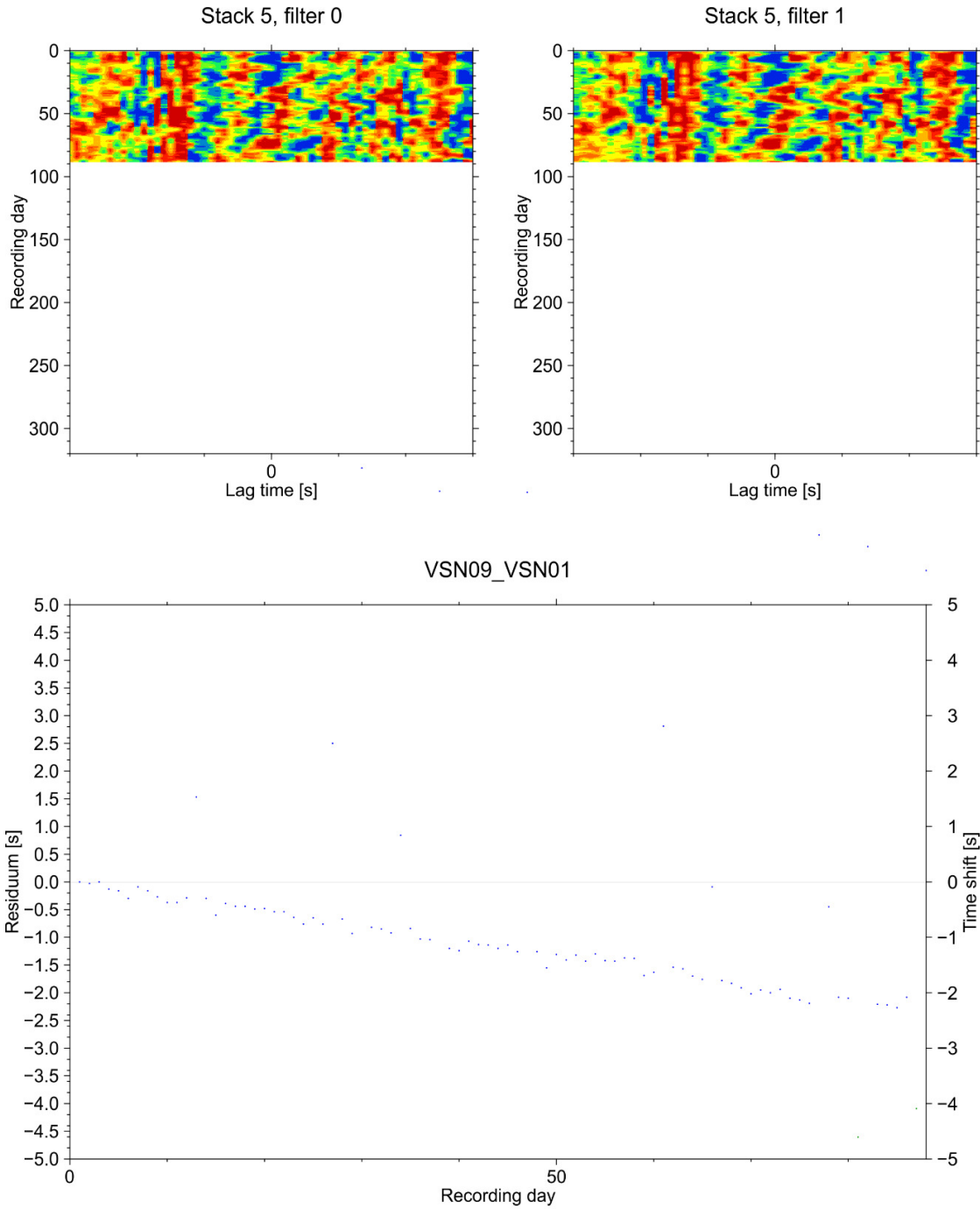


Figure S10. Daily cross-correlation plots (with and without bandpass filter of between 0.1-1.0 Hz) for the reference station VSN01 and the station VSN09 and the estimated clock drift curve for this station.

VSN10_VSN01, HH, Bandpass 1–10 s

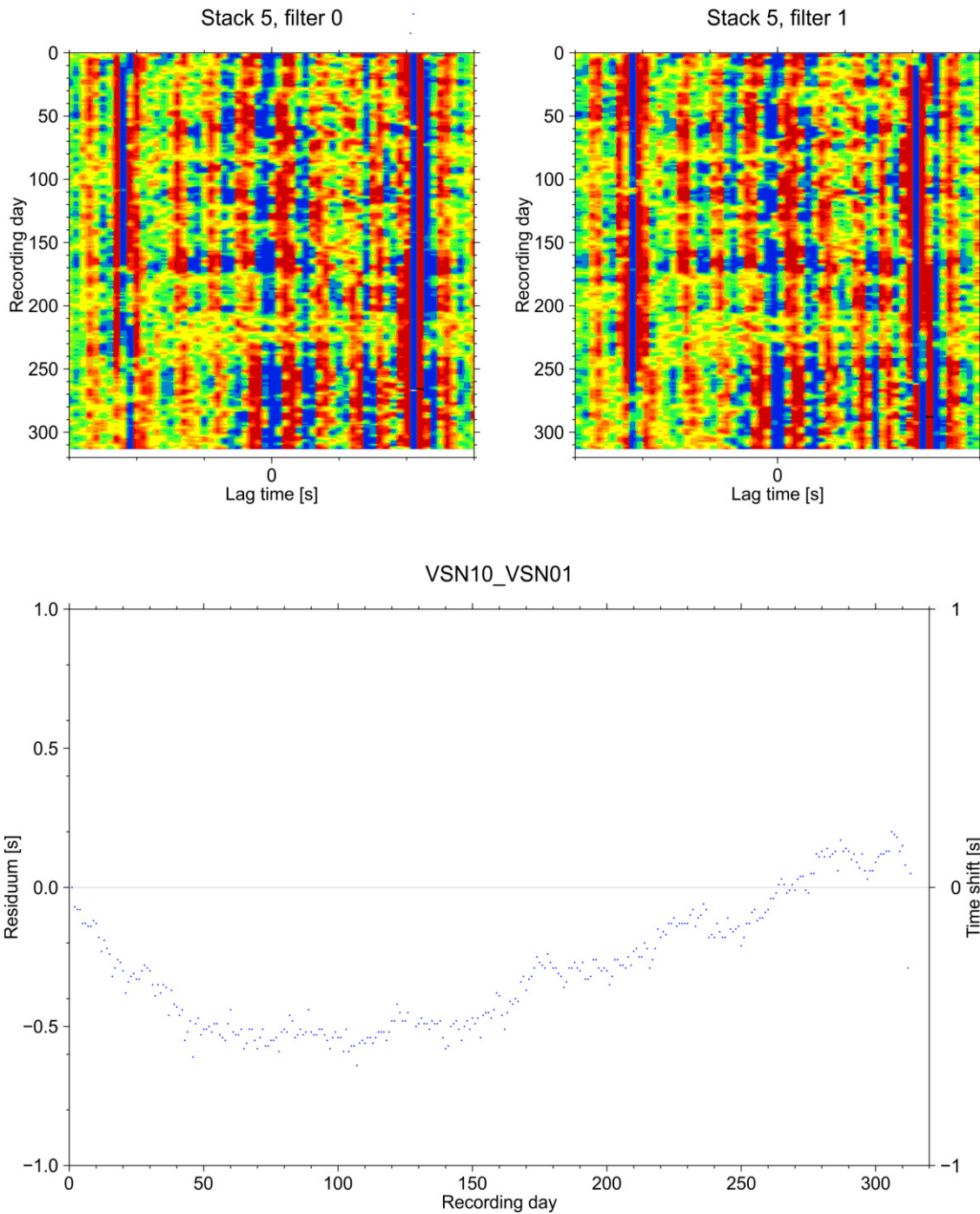


Figure S11. Daily cross-correlation plots (with and without bandpass filter of between 0.1-1.0 Hz) for the reference station VSN01 and the station VSN10 and the estimated clock drift curve for this station.

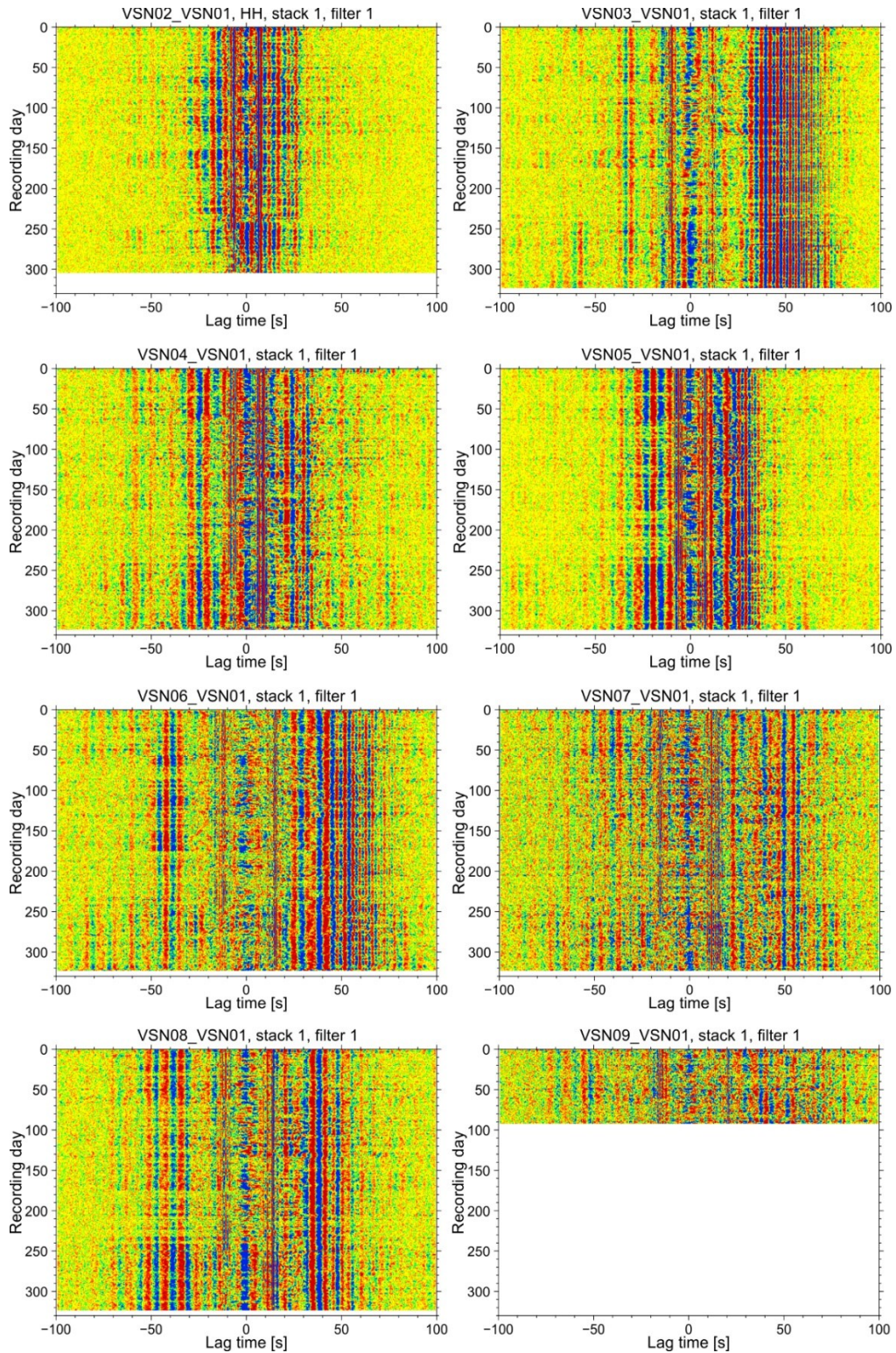


Figure S12. Daily cross-correlation plots between reference station VSNo1 and stations VSNo2-VSNog after the drift correction was applied.

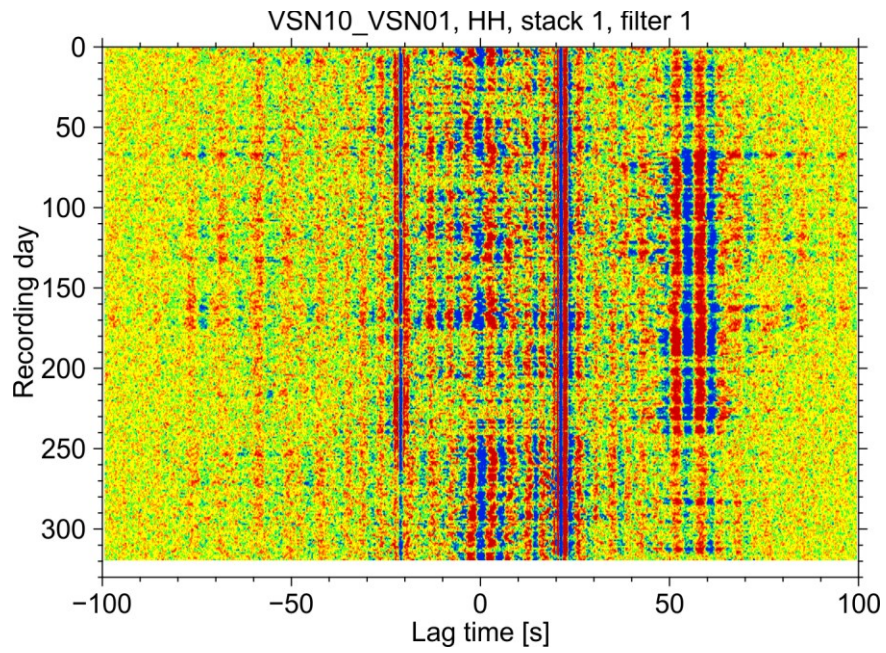


Figure S13. Daily cross-correlation plot between the reference station VSNo1 and the station VSN10 after the drift correction was applied.

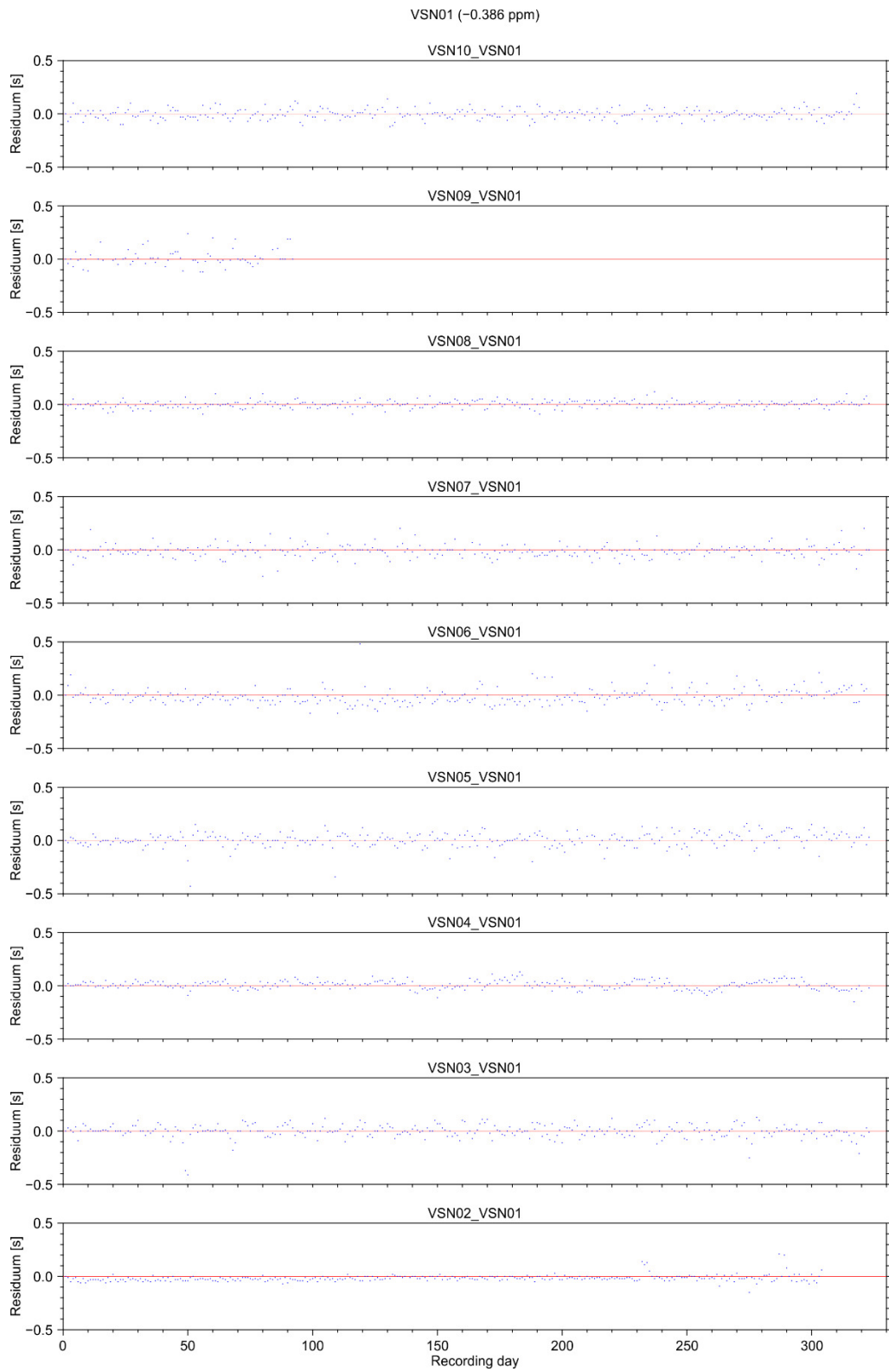


Figure S14. Residual clock drift after the cross-correlation procedure for all stations with the reference station VSN01.

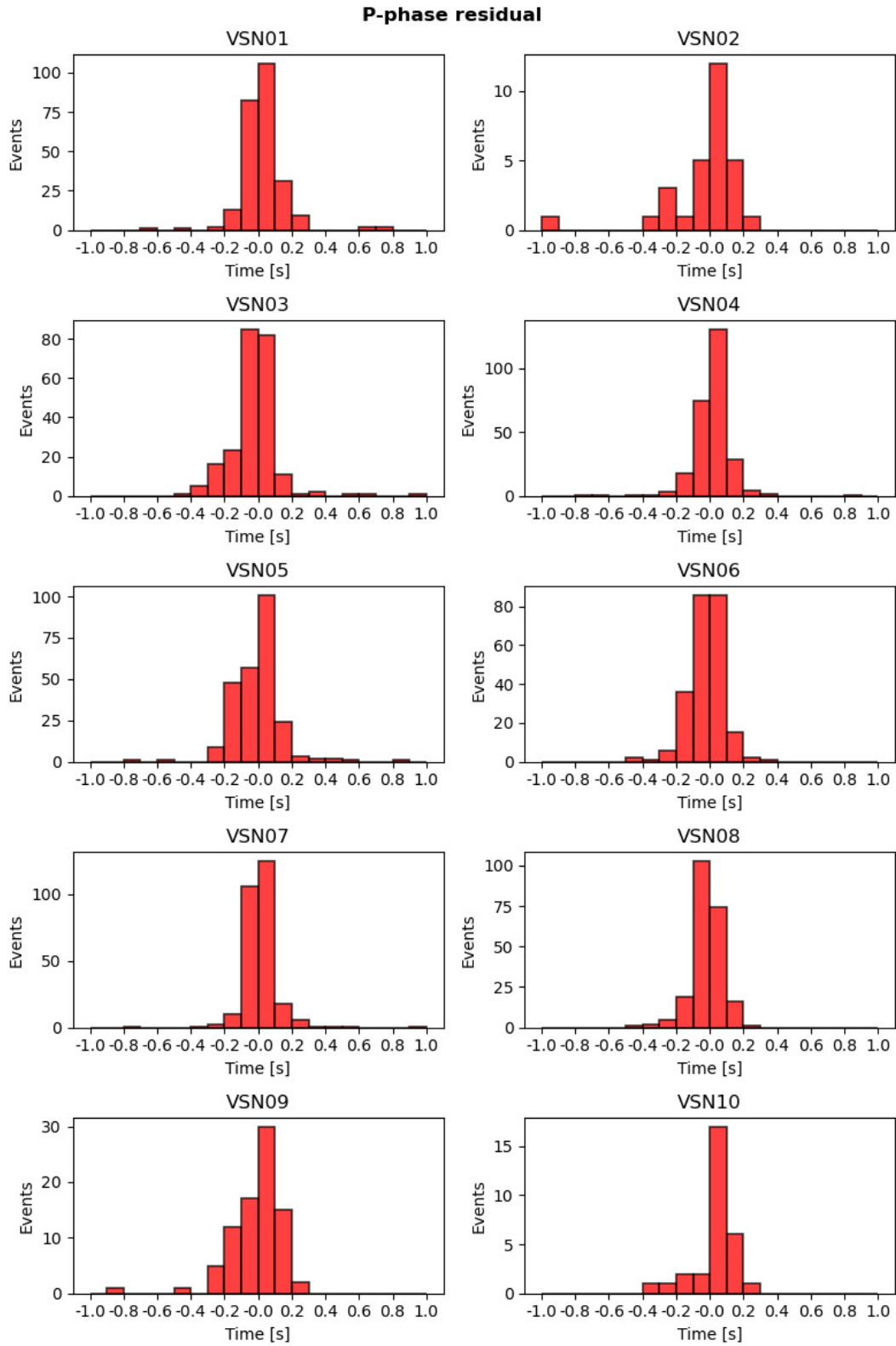


Figure S15. P wave travel time residuals for earthquake locations investigated in this study (locations using only picks from ocean bottom data).

S-phase residual

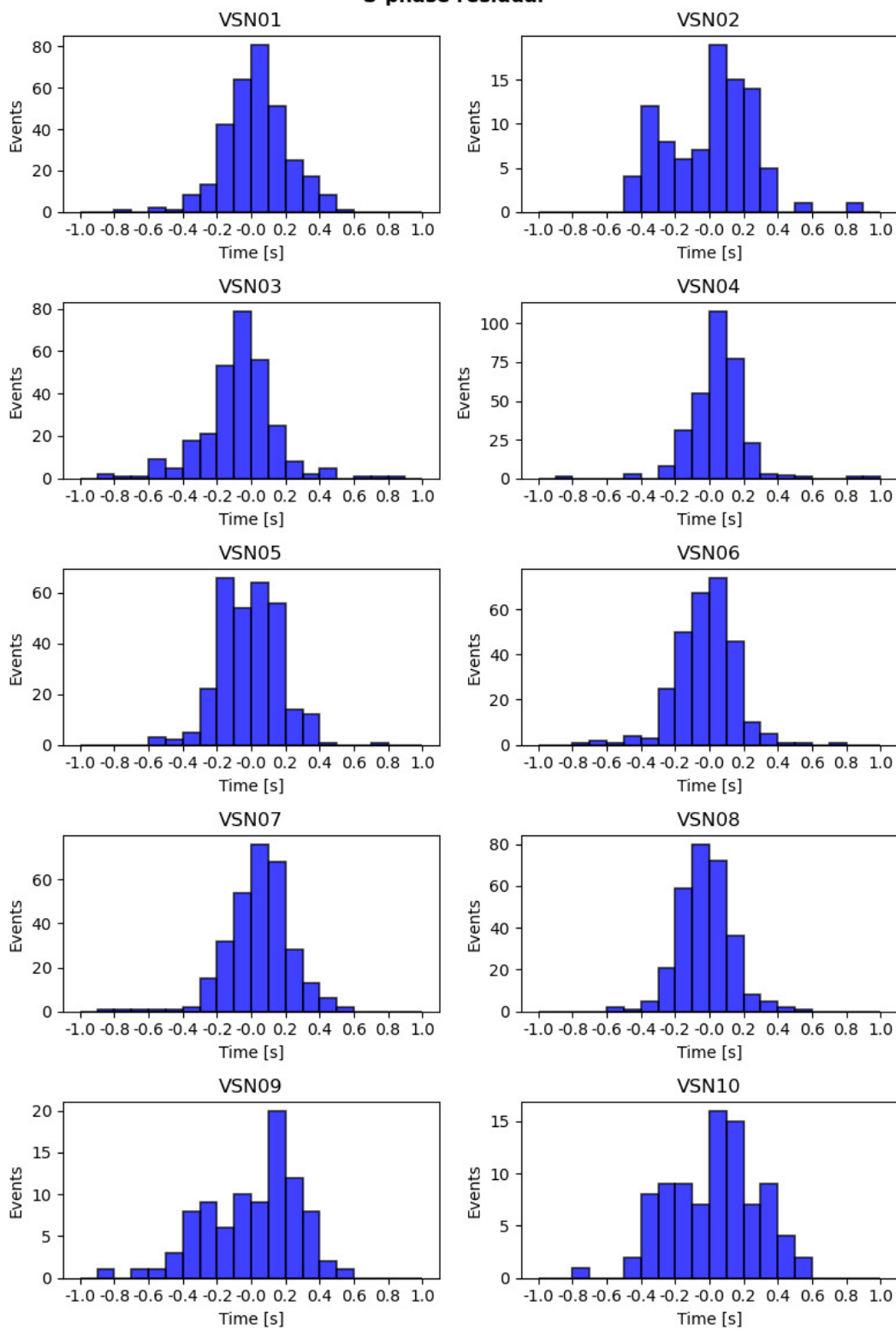


Figure S16. S wave travel time residuals for earthquake locations investigated in this study (locations using only picks from ocean bottom data).

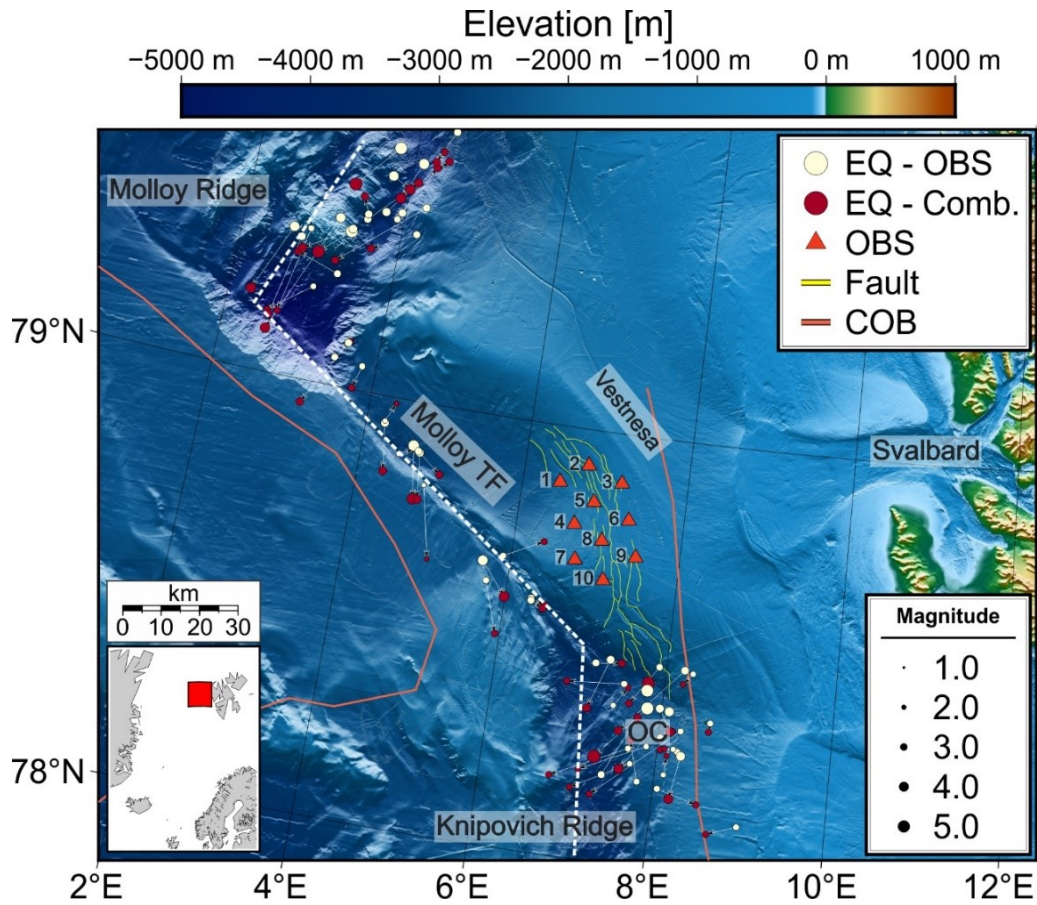


Figure S17. Regional map of seismicity showing the difference between observations from ocean bottom survey (OBS; white circles) and earthquake locations when phase picks from Norwegian National Seismic Network (NNSN) are included (Combined; red circles), with arrows showing the change in each individual event position.

Station	Longitude [°]	Latitude [°]	Water depth [m]	Duration [days]	Clock drift/skew from GPS [s]	Clock drift/skew from cross-correlation [s]
VSN01	6.448804	78.86864	1964	326	-10.84	-
VSN02	6.768042	78.91616	1507	326	-5.25	-3.69
VSN03	7.196293	78.88459	1251	326	-	-0.01
VSN04	6.691678	78.77620	1689	326	-	-15.59
VSN05	6.889579	78.83251	1544	325	-0.41	0.51
VSN06	7.334503	78.80105	1215	324	-	-11.14
VSN07	6.756920	78.69354	1526	326	-3.73	-3.79
VSN08	7.045052	78.74571	1415	325	-2.77	-2.80
VSN09	7.474187	78.71705	1164	94	-	-2.55
VSN10	7.122354	78.65478	1430	321	0.15	0.07

Table S1. True positions at the seafloor for seismometers used in the study (from active seismic survey), together with the water depth, data record duration in days, clock drift established from synchronization before deployment and after recovery (where possible), and clock drift estimated using cross-correlation.

